STRUCTURAL BEHAVIOUR AND DESIGN OF ALUMINIUM ALLOY-CONCRETE COMPOSITE STRUCTURAL MEMBERS

SHAFAYAT BIN ALI

A thesis submitted in partial fulfilment of the requirements of
Liverpool John Moores University
for the degree of Doctor of Philosophy

April 2023

List of Publications

Based on the present PhD study the following journal articles and conference papers have been published.

Journal papers:

Ali, S.B., Kamaris, G.S. and Gkantou, M. (2023) 'Flexural buckling behaviour of concrete-filled double skin aluminium alloy columns', *Engineering Structures*, 275, 115316.

Ali, S.B., Kamaris, G.S. and Gkantou, M. (2022) 'Flexural behaviour of concrete-filled double skin aluminium alloy tubes', *Engineering Structures*, 272, 114972.

Ali, S.B., Kamaris, G.S., Gkantou, M. and Kansara, K.D. (2022) 'Concrete-filled and bare 6082-T6 aluminium alloy tubes under in-plane bending: Experiments, finite element analysis and design recommendations', *Thin-Walled Structures*, 172, 108907.

Georgantzia, E., **Ali, S.B.**, Gkantou, M., Kamaris, G.S., Kansara, K.D. and Atherton, W. (2020) 'Flexural buckling performance of concrete-filled aluminium alloy tubular columns', *Engineering Structures*, 242, 112546.

Conference papers:

Ali, S.B., Kamaris, G.S. and Gkantou, M. (2022) 'Experimental investigation of concrete-filled double skin aluminium alloy tubes under in-plane bending', *131th HSTAM International Congress on Mechanics*, Patras, Greece.

Ali, S.B., Kamaris, G.S., Gkantou, M. and Kansara, K.D. (2022) 'Experimental investigation of concrete-filled and bare 6082-T6 aluminium alloy tubes under in-plane bending', *SLIIT International Conference on Engineering and Technology (SICET 2022)*, Paper No. 40.

Ali, S.B., Georgantzia, E., Kamaris, G.S., Gkantou, M. and Kot, P. (2022) 'Experimental study of square and rectangular hollow section aluminium alloy columns', *Journal of Physics: Conference Series*, 2198, 012046.

Georgantzia, E., **Ali, S.B.**, Gkantou, M., Kamaris, G.S., Kot, P. and Hashim, K. (2022) 'Finite element modelling of concrete-filled aluminium alloy tubular columns', *Journal*

of Physics: Conference Series, 2198, 012045.

Ali, S. B., Kamaris, G. S., Gkantou, M., Kansara, K. and Hashim, K. (2021) 'Numerical study of concrete-filled aluminium alloy tubular columns under eccentric compression', *IOP Conf. Series: Materials Science and Engineering*, 1058, 012010.

Georgantzia, E., **Ali, S.B.**, Gkantou, M., Kamaris, G.S., Kansara, K.D. and Atherton, W. (2021) 'Structural response of aluminium alloy concrete filled tubular columns', *9th European Conference on Steel and Composite Structures (Eurosteel 2021)*, Sheffield, UK.

Abstract

The use of aluminium alloys in the construction industry is rising due to their profound features including high strength-to-weight ratio, good corrosion resistance, ease of processing, low maintenance, high recyclability and aesthetic appearance. However, the low modulus of elasticity, welding difficulty and low melting point of aluminium have adverse effects on the performance of structural members made of aluminium alloys. In case of aluminium alloy tubular members, the structural performance can be improved with the addition of concrete infill, despite the different expansion of aluminium alloy and concrete. In concrete-filled aluminium tubular (CFAT) structural members, the aluminium tube increases the compressive performance of the concrete core due to the confinement effect, while the concrete core delays inward local buckling of the aluminium tube. Moreover, the self-weight of these structural members can be decreased further by replacing the inner concrete core with a hollow tube. Concrete-filled double skin aluminium alloy tubular (CFDSAT) member is made with two aluminium tubes and concrete infill between them. CFDSAT members retain all advantages of CFAT ones and additionally they have less self-weight. Moreover, these members offer better local and global stability because of the interaction of three components. Therefore, compared to steel-concrete composite members, CFDSAT members can be more efficient for structures situated in offshore areas and seismic-prone regions.

However, the research on the structural performance of aluminium alloy-concrete composite members is minimal. Therefore, this study investigates the behaviour of CFAT and CFDSAT structural members subjected to axial compression and bending. In the experimental programme of CFAT structural members, a total of 18 columns, including 9 CFAT and 9 bare aluminium tubular (BAT) specimens and 20 beams, including 10 CFAT and 10 BAT specimens are tested. The BAT structural members are tested for reference purposes and to assess the applicability of Eurocode 9 design standard. The experimental investigation of CFDSAT structural members includes 8 columns and 10 beams. The column tests are conducted using a pin-ended set-up for allowing the specimens to rotate around the buckling axis. The flexural members are tested in a four-point bending arrangement to spread out the maximum stress over the area between the two loading points. The material properties of aluminium alloy are

determined by tensile coupon tests. The structural responses obtained from the experiments are presented in terms of ultimate capacity, failure modes and load/moment versus mid-length defections curves. Finite element (FE) models of the structural members are developed by taking into account the geometric and material nonlinearities and validated against the experimental results. The validated models are adopted to conduct parametric studies to examine the effects of different design parameters on the behaviour of the structural members. In the absence of design rules for aluminium alloy-concrete composite structural members, design methodologies are proposed to predict the ultimate capacity of these composite members based on the Eurocode 4 framework.

To obtain information about the sustainability of aluminium alloy-concrete composite structural members, the life-cycle performance of CFAT and CFDSAT columns is investigated. Life-cycle assessment and life-cycle cost analysis methods are applied to evaluate the long-term environmental and economic aspects of these members, respectively. The cradle-to-grave system boundary is considered for these analyses to cover all the aspects of life-cycle. Finally, a comparison of the self-weight of these members is also presented.

The experimental results show that compared to the bare specimens, the counterpart composite specimens have remarkably improved ultimate capacity, stiffness and ductility due to the concrete infill and the improvement is more pronounced for the specimens with thinner sections. The FE parametric investigation reveals that the larger cross-sectional dimensions of the outer tube of composite members substantially improved the load-bearing capacity, while the cross-sectional dimensions of the inner tube have a negligible effect. Moreover, FE results show that higher grade concrete remarkably increased the strength of composite columns, while it has a less significant influence on the improvement of the flexural strength of composite beams. In the absence of design standards for aluminium alloy-concrete composite structural members, design methodologies are provided based on Eurocode 4 (2004) to determine the strength of these members. The self-weight comparison and sustainability study results indicate that CFDSAT structural member is lighter, while the CFAT member is less expensive and provides the lowest environmental impact than the other alternatives considered in this study.

Acknowledgements

The work presented in this thesis was conducted under the supervision of Dr Georgios Kamaris and Dr Michaela Gkantou. I would like to express my deepest gratitude for their exceptional technical support, mentoring guidance and continuous encouragement during the period of my candidature.

I also would like to extend my gratefulness to Dr Kunal D. Kansara and Dr William Atherton for their guidance and support.

I gratefully acknowledge the financial support of the Faculty of Engineering and Technology of Liverpool John Moores University.

My sincere appreciation is dedicated to all the staff of the School of Civil Engineering and Built Environment of Liverpool John Moores University. Especially, I would like to thank Mr Clive Eyre, Mr Anthony Owens, Mr Mal Feegan, Mr Neil Kilpatrick, Mr Harvey Thompson, Mr Chris Byrne, Mr Nathan Prendergast, Mr Alan Jones and Mr Ian Munford for their continuous technical support during my experimental work. I am also thankful to Alexia Montaubin, Tricia Waterson and Natasha Walden-Jones for their administrative assistance.

I wish to thank my friends and colleagues for their support and engouement during my work.

Last but not least, I would like to express my heartfelt thankfulness to my parents, my wife, my brother and my aunty for their endless support, motivation and unconditional love.

Table of Contents

List of Figures

List of Tables

Nomenclature

Latin letters

A	Cross-sectional area of aluminium tube
A_{eff}	Effective cross-sectional area of aluminium tube
A_i	Cross-sectional area of inner tube
A_o	Cross-sectional area of outer tube
A_c	Cross-sectional area of concrete infill
B	Outer width of cross-section
B_i	Width of inner tube
B_o	Width of outer tube
BAT	Bare aluminium tube
CDP	Concrete damage plasticity
COV	Coefficient of variation
CFAT	Concrete-filled aluminium alloy tube
CFDSAT	Concrete-filled double skin aluminium alloy tube
CFDSST	Concrete-filled double skin steel tube
CFRP	Carbon fibre-reinforced polymer
CFST	Concrete-filled steel tube
D	Outer depth of cross-section
D_i	Depth/diameter of inner tube
D_o	Depth/diameter of outer tube
E	Modulus of elasticity
E_a	Modulus of elasticity of aluminium tube
$E_{a,i}$	Modulus of elasticity of inner aluminium tube
$E_{a,o}$	Modulus of elasticity of outer aluminium tube
E_c	Modulus of elasticity of concrete infill
e_0	Initial loading eccentricity
FE	Finite element
FEA	Finite element analysis
f	Tensile stress
f_c	Concrete cylinder compressive strength

f_{cu}	Concrete cube compressive strength
$f_{0.1}$	0.1% proof stress
$f_{0.2}$	0.2% proof stress
$f_{0.2,i}$	0.2% proof stress of inner tube
$f_{0.2,o}$	0.2% proof stress of outer tube
f_{true}	True stress
f_u	Static ultimate tensile stress
h_n	Distance between plastic neutral axis and centre line of cross-section
I_a	Moment of inertia of aluminium tube
$I_{a,i}$	Moment of inertia of inner aluminium tube
$I_{a,o}$	Moment of inertia of outer aluminium tube
I_c	Moment of inertia of concrete infill
k_e	Correction factor for concrete infill
K_i	Initial flexural stiffness
K_s	Flexural stiffness at serviceability limit state
L	Length of specimen
L_{eff}	Effective length of column
L_l	Distance between two loading points
L_s	Distance between two supports
LCA	Life-cycle assessment
LCCA	Life-cycle cost analysis
LVDT	Linear variable displacement transducers
n	Strain hardening exponent in Ramberg-Osgood expression
N	Applied compressive load
N_{pl}	Plastic resistance under uniform compression
N_{cr}	Critical elastic buckling load
N_c	Design resistance under uniform compression
N_u	Ultimate load of column resulted from test and FEA
$N_{u,EC9}$	Ultimate load based on Eurocode 9
$N_{u,Test}$	Ultimate load of tested column
$N_{u,FE}$	Ultimate load of column resulted from FEA
$N_{u,prop}$	Design ultimate load of column

M_{el}	Elastic moment capacity of cross-section
M_{pl}	Plastic moment capacity
$M_{pl,m}$	Plastic moment capacity of member
$M_{pl,cr}$	Plastic moment capacity of cross-section
M_u	Flexural strength
$M_{u,EC9}$	Flexural strength based on Eurocode 9
$M_{u,FE}$	Flexural strength obtained from FE analysis
$M_{u,prop}$	Design flexural strength
$M_{u,Test}$	Flexural strength obtained from test
P	Applied load on beam
R	Rotation capacity
RHS	Rectangular hollow sections
SHS	Square hollow sections
t	Thickness of cross-section
t_o	Thickness of outer tube
t_i	Thickness of inner tube
W_{el}	Elastic modulus
W_{eff}	Effective modulus
W_{pl}	Plastic modulus
W_{pla_i}	Plastic modulus of inner tube
W_{pla_o}	Plastic modulus of outer tube
W_{plc}	Plastic modulus of concrete
$W_{pla_i,n}$	Plastic modulus of inner tube at $2h_n$
$W_{pla_o,n}$	Plastic modulus of outer tube at $2h_n$
$W_{plc,n}$	Plastic modulus of concrete at $2h_n$

Greek letters

α	Hollow ratio
α_1	Imperfection factor
α_c	Concrete coefficient
α_s	Shape factor
β	Width-to-thickness ratio

γ_{M1}	Partial factor of safety
δ	Lateral deflection at the mid-height
δ_{av}	Average vertical displacement at two loading points
δ_v	Vertical displacement at the mid-span
δ_i	Vertical displacement at the mid-span corresponding to $0.2M_u$
δ_s	Vertical displacement at the mid-span corresponding to $0.6M_u$
δ_u	Vertical displacement at the mid-span corresponding to M_u
δ_y	Vertical displacement at the mid-span corresponding to yield moment
ε	Strain
ε_{ln}^{pl}	Logarithmic plastic strain
ε_f	Elongation after fracture
ε_{max}	Maximum strain
ε_{min}	Minimum strain
κ_{pl}	Curvature at M_{pl}
κ_u	Curvature at which the moment drops back to M_{pl}
$\bar{\lambda}$	Member slenderness
$\bar{\lambda}_0$	Limit of horizontal plateau
μ	Ductility index
ϕ	Parameter
ρ_c	Reduction factor for local buckling
χ	Reduction coefficient for flexural buckling
ω_g	Global imperfection amplitude
ω_l	Local imperfection amplitude

CHAPTER 1 : INTRODUCTION

1.1 Background

The earliest application of aluminium alloys in building structures started in the 1950s (Mazzolani, 1995) and then its use spread to various structural applications. The increasing growth of aluminium alloys as structural metal in load-bearing structures is due to their high strength, low density, good corrosion resistance, ease of processing, low maintenance, high recyclability and aesthetic appearance (Georgantzia *et al.* 2021). The density of aluminium alloy is approximately one-third of steel. Due to their high corrosion resistance, aluminium alloys often need no treatment, paint or coating against rust and corrosion which reduces maintenance costs. The recycling process of aluminium alloys requires only 5% energy of the production of the original metal, resulting in environmental and economic benefits. Moreover, recycled aluminium retains all the properties of virgin metal. Furthermore, the aesthetic appearance of aluminium alloys makes them suitable for architectural and structural applications. Despite these profound advantages, the low modulus of elasticity, welding complexity and low melting point of aluminium alloys affect the performance of aluminium alloy structures. The structural performance of aluminium alloy hollow members can be improved by filling concrete in the hollow space.

Concrete-filled steel tubular (CFST) structural members are increasingly used in the construction sector due to their advantages over reinforced concrete or bare steel members. The advantages include higher load-bearing capacity with the same cross-sectional area, good ductility, elimination of temporary formwork for concrete casting and high-speed construction (Morino *et al.*, 2001; Morino and Tsuda, 2002; Lam and Wong, 2005; Starossek *et al.*, 2010). The self-weight of CFST members can be reduced by using aluminium tubes instead of steel ones. Concrete-filled aluminium alloy tubular (CFAT) structural members benefit from both materials, i.e., the compressive behaviour of concrete improves by the confinement provided by the hollow aluminium tube and the inward buckling of aluminium section is prevented by the concrete infill.

The self-weight of CFAT structural members can be decreased further by applying the double skin technique. Concrete-filled double skin aluminium alloy tubular (CFDSAT) structural members are usually made with two aluminium alloy tubes and the space

between them is filled with concrete. Due to the absence of inner concrete core, these members are much lighter than the CFAT ones. By using these members, the dead load of structures can be reduced remarkably which results in decreasing the size of the foundation and saving the materials, labour costs and construction time (Wang *et al.*, 2021). Moreover, these less self-weight members can provide better seismic performance to structures, as the internal forces developing in the elements is proportional to the mass of the structure (Chopra, 2017). Furthermore, these members have better local and global stability because of the interaction of three components (Alqawzai *et al.*, 2020) and improved fire resistance owing to the concrete infill and inner tube being thermally protected by the outer tube (Li *et al.*, 2012). Therefore, these structural members can be used for offshore wind turbines, offshore oil platforms, seaside piers, tall buildings and bridges in seismic-prone regions.

Despite all these advantages, the research on CFAT and CFDSAT structural members is still limited. Moreover, existing design standards for composite members are mainly developed based on the design specifications of steel structural members which may not suit for the design of CFAT and CFDSAT members. To complement the existing knowledge and expand the usage of aluminium alloy concrete-composite members in structural applications, sound research needs to be carried out. Hence, the present study aims to investigate the structural behaviour of CFAT and CFDSAT columns and beams by means of experimental study and numerical analysis. In this study, 6082-T6 aluminium alloy is used, as it is gaining popularity in structural applications owing to its favourable properties, such high strength, good corrosion resistance and weldability (Mazzolani, 1995; Kissell and Ferry, 2002).

To achieve a balance between the environment and the economy, it is important to have the sustainable design of structures (McLennan, 2004). Sustainability of structural members can be evaluated by determining their environmental loads and economic impacts across their life-cycle. Life-cycle assessment (LCA) and life-cycle cost analysis (LCCA) are well-known analytical frameworks for assessing the sustainability of a product. LCA method determines the environmental performance of a product during different stages of life-cycle, including raw material collection, production, transportation, construction and disposal after end-of-life (BS EN ISO 14040, 2006). LCCA method estimates the cost of a product related to its life span (Russell-Smith and

Lepech, 2009). In this study, these two frameworks are applied to evaluate the sustainability of aluminium alloy-concrete composite structural members.

1.2 Aim

This study aims to investigate the structural behaviour of CFAT and CFDSAT structural members subjected to axial compression and pure bending, provide design recommendations and determine the sustainability of these members.

1.3 Objectives

The key objectives of this research have been identified as follows:

- Investigate the structural performance of CFAT columns under concentric axial compression, for varying cross-sectional slenderness, cross-sectional aspect ratios and concrete strengths.
- Study the flexural behaviour of CFAT beams subjected to pure in-plane bending, for different cross-sectional slenderness, cross-sectional aspect ratios and concrete strengths.
- Investigate the structural response of CFDSAT columns under concentric axial compressive load, for varying hollow ratios, member slenderness, cross-sectional slenderness of hollow tubes and concrete strengths.
- Examine the flexural performance CFDSAT beams subjected to pure in-plane bending, for varying hollow ratios, cross-sectional slenderness of the outer and inner sections and concrete strengths.
- Propose design methodologies to predict the ultimate capacity of aluminium alloy-concrete composite columns and beams.
- Assess the sustainability of CFAT and CFDSAT structural members by calculating the amount of CO_2 emission and cost related to their life-cycle.

1.4 Outline of the thesis

This thesis has been structured into the following 9 chapters:

Chapter 1 presents a brief introduction of the birth of aluminium alloy, the advantages of aluminium alloy-concrete composite structural members and the necessity of

evaluating life-cycle performance. In addition, the main aim, objectives and the outline of the thesis are also included.

Chapter 2 contains a comprehensive review of the literature relevant to the present study. The related experimental, theoretical and numerical studies of BAT, CFST CFAT, concrete-filled double skin steel tube (CFDSST) and CFDSAT structural members are presented.

Chapter 3 provides the methodology used to investigate the structural behaviour of CFAT and CFDSAT columns and beams. Some general assumptions related to finite element (FE) modelling and analysis conducted throughout the study are also described in this chapter.

Chapter 4 presents the structural performance of BAT and CFAT columns subjected to concentric axial compression. The results obtained from the experimental programme and FE analysis are described. Design recommendations for CFAT columns are also provided.

Chapter 5 reports experimental and numerical studies on the flexural behaviour of BAT and CFAT beams. Using the test and FE data, the cross-sectional slenderness limits of Eurocode 9 (2007) are assessed and design methodology for CFAT flexural members is suggested.

Chapter 6 experimentally and numerically studies the flexural buckling behaviour of CFDSAT columns. The effect of the hollow ratio, the member slenderness, the cross-sectional slenderness of the hollow tubes and the concrete strength on the structural response of CFDSAT columns are evaluated and presented. Finally, a design methodology for CFDSAT columns is proposed.

Chapter 7 presents the structural response of CFDSAT members under in-plane bending by means of experimental study and numerical analysis. The influence of cross-sectional slenderness of inner and outer tubes, hollow ratio and concrete compressive strength on the flexural behaviour of CFDSAT beams are investigated and reported based on the results of a numerical parametric study. In the end, design guidelines are suggested for this structural member.

Chapter 8 assesses the sustainability of CFAT and CFDSAT columns and compared the results with that of conventional a CFST column. A comparison of the self-weight of the columns is also presented.

Chapter 9 provides the key findings and overall conclusions of this research study. Moreover, some recommendations for future study are also given.

CHAPTER 2 : LITERATURE REVIEW

2.1 Introduction

Research on aluminium alloy structural members has been started in the middle of the previous century. This chapter covers a review of previous research works on BAT, CFST, CFAT, CFDSST and CFDSAT structural members along with the definition, advantages and extrusion process of aluminium alloys.

2.2 Aluminium Alloy

2.2.1 Definition and benefits

Aluminium alloys are made by adding different alloying elements, such as copper, silicon, manganese, magnesium, zinc and lithium (Davis, 2001). The alloys are divided into two major categories, namely wrought alloys and casting alloys. Both alloys are further subdivided into heat-treatable and non-heat-treatable alloys. Alloys are identified by a four-digit numbering system, where the first digit refers to the alloying element, the second digit indicates the modification of the specific alloy and the third and fourth digits identify the specific alloy in the series (Kaufman, 2000). For example, in alloy 6105, the digit 6 indicates that it is from the aluminium-magnesium-silicon family, 1 indicates that it is the first modification to the original alloy 6005 and 05 identifies that it is in the 6xxx series. Table 2.1 features the different alloying elements assigned to each series.

Table 2.1: Different alloying elements assigned to each series (Davis, 2001).

Alloy series	Alloying element
1xxx	Pure Aluminium (99%)
2xxx	Copper
3xxx	Manganese
4xxx	Silicon
5xxx	Magnesium
6xxx	Magnesium and Silicon
7xxx	Zinc
8xxx	Other

The temper designations are used along with the numbering system to indicate what type of tempering treatment has been done to improve the mechanical properties of the aluminium alloys. These designations are alphabetic and added to the alloy number with

a dash. The basic temper designations are described in Table 2.2.

Table 2.2: Summary of basic tempers of aluminium alloys and the corresponding subdivisions (Kaufman, 2000).

Temper designation	Description	Subdivision
F (fabricated)	Applies to wrought and cast alloys that are fabricated using some shaping process without any special control over heat treatment or strain hardening process	-
O (annealed)	Applies to wrought alloys which are annealed to improve workability, ductility and toughness	-
H (strain-hardened)	Applies to alloys which have their strength increased by strain hardening, with or without additional thermal treatments	1st digit - thermal treatment type 2nd digit - degree of strain hardening
W (solution heat-treated)	Applies to alloys that are aged naturally and spontaneously at ambient temperature after solution heat treatment	-
T (thermally treated)	Applies to wrought and cast alloys that are strengthened by thermal treatment, followed by, natural ageing or artificial ageing. Naturally aged alloys are T1, T2, T3 and T4 and artificially aged alloys are T5, T6 and T9.	1st digit - thermal treatment type

The increasing growth of aluminium alloys in the construction industry is due to their advantageous properties, such as lightweight, good corrosion resistance, easily to be extruded, high strength at lower temperature and high recyclability. The density of aluminium alloy is 2700 kg/m^3 which is approximately one-third of the density of steel (7850 kg/m^3). Naturally generated oxide layer protects the aluminium from corrosion. Therefore, it can be used in humid environments. Aluminium has a low melting point which varies from 500 to 660°C, whereas the melting point of steel differs from 1370 to 1540°C. Hence, it can be extruded easily (Kissell and Ferry, 2002). At lower temperatures, most of the metals lose their strength. However, aluminium sustains or even improves both ductility and toughness at very low temperatures (Mazzolani, 1995, Gruber *et al.* 2020) which extends its applicability in structures located in cold weather climates. Aluminium can be recycled easily by retaining all properties of virgin metal. The recycling process requires only 5% energy of the production of the original metal,

resulting in environmental and economic benefits.

2.2.2 Stress-strain curves

Aluminium alloys exhibit a rounded stress-strain relationship with significant strain hardening and considerable ductility. Some alloys display a higher level of strain hardening compared to carbon steel and stainless steel. The normal strength alloys, i.e., T1, T2, T3, T4 and T5 which are considered buckling Class B materials in Eurocode 9 (2007) have shown lower yield strength. On the contrary, the high strength alloys, i.e., T6, T7, T8 and T9 which are referred to as buckling Class A materials in Eurocode 9 (2007) exhibit higher yield strength. The stress-strain relationship of typical normal-strength and high-strength aluminium alloys is presented in Figure 2.1. However, aluminium alloys are less ductile than stainless steel. The higher strength aluminium alloys have lower ductility and the elongation at fracture is about 10% to 25% (Mazzolani, 1995, Jiang *et al.*, 2022). To predict the post-elastic response of aluminium alloys, special attention has been paid in Eurocode 9 (2007) to the possibility of premature tensile failure because of low material ductility.

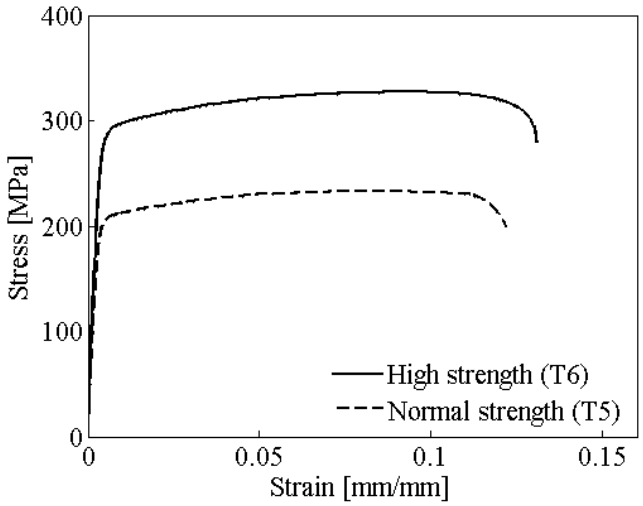

Figure 2.1: Static stress-strain curves for T5 (normal-strength) and T6 (high-strength) aluminium alloys.

Many studies have been conducted to model the material properties of aluminium alloys. Two material models, i.e., the continuous model and the piecewise model are available for aluminium alloys and are shown in Figure 2.2. A popular continuous model was developed by Ramberg and Osgood (1943) which was modified by Hill

(1944). Other continuous models were proposed by Baehre (1966) and Mazzolani (1972). In the piecewise model, the bi-linear or tri-linear model is used to represent the stress-strain behaviour of aluminium alloys, as presented in Annex E of Eurocode 9 (2007). In different material models the strain hardening has been accounted for in the following ways:

- In the Ramberg and Osgood (1943) expression, a strain hardening exponent *n* has been considered to define the shape of the curve.

- In the straight-line equations provided by Hill and Clark (1955), an exponent has been used to characterize the strain hardening rate of different aluminium alloys.

- Mazzolani (1995) considered a generalised shape factor to take into account the strain hardening properties of the alloys.

- In Eurocode 9 (2007), a strain hardening modulus has been adopted.

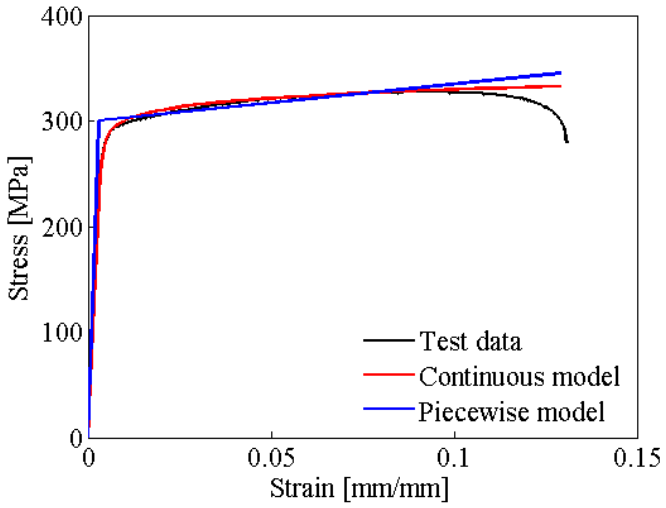

Figure 2.2: Continuous and piecewise stress-strain curves of aluminium alloys.

2.2.3 Design rules

A number of established design rules are currently available for the design of aluminium alloy structural members. In 1930, the earliest design specifications for aluminium structures were developed by the Aluminium Company of America (Alcoa) (Kissell and Ferry, 1995). Alcoa subsequently updated the design specifications in 1958 (Alcoa, 1958), with a number of contributors. In 1962, several research reports on the

design of aluminium alloy structural members were published by the American Society of Civil Engineers (ASCE Committee on Metals, 1962a; 1962b). The scope of these reports was limited to a few aluminium alloys, such as 6061, 6062 and 6063. Aluminium Association published the 'Aluminium Design Manual' in 1967 (AA, 1967) which addressed 13 wrought alloys and provided design equations for the strength of aluminium structures, members and connections according to the allowable stress design method (ASD). The manual was revised in 1994 by adding the load and resistance factor design (LFRD) (AA, 1994). In the 2010 edition, both ASD and LRFD methods were merged to provide a unified specification (AA, 2010). The resent version of the manual was published in 2020 (AA, 2020) which considered twenty-seven wrought, seven casting and nine weld filler alloys and provided new provisions for block shear, pull-out strength of screws in screw chases, weld-affected strengths, post-weld heat-treated strengths, new alloy-tempers and flanges and webs subjected to concentrated forces. In 1967, the board of European Convention for Constructional Steelwork (ECCS) first studied aluminium alloys. Later in 1992, a sub-committee in European Committee for Standardization (CEN) was formed and worked on aluminium alloy structures. In 2007, the design standard for aluminium alloy structures Eurocode 9 (2007) was developed by CEN by addressing seventeen wrought and six casting alloys. The Australian/New Zealand Standard (AS/NZS, 1997) was jointly prepared by the Australian/New Zealand standard committee. These design standards are mainly developed based on the design guidelines of steel structures and limited data on aluminium alloys (Su, 2014).

However, up to date, no design rules have been established for CFAT composite structures. Existing design rules for composite structural members are mainly developed based on the design specifications of steel structural members which may not suit for the design of CFAT members (Zhou and Young, 2008; 2009; Feng *et al.*, 2017; Chen *et al.*, 2018). The well-known design specifications for CFST structural members are Eurocode 4 (2004), BS5400 (2005), AISC (2010) and AIJ (1997).

2.3 Literature review

The volume of research on CFAT, CFDSAT structural members is relatively low, compared to CFST, CFDSST structural members. In this study, to get a better understanding, previous research studies on aluminium alloy, CFST, CFDSST members

are reviewed along with available literature on CFAT, CFDSAT members. Subsections 2.3.1 and 2.3.2 present literature on aluminium alloy structural members under compression and bending, respectively; subsections 2.3.3 and 2.3.4 cover the structural behaviour of CFST and CFAT columns, respectively; subsections 2.3.5 and 2.3.6 summarise the literature on CFST and CFAT beams, respectively; subsections 2.3.7 and 2.3.8 report the previous studies on CFDSST and CFDSAT members, respectively; and subsection 2.3.9 presents the research on evaluating the sustainability of composite structural members.

2.3.1 Aluminium alloy members in compression

Research on aluminium alloy columns has been started in the early 1940s. At the early stage of aluminium alloy column research, a number of tests were conducted by Templin *et al.* (1938), Osgood and Holt (1939), Marin (1947), Hill and Clark (1951, 1955), Clark (1955), Hill *et al.* (1956), Brungraber and Clark (1962), Bernard and Frey (1971), Tsuruta *et al.* (1972), Valtinat and Müller (1977), Benson (1990), Lai and Nethercot (1992), Hopperstad *et al.* (1999), Rasmussen and Rondal (2000) and Faella *et al.* (2000) to study the cross-sectional and member performance under axial compression. A wide range of cross-sectional shapes, such as square hollow section (SHS), rectangular hollow section (RHS), circular hollow section (CHS), I-section, H-section and angle and different alloys, such as 17s-T, 2024-T4, 6061-T6, 6063-T5, 6063-T6, 6082-T4, 6082-T6 and 7019 were used for the test specimens. Based on the tests results some studies proposed design formulas to predict the strength of the columns. More recently, a considerable amount of stub columns was tested to investigate the cross-sectional performance. A series of stub columns tests were carried out by Su *et al.* (2014a) on box sections and Liu *et al.* (2015a; 2015b) on stiffened and irregular-shaped cross-sections. It was demonstrated that the current design stranders are conservative for these cross-sections whereas deformation-based continuous strength method (CSM) offered improved design capacities with average value of test and predicted strength ratio ($N_u/N_{u,pred}$) is 1.04. Wang *et al.* (2015) experimentally investigated the compressive response of aluminium alloy circular columns. They assessed the applicability of existing design specifications and showed that Australian/New Zealand standard is accurate with the mean value of $N_u/N_{u,pred}$ is 0.97. Feng and Young (2015) and Feng *et al.* (2016; 2018) reported test programme on perforated aluminium alloy SHS, RHS and CHS stub columns with member slenderness

varied from 13.9 to 93.2 and demonstrated that existing design guidelines are inappropriate for the perforated aluminium stub columns. Zhu *et al.* (2019a) conducted research on the behaviour of aluminium alloy channel section short columns and showed that the existing international codes for aluminium structures are conservative except the direct strength method (DSM) and CSM as they provided mean values of $N_u/N_{u,pred}$ are 1.01 and 1.10 for plain and lipped channel sections, respectively. Over the last twenty years, a good number of studies has been performed to investigate the member performance of aluminium alloy columns. Zhu and Young (2006) experimentally investigated the compressive behaviour of SHS and RHS aluminium alloy columns with and without welding. They demonstrated that American, Australian/New Zealand, and European design rules are conservative for the non-welded columns as the mean values of strength ratios are higher than 1.38. Zhai *et al.* (2010), Adeoti *et al.* (2015), Wang *et al.* (2016a; 2016b) and Zhao *et al.* (2016) conducted experimental and numerical research on the stability of RHS, I and L section aluminium alloy columns under axial compression and proposed a modified design method to predict the buckling resistance of the columns. Chang *et al.* (2016; 2017) and Wang *et al.* (2017; 2018) investigated buckling failure of aluminium alloy columns having irregular-shaped and I-shaped, respectively and demonstrated the conservatism of existing rules as they underestimated the ultimate capacity of more than 9%. Zhao *et al.* (2019a; 2019b) carried out experimental and numerical investigations on the stability behaviour of aluminium alloy under eccentric compression and proposed revised correction factors of 0.50 and 0.60 for the SHS columns and CHS columns to the Chinses code to predict the strength of the columns more accurately. Feng and Liu (2019), Feng *et al.* (2020) and Liu *et al.* (2022) studied the behaviour of aluminium alloy perforated columns under axial compression. It was shown that web opening weakened the section and reduced the bearing capacity of the studied member up to 8.3%. Table 2.3 provides a summary of all available work on aluminium alloy columns.

The above mentioned test and numerical studies showed that the existing international guidelines are conservative for aluminium alloy short, long and perforated columns. Hence additional research is needed to improve the design accuracy.

Table 2.3: Previous studies on aluminium alloy columns.

Reference	Synopsis	Alloy	Section	Test No.	Studied parameters
Templin *et al.* (1938)	Experimental study of columns	17S-T	CHS, Angle	-	Tangent modulus
Osgood and Holt (1939)	Experimental study of H-section columns	2024-T4	I-section	-	Double modulus
Marin (1947)	Experimental study of columns	-	RHS	8	Creep deflection
Hill and Clark (1951)	Experimental study of beam-columns	-	I-section	33	Column length, eccentricity
Hill and Clark (1955)	Straight-line column formulas	17S-T	-	-	Buckling constant
Clark (1955)	Experimental study of beam-columns under eccentric loading	6061-T6	RHS	36	Eccentricity
Hill *et al.* (1956)	Experimental study of columns under eccentric loading	-	CHS	12	Eccentricity
Brungraber and Clark (1962)	Experimental study of welded columns	6061-T6	Solid RS	-	Longitudinal and transverse welding
Bernard and Frey (1971)	Experimental study of columns under buckling	6082	CHS, I-section	66	Buckling curves
Tsuruta *et al.* (1972)	Experimental study of welded columns	6061-T6, 6063-T5	RHS, Solid RS	151	Column slenderness
Valtinat and Müller (1977)	Numerical study of beam-columns	6082-T6	I-section	-	Longitudinal and transverse welding
Benson (1990)	Experimental study of columns under eccentric loading	6063-T6	SHS	19	Eccentricity
Lai and Nethercot (1992)	Experimental study of welded columns	7019	I-section	-	Location of welds
Hopperstad *et al.* (1999)	Experimental study of columns	6082-T4, 6082-T6	-	10	Cross-section dimensions, thickness
Faella *et al.* (2000)	Experimental study of columns	6000-series	SHS, RHs	80	Cross-section dimensions, slenderness
Rasmussen and Rondal (2000)	Strength curves for aluminium alloy columns	-	-	-	Strength curve

Table 2.4 (continued): Previous studies on aluminium alloy columns.

Reference	Synopsis	Alloy	Section	Test No.	Studied parameters
Zhu and Young (2006)	Tests and design of columns	6063-T5, 6061-T6	SHS, RHS	41	Welding to end plates
Zhai et al. (2010)	Experimental and numerical studies of columns	6082-T6	RHS, I-section	17	Cross-section dimensions, slenderness
Su *et al.* (2014a)	Tests and design of stub-columns	6061-T6, 6063-T5	SHS, RHS	15	Cross-section dimensions, internal cross stiffener
Liu *et al.* (2015a)	Experimental and numerical studies of irregular shape columns	6063-T5	Irregular shape	7	Column length, initial geometric imperfection
Liu *et al.* (2015b)	Experimental and numerical studies of stiffened closed-section columns	6063-T5	Irregular shape	10	Local buckling
Feng and Young (2015)	Experimental study of perforated stub columns	6061-T6	SHS	28	Cross-section slenderness, opening size
Wang *et al.* (2015)	Experimental study of circular stub columns	6082-T6	CHS	15	Column length, cross-section dimensions
Adeoti *et al.* (2015)	Experimental and numerical studies of columns	6082-T6	RHS, I-section	30	Column length, cross-section dimensions
Wang *et al.* (2016a)	Numerical study of columns with different cross-sections	6082-T6	I-, L - section, RHS, CHS	-	Column length, cross-section dimensions, slenderness
Wang *et al.* (2016b)	Experimental and numerical studies of high-strength columns	7A04	L - section	42	Cross-section dimensions, column slenderness,
Zhao *et al.* (2016)	Experimental and numerical studies of columns under eccentric compression	6082-T6	L - section, RHS	29	Cross-section dimensions, column slenderness, eccentricity
Feng *et al.* (2016)	Experimental study of circular columns with circular openings	6061-T6, 6063-T5	CHS	27	Column and cross-section slenderness, opening size and number

Table 2.5 (continued): Previous studies on aluminium alloy columns.

Reference	Synopsis	Alloy	Section	Test No.	Studied parameters
Chang *et al.* (2016)	Numerical study of irregular-shaped columns	6061-T6, 6063-T5	Irregular shape	-	Column slenderness
Wang *et al.* (2017)	Experimental and numerical studies of columns with fixed-pinned end conditions	6061-T6, 6063-T5	I-section	11	Column slenderness, cross-section slenderness
Chang *et al.* 2017	Experimental and numerical studies of thin-walled irregular-shaped columns	6063-T5 6082-T6	Irregular shape	6	Column length, cross-section slenderness
Wang *et al.* (2018)	Experimental and numerical studies of large-section columns	6061-T6	I-section, RHS	7	Column length
Feng et al. (2018)	Experimental study of perforated columns	6061-T6, 6063-T5	SHS, RHS	64	Column length, cross-section dimensions, slenderness
Feng and Liu (2019)	Numerical study of perforated columns	6061-T6, 6063-T5	SHS, RHS	-	Column and cross-section slenderness, opening number and location
Zhu *et al.* (2019a)	Experimental and numerical studies of plain and lipped channel columns	6061-T6, 6063-T5	C-section	20	Column length
Zhu *et al.* (2019b)	Numerical study of channel section columns with welds	6061-T6, 6063-T5	C-section	-	Column length, width-to-thickness ratios
Zhao *et al.* (2019a, 2019b)	Experimental and numerical studies of columns eccentric compression	6082-T6	SHS, CHS	30	Column length, width/diameter-to-thickness ratios, eccentricity
Feng *et al.* (2020)	Numerical study of columns with holes	6061-T6, 6063-T5	CHS	-	Column length, diameter-to-thickness ratios
Liu *et al.* (2022)	Experimental and numerical studies of H-shaped columns	6061-T6	H-section	12	Web opening rate, slenderness ratio

2.3.2 Aluminium alloy members in bending

Many studies have been carried out to study the flexural behaviour of aluminium alloy beams. Hill (1942; 1954) conducted research on lateral instability of unsymmetrical aluminium alloy I-beams, channel and Z-sections and derived expressions for calculating the buckling strength of the beams. Panlilo (1947) experimentally investigated the deformation and bending capacities of aluminium alloy continuous beams. Clark and Jombock (1957) experimentally studied the elastic and inelastic buckling of aluminium alloy I-beams and rectangular bars subjected to bending moments and proposed an approximate method to calculate the inelastic buckling strength of these types of beams. Lai and Nethercot (1992) developed FE model and validated it against test results to investigate the flexural capacity of welded and non-welded aluminium alloy beams. The study recommended to consider softening effects of transverse welds located at the ends of the specimens. Moen *et al.* (1999a; 1999b) experimentally and numerically studied the strength and rotation capacity of aluminium alloy beams with welded stiffeners. They observed that in the vicinity of welds a local yield stress reduced by around 0.4 times of the parent material yield stress. De Matteis *et al.* (2001) numerically studied the effects of the strain hardening of the material, flange slenderness, the shape factor of the section and the web stiffness on the bending capacity of aluminium alloy beams. It was shown that the classification system of aluminium provided by the European code is generally conservative, especially for non-heat-treated alloys due to a misunderstanding in accounting for the effect of strain hardening. Zhu and Young (2009) presented experimental and numerical investigations of aluminium alloy beams subjected to pure bending. They showed that strengths predicted by the existing specifications and the DSM are conservative as mean values of test and predicted flexural strength ratios ($M_u/M_{u,pred}$) are more than 1.20. Kim and Peköz (2010) carried out tests and developed FE models of aluminium alloy beams with stocky sections to study the effects of strain hardening and ductility on the bending capacity. They proposed modifications to the existing weighted average strength approach to predict the inelastic flexural capacity of aluminium beams. Su *et al.* (2014b) reported data from a test programme and numerical simulation of simply supported aluminium alloy beams. The test and FE results were compared with bending resistance predicted by existing design provisions and found that the CSM is more accurate as the mean value of $M_u/M_{u,pred}$ is 1.11. Su *et al.* (2015) experimentally and numerically

studied the bending capacity of aluminium alloy two-span continuous beams and proposed design rules for indeterminate aluminium structures. Su *et al.* (2016) conducted research on the flexural response of aluminium alloy SHS and RHS beams with internal stiffeners. Thay demonstrated that the current design rules underestimate the ultimate strength of aluminium alloy stiffened SHS and RHS beams with mean values of $M_u/M_{u,pred}$ are higher than 1.30. Feng *et al.* (2017) experimentally studied the flexural behaviour of SHS and RHS aluminium beams with circular perforations. It was shown that the perforated sections close to the mid-span of the beams are the critical sections under gradient and constant bending moment. Georgantzia *et al.* (2022) report a test programme and FE investigation of simply-supported and two-span continuous aluminium alloy beams. It was concluded that the plastic hinge method and CSM are suitable for the design of aluminium alloy indeterminate structures as they provided the mean values of $M_u/M_{u,pred}$ are 0.90 and 0.95, respectively. Table 2.4 provides a summary of previous studies on aluminium alloy beams.

Overall, the studies reveal that the current design standards underestimate the flexural capacity of aluminium alloy beams. In addition, relatively little attention has been given to studying the plastic performance of indeterminate aluminium alloy beams.

Table 2.6: Previous studies on aluminium alloy beams.

Reference	Synopsis	Alloy	Section	Type of tests	Test No.	Studied parameters
Hill (1942)	Experimental study of unsymmetrical I-beams	17S-T	I-section	3-point bending	4	Elastic buckling strength
Panlilo (1947)	Experimental study of continuous beams	61S-T, R303-T315, 24S-T,	Square bar	5-point bending	3	Buckling strength
Hill (1954)	Experimental study of Channel and Z-beams	17S-T6	Channel, Z-section	-	8	Buckling strength
Clark (1957)	Experimental study of I-beams subjected to unequal end moments	2014-T6	I-section	-	-	Buckling strength

Table 2.7 (continued): Previous studies on aluminium alloy beams.

Reference	Synopsis	Alloy	Section	Type of tests	Test No.	Studied parameters
Clark *et al.* (1966)	Experimental study of rectangular beams	2024-0, 2024-T4	Rectangu-lar bar	-	-	Buckling strength
Lai and Nethercot (1992)	Experimental and numerical studies of beams with transverse welds	7019	RHS	4-point bending	27	Location of welds
Moen *et al.* (1999a)	Experimental study of beams under moment gradient	6082-T4, T6, 7108-T7	I-section, SHS, RHS	3-point bending	38	Different tempers, cross-sections dimensions, beam length
Moen *et al.* (1999b)	Numerical study of beams under moment gradient	6082-T4, T6, 7108-T7	I-section, SHS, RHS	3-point bending	-	Cross-section slenderness
De Matteis *et al.* (2001)	Numerical study of beams	T6, 7108-T7	RHS	3-point bending	-	Flange slenderness, strain hardening, shape factor of the section, web stiffness
Zhu and Young (2009)	Experimental and numerical studies of beams	6061-T6	SHS	4-point bending	10	Cross-section dimensions, slenderness
Kim and Peköz (2010)	Experimental and numerical studies of I-beams	6063-T6	I-section	4-point bending	3	Compressive stresses of flexural member, shape factor of section
Su *et al.* (2014)	Experimental and numerical studies of beams	6061-T6, 6063-T5	SHS, RHS	3-, 4-point bending	29	Cross-section size, width-to-thickness ratio

Table 2.8 (continued): Previous studies on aluminium alloy beams.

Reference	Synopsis	Alloy	Section	Type of tests	Test No.	Studied parameters
Su *et al.* (2015)	Experimental and numerical studies of continuous beams	6061-T6, 6063-T5	SHS, RHS	5-point bending	27	Cross-section dimensions, slenderness, position of load
Su *et al.* (2016)	Experimental and numerical studies of beams with internal stiffeners	6061-T6, 6063-T5	SHS, RHS	3-, 4-, 5-point bending	30	Cross-section dimensions, internal stiffener
Feng *et al.* (2017)	Experimental and numerical studies of beams with circular perforations	6061-T6, 6063-T5	SHS, RHS	3-, 4-point bending	13	Aspect ratio, plate width, plate slenderness, perforation dimension, number of perforations
Georgantzia *et al.* (2022)	Experimental and numerical studies of continuous beams	6082-T6	RHS	3-, 4-, 5-point bending	15	Aspect ratio, slenderness ratio

2.3.3 CFST members in compression

Early tests on CFST columns have been reported by Gardner and Jacobson (1967), Knowles and Park (1969), Kato (1995), Schneider (1998), Yamamoto *et al.* (2000), Johansson and Gylltoft (2002), Huang *et al.* (2002), Hu *et al.* (2003), Sakino *et al* (2004), Fam *et al.* (2004) and McAteer *et al.* (2004). Han *et al.* (2005), Yu *et al.* (2007) and Yu *et al.* (2008) investigated the compressive behaviour of CFST short columns filled with normal and high self-consolidating concrete. Han *et al.* (2005) proposed a mechanical model to predict the compressive capacity of the short columns and showed that the model can predict sufficiently the strength with mean values of $N_u/N_{u,pred}$ are 0.92 and 0.95 for circular and square sections, respectively. Yu *et al.* (2007) and Yu *et al.* (2008) found that the ultimate strength of the CFST columns increased up to 18% when the self-consolidating concrete cube strength increased from 30 MPa to 60 MPa. Gupta *et al.* (2007) studied the response of concentrically loaded CFST stub columns

and observed that the ultimate capacity of the columns decreased with the increase in percentage volume of fly ash up to 20%, however, it increased when 25% fly ash volume was added to the concrete. Structural behaviour of CFST columns was investigated by Hatzigeorgiou (2008) under biaxial and triaxial loading and Oliveira *et al.* (2010) under axial compression load only on the concrete core. Hatzigeorgiou (2008) proposed a new empirical relation to determine confining effect and Oliveira *et al.* (2010) suggested a correction factor for the available analytical models to predict the ultimate load of slender column having length over depth ratio larger than 3 and loaded only on concrete core. Abed *et al.* (2013) investigated the compressive behaviour of CFST stub columns and found that when the diameter is constant the strength of the studied columns increased up to 70% with the decrease of diameter-to-thickness ratio. Aslani *et al.* (2017) experimentally evaluated the behaviour of concrete-filled spiral welded tube (SWT) columns subjected to axial compressive loading and compared the results with that of longitudinally welded tubes (LWTs). They concluded that SWT columns are as good as LWT ones in terms of strength. A series of tests on the compressive behaviour of CFST columns was conducted by Ibañez *et al.* (2018) using square, circular and rectangular shapes and Zhu and Chan (2018) using octagonal shape. Ibañez *et al.* (2018) found that for circular section ultimate strength increased up to 29% compared to the other sections. Zhu and Chan (2018) proposed modification of the current design code for designing the CFST columns with octagonal cross-section. Song *et al.* (2019) numerically studied the buckling failure of CFST short columns and proposed design formulas to predict the local buckling and post-buckling ultimate strengths of the column. Liao *et al.* (2019) and Zhang *et al.* (2022) presented an experimental study on the behaviour of concrete-filled stainless steel tube (CFSST) constructed with sea sand and recycled aggregate concrete, respectively. Liao *et al.* (2019) demonstrated that the confinement effect of stainless steel on the sea sand concrete is as reliable as that on the river sand concrete counterpart. Zhang *et al.* (2022) found that with the increase of coarse recycled aggregate content in the concrete from 0% to 50% and 100% the ultimate strength of the columns decreased by up to 17.8% in the studied columns. A summary of these studies is presented in Table 2.5.

According to the literature, most of the work focused on the structural behaviour of CFST short columns. However, research on CFST long columns is relatively low and further research is essential. Moreover, the post-local buckling strength of the steel

section can improve the strength of composite columns. Therefore, modification of current design guidelines is needed to consider the post-local buckling strength for slender plates.

Table 2.9: Previous studies on CFST columns.

Reference	Synopsis	Section	Length of specimen	Test No.	Studied parameters
Gardner and Jacobson (1967)	Experimental and analytical studies of stub and long columns	CHS	Stub columns	32	Column length, depth-to-thickness ratio, concrete strength
Knowles and Park (1969)	Experimental study of stub columns	CHS, SHS	Stub column	28	Depth-to-thickness ratio
Kato (1995)	Experimental and analytical studies stub columns	CHS, SHS	Stub column	12	Depth-to-thickness ratio, concrete strength
Schneider (1998)	Experimental and analytical studies of stub columns	CHS, SHS, RHS	Stub column	14	Depth-to-thickness ratio, length-to-depth ratio
Yamamoto *et al.* (2000)	Experimental study of scale effects of stub columns	CHS, SHS	Stub column	13	Column length, depth-to-thickness ratio, concrete strength, loading condition
Johansson and Gylltoft (2002)	Experimental and analytical studies of stub columns	CHS	Stub column	13	Mechanical behaviours, loading condition
Huang *et al.* (2002)	Experimental and numerical studies of columns	SHS	Long column	17	Cross-section dimension, width-to-thickness ratio
Hu *et al.* (2003)	Numerical study of columns	CHS, SHS	Long column	-	Cross-section shape, effect of reinforcing tie

Table 2.10 (continued): Previous studies on CFST columns.

Reference	Synopsis	Section	Length of specimen	Test No.	Studied parameters
Sakino *et al* (2004)	Experimental study of stub columns	CHS	Stub column	114	Cross-section dimension, diameter-to-thickness ratio, concrete strength
Fam *et al.* (2004)	Experimental and analytical studies of stub columns	CHS	Stub column	5	Loading conditions
McAteer *et al.* (2004)	Experimental study of stub columns	CHS	Stub column	4	Partial loading (on concrete only), concrete strength
Han *et al.* (2005)	Experimental study of stub columns filled with self-consolidating concrete	CHS, SHS	Stub column	50	Steel yield strength, diameter-to-width ratio
Gupta *et al.* (2007)	Experimental and numerical studies of stub columns	CHS	Stub column	81	Diameter-to-thickness ratio, concrete strength
Yu *et al.* (2007)	Experimental study of stub columns filled with self-compacting concrete	CHS	Stub column	17	Concrete strength, notched holes or slots, loading condition
Hatzigeorgiou (2008)	Numerical study of stub columns	CHS	Stub column	-	Steel yielding strength, loading condition
Yu *et al.* (2008)	Experimental study of stub columns filled with self-compacting concrete	CHS, SHS	Stub column	28	Cross-section dimensions, slenderness ratio, load eccentricity
Oliveira *et al.* (2010)	Experimental study of columns loaded on concrete core	CHS	Long column	32	Length-to-diameter ratio, diameter-to-thickness ratio

Table 2.11 (continued): Previous studies on CFST columns.

Reference	Synopsis	Section	Length of specimen	Test No.	Studied parameters
Abed *et al.* (2013)	Experimental and numerical studies of stub columns	CHS	Stub column	16	Diameter-to-thickness ratio, concrete strength
Aslani *et al.* (2017)	Experimental study of concrete-filled spiral welded steel tube columns	CHS, SHS	Stub and long column	20	Weld's spiral geometry, initial imperfection
Ibañez *et al.* (2018)	Experimental study of stub columns filled high strength concrete	CHS, SHS, RHS	Stub column	12	Cross-section dimensions, concrete strength
Zhu and Chan (2018)	Experimental study of octagonal stub columns	CHS, SHS, Octagonal	Stub column	21	Cross-section dimensions, steel yield strength, concrete strength
Song *et al.* (2019)	Numerical study of local and post-local buckling of stub columns	RHS	Stub column	-	Local and post-local buckling
Li *et al.* (2019)	Experimental and numerical study of spiral-welded stainless steel tube columns	CHS	Stub and long column	15	Depth-to-thickness ratio, slenderness, concrete strength
Liao *et al.* (2019)	Experimental study of sea sand concrete-filled stainless steel tube stub columns	CHS, SHS	Stub column	48	Concrete type, depth-to-thickness ratio, cross-section dimension
Zhang *et al.* (2022)	Experimental study of stub columns with external stainless steel and recycled aggregate concrete	CHS	Stub column	24	Coarse recycled aggregate content, steel ratio, concrete strength

2.3.4 CFAT members in compression

Zhou and Young (2008) reported an experimental investigation on CFAT stub columns with SHSs and RHSs subjected to axial compression. A series of tests were carried out to examine the effects of cross-section size, thickness and concrete strength. It was concluded that the strength of CFAT columns improved by up to 210% compared to hollow columns. Structural performance of circular CFAT stub columns under compressive load was evaluated by Zhou and Young (2009). The specimens were prepared with 6061-T6 heat-treated aluminium alloy. The test results were compared with design capacities determined using American and Australian/New Zealand standards and it was demonstrated that these design standards are conservative as the mean values of $N_u/N_{u,pred}$ are higher than 1.24 for the studied columns. A numerical study on circular CFAT columns was also conducted by Zhou and Young (2012). In this study, design formulae of composite columns were proposed considering the benefits of composite action between the circular aluminium tube and the concrete core. Wang *et al.* (2019) investigated the analytical behaviour of CFAT stub columns under axial compression. The effects of geometry and key material properties were evaluated and design equations were proposed to determine the ultimate strength of the columns. Patel *et al.* (2020) conducted a fibre-based numerical analysis of CFAT stub columns under concentric load. A design equation was proposed and it was shown that the proposed equation yields a good estimation of the ultimate capacity of CFAT stub columns with mean value and coefficient of variance (COV) of ratios of $N_u/N_{u,pred}$ are 0.993 and 0.061, respectively. Table 2.6 provides a summary of available research studies on CFAT columns.

These studies mainly focused on investigating the behaviour of CFAT stub columns and demonstrated their potentiality, whereas no reported research has been found on the structural response of CFAT slender columns. Moreover, the examined CFAT columns in these studies are manufactured with 6061-T6 aluminium alloy. However, structural performance data of CFAT columns constructed using other high-strength alloys, such as 6082-T6 and 7000 series is missing in the literature.

Table 2.12: Previous studies on CFAT columns.

Reference	Synopsis	Alloy	Section	Length of specimen	Test No.	Studied parameters
Zhou and Young (2008)	Experimental study of SHS and RHS stub columns	6061-T6	SHS, RHS	Stub column	11	Column length, depth-to-thickness ratio, concrete strength
Zhou and Young (2009)	Experimental study of stub columns	6061-T6	CHS	Stub column	42	Column length, diameter-to-thickness ratio, concrete strength
Zhou and Young (2012)	Numerical study of stub columns	6061-T6	CHS	Stub column	-	Column length, diameter-to-thickness ratio, concrete strength
Wang *et al.* (2019)	Analytical study of stub columns	-	CHS	Stub column	-	Column length, diameter-to-thickness ratio, concrete strength
Patel *et al.* (2020)	Numerical study of stub columns	-	CHS	Stub column	-	Column length, diameter-to-thickness ratio, concrete strength

2.3.5 CFST members in bending

Early studies on flexural behaviour of CFST beams were conducted by Furlong (1967), Lu and Kennedy (1994) and Han (2004). Lu *et al.* (2007) performed flexural tests on rectangular CFST beams with non-uniform wall thickness steel tubes and proposed a range of thickness ratio is 1.5 to 2, which improved the bending moment capacity is around 5%. Montuori and Piluso (2015) experimentally evaluated the behaviour of CFST flexural members under non-uniform bending moment and suggested a fibre model to determine the bending capacity of these members. Hou *et al.* (2016) studied the flexural response of CFST members under sustained load and chloride corrosion and

observed that the flexural capacity and ductility of these members deteriorated noticeably due to the chloride corrosion. A series of tests on the square, rectangular and circular concrete-filled stainless-steel tubular members under in-plane bending were performed by Chen *et al.* (2017a; 2017b). They compared the experimental initial and serviceability limit state flexural stiffnesses with the design stiffnesses determined by American, European, British and Japanese specifications and demonstrated that the design specifications are conservative in predicting these values. Abed *et al.* (2018) experimentally and numerically studied the flexural response of CFST members made of seamless steel which can handle more pressure than welded ones. It was concluded that the contribution of concrete infill to flexural strength was more prominent for the members having higher diameter-to-thickness ratios. Chen and Chan (2019) presented an experimental study to examine the behaviour of CFST flexural members with octagonal cross sections (OCFST) under monotonic or cyclic flexural loading. Test results indicated that the OCFST flexural members exhibited ductile plastic failure and excellent energy dissipation capacity. Liu *et al.* (2020) reported an experimental investigation on the flexural response of steel fibre-reinforced self-stressing recycled aggregate concrete-filled steel tubes. It was shown that through reasonable mix design, this type of concrete-filled steel tubes exhibited similar flexural behaviour as the CFST members filled with normal concrete whereas steel fibres prolonged the elastic response and improved the flexural capacity of these members. Gunawardena and Aslani (2020) conducted an experimental programme to study the flexural response of concrete-filled spiral-welded mild-steel tubes and examined the feasibility of the existing design codes to predict the strength of these flexural members. They demonstrated that the existing design standards provide conservative estimation of flexural strength of these members. Zhang *et al.* (2021) experimentally and numerically investigated the structural behaviour of CFST flexural members with elliptical sections. They proposed a design methodology that can accurately predict the moment capacity with average and COV values of $M_u/M_{u,pred}$ are 0.98 and 0.05, respectively of the elliptical CFST members. Research on the flexural behaviour of CFST members is summarised in Table 2.7.

The number of reported studies on the flexural behaviour of CFST members is much less than of those dealing with CFSTs under compression. This is especially so for circular CFST flexural members. Hence understanding the behaviour of these members under flexure is of fundamental importance.

Table 2.13: Previous studies on CFST beams.

Reference	Synopsis	Section	Type of test	Tests No.	Studied parameters
Furlong (1967)	Experimental study of beams	CHS, SHS	-	52	Flexural strength
Lu and Kennedy (1994)	Experimental study of beams	SHS, RHS	-	16	Depth-to-width ratio, shear span-to-depth ratio
Han (2004)	Experimental study of beams	SHS, RHS	4-point bending	16	Depth-to-width ratio, Depth-to-thickness ratio
Lu *et al.* (2007)	Experimental study of concrete filled non-uni-thickness walled steel tube beams	RHS	4-point bending	3	Depth-to-thickness ratio
Montuori and Piluso (2015)	Experimental and analytical studies of beams	SHS	3-point bending	8	Failure mode
Hou *et al.* (2016)	Experimental and numerical studies of beams under chloride corrosion	CHS	4-point bending	7	Effect chloride corrosion on flexural strength
Chen *et al.* (2017a)	Experimental study of beams	SHS, RHS	4-point bending	16	Failure mode, flexural stiffness, ductility
Chen *et al.* (2017b)	Experimental study of beams	CHS	4-point bending	27	Failure mode, flexural stiffness, ductility
Abed *et al.* (2018)	Experimental and numerical studies of concrete-filled seamless steel tube beams	CHS	4-point bending	9	Depth-to-thickness ratio
Chen and Chan (2019)	Experimental study of beams with octagonal sections	Octagonal section	3-point bending	8	Concrete strength, loading conditions

Table 2.14 (continued): Previous studies on CFST beams.

Reference	Synopsis	Section	Type of test	Tests No.	Studied parameters
Gunawardena and Aslani (2020)	Experimental study of concrete-filled spiral-welded mild-steel tube beams	CHS	4-point bending	12	Depth-to-thickness ratio, concrete strength
Liu *et al.* (2020)	Experimental study of steel fibre reinforced self-stressing recycled aggregate concrete-filled steel tube beams	CHS	4-point bending	54	Steel fibre volume content, recycled aggregate content, water cement ratio, cement type, steel tube thickness
Zhang *et al.* (2021)	Experimental and numerical studies of beams with elliptical section	Elliptical	4-point bending	4	Confinement effect, steel strength, concrete strength

2.3.6 CFAT members in bending

Feng *et al.* (2017) experimentally studied the flexural behaviour of concrete-filled SHS and RHS aluminium tubes subjected to in-plane bending. In this study, a total of 30 specimens including 10 CFAT square, 10 CFAT rectangular and 10 BAT were prepared with 5083 aluminium alloy tubes and tested under 4-point bending. The test results were compared with the design flexural stiffness calculated using AIJ standard, BS 5400, Eurocode 4 and AISC specification and it was concluded that the current design rules are generally inappropriate for CFAT beams subjected to in-plane bending. Chen *et al.* (2017) investigated the structural performance of carbon fibre-reinforced polymer (CFRP) strengthened concrete-filled CHS tubes under pure bending. The hollow sections were manufactured with 6061 aluminium alloy. It was shown that when the area ratio of aluminium alloy over cross-section is equal to or less than 0.2 the initial flexural stiffness and post-yield flexural stiffness of the CFAT specimens generally decreased by reinforcing with the CFRP. Chen *et al.* (2018) examined the flexural response of concrete-filled CHS tubes under in-plane bending. In total 28 specimens

with nominal concrete strengths of 30 MPa and 50 MPa were tested in a 4-point bending arrangement. It was demonstrated that the flexural strength of studied members enhanced up to 41.58% and 156.85% by increasing the thickness of aluminium alloy CHS tube from 4.5 mm to 7.8 mm with nominal concrete cube strength of 30 MPa and 50 MPa, respectively. Zhu *et al.* (2020) experimentally and numerically studied the flexural response of concrete-filled SHS and RHS aluminium alloy tubes reinforced with CFRP. A total of 40 beams including 30 square and rectangular CFAT beams with three arrangement schemes of CFRP and 10 BAT were tested under pure bending. It is concluded that the ductility of square and rectangular CFAT beams decreased around up to 67% due to CFRP strengthening. Table 2.8 presents a brief description of these studies.

Research studies on the flexural behaviour of CFAT members are very limited. Moreover, the existing studies mainly focused on the response of 6081-T6 aluminium alloy composite members. However, research related to CFAT beams made with other high-strength alloys, such as 6082-T6 and 7000 series is not available.

Table 2.15: Previous studies on CFAT beams.

Reference	Synopsis	Alloy	Section	Type of test	No. of tests	Studied parameters
Feng *et al.* (2017)	Experimental study of SHS and RHS beams	5083	SHS, RHS	4-point bending	30	Cross-section dimensions, concrete strength
Chen *et al.* (2017)	Experimental study of CFRP strengthened CHS beams	6061-T6	CHS	4-point bending	30	Cross-section dimensions, CFRP strengthening
Chen *et al.* (2018)	Experimental study of CHS beams	6061-T6	CHS	4-point bending	28	Cross-section dimensions, concrete strength
Zhu *et al.* (2020)	Experimental and numerical studies of CFRP strengthened SHS and RHS beams	6061-T6	SHS, RHS	4-point bending	40	Cross-section dimensions, location of CFRP strengthening

2.3.7 Research on CFDSST members

A series of experiments were conducted on CFDSST short columns consisting of carbon steel square (Zhao and Grzebieta, 2002), rectangular (Tao and Han, 2006), circular (Tao *et al.*, 2004, Uenaka *et al.*, 2010, Yan and Zhao, 2020), circular-square (Elchalakani *et al.*, 2002) and square-circular (Han *et al.*, 2004) outer and inner sections, respectively. In these studies, the failure mechanism and compressive strength of CFDSST members were investigated and design formulae were proposed to determine their capacity. Wang *et al.* (2020a; 2020b) investigated the compressive response of square CFDSST cross-sections constructed with stainless outer hollow sections and proposed modifications of the current design standards to predict their design strength. Tziavos *et al.* (2020) conducted a numerical study to examine the compressive response of grout-filled double-skin tubular steel short columns and suggested design equations for these columns. Zhao *et al.* (2010), Han *et al.* (2011) and Zheng *et al.* (2018) studied the behaviour of CFDSST short columns subjected to large axial deformation, long-term sustained load and cyclic load. Hassanein and Kharoob (2014), Sulthana and Jayachandran (2017), Zhao *et al.* (2021) and Ahmed *et al.* (2022) investigated the behaviour of CFDSST slender columns made with different cross-sectional configurations and steel materials and suggested design equations to predict the strength of these columns. Experimental studies were carried out on CFDSST beams with different profiles: circular profiles were used by Uenaka *et al.* (2008), Xiong *et al.* (2017) and Eom *et al.* (2019); square profiles by Zhao and Grzebieta (2002); rectangular profiles by Tao and Han (2006); dodecagonal profile by Chen *et al.* (2016) and square outer and circular inner profiles by Han *et al.* (2004). In these studies, the effect of cross-section dimensions of outer and inner tubes on the bending performance of CFDSST members was investigated and design methodologies were provided to estimate their flexural capacity. Wang *et al.* (2021) and Zhao *et al.* (2021) experimentally and numerically studied the response of circular CFDSST beams made of stainless-steel outer tubes. Based on the results they assessed the applicability of current design rules available for CFST beams for the design of CFDSST flexural members. A summary of all available studies on CFDSST structural members is provided in Table 2.9.

Available studies on the structural behaviour of CFDSST members demonstrated the potentiality of the double skin technique in terms of strength and energy absorption

capacity. Despite the potentiality, no design rules have been established so far for these structural members.

Table 2.16: Previous studies on CFDSST structural members.

Reference	Synopsis	Section	Type of member	Tests No.	Studied parameters
Zhao and Grzebieta (2002)	Experimental study of stub columns	SHS outer and inner skin	Stub column	32	Cross-section dimensions, width-to-thickness ratio
Elchalakani, *et al.* (2002)	Experimental study of stub columns	CHS outer and SHS inner skin	Stub column	16	Diameter-to-thickness ratio, width-to-thickness ratio
Han *et al.* (2004)	Experimental study of stub and long columns and beams	SHS outer and CHS inner	Stub and long column, beam	26	Failure mode, load-deformation behaviour
Tao *et al.* (2004)	Experimental study of stub and long columns	CHS outer and inner	Stub and long column	26	Diameter-to-thickness ratio, hollow ratio, slenderness
Tao and Han (2006)	Experimental study of long columns and beams	RHS outer and inner	Long column, beam	6	Failure mode, load-deformation behaviour
Uenaka *et al.* (2008)	Experimental study of beams	CHS outer and inner	Beam	12	Inner-to-outer diameter ratio, diameter-to-thickness ratio
Uenaka *et al.* (2010)	Experimental study of stub columns	CHS outer and inner	Stub column	12	Inner-to-outer diameter ratio, diameter-to-thickness ratio
Zhao *et al.* (2010)	Experimental study of stub under large deformation	CHS outer and inner	Stub column	9	Diameter-to-thickness ratio, failure mode
Han *et al.* (2011)	Experimental and numerical studies of columns under long-term loading	CHS/SHS outer and CHS inner	Long column	16	Loading condition

Table 2.17 (continued): Previous studies on CFDSST structural members.

Reference	Synopsis	Section	Type of member	Tests No.	Studied parameters
Hassanein and Kharoob (2014)	Numerical study of columns with external stainless-steel tube	CHS outer and inner	Long column	-	Confinement effect, hollow ratio, slenderness ratio
Chen *et al.* (2016)	Experimental and numerical studies of dodecagonal section beams	Dodecagonal section	Beam	7	Width-to-thickness ratio, failure mode
Sulthana and Jayachandran (2017)	Experimental study of long columns	SHS outer and SHS/CHS inner	Long column	5	Length-to-depth ratio, shape of inner tube
Xiong *et al.* (2017)	Experimental study of beams with high tensile steel and ultra-high strength concrete	SHS/CHS outer and SHS/CHS inner	Beam	8	Steel strength, concrete strength
Zheng *et al.* (2018)	Experimental and numerical studies of columns under long-term cyclic loading	CHS outer and inner	Long column	8	Loading condition, diameter ratio of inner tube to outer tube
Eom *et al.* (2019)	Experimental and numerical studies of beams with a joint	CHS outer and inner	Beam	4	Effect of shear connectors and joints
Yan and Zhao (2020)	Experimental study of stub columns	CHS outer and inner	Stub column	24	Confinement effect
Wang *et al.* (2020a, b)	Experimental and numerical studies of stub columns	SHS outer and inner, SHS outer & CHS inner	Stub column	-	Failure mode, load-deformation behaviour
Tziavos *et al.* (2020)	Numerical study of stub columns	CHS outer and inner	Stub column	-	Hollow ratio, cross-section slenderness
Zhao *et al.* (2021)	Experimental and numerical studies of slender columns and beams	CHS outer and inner	Long column, beam	18	Hollow ratio, eccentric ratio, material strength

Table 2.18 (continued): Previous studies on CFDSST structural members.

Reference	Synopsis	Section	Type of member	Tests No.	Studied parameters
Wang *et al.* (2021)	Experimental and numerical studies of beams with stainless steel outer tube	CHS outer and inner	Beam	22	Material strength, cross-section slenderness
Ahmed *et al.* (2022)	Analytical study of columns with external stainless-steel tube	RHS outer and inner	Stub and long column	-	Slenderness ratio, eccentricity ratio, hollow ratio, width-to-thickness ratio, depth-to-width ratio, concrete strength

2.3.8 Research on CFDSAT members

Zhou and Young (2018) conducted experimental and numerical studies on the compressive behaviour of CFDSAT stub columns made with 6061-T6 CHS inner and outer tubes. The effects of geometric dimensions and concrete strength on the structural behaviour of composite columns were investigated. The test and numerical results were compared with current design rules and proposed design equations to assess their reliability. Zhou and Young (2019) carried out a series of tests on CFDSAT stub columns with outer CHS and inner SHS skins. A FE model was developed and verified against experimental results. The validated model was used in a numerical parametric study to evaluate the effects of different parameters on the compressive behaviour of the columns. Patel *et al.* (2019) proposed a new concrete confinement model for the numerical study of circular CFDSAT stub columns. The study revealed that the design approach AISC 360-16 underestimated the ultimate strength of the columns as the mean value and COV of $N_u/N_{u,pred}$ are 0.999 and 0.063, respectively, whereas Eurocode 4 overestimated the capacity of the columns with the mean value and COV of strength ratios are 1.076 and 0.59, respectively. Ye *et al.* (2021) experimentally studied the compressive behaviour of aluminium alloy-concrete composite stub columns made with inner carbon steel tube. It was demonstrated the ultimate capacity of the columns improved by 4.40% and 36.17% with the increase of inner tube dimensions and the

concrete strength, respectively. Table 2.10 summarises the existing research studies on these structural members.

Research on CFDSAT structural members is rarely found in the literature. All previous studies are related to the compressive response of CFDSAT stub columns. However, no research study is available on the flexural buckling and bending response of these members so far. Moreover, no design rules have been developed for the design of these members.

Table 2.19: Previous studies on CFDSAT structural members.

Reference	Synopsis	Alloy	Section	Length of specimen	No. of test	Studied parameters
Zhou and Young (2018)	Experimental and numerical studies of stub columns	6061-T6	CHS outer and inner skin	Stub column	24	Cross-section dimensions, concrete strength
Zhou and Young (2019)	Experimental and numerical studies of stub columns	6061-T6	CHS outer and SHS inner skin	Stub column	24	Cross-section dimensions, concrete strength
Patel *et al.* (2019)	Numerical study of stub columns	-	CHS outer and inner skin	Stub column	-	Cross-section dimensions, material strength
Ye *et al.* (2021)	Experimental study of stub columns with inner carbon steel tube	-	CHS outer and inner skin	Stub column	10	Cross-section dimensions, concrete strength

2.3.9 Research on sustainability of concrete-filled tubular members

Hastak and Halpin (2000) assessed the life-cycle benefit-cost of composite members. They developed a life-cycle benefit-cost model and used this model to evaluate the cost of CFST and FRP-confined concrete columns. However, the authors did not get a chance to validate the model at that time because of the limited number of test data of

composite structural members. Hastak *et al.* (2003) proposed a unique framework for life-cycle cost assessment model for composite materials. The model was developed using available life-cycle performance data of traditional materials, knowledge about material properties and deterioration characteristics of different structural components subjected to different loading conditions. It was demonstrated that the proposed model effectively determine the economic aspects of composite materials used in construction. Rossi *et al.* (2011) conducted life-cycle assessment of steel, steel-concrete composite, reinforced concrete and wooden columns. The cradle-to-gate system boundary was used to assess different environmental impacts, such as global warming potential, acidification potential and energy consumption of these columns. The study concluded that the steel column provides the lowest environmental impact compared to the other column alternatives. Hou and Han (2018) studied the life-cycle performance of deteriorated CFST columns under lateral impact. A FE model was developed to investigate the structural behaviour of deteriorated CFST columns. Different factors including chloride corrosion, residual stress, geometric imperfection and loading conditions such as axial load and lateral impact load were considered in the numerical analysis. It was shown that the current design methods overestimate the residual capacity of the CFST columns subjected to these loading conditions and environmental aggressiveness. Duarte *et al.* (2018) presented a comparative assessment of the sustainability of CFST columns filled with rubberized concrete. The sustainability of these columns was evaluated in terms of cost, thermal performance and embodied energy and compared with those of conventional CFST and RC columns. The results demonstrated that the cost and embodied energy of rubberized CFST is slightly higher which is around 1% than the CFST column. However, RC column contains 35% more embodied energy and 25% less costly compared to the composite columns. Zhao *et al.* (2021) conducted life-cycle assessment (LCA) and life-cycle cost analysis (LCCA) of composite structural members incorporating uncertainty. Three composite columns including CFST column, concrete-filled FRP tubular (CFFT) column, hybrid FRP-concrete-steel double-skin tubular (DSTC) column with a service life of 100 were considered in this study. The deterministic LCA results concluded that CFST column emits 50% and 60% less CO_2 than the DSTC and CFFT columns. The LCCA study indicated that DSTC 15% less costly compared to the other design alternatives. Available studies related to the assessment of the sustainability of composite structural members are listed in Table 2.11.

Previous research mainly focused on the sustainability assessment of CFST columns and composite materials. However, up to date, no reported study on the assessment of long-term environmental impact and economic aspect of aluminium alloy concrete-composite structural members is available.

Table 2.20: Previous studies on the sustainability of composite structural members.

Reference	Synopsis	Functional Unit	Method	System boundary
Hastak and Halpin (2000)	Life-cycle benefit-cost of composites in construction	CFST and FRP-confined concrete columns	LCCA	Cradle-to-use
Hastak *et al.* (2003)	Framework for life-cycle cost assessment of composite materials	Composites materials	LCCA	Cradle-to-use
Rossi *et al.* (2011)	LCA of different types of columns	Steel, steel-concrete composite column with steel reinforcement, reinforced concrete, wooden columns	LCA - assessed impact: global warming potential, acidification potential, energy consumption	Cradle-to-gate
Hou and Han (2018)	Life-cycle performance of deteriorated CFST column	CFST column	FE analysis considering environmental aggressiveness, extreme hazard and construction issues	Cradle-to-grave
Duarte *et al.* (2018)	Sustainability of CFST columns filled with rubberized concrete	Rubberized CFST, CFST and reinforced concrete columns	LCA - assessed impact: embodied energy, thermal performance, LCCA	Cradle to gate
Zhao *et al.* (2021)	Life-cycle assessment of composite columns incorporating uncertainty	CFST, concrete-filled FRP tubular, hybrid fibre-reinforced polymer-concrete-steel double-skin tubular columns	LCA - assessed impact: CO_2 emission, LCCA	Cradle-to-grave

2.4 Research gap

The self-weight of CFAT structural members is less compared to CFST ones owing to the use of lightweight aluminium alloys. The weight of these structural members can be reduced further by applying the double skin technique. Therefore, CFDSAT structural members can provide better seismic performance and can improve the cost-effectiveness of structures by saving materials and labour costs. Despite all these advantages, the research on CFAT and CFDSAT structural members is relatively limited and some areas are still unexplored. After reviewing the literature, it is observed that most of the past studies mainly focused on the structural responses of CFAT and CFDSAT short columns and very few studies dealt with the flexural behaviour of CFAT members. No research study is available on the buckling response of CFAT and CFDSAT columns and the flexural response of CFDSAT beams. In addition, most existing research on aluminium alloy-concrete composite structural members is conducted for low and medium-strength aluminium alloys, while experimental data of structural members made with high-strength alloys are rarely found in the literature. Moreover, to date, no design rules have been established for aluminium alloy-concrete composite structural members.

For sustainable design, it is essential to have information on the environmental and economic aspects of aluminium alloy-concrete composite structural members across their life-cycle. Past research studies are mainly concentrated to assess the life-cycle performance of CFST columns and composite materials. However, no effort has been devoted so far to study the long-term environmental impact and economic characteristics of CFAT and CFDSAT structural members.

To bridge these knowledge gaps, this research study presents a series of experimental and numerical studies on the structural performance of CFAT and CFDSAT structural members, including columns and beams. All specimens are made of 6082-T6 heat-treated high-strength aluminium alloy. Moreover, based on the observed structural response, design recommendations are provided for the design of these structural members. Finally, the sustainability of these structural members is evaluated by life-cycle assessment (LCA) and life-cycle cost analysis (LCCA).

CHAPTER 3 : METHODOLOGY

3.1 Introduction

To investigate the structural response of CFAT and CFDSAT structural members and determine the sustainability of these composite members, a methodology is adopted that consists of the following stages:

- Experimental programme
- FE modelling
- Validation of the developed FE model
- FE parametric study
- Results analysis and design recommendations
- Sustainability assessment

The current chapter briefly discusses the methodology adopted in the experimental programme, FE modelling and sustainability assessment of CFAT and CFDSAT structural members. Moreover, some general assumptions related to FE modelling and analysis technique are also described in this chapter. However, the procedures of FE model validation, parametric study, results analysis and design recommendations are discussed in the respective chapters.

3.2 Experimental programme

A series of tests were conducted to study the behaviours of BAT, CFAT and CFDSAT structural members. The test programme consisted of four major steps, i.e., specimen preparation, determination of material properties, measurement of initial geometric imperfections and structural performance tests. These steps are described in the following sections of this chapter.

3.2.1 Specimen preparation

The test specimens were cut to the desired length. The inner surfaces of the aluminium alloy hollow tubes were meticulously cleaned to ensure adequate interaction between concrete and tube interfaces. To avoid any localised failure, each end of the column specimens was strengthened by carbon fibre reinforced polymer (CFRP) sheet. A layer of CFRP sheet with 50 mm width was wrapped around the ends of the outer section

using a strong adhesive. A similar strengthening approach is applied by Zhou and Young (2009; 2018) for CFAT and CFDSAT short columns. Moreover, both ends of the column specimens were milled flat by a finishing machine and a layer of plaster was applied on the top surface of the concrete of each end to ensure uniform distribution of the axial compressive load (Figure 3.1(b)). The same approach was used in previous research studies (Zhou and Young, 2009; 2018). For CFDSAT specimens, the inner tubes were precisely located at the centroid of the outer tubes using top and bottom wooden plates (Figure 3.1(c)). The wooden plates were prepared by attaching two parts, i.e., an outer part and an inner part. The dimensions of the outer part were similar to the dimensions of the outer tube, whereas the dimensions of the inner part were same as the dimensions of the interspace between two tubes of the respective specimen. Before casting, the lower end of each specimen was sealed properly to prevent leakage of concrete. For concrete casting, specimens were bundled and placed vertically in a vibrating table. Concrete was poured in layers in the hollow space and compacted using the vibrating table. To remove the air bubbles each layer of the concrete was vibrated for less than 1 min.

(a) (b)

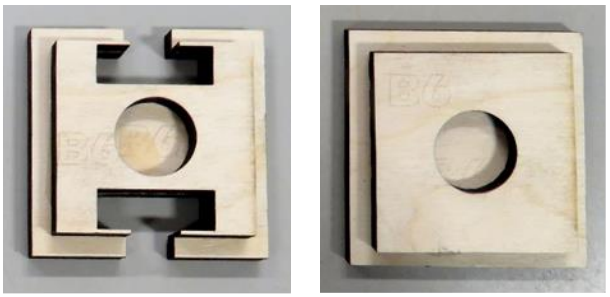

(c)

Figure 3.1: (a) Column top and bottom ends wrap with CFRP, (b) column edges cast in plaster, (c) wooden plates for CFDSAT members

After casting, the specimens were wrapped using plastic sheets to prevent moisture evaporation from the concrete. The specimens were cured for 28 days and then wooden plates were removed. Figure 3.2 presents the cross-sectional geometry of typical BAT, CFAT and CFDSAT specimens, where D is the depth/diameter, B is the width, t is the thickness and the subscripts 'o' and 'i' denote the outer and inner tubes, respectively.

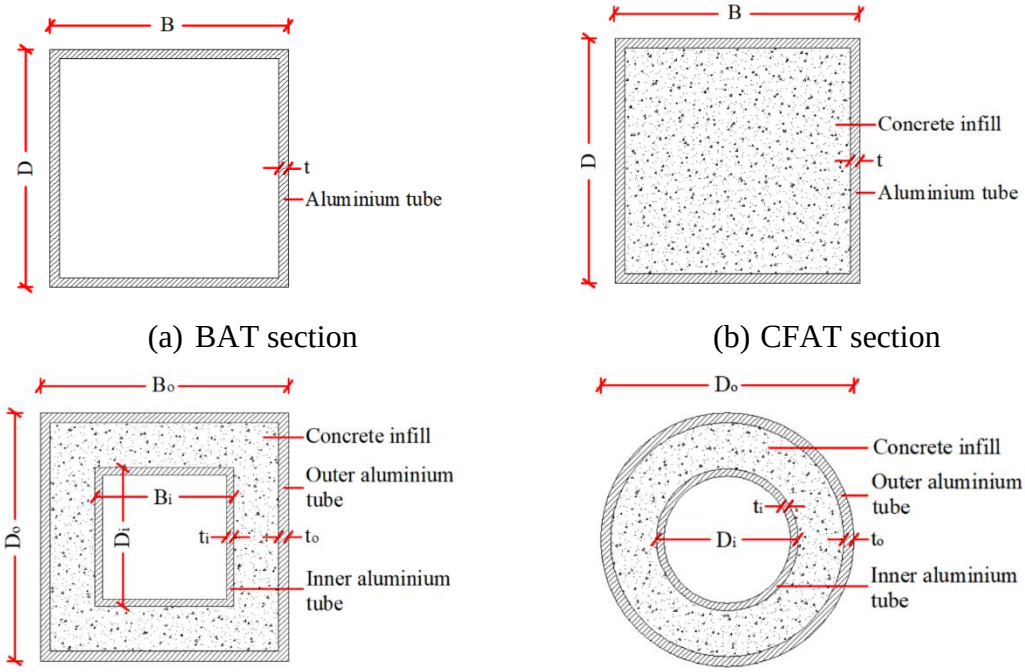

(a) BAT section

(b) CFAT section

(c) Square outer-square inner CFDSAT section

(d) Circular outer-circular inner CFDSAT section

Figure 3.2: Cross-sectional geometry of typical BAT, CFAT and CFDSAT specimens.

3.2.2 Material properties

The material properties of the aluminium alloy hollow tubes were obtained from tensile coupon tests. Two coupons with 12 mm width and 100 mm gauge length were cut longitudinally from random locations of each square/rectangular (flat coupons) and circular (curved coupons) tubes according to the recommendation of BS EN ISO 6892-1 (2009). A 50 kN servo-hydraulic tensile machine was used for the tests. During the tests, flat grip faces were used for the flat coupons (Figure 3.3(a)) and grip faces with a pitch serration were applied for the curved coupons for ensuring better contact between the specimen and the grip faces (Figure 3.3(b)). A displacement-control load with a rate of 0.2 mm/min was applied during the tests. The longitudinal strains of the specimens were recorded using an extensometer. The experimental stress-strain curves were

replicated using the Equations (3.1) and (3.2) recommended by Ramberg and Osgood (1943) and revised by Hill (1944).

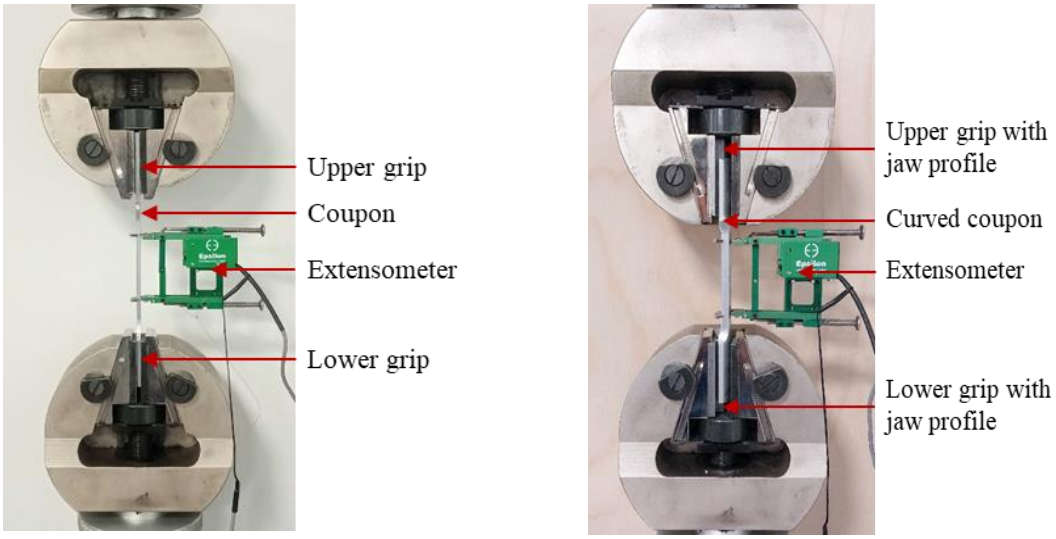

(a) Flat coupon test (b) Curve coupon test

Figure 3.3: Photographs of tensile coupon test.

$$\varepsilon = \frac{f}{E} + 0.002\left(\frac{f}{f_{0.2}}\right)^{n} \tag{3.1}$$

$$n = \frac{ln\,2}{ln\left(\frac{f_{0.2}}{f_{0.1}}\right)} \tag{3.2}$$

where ε represents the strain, f denotes the tensile stress, E is the modulus of Elasticity, $f_{0.1}$ is the 0.1% proof stress, $f_{0.2}$ is the 0.2% proof stress and n is the strain hardening parameter. The measured material properties of the aluminium alloy of tubes are provided in Tables 4.2, 5.2, 6.2 and 7.2 in the respective chapters, including the strain at maximum stress (ε_u) and the strain at fracture (ε_f) values.

The concrete was produced by mixing ordinary Portland cement, sand, stone (≤10 mm) and water with a ratio of 1:1.5:2.5:0.5 by weight. The material properties of concrete were obtained from the compressive tests of concrete cubes and concrete cylinders. The concrete cylinders with a nominal height of 300 mm and a diameter of 150 mm and the concrete cubes with 100 × 100 × 100 mm dimensions are prepared from the same concrete mixture used for specimens casting. The compressive tests were conducted at the test day of specimens based on the guidance of BS EN 12390-3 (2009) and the test

results are provided in Table 4.3, 5.3 and 6.3 in the respective chapters.

3.2.3 Initial geometric imperfections and loading eccentricity

Initial geometric imperfections mean the deviation of a structural member from ideal geometry. Initial geometric imperfections can be classified into two categories, i.e., local or cross-sectional imperfection and overall or global imperfection (Gendy and Hanna, 2017, Elchalakani *et al.,* 2022). Initial local geometric imperfection represents the change of cross-section from its ideal shape. This imperfection can be found in the perpendicular direction of the outer or inner surfaces of a structural member. Initial global geometric imperfection represents the deviation of the centreline of a structural member from its straightness. These imperfections can be originated during the manufacturing process, handling, storage and erection of metals.

The initial geometric imperfections can remarkably affect the behaviour of structural members. Hence, the initial local and global geometric imperfections of all specimens were measured before the tests and their magnitudes were considered in the FE analysis. A linear height gauge with an accuracy of 0.0005 mm was used to measure the deviation from a flat surface at regular intervals along the centreline of the longitudinal direction of all sides of each specimen (Figure 3.4). The maximum value recorded was considered as the amplitude of initial local geometric imperfection of the specimens. The value of initial global geometric imperfection corresponding to the buckling axis was determined by measuring the deviation at mid-height of a face parallel to the buckling axis from the reference line connecting to both ends of a specimen.

(a) Imperfection measurement set-up

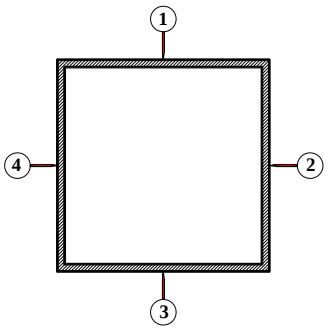

(b) Location of imperfection measurements

Figure 3.4: Measurement of initial geometric imperfections.

At the beginning of flexural buckling tests, the actual initial loading eccentricity (e_0) of column specimens was determined based on the observed lateral displacement and strain values to ensure that the e_0 value was less than L_{eff}/1000 (Yao *et al.* 2020). The e_0 was calculated using Equation (3.3) (Zhao and Gardner, 2016). It should be noted that the loading eccentricities of all specimens were considered in the numerical study.

$$e_0 = \frac{E_a I_a \left(\varepsilon_{max} - \varepsilon_{min}\right)}{DN} - \delta - \omega_g \tag{3.3}$$

where I_a represents the moment of inertia of the cross-section, N is the axial compressive load, δ is mid-height lateral displacement and ε_{max} and ε_{min} are the maximum and minimum strain values at recorded N, respectively.

3.2.4 Structural performance tests

A servo-hydraulic testing machine with 600 kN capacity is used for conducting the structural performance tests. For compression members, a bearing system, consisting of a steel plate with V-shaped grooves and a wedge plate containing a knife-edge wedge is adopted at both top and bottom supports to simulate pin-ended support conditions and allow rotation of the specimens about the buckling axis. Moreover, in both ends of each specimen, plates bolted to channel sections allowed the adjustment of the specimen's relative position and prevented springing out of specimens during testing, without providing any additional restraint. The compressive load was applied using a displacement-control rate of 0.2 mm/min. An initial load of 2 kN was applied to eliminate any gap at the loading point. For flexural members, specimens are supported by two pinned supports to allow rotation around the bending axis and movement along the longitudinal direction of the specimens. The pinned supports are located 900 mm away from each other. The distance between support and loading point (shear span) is 300 mm. The gap between two loading points (moment span) is also 300 mm. The transverse compressive load is employed by two loading points at the central span of the specimens with a displacement-controlled rate of 1.5 mm/min. During the tests, strain gauges are instrumented at specified locations of the specimens to record the strain distribution. For columns, four strain gauges are attached symmetrically on the four outer surfaces of the specimen's mid-height (Figure 3.5(c)) and for beams, two strain gauges are positioned on the outer surface of the mid-span of the top and bottom flange

of the specimen (Figure 3.5(d)). Before instrumenting the strain gauges, the surfaces of specified locations of the specimens are smoothed and cleaned. A strong adhesive is used to attach the strain gauges to the surfaces. After attaching, the resistance of the strain gauges is checked using a multimeter. Finally, a rubber coating is applied to protect the strain gauges from humidity and moisture. Linear variable displacement transducers (LVDTs) were used to measure the displacements. A data acquisition system is used to record all the data during the tests. Figure 3.5 presents schematic diagrams of the experimental set-up of the axial compression test and flexural test.

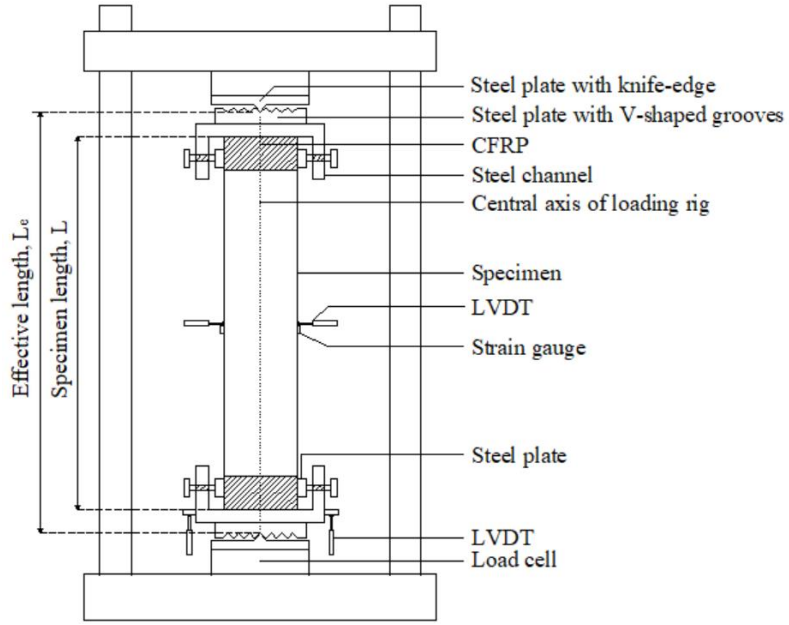

(a) Schematic diagram of axial compression test

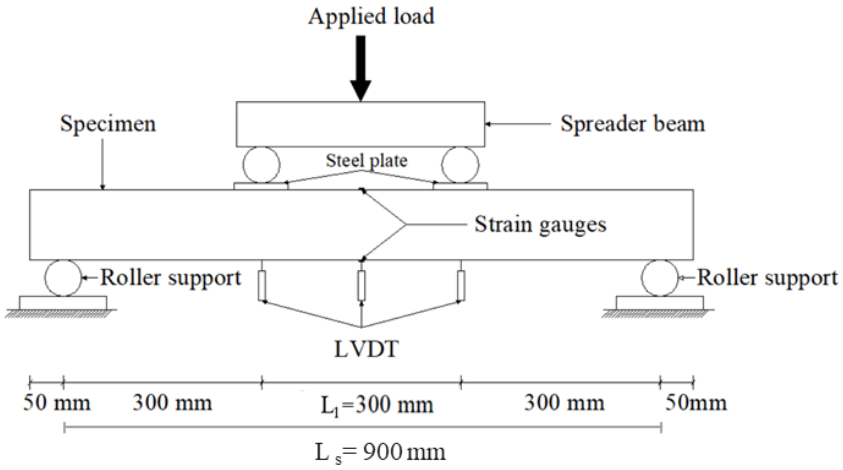

(b) Schematic diagram of flexural test

Figure 3.5: Schematic diagram of the experimental set-up.

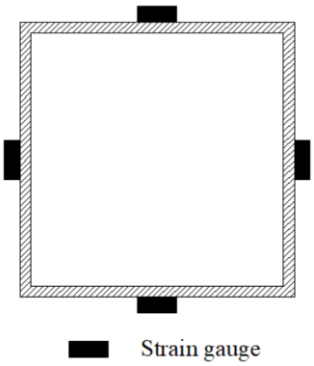

(c) Strain gauge arrangement for column

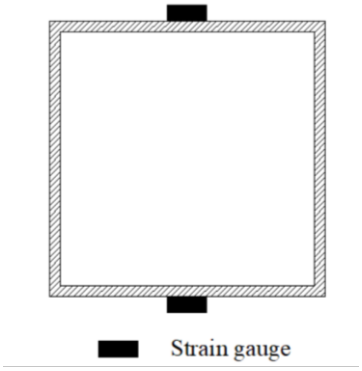

(d) Strain gauge arrangement for beam

Figure 3.6 (continued): Schematic diagram of the experimental set-up.

3.3 Development of FE models

The FE method was used to conduct the numerical investigation of the structural behaviour of BAT, CFAT and CFDSAT structural members. Non-linear FE models of tested specimens were developed by taking into account the material and geometric nonlinearities. The models were validated against test results and numerical parametric studies were carried out using the validated models. The following section discusses the procedures and assumptions considered in the FE analyses conducted in this study.

3.3.1 FE modelling

FE method is a numerical approach which provides solutions to mathematical problems in two or three-dimensional space variables. In this method, a large system is subdivided into small parts and connected by nodes. The elements are arranged in a particular way which is called a mesh. Numerically meshes are represented by a set of algebraic equations which need to be solved to obtain unknown quantities. FE method has many benefits for researchers, i.e., it can be used to solve any problem in the fields of engineering and the physical sciences, with any geometric shape, boundary, loading conditions and material properties. The FE analysis consists of three steps, i.e., pre-processing, solution and post-processing. In the pre-processing step, the FE model is developed by defining geometry in a two or three-dimensional space, material properties and discretising it using meshing technique. In the solution step, calculations of the mathematical equations are conducted. In the post-processing step, the solutions obtained from the previous step are presented.

For conducting the FE investigation in this study the FE analysis software ABAQUS (Hibbitt *et al.*, 2012) is applied. ABAQUS has a simpler interface which makes it easy for users to set up and run simulations compared to other FE analysis software. In ABAQUS two types of solvers, i.e., implicit and explicit are used to solve the problem. Implicit solver is generally used for static stress analyses, where the dynamic effect is ignored. Explicit solver is commonly applied for dynamic problems, especially where the response of a system needs to be recorded over a small time period. In this study, the implicit solver is used for analysing the bare hollow structural members. However, for the concrete-filled composite structural members, the explicit solver is applied to avoid any convergence issue that may be appeared due to the concrete cracks that develop at the early stage of loading (Hamunzala and Teklemariam, 2016, Earij *et al.*, 2017). In subsection 3.3.7, further discussion is provided related to the analysis techniques used in this study.

In the FE method, the direct stiffness method is used for solving mathematical problems. In this process, the equations are developed based on the virtual work method, which refers that the system forces, stresses and tractions are in equilibrium condition when the internal virtual work equals the external virtual work. Here the word virtual work means the infinitesimal change of the global system coordinates. By following this process, the FE method provides an approximate solution to the mathematical problem. The basic algebraic equation of the direct stiffness method is $\{F\} = [K]\{u\}$, where [K] is the stiffness matrix, $\{u\}$ is the displacement vector and {F} is the force vector of the system. When the stiffness and applied force are known, the displacements which are considered as the primary unknowns of the system can be obtained by solving this equation. The secondary quantities of the system, such as stress and strain can be found from the relationships of these quantities with the displacements.

3.3.2 Elements

In FE analysis software, a wide range of elements is available for modelling different geometries. Five aspects are followed to characterise an element, including, family based on the structural point of view (i.e., continuum, shell, rigid, membrane, beam, truss etc.), degrees of freedom (i.e., displacement, rotation, temperature etc.), number of nodes (i.e., linear, quadratic, cubic), formulation (i.e., small, finite-strain shell) and

integration (i.e., reduced, full integration) (Hibbitt *et al.*, 2012). In this study, solid and shell element are used to model the structural members which are presented in Figure 3.6.

Solid or continuum elements are developed for two-dimensional and three-dimensional modelling. These elements can be used for linear or complex nonlinear analyses involving plasticity, contact and large deformations. Shell elements are applied to model components in which one dimension, i.e., thickness is much smaller than the other dimensions. For these elements, the stresses in the thickness direction are considered negligible. The degrees of freedom refers to the fundamental variables of nodes of the elements along the local coordinate system. Solid elements have only three translational degrees of freedom per node. Therefore, the nodes of these elements only allow translations without transmitting any moment. Shell elements possess both translational and rotational degrees of freedom. Hence, each node of these elements contains six degrees of freedom.

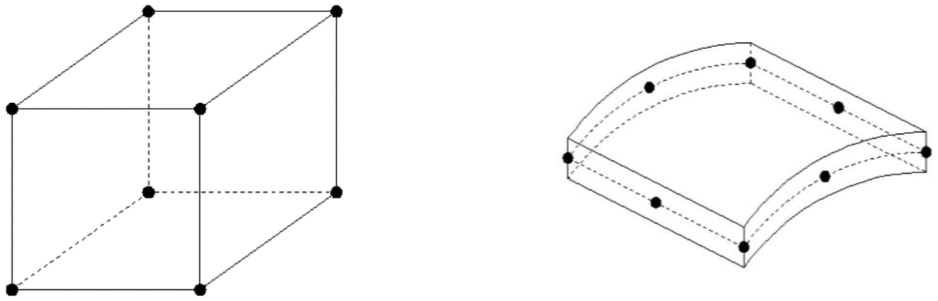

(a) (b)

Figure 3.7: Element used in this study (a) solid element and (b) shell element (Hibbitt *et al.*, 2012).

Formulation of an element represents the mathematical theory that is used to define the behaviour of the element. Two methods are widely used to define elemental behaviour, i.e., Lagrangian and Eulerian methods (Hibbitt *et al.*, 2012). The Lagrangian method considers that elements are deformed with the material. On the other hand, the Eulerian method assumes that elements are fixed in space as the material flows through them. Therefore, Eulerian elements are appropriate for fluid flow analyses, whereas the Lagrangian elements are suitable for stress/displacement analyses which is considered in this study.

In FE analysis the stiffness and mass of the elements are determined by numerical integration. The points where these properties are evaluated are known as the integration points. Gaussian quadrature method is generally used to calculate the material response at integration points of the elements. Two types of integration techniques are usually applied in the FE analysis, i.e., full and reduced integration (Hibbitt *et al.*, 2012). In the full integration procedure, sufficient integration points are required to integrate the virtual work expression exactly. In the reduced integration procedure, lesser integration points are used to solve the integral. Figure 3.7 shows the typical cases of full and reduced integration for first-order and second-order interpolation elements.

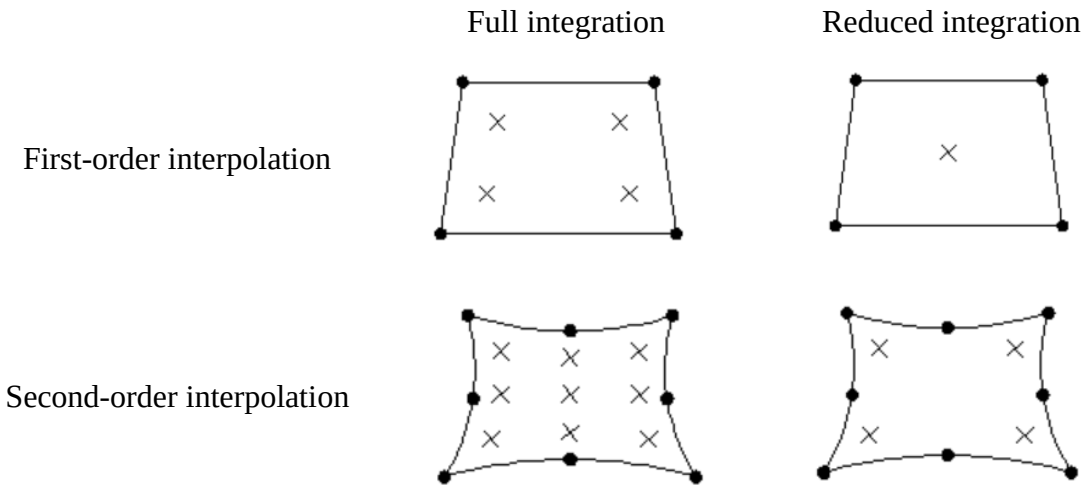

Figure 3.8: Full and reduced integration for first and second order interpolation elements (Hibbitt *et al.*, 2012).

In FE analysis, shear locking and hourglassing are two phenomena that may lead to spurious results in some cases. Shear locking can be a problem for fully integrated elements, whereas hourglassing may affect the reduced integrated elements. Shear locking is observed when fully integrated linear elements (i.e., the elements have nodes only at the corners of their edges) are used to model beams or plates. The linear elements cannot accurately model the curved shape of actual material under bending. When pure bending moment is applied, the tensile and compressive stresses are developed at the top and bottom surface of these elements. Therefore, artificial shear stress is introduced instead of bending deformation, which causes the elements to become too stiff (Figure 3.8(a)). This phenomenon can be reduced by increasing the element numbers of the component or applying reduced integrated elements. However,

reduced integrated elements may suffer from hourglassing subjected to bending which indicates that the normal and shear stresses and the strain energy are zero at the integration points when the elements deform (Figure 3.8(b)). This phenomenon is mainly developed when the coarse mesh is used in the structure. To avoid this phenomenon, at least three elements should be used along the thickness of the structures when reduced integration elements are adopted to simulate the bending response.

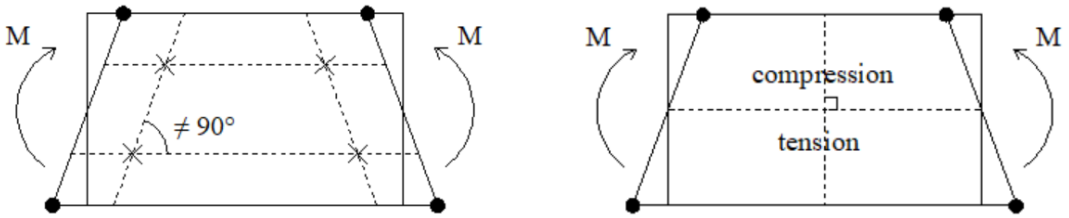

(a) Shear locking (b) Hourglassing

Figure 3.9: Phenomena on linear elements under pure bending (Hibbitt *et al.*, 2012).

In ABAQUS each element has a unique name, such as S4R indicates the 4-node shell element with reduced integration and C3D8R denotes the 3-dimensional 8-node solid element. In this study, S4R and C3D8R elements were used to develop the models. The S4R element is used to model structural elements in which one dimension is much smaller than the other two dimensions. This element does not consider the stress in the direction perpendicular to the shell surface. Therefore, this element is suitable for thin-walled structures where the change of the analysed feature along the smaller dimensions, i.e., thickness is neglected. C3D8R is a first-order brick element with reduced integration. This element can be applied to simulate thin-walled structures by using at least three elements through the thickness. Because of having one integration point, S4R and C3D8R elements do not suffer from any numerical difficulties, such as shear locking or hourglassing. In the previous studies, both S4R (Zhao *et al.*, 2016; Wang *et al.*, 2017 and Feng and Liu, 2019) and C3D8R (Zhou and Young, 2012; Zhou and Young, 2018; Zhao *et al.*, 2019 and Zhu *et al.*, 2020) elements have been applied successfully for modelling the hollow aluminium sections. In this study, both elements were used to capture the structural behaviour of aluminium tubes. In line with the previous studies (Zhou and Young, 2012; Zhou and Young, 2018; Zhu *et al.*, 2020) C3D8R element has been adopted to model the concrete infill.

3.3.3 Mesh

In FE analysis, the arrangement of finite elements is defined by mesh. A coarser mesh may lead to inadequate results, while a refined mesh can provide more accurate results. In ABAQUS different meshing techniques are available, i.e., structured meshing, swept meshing, free meshing, etc. Structured meshing technique provides the most control over the mesh as it uses predefined mesh patterns. This technique can be applied to a two-dimensional region which has no holes or isolated edges. For a complex model, the structured mesh can be achieved by manually partitioning the geometry into simple regions. Swept meshing technique is suitable for complex geometry. This technique begins by meshing from one side of geometry which is known as the source side. Then, the source mesh sweeps through the body. Free meshing technique does not require any pre-established pattern to generate the mesh. In this study, the structured meshing technique is used to mesh the models.

Selecting a suitable mesh size is important for FE analysis. The suitable mesh size can be chosen by conducting a mesh sensitivity analysis. In this analysis, a FE model is run with different mesh sizes to check how much the results change with each size. Based on the comparison an optimum mesh size is selected which provides a solution in a reasonable analysis time without compromising its accuracy. In this study, a mesh sensitivity analysis was conducted which is described in Chapter 4.

3.3.4 Material properties

According to ABAQUS manual (Hibbitt *et al.*, 2012) the material properties need to be inputted in the form of true stress and true strain (logarithmic strain). Therefore, the engineering stress-strain data of aluminium tubes determined from tensile coupon tests are converted into true stress-strain data using Equations (3.4) and (3.5).

$$f_{true} = \sigma\left(1+\varepsilon\right) \tag{3.4}$$

$$\varepsilon_{\ln}^{pl} = \ln\left(1+\varepsilon\right) - \frac{f_{true}}{E_a} \tag{3.5}$$

where f_{true} is the true stress and ε_{ln}^{pl} is the logarithmic plastic strain.

To consider the elastic response of aluminium alloy, the values of modulus of elasticity obtained from the coupon test and a Poisson's ratio of 0.33 were used. To account for

the plastic response, the von Mises yield criterion with isotropic hardening was used. Von Mises yield criterion define the yielding point of the metals. According to this criterion yielding occurs when second invariant of deviatoric stress reaches a critical value, while the stress-strain relationship is considered to be elastic until that point. For the multiaxial stress state this criterion can be expressed by Equation (3.6) (von Mises, 1913).

$$f_y = \sqrt{0.5\left[(f_1 - f_2)^2 + (f_2 - f_3)^2 + (f_3 - f_1)^2 \right]} \tag{3.6}$$

where f_1, f_2 and f_3 are the principal stresses. This expression leads to a cylindrical yield surface with radius of $\sqrt{2/3}\ f_y$ around the hydrostatic axis ($f_1 = f_2 = f_3$), as shown in Figure 3.10.

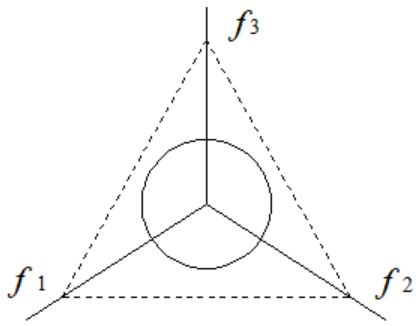

Figure 3.10: Von Mises yield criterion (von Mises, 1913).

For metal sections, isotropic hardening means that the yield surface remains the same in shape and expands in a uniform way around the hydrostatic axis with increasing stress. Under monotonic load, the isotropic hardening of metal can be expressed by the following equation.

$$f\left(\sigma_{ij}\right) - K = 0 \tag{3.7}$$

where $f(\sigma_{ij})$ and K are the yield function and hardening parameter, respectively.

The material model of the concrete infill is established based on the data obtained from the compressive strength tests of concrete cubes or cylinders. The elastic response is considered according to the modulus of elasticity and Poisson's ratio of concrete. The modulus of elasticity is calculated using Equation (3.8) as recommended by the European standard (Eurocode 4, 2004) and the Poisson's ratio is assumed 0.2. The

concrete damaged plasticity (CDP) model available in ABAQUS (Hibbitt *et al.,* 2012) is adopted to consider the plastic behaviour of concrete. The CDP model consists of three aspects, i.e., the plasticity parameters, the compression behaviour and the tensile behaviour.

The plasticity parameters include the dilation angle (ψ), the ratio of the compressive strength under biaxial loading to uniaxial compressive strength (f_{b0}/f_c), flow potential eccentricity (e), compressive meridian (K_c) and viscosity parameter. In this study, the value of ψ is taken 40° as suggested by Tao *et al.* (2013) for infilled concrete. The viscosity parameter and the flow potential eccentricity are taken as the default values of 0 and 0.1 respectively, as they have no significant influence on concrete-filled hollow tubes (Tao *et al.* 2013). The ratio of f_{b0}/f_c and the K_c are determined by Equations (3.9) (Papanikolaou and Kappos, 2007) and (3.10) (Yu *et al.*, 2010), respectively.

$$E_c = 22000\left(\frac{f_c + 8}{10}\right)^{0.3} \tag{3.8}$$

$$\frac{f_{b0}}{f_c} = 1.5\left(f_c\right)^{-0.075} \tag{3.9}$$

$$K_c = \frac{5.5 f_{b0}}{3 f_c + 5 f_{b0}} \tag{3.10}$$

where f_c is the concrete compressive strength.

To account for the beneficial effect due to the full confinement of the concrete core by the aluminium tube, an equivalent uniaxial compressive stress-strain model of confined concrete proposed by Tao *et al.* (2013), as shown in Figure 3.11 is considered in this study. In this model, no interaction is considered between the outer section and concrete infill up to peak compressive strength because of the variation of Poisson's ratio of the two materials. Therefore, up to ultimate strength, the stress-strain behaviour of both confined and unconfined concrete remains identical. Beyond the ultimate strength, the lateral displacement of concrete rises rapidly compared to the outer section and confining pressure between two materials develops. This beneficial confinement effect is considered in stress-strain response by adding a horizontal plateau and a softening branch with improved ductility. It is assumed that the concrete infill in the double skin metal tubes exhibits similar behaviour to that of the single skin section, as the inner

hollow tube of the double skin section prevented the inward lateral deformation of the concrete (Huang *et al.*, 2010). Therefore, the uniaxial compressive stress-strain response for concrete infill of CFST section (Tao *et al.*, 2013) is used in this study with the modified confinement factor suggested by the authors (Wang *et al.*, 2019, 2020a, b) for concrete-filled double skin metal sections.

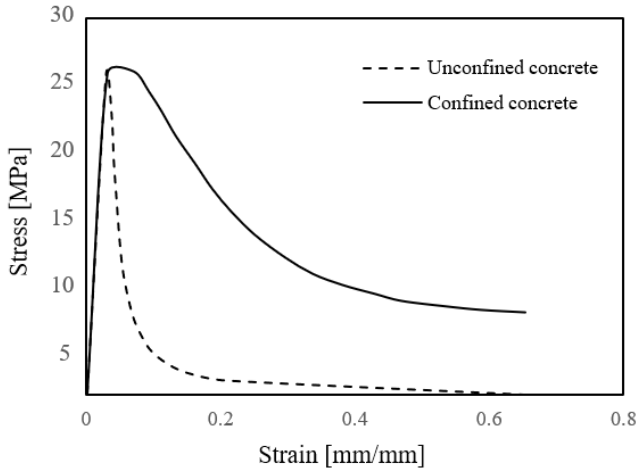

Figure 3.11: Confined concrete's compressive stress-strain model (Tao *et al.*, 2013).

The model has three stages as follows:

$$\sigma = \begin{cases} \left[\dfrac{A(\varepsilon/\varepsilon_{c0}) + B(\varepsilon/\varepsilon_{c0})^2}{1+(A-2)(\varepsilon/\varepsilon_{c0}) + (B+1)(\varepsilon/\varepsilon_{c0})^2}\right] f_c, & 0 < \varepsilon \le \varepsilon_{c0} \\ f_c, & \varepsilon_{c0} < \varepsilon \le \varepsilon_{cc} \\ f_r + (f_c - f_r)\exp\left[-\left(\dfrac{\varepsilon - \varepsilon_{cc}}{\alpha}\right)^{\beta}\right], & \varepsilon_{cc} < \varepsilon \end{cases} \tag{3.11}$$

where $A = E_c\varepsilon_{c0}/f_c$, $B = \{(A-1)^2/0.55\} - 1$; ε_{c0}, ε_{cc} are the strains corresponding to the maximum compressive strength of unconfined and confined concrete which are calculated by Equations (3.12) (De Nicolo *et al.*, 1994) and (3.13) (Samani and Attard, 2012), respectively; f_r is the residual stress of concrete; α and β are the parameters determining the shape of softening stage. In this study, α is computed according to Equation (3.15) and β is taken as 0.92.

$$\varepsilon_{c0} = 0.00076 + \sqrt{(0.626 f_c - 4.33)\times 10^{-7}} \tag{3.12}$$

$$\varepsilon_{cc} = \varepsilon_{c0} \exp\left\{ \left(2.9224 - 0.00367 f_c\right) \left(\frac{f_B}{f_c} \right)^{0.3124+0.002 f_c} \right\} \tag{3.13}$$

$$f_B = \frac{0.25\left(1+0.027 f_y\right) \exp\left\{ \left(-0.02\sqrt{B^2 + D^2} \right) \Big/ t \right\}}{1+1.6\exp\left\{ -10\left(f_c \right)^{4.8} \right\}} \tag{3.14}$$

$$\alpha = 0.005 + 0.0075 \left(\frac{A_a f_y}{A_c f_c} \right) \tag{3.15}$$

For considering the tensile behaviour of concrete, the stress-strain relationship is assumed to be linear up to 10% of compressive cylinder strength (Tao *et al.*, 2013). The inelastic region of the concrete tensile stress-strain curve is defined according to the stress-crack opening displacement relationship (Equation (3.16)) (Hordijk, 1991), based on fracture energy (G_f). The G_f is determined according to Equation (3.18) (FIP, 1993; Bažant and Becq-Giraudon, 2002).

$$\frac{f_t}{f_{tc}} = \left[\left\{ 1 + \left(c_1 \frac{w_t}{w_{cr}} \right)^3 \right\} \exp\left(-c_2 \frac{w_t}{w_{cr}} \right) \right] - \frac{w_t}{w_{cr}} \left(1 + c_1^{\,3}\right) \exp\left(-c_2\right) \tag{3.16}$$

$$w_{cr} = 5.14 \frac{G_F}{f_{tc}} \tag{3.17}$$

$$G_F = \left(0.0469 d_a^2 - 0.5 d_a + 26\right) \left(\frac{f_c}{10} \right)^{0.7} \tag{3.18}$$

where f_t is the tensile stress normal to the crack direction, f_{tc} is the uniaxial tensile strength of concrete, w_t is the crack opening displacement, w_{cr} is the crack opening displacement corresponding to the complete loss of tensile strength, c_1, c_2 are the constants equal to 3 and 6.93 respectively and d_a is the maximum aggregate size of concrete mix which is 10 mm.

3.3.5 Contact interaction

The contact behaviour between the aluminium tube and the concrete infill was modelled by the surface-to-surface contact option provided by ABAQUS (Hibbitt *et al.*, 2012). For the CFAT specimens, a contact set was created including the inner and outer surfaces of the aluminium tube and concrete infill, respectively, where the former performed as the slave surface and the latter performed as the master surface. However, for the CFDSAT specimens, the outer faces of the concrete were set as the master

surfaces, while the outer faces of the inner section and the inner faces of the outer section were assigned as the slave surfaces. A hard contact pressure-overclosure relationship was considered in the normal direction for considering the development of normal stresses between surfaces without penetration in compression and releasing stresses by separating from each other in tension. The Coulomb friction model was adopted in the tangential direction for allowing slippage between the aluminium tube and the concrete. Based on the previous study (Dai and Lam, 2010) a value of 0.3 was used for the friction coefficient, which retains sufficient accuracy and offers a quick convergence.

3.3.6 Geometric imperfections and residual stresses

As mentioned earlier that the structural members may contain initial geometric imprecations, which can significantly affect their structural performance (Gardner *et al.*, 2006; Zhao and Gardner 2016). Therefore, in this study, initial local and global imperfections were explicitly included in the FE models of the structural members. For considering initial geometric imperfections in the FE model, a proper selection of local and global imperfection patterns and amplitudes is required. The eigenvalue buckling analysis was initially performed and the lowest buckling mode shapes were introduced as the initial geometric imperfections in the nonlinear FE model. Figure 3.12 represents typical local and global buckling mode shapes obtained from a linear buckling analysis of a typical column of Chapter 4. The geometric imperfections sensitivity studies were conducted to determine suitable imperfection amplitudes for the structural members of Chapters 4-7.

(a) Local geometric imperfection (b) Global geometric imperfection

Figure 3.12: Typical linear buckling mode shapes.

The residual stresses generated during the production of aluminium alloy are very low (Feng and Liu, 2019; Feng *et al.*, 2020). Therefore, the effect of residual stresses was not considered in the FE modelling.

3.3.7 Analysis techniques

In this study, three analysis techniques, i.e., linear buckling analysis, Riks analysis and dynamic explicit analysis were used.

The linear buckling analysis is a linear perturbation procedure which is generally applied to determine the critical buckling load of the structural members. In this analysis, an incremental loading pattern is defined. The critical buckling load is evaluated by solving the following equation:

$$\left(K_0^{NM} + \lambda_i K_\Delta^{NM}\right) u_i^M = 0 \tag{3.19}$$

where K_0^{NM} is the stiffness matrix related to the base state, K_Δ^{NM} represents the differential initial stress and load stiffness matrix due to the incremental loading pattern, λ_i and u_i^M are the eigenvalues and eigenvectors of the i^{th} buckling mode, respectively and M and N reparent the degrees of freedom. For solving the above equation, the subspace iteration method proposed by Bathe and Wilson (1973) is widely applied in FE analysis. In this study, the lowest respective buckling mode shapes obtained from the linear buckling analysis were considered as the geometric imperfections patterns which were incorporated in the nonlinear analyses by multiplying them with appropriate magnitudes.

The Riks analysis is usually performed to analyse the model that considers the geometric and material nonlinearity. This analysis is useful for obtaining the solution to unstable problems. The Riks analysis applies the Newton-Raphson method to solve the problems. In this method, load magnitude uses as an additional unknown and solutions are simultaneously provided for loads and displacements. To measure the progress of the solution another quantity called arc length is used along the load-displacement path. In Riks analysis, the load is always multiplied by a load proportional factor. This factor is determined using a user-defined total arc length scale factor and applied during the first iteration of a Riks step. For the next iteration and increment, the proportional factor is evaluated automatically. Therefore, the user has no control over the load magnitude.

The Riks analysis will end when the load proportionality factor or the displacement value crosses the maximum value defined by the user. Compared to the conventional Newton-Raphson method which fails to converge when the tangent stiffness matrix becomes singular, the Riks analysis is capable to provide converged solutions and capture ultimate capacity by applying the arc-length method (Ellobody and Young, 2006; Tao *et al.*, 2011; Dai *et al.*, 2020; Zhu *et al.*, 2019b; Feng and Liu, 2019).

Dynamic explicit analysis is computationally efficient for analysing models that undergo large deformation (Hibbitt *et al.*, 2012). This analysis performs a large number of small time increments efficiently using the central difference rule. The dynamic equilibrium shown in the following equation is solved at the beginning of each time increment.

$$M\ddot{u} = P - I \tag{3.20}$$

where M is the nodal mass matrix, $\ddot{u}$ is the nodal accelerations, P is the externally applied force and I is the internal element force. For the first time step t, $\ddot{u}$ is calculated by Equation (3.21) using the lumped mass matrix, M which is a diagonal matrix always used by the explicit analysis.

$$\ddot{u}_t = \left(M\right)^{-1}\left(P - I\right)_t \tag{3.21}$$

In the explicit procedure, the time increment, Δt must be less than the stability limit which is defined by Equation (3.22).

$$\Delta t \le \frac{2}{\omega_{\max}}\left(\sqrt{1+\xi^2} - \xi\right) \tag{3.22}$$

where ω_{max} is the highest eigenvalue in the model and ξ is the damping factor. The explicit procedure solves every problem as a wave transmission problem. Sometimes the stability limit can be approximately estimated by determining the minimum time of a dilatational wave (c_d) takes to travel through an element in the mesh. This is expressed by Equation (3.23).

$$\Delta t = L_{\min}/C_d \tag{3.23}$$

where L_{min} is the smallest dimension of an element. The c_d can be determined by the following equation.

$$c_d = \sqrt{E/\rho} \tag{3.24}$$

where E is the modulus of elasticity and ρ is the density of the material.

The energy balance in the explicit procedure is expressed by the following equation.

$$E_I + E_{VD} + E_{FD} + E_{KE} - E_W = E_{TOT} \tag{3.25}$$

where E_I is the internal energy (i.e., elastic, inelastic, strain energy), E_{VD} is the energy absorbed by viscous dissipation, E_{FD} is the frictional dissipation energy, E_{KE} is the kinetic energy, E_W is the work of external forces, E_{TOT} is the total energy of the system. According to the ABAQUS manual (Hibbitt *et al.*, 2012), for quasi-static analysis, the kinetic energy, E_{KE} should be a small fraction, typically 5 to 10% of the work of external forces, E_W or the internal energy, E_I.

In this study, the Riks analysis is used for analysing the BAT structural members. However, for the CFAT and CFDSAT structural members, the Dynamic explicit analysis is used to prevent the convergence problems that may be generated due to the development of cracks in the concrete at the early stage of analysis (Hamunzala and Teklemariam, 2016, Earij *et al.*, 2017). In the explicit procedure, displacement is applied slowly to eliminate any significant change in the acceleration from one increment to another and to obtain the quasi-static solution.

3.4 Sustainability assessment

Sustainability of aluminium alloy concrete-composite structural members is evaluated by determining their environmental and economic characteristics throughout their lifespan. For this, two well-known analytical approaches, i.e., Life-cycle assessment (LCA) and Life-cycle cost analysis (LCCA) are used in this study. This section discusses the methodology of these approaches.

3.4.1 Life-cycle assessment (LCA)

ISO 14040 (2006) standard provides the definitions, background information and process of carrying out an LCA. This analysis can be applied to determine the

quantitative information about harmful air emissions and energy consumption of a product during different stages of its life cycle, including raw material collection, production, transportation, construction and disposal after end-of-life (Hauschild *et al.*, 2018). By knowing this information, it is possible to improve the environmental performance of a product at various life stages (ISO 14040, 2006). LCA includes four major steps, i.e., goal and scope definition, inventory analysis, impact assessment and results interpretation (ISO 14040, 2006). Figure 3.13 illustrates the framework of LCA approach.

According to ISO 14040 (2006), the first step of LCA is defining the goal and scope of the study clearly. Moreover, all general decisions related to the study are taken in this step. For setting the goal, the following points need to be addressed:

- Purpose: The purpose of the study needs to be defined comprehensively. For example, the purpose of conducting LCA in this research is to assess the environmental loads related to the life stages of the structural members.

- Intended applications: The information obtained from the study can be used to minimize the environmental loads at a certain stage or entire life span and improve the environmental performance of the members.

- Target audiences: The audiences of an LCA have to be specified properly. The targeted audiences of this study are researchers, structural engineers, product manufacturers, consumers, decision-makers of government, etc.

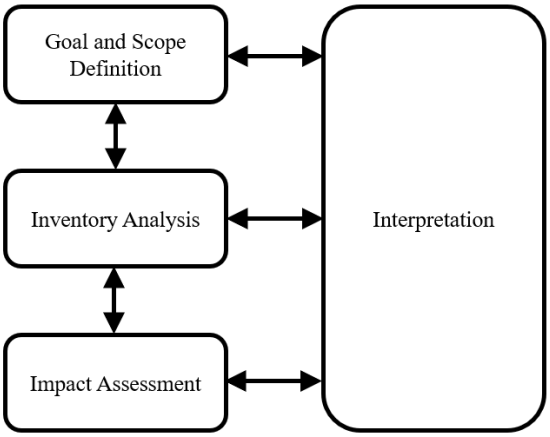

Figure 3.13: Framework of LCA approach (ISO 14040, 2006).

In the scope definition, the studied product is characterised, the assumptions of the study are defined and the system boundary of the product system is described (ISO 14040, 2006). For defining the scope, the following points need to be clarified:

- Function of the product: The products are produced to perform one or more functions which need to be defined. It is better to have products with similar functionality when the LCA results of different products are compared. For example, the function of chosen structural members in this study is to carry compressive load.

- Functional unit: The functional unit is used to quantify the function of a product. For comparing different products the functional unit must be the same. For example, in this study, it is considered that the ultimate capacity (i.e., functional unit) of the structural members is the same.

- System boundary: The system boundary defines different processes considered in the life cycle of a product. Sometimes cut-off criteria are used to exclude any process from the life cycle. System boundaries can be defined in four ways, i.e., cradle-to-grave, cradle-to-gate, gate-to-grave and gate-to-gate. In the cradle-to-grave boundary, all processes from the raw material extrusion to the end-of-life of a product are included. The cradle-to-gate boundary only includes the processes from the raw material extrusion to the production stage of a product. The gate-to-grave boundary considers the processes from the use to the end-of-life of a product. The gate-to-gate boundary includes the processes related to the production stage. In this study cradle-to-grave boundary is considered for the analysis. Figure 3.14 illustrates different types of system boundaries.

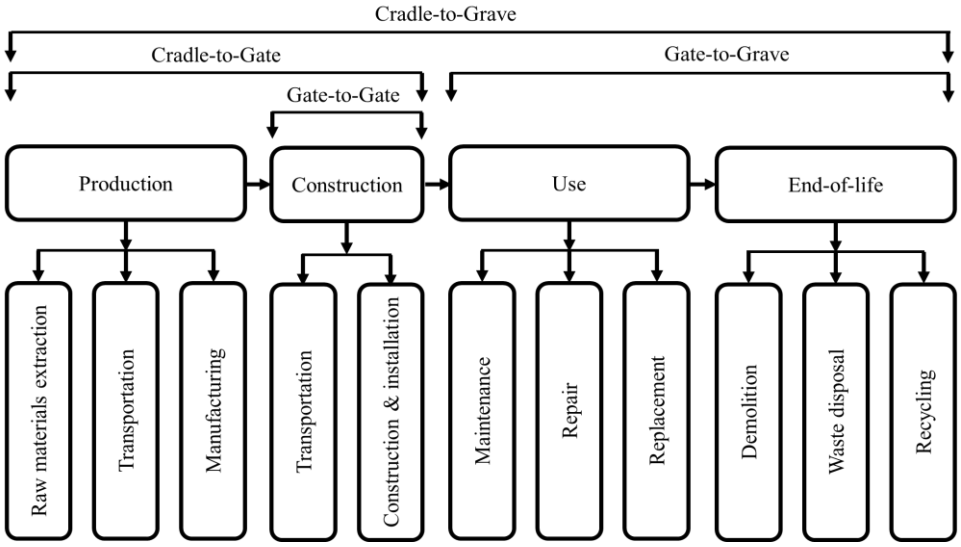

Figure 3.14: Different types of system boundaries of LCA.

Once the goal and scope of a LCA are defined, the next step is to conduct the life cycle inventory (LCI) analysis. In this step, the input and output of materials in each unit process for a product are quantified and compiled. The result of this analysis is obtained by summing up the environmental loads related to every life step of a product. Therefore, this analysis reveals qualitative information on the environmental loads that are emitted to the air, water, soil and other environmental media by a product during its entire life. The LCI consisted of two phases, i.e., data collection and calculation process. The data collection phase includes the collection of qualitative and quantitative information related to the different stages of a product. The data can be categorized as raw material inputs, energy inputs, products, co-products, wastes, emissions to air, water and soil etc. Before conducting the calculation of LCI, the collected data need to be validated. During the calculation process, the environmental loads of each unit process are determined and summed up to generate the total amount of loads of a product.

Life cycle impact assessment (LCIA) evaluates the environmental impacts due to environmental loads that are emitted throughout the life cycle of a product. LCIA consists of four steps, i.e., classification, characterisation, normalisation and weighting. At first, the environmental loads have to be categorized based on environmental concerns, i.e., energy consumption, global warming potential (GWP), acidification potential (AP), abiotic depletion potential (ADP), eutrophication potential (EP), ozone depletion (ODP), etc. Then, the loads are multiplied by the characterisation factors to

determine their relative contribution to the environmental impact. For example, if the CO_2 emission is considered as the reference substance for global warming potential, then all other emissions that contribute to global warming are converted to equivalent CO_2 emissions using the relevant characterization factors. Two types of approaches are used to characterise the environmental impacts, such as the mid-point approach and the end-point approach. In the mid-point approach, mid-point refers to any point of the cause-effect chain before reaching the end-point. Here, the cause-effect chain means a free diagram which is developed by logically organising the possible causes of a specific problem or effect. The mid-point approach is also known as the problem-oriented approach which translates the environmental impact category into the real phenomenon, i.e., climate change, human toxicity, acidification, etc. In the end-point approach, the end-point indicates to end of the cause-effect chain. This approach is known as the damage-oriented approach which translates the environmental impact category to the damage categories at the level of damages to human health, environment, natural resources and man-made environment, via damage indicators.

In the interpretation stage, the significant environmental issues are identified and the results are checked in terms of completeness, consistency and sensitivity. This stage includes two primary steps, i.e., identification and evaluation. In the first step, the results of LCI and LCIA are structured and the issues or data elements are identified that contribute significantly to the results. These issues should be identified based on the goal and scope definition. Significant issues include the inventory elements, such as energy consumption, emissions, wastes, etc. and the impact category indicator that significantly contributes to the results. In the evaluation step, the reliability of the results is evaluated using the completeness check, sensitivity check and consistency check. In the completeness check, any missing or incomplete data is identified and check its importance to satisfy the goal or scope of the study. If so, the data must be added and revised the study. In the sensitivity check the influence of uncertainties in the data, assumptions, methods and calculation process on the results is determined. In the last stage of evaluation, the consistency of the used methods is checked.

3.4.2 Life-cycle cost analysis (LCCA)

The LCCA method is used to evaluate the total cost associated with the entire life of a product. It is normally used to select the less expensive product among the multiple

options. This method helps to track the stages which contribute more to the total cost of a product. This information is useful to minimise expenses at certain stages of the product. The general framework of LCCA method is similar to the LCA method which includes four major steps, i.e., goal and scope definition, inventory analysis, determination of life cycle cost and results interpretation.

In the first step of the LCCA method, the goal and scope of the study are set. The main goal of a LCCA method is to determine the overall cost of a product related to any certain life stage or its entire life. During setting the goal the intended audiences, the reasons and applications of the study need to be defined clearly. The scope of the study is set by clarifying the functional unit and system boundary of the product. Usually, the cradle-to-grave system boundary is applied since it considers all life stages of the product.

In the second step of the LCCA method, life cycle inventory (LCI) analysis is conducted. As mentioned earlier that in this step the materials input and output in each stage are tracked and quantified. The cost related to each stage is then calculated. The cost components generally considered are material cost, transportation cost, construction cost, maintenance cost and end-of-life cost. Material cost is associated with the collection of raw materials for a product. Transportation cost indicates the cost related to the transportation of materials and products. Construction cost comprises the costs for labour and equipment used during the construction stage. Maintenance cost refers to all expenses related to the maintenance actions required for a product. This includes periodic inspections, minor or major repairs and material replacement or reproduction. The end-of-life cost includes the cost associated with the demolition and disposal of a product after it reaches at the end of its service life. Figure 3.15 shows different cost components of LCI analysis.

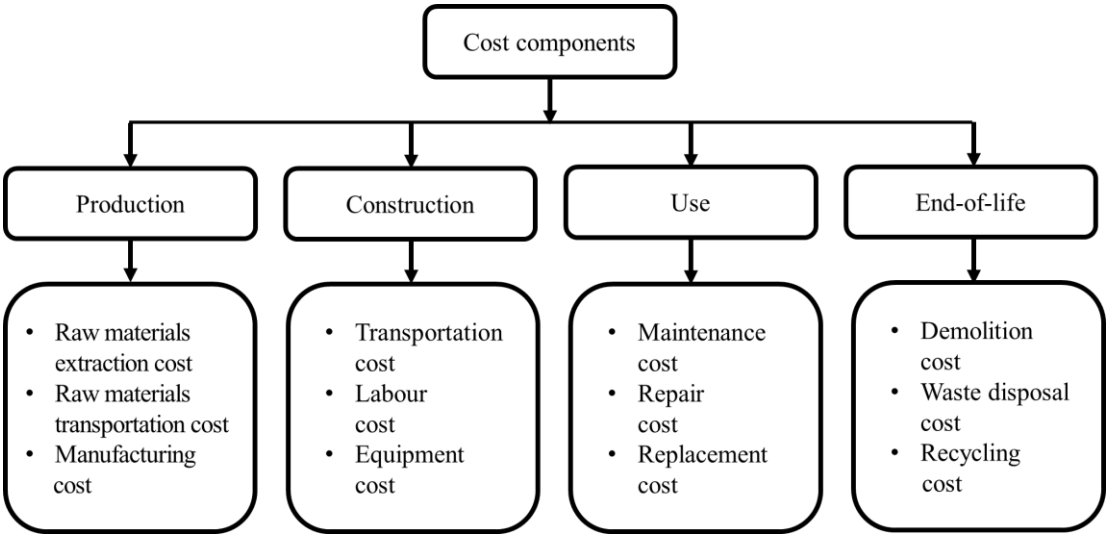

Figure 3.15: Different cost components of LCI analysis.

The total cost of a product is calculated by summing up the costs incurred at different stages of its life span. Then the total cost is converted to the present value considering the discount rate. The discount rate refers to the time value of money. It is applied to determine the future value by accounting for the nominal interest rate and inflation rate. The discount rate is not considered at the initial stage. This rate is used only for calculating future costs related to the maintenance and end-of-life stages.

The final step of the LCCA study is result interpretation. In this step, the obtained results are assessed in terms of completeness, consistency and sensitivity. Critical assessment of results helps to provide robust conclusions and recommendations.

CHAPTER 4 : BAT AND CFAT MEMBERS IN COMPRESSION

4.1 Introduction

This chapter reports the flexural buckling behaviour of BAT and CFAT columns subjected to concentric axial compression. The experimental results are presented in terms of failure modes, ultimate strengths and load versus mid-height lateral displacement curves. FE models are developed and validated against the test results. A parametric study is subsequently conducted to study the buckling behaviour for a range of cross-sections and concrete strengths. The test and numerical results are utilised to assess Eurocode 9 design equations for Class A aluminium alloy columns. Finally, a design methodology is proposed to predict the ultimate strength of the CFAT columns.

4.2 Experimental programme

4.2.1 Test specimens and material properties

In this study, a total of 9 CFAT and 9 BAT columns were tested under axial compression. The nominal lengths (L) of all columns were 1000 mm. The specimens were chosen to cover a wide range of cross-sectional slenderness (β/ε) and member slenderness ($\bar{\lambda}$). The β/ε and $\bar{\lambda}$ are calculated by Equations (4.1) and (4.2) as specified in Eurocode 9 (2007) and Eurocode 4 (2004), respectively.

$$\frac{\beta}{\varepsilon} = \frac{B/t}{\sqrt{250/f_{0.2}}} \tag{4.1}$$

$$\bar{\lambda} = \sqrt{\frac{N_{pl}}{N_{cr}}} \tag{4.2}$$

In Equation (4.1), B is the outer width, t is the thickness and $f_{0.2}$ is the 0.2% proof stress of aluminium tube. In Equation (4.2), N_{pl} is the plastic resistance of the specimen under uniform compression. The calculation process of N_{pl} of BAT and CFAT columns is provided in the design recommendations section. N_{cr} is the critical elastic load, which is determined by Equation (4.3).

$$N_{cr} = \frac{\pi^2 EI}{L_{eff}^{\ 2}} \tag{4.3}$$

where $EI = \begin{cases} E_a I_a & \textit{for BAT columns} \\ E_a I_a + k_e E_c I_c & \textit{for CFAT columns} \end{cases}$

where E_a and E_c are the modulus of elasticity of aluminium tube and concrete infill respectively, I_a and I_c are the moment of inertia of the aluminium tube and concrete infill, respectively and k_e is the correction factor for concrete.

The specimens were labelled according to the shape of the cross-section and the nominal dimensions. For example, the label 101.6×25.4×3.25-C defines a test specimen with nominal outer depth (D), outer width (B) and thickness (t) of 101.6 mm, 25.4 mm and 3.25 mm, respectively. The symbol '-C' indicates that the specimen is filled with concrete. Table 4.1 summarises the measured geometric dimensions of specimens. The initial local (ω_l) and global (ω_g) imperfections of all specimens were measured by following the procedure mentioned in subsection 3.2.3 in Chapter 3 and the values are also listed in Table 4.1.

Table 4.1: Measured geometric dimensions of specimens.

Specimen	D (mm)	B (mm)	t (mm)	β/ε	$\bar{\lambda}$	L (mm)	ω_l (mm)	ω_g (mm)	e_o (mm)
50.8×50.8×1.6	50.7	51.0	1.61	34.06	1.11	1000.0	0.11	0.03	0.45
50.8×50.8×1.6-C					0.98	1001.0	0.28	0.09	0.23
50.8×50.8×3.3	50.6	50.6	3.13	17.77	1.13	999.0	0.17	0.04	1.25
50.8×50.8×3.3-C					1.09	1000.6	0.96	0.11	0.96
50.8×50.8×4.8	50.6	50.6	4.67	11.99	1.21	1000.0	0.19	0.01	1.83
50.8×50.8×4.8-C					1.18	999.9	0.14	0.08	1.4
76.2×76.2×3.3	76.4	76.4	3.23	25.87	0.76	1000.0	0.31	0.19	1.03
76.2×76.2×3.3-C					0.70	1000.9	0.80	0.06	0.11
76.2×76.2×4.8	76.2	76.1	4.76	17.69	0.80	1000.0	0.08	0.05	0.7
76.2×76.2×4.8-C					0.76	1001.0	0.72	0.13	0.55
76.2×76.2×6.4	76.3	76.3	6.28	13.20	0.77	1000.0	0.18	0.04	0.62
76.2×76.2×6.4-C					0.75	1000.8	0.19	0.07	0.11
76.2×38.1×3.3	76.2	38.2	3.27	12.29	1.39	1000.0	0.06	0.02	1.12
76.2×38.1×3.3-C					1.38	1001.0	0.49	0.18	0.01
76.2×50.8×3.3	76.1	50.7	3.18	17.16	1.09	1000.0	0.68	0.42	2.55
76.2×50.8×3.3-C					1.05	1000.5	0.38	0.11	0.02
101.6×50.8×3.3	101.8	51.4	3.42	12.89	0.88	1000.0	0.17	0.05	0.75
101.6×50.8×3.3-C					0.91	1000.6	0.19	0.04	0.29

The material properties of aluminium alloy hollow tubes and concrete were obtained

from tensile coupon tests and compressive tests of concrete cubes, respectively. Tables 4.2 and 4.3 present the material properties of aluminium alloy and concrete, respectively. Figure 4.1 shows typical failure patterns and the measured stress-strain curves of some tensile coupon specimens along with the corresponding Ramberg-Osgood curve.

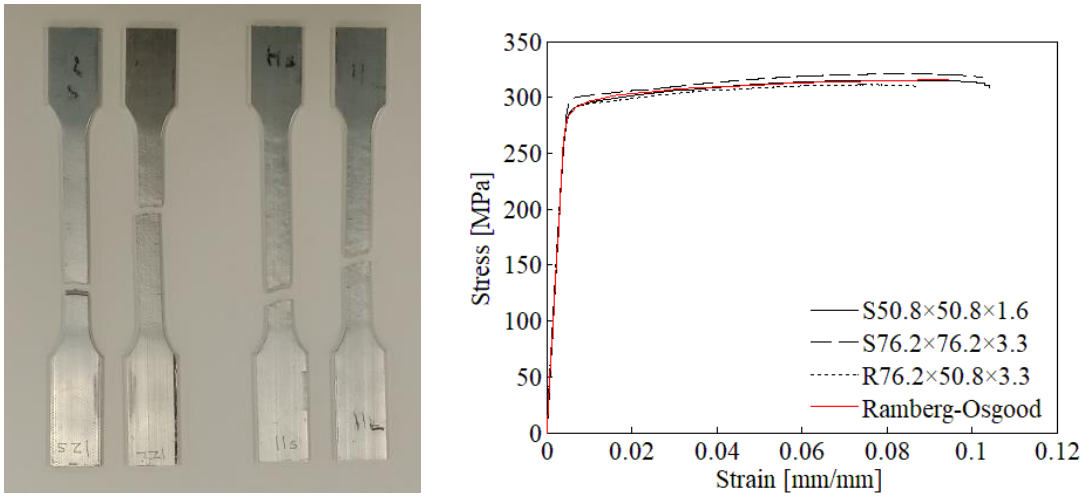

(a) (b)

Figure 4.1: (a) Failure modes of typical coupons, (b) Comparison of measured and Ramberg-Osgood curves.

Table 4.2: Measured material properties of aluminium alloy determined from tensile coupon tests.

Specimen	E_a (GPa)	$f_{0.1}$ (MPa)	$f_{0.2}$ (MPa)	f_u (MPa)	n	ε_f (mm/mm)
50.8×50.8×1.6(-C)	65	284.4	289.1	315	42.3	10.5
50.8×50.8×3.3(-C)	71.7	297.5	302.2	330	44.2	8.97
50.8×50.8×4.8(-C)	67.5	302.8	305.9	325	68.1	15.5
76.2×76.2×3.3(-C)	66.2	295.2	299.1	321	52.8	10.5
76.2×76.2×4.8(-C)	64.7	303.7	306.1	316	88.1	9.65
76.2×76.2×6.4(-C)	69.3	290.4	295.3	326	41.4	15.3
76.2×38.1×3.3(-C)	68.5	270.4	276.8	315	29.6	9.29
76.2×50.8×3.3(-C)	67.5	285.9	289.5	312	55.4	9.12
101.6×50.8×3.3(-C)	60	176.9	183.8	225	18.1	14.9

Table 4.3: Compressive strength of concrete cubes.

Compressive strength of cylinder (MPa)	Mean (MPa)
32.81 32.36 31.22 29.87	31.57

4.2.2 Flexural buckling tests

The flexural buckling tests were performed using a servo-controlled hydraulic testing machine. Specimens were placed accurately into the testing machine to avoid the possibility of eccentric loading. The pin-ended support condition which is discussed in subsection 3.2.4 in Chapter 3 was applied for allowing the rotation of a specimen about the weak axis. A displacement control loading was applied at a constant speed of 0.2 mm/min excluding the presence of dynamic effects and allowing to capture the post-peak behaviour of the specimens (Chen *et al.*, 2018). During the tests, LVDTs were installed; two were positioned at the mid-height of the specimen to record the lateral deflection about the minor axis and two were located at the bottom channel section to monitor the rotation. A total of four strain gauges were attached symmetrically to the four outer surfaces at the mid-height of each specimen to investigate strain distribution under in-plane and out-of-plane bending. The experimental setup and arrangement of LVDTs and strain gauges are shown in Figure 4.2.

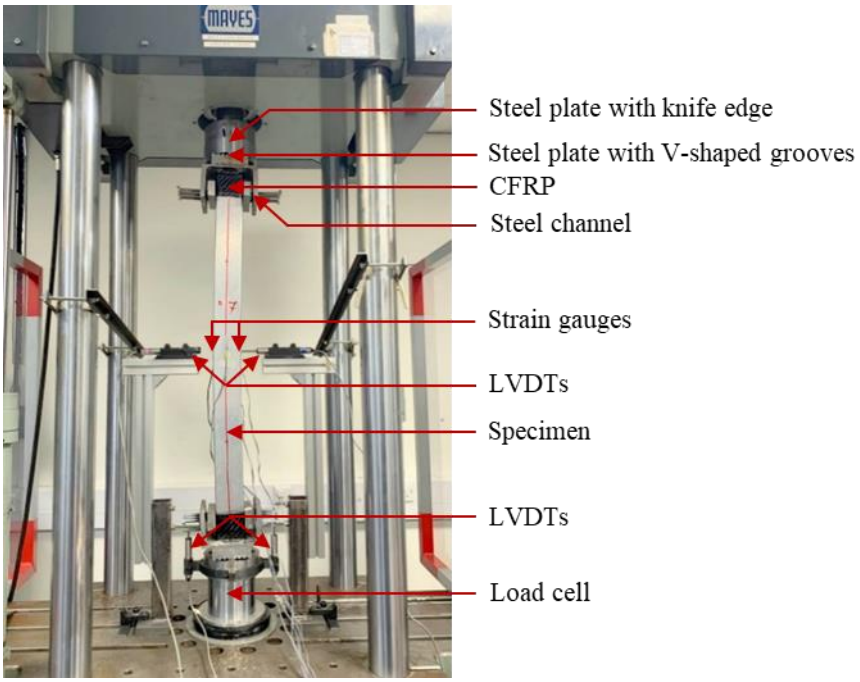

Figure 4.2: Experimental setup and instrumentation.

4.3 Experimental observations

4.3.1 Failure mode

Figure 4.3 shows typical failure modes of BAT and CFAT columns observed during the tests. As the knife-edge allowed rotation about the weak axis, all specimens failed due

to flexural buckling about that axis. No rupture or crack was identified in any specimen. In addition to flexural buckling, the specimens 50.8×50.8×1.6 and 76.2×76.2×3.3 (both for BAT and CFAT columns) which have slender cross-sections, i.e., higher β/ε ratios, also experienced local buckling near the mid-height. Both inward and outward local buckling appeared in the above-mentioned specimens, however, inward local buckling was absent in the CFAT counterparts due to the presence of concrete infill.

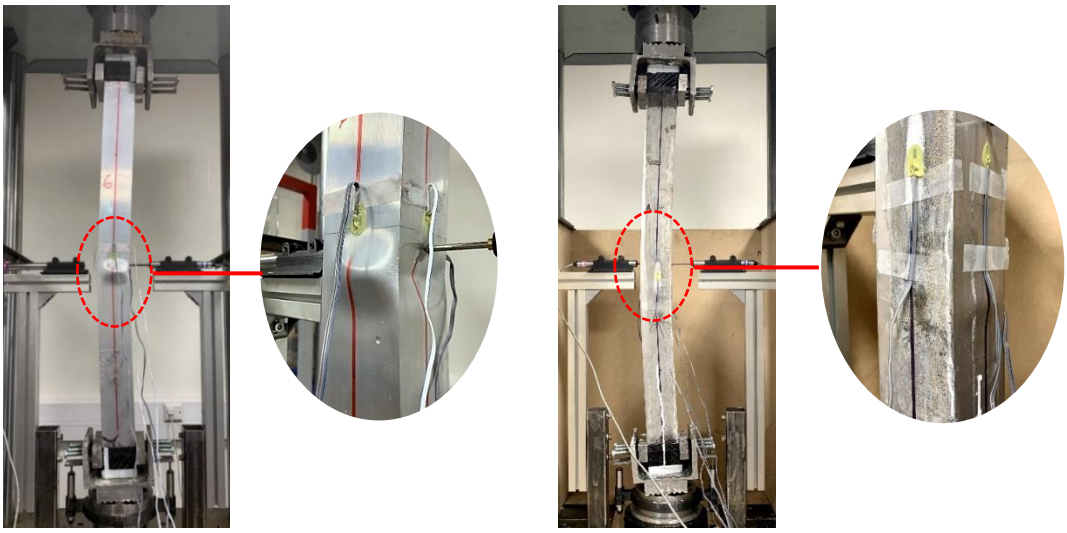

(a) 76.2×76.2×3.3 (b) 76.2×76.2×3.3-C

(c) 101.6×50.8×3.3 (d) 101.6×50.8×3.3-C

Figure 4.3: Typical failure modes of tested columns: (a) and (b) combination local and flexural buckling; (c) and (d) flexural buckling.

4.3.2 Axial load versus mid-height lateral displacement curves

During the tests, the axial load versus mid-height lateral displacement relationships

were recorded and studied to understand the overall structural behaviour of all tested columns. The axial compressive loads and the lateral displacements were obtained from the load cell and the LVDTs mounted at the mid-length of the specimens, respectively. Figure 4.4 presents the load versus mid-height lateral displacement curves of all BAT and CFAT columns. All the curves show an almost similar trend and can be divided into three different regions, i.e., the elastic region, the elastic-plastic region and the softening region. In the elastic region, the lateral displacement increases gradually and linearly with the increase of the axial load. In this stage, the maximum percentage increase of the ultimate load of the composite columns is 62% compared to the bare ones. At the elastic-plastic region, the increase of axial load slows down to reach the ultimate load ($N_{u,Test}$) while the development of lateral displacement accelerates. In this region, non-linear behaviour is evident. At the last region, the lateral displacement increases rapidly together with a gradual fall of the load. Table 4.4 reports the ultimate capacity, cross-sectional slenderness ratio (β/ε), column slenderness ratio ($\bar{\lambda}$), observed failure modes and ductility index (μ) of all tested columns. Here, μ is δ_u/δ_y, where δ_y represents the mid-span displacement at the yield bending moment and δ_u denotes the mid-span displacement at the ultimate bending moment. It can be observed from the table that the BAT columns reached failure at a lower load compared to the CFAT columns, as expected. Moreover, it can be also seen from the table that the ductility of BAT specimens increased noticeably due to the concrete infill. Figure 4.5 shows the percentage increase of the ultimate load of the tested columns due to concrete infill. It can be observed that the percentage increase appears more pronounced for the specimens with higher β/ε ratios, i.e., thinner plate elements. For example, the highest increase, which was equal to 72%, has been observed for specimen 50.8×50.8×1.6 and can be related to the delay in the local buckling offered by the concrete infill. The specimen 76.2×76.2×6.4 experienced the least benefit due to the concrete infill. This is related to the fact that this specimen comprises stocky aluminium plate elements providing significant resistance to buckling and thus the increased stiffness owing to the concrete led to a relatively small additional increase of the ultimate load.

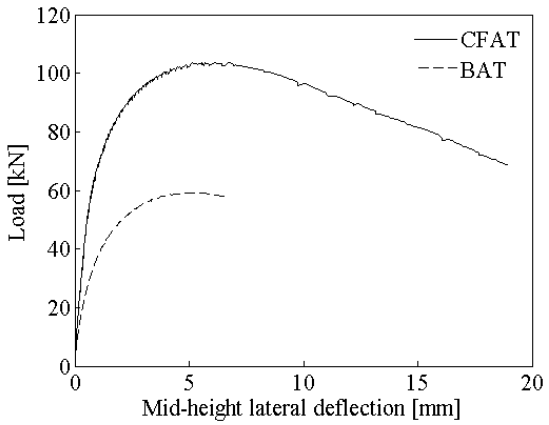

(a) 50.8×50.8×1.6(-C)

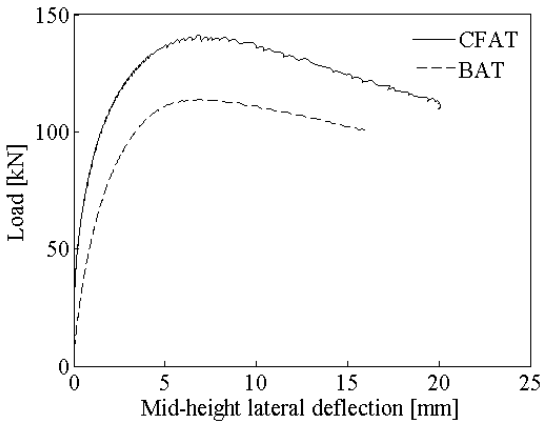

(b) 50.8×50.8×3.3(-C)

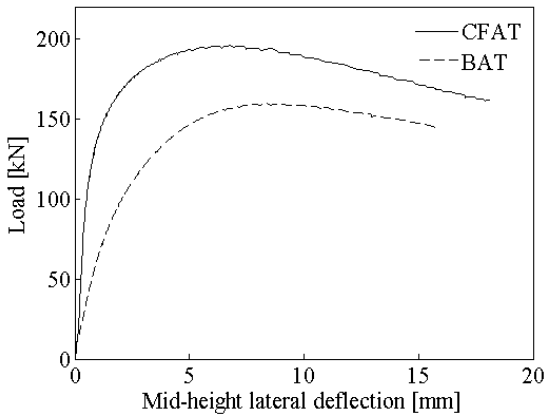

(c) 50.8×50.8×4.8(-C)

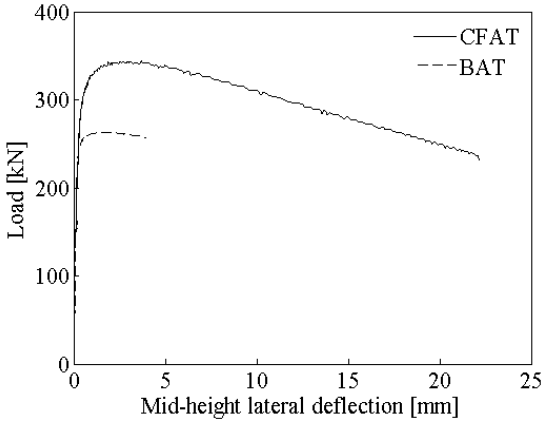

(d) 76.2×76.2×3.3(-C)

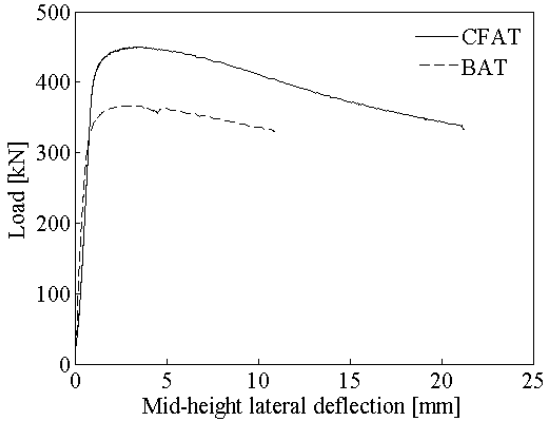

(e)

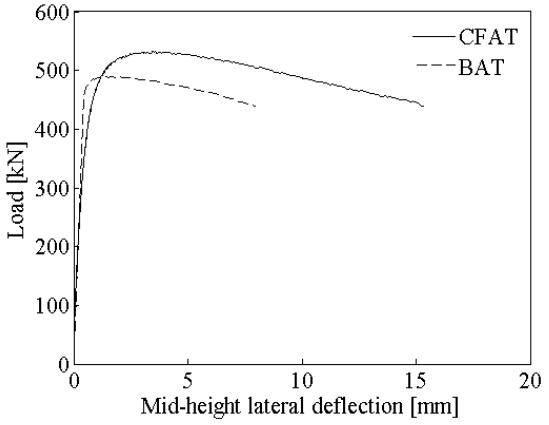

(f)

Figure 4.4: Load versus mid-height lateral displacement curves of tested columns.

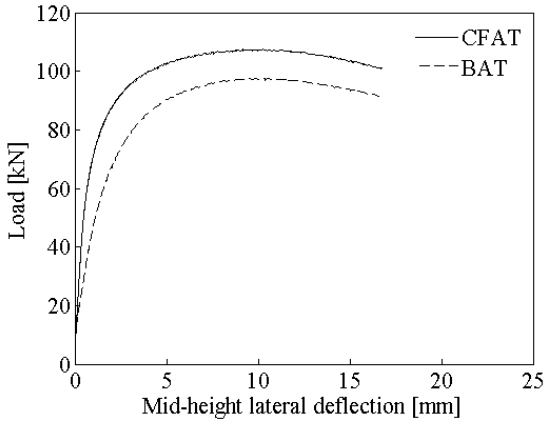

(g) 76.2×38.1×3.3(-C)

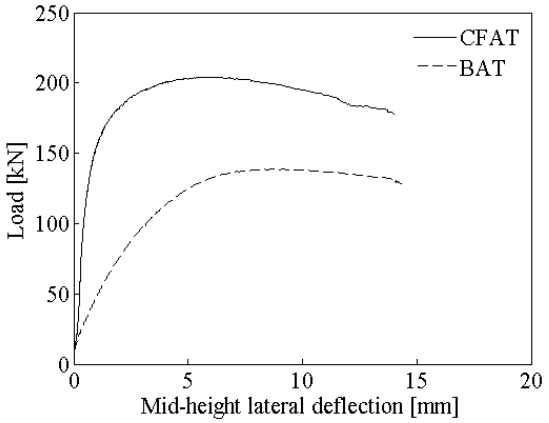

(h) 76.2×50.8×3.3(-C)

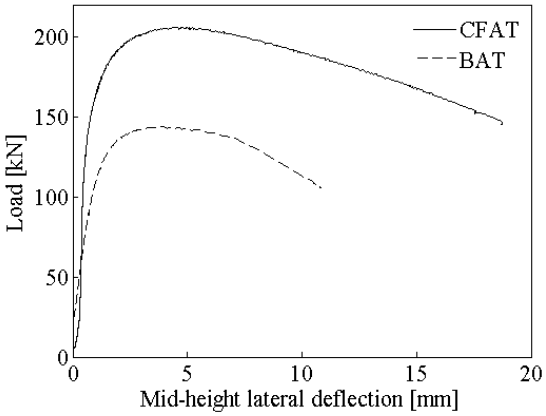

(i) 101.6×50.8×3.3(-C)

Figure 4.5 (continued): Load versus mid-height lateral displacement curves of tested columns.

Table 4.4: Ultimate capacity, cross-sectional slenderness ratio, column slenderness ratio and observed failure modes of tested columns.

Specimen	β/ε	$\bar{\lambda}$		$N_{u,Test}$ (kN)		μ		Failure mode
		BAT	CFAT	BAT	CFAT	BAT	CFAT	
50.8×50.8×1.6	34.06	1.11	0.98	60.22	103.71	5.70	16.15	FB+LB
50.8×50.8×3.3	17.77	1.13	1.09	113.83	141.18	5.94	9.31	FB
50.8×50.8×4.8	11.99	1.21	1.18	161.48	195.77	5.97	13.80	FB
76.2×76.2×3.3	25.87	0.76	0.70	263.28	344.07	12.31	42.85	FB+LB
76.2×76.2×4.8	17.69	0.80	0.76	367.36	449.68	12.79	19.34	FB
76.2×76.2×6.4	13.20	0.77	0.75	489.85	532.08	15.62	22.20	FB
76.2×38.1×3.3	12.29	1.39	1.38	97.62	107.47	8.41	15.79	FB
76.2×50.8×3.3	17.16	1.09	1.05	138.72	204.27	13.65	15.75	FB
101.6×50.8×3.3	12.89	0.88	0.91	143.72	206.15	9.07	24.34	FB

Note: FB = Flexural buckling, LB=Local buckling

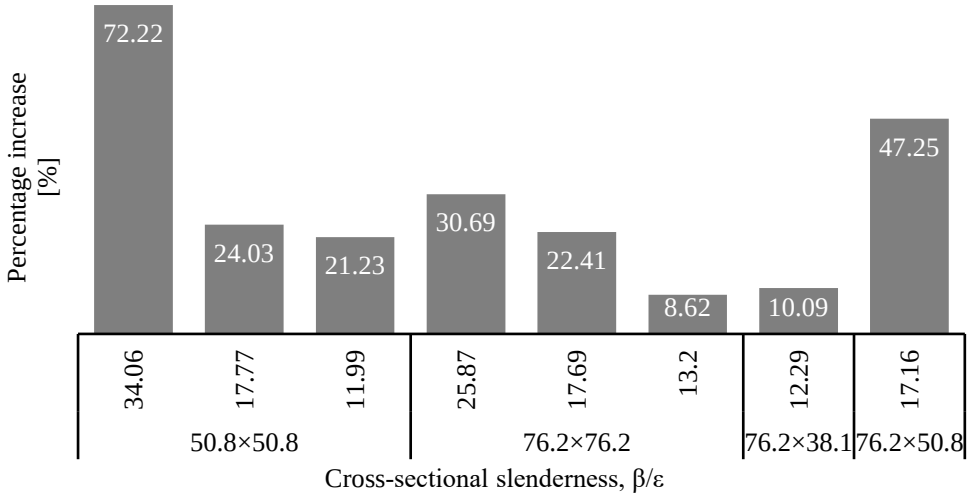

Figure 4.6: Percentage increase of ultimate capacity between BAT and CFAT columns.

4.4 Numerical investigation

4.4.1 FE modelling

In parallel with the experimental programme, a numerical investigation was conducted using FE software ABAQUS (2018). The FE models of the tested specimens were developed by following the modelling assumptions described in Chapter 3. The measured cross-section dimensions and material properties reported in Tables 4.1, 4.2 and 4.3 are used for the modelling. The BAT columns were modelled using 4-node quadrilateral shell elements with reduced integration (S4R) to capture the buckling behaviour of slender sections. For CFAT columns, 8-node hexahedral solid elements with reduced integration (C3D8R) were adopted for simulating both core concrete and aluminium tube. To choose the optimum mesh size that would provide accurate results in a reasonable time a mesh sensitivity analysis was conducted using coarser and finer mesh. Figure 4.6 shows the FE models with different mesh sizes, i.e., *L*/500, *L*/200, *L*/125, *L*/91 and *L*/72 that were considered for this analysis. Moreover, the load versus mid-height lateral displacement curves of 50.8×50.8×1.6-C column obtained from the test and the FE analysis are presented in this figure. It can be observed from Figure 4.6(b) that, the accuracy of the results decreased with the increase of mesh sizes. This is more prominent in the post-buckling region, while the ultimate capacity of the column is less sensitive to the mesh size. It was found that elements with an average mesh size equal to 5 mm (*L*/200) provided accurate results with optimal running time. Therefore, this mesh size was assigned using the structured meshing technique.

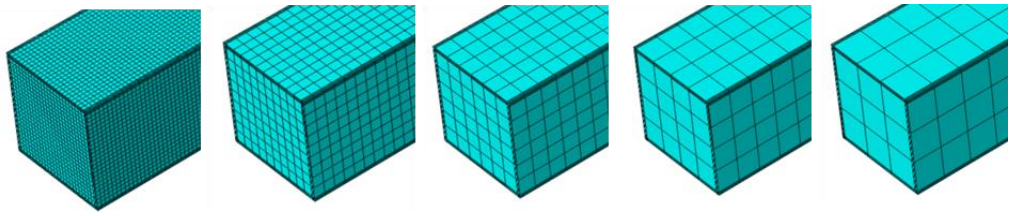

(a) Typical meshes from finer (left) to coarser (right)

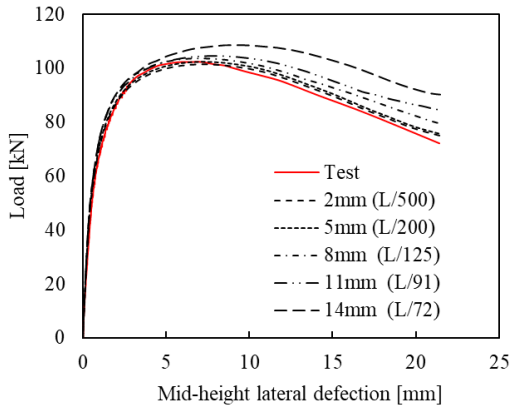

(b) Load versus mid-height lateral displacement curve

Figure 4.7: Mesh sensitivity study.

For CFAT columns a minimum of three elements were used to discretise the wall thickness in order to precisely capture the nonlinear behaviour of the aluminium tube (Milan *et al.*, 2019). Typical CFAT and BAT columns were discretised in around 40000 and 6000 elements respectively. Mechanical behaviours of aluminium alloy hollow tubes and concrete were simulated based on the procedure and assumptions stated in Chapter 3. The contact behaviour between hollow tube and concrete was modelled by applying surface-to-surface contact methodology. To determine suitable imperfection amplitudes for subsequent parametric study, an imperfection sensitivity study was conducted for BAT and CFAT columns shown in Table 4.5. Four global imperfection amplitudes including the measured values and three fractions of the specimen length, i.e., L_{eff}/1000, L_{eff}/1500 and L_{eff}/2000 were considered for CFAT columns. However, for BAT columns, besides the measured values, six additional imperfection combinations were adopted with two local values equal to 1/10 and 1/100 of the cross-section thickness and three global values equal to 1/1000, 1/1500 and 1/2000 of the specimen's length.

In order to simulate pin-ended boundary conditions, a reference point was created on the centroid of the cross-section for each column end by considering the effective height of

specimens measured in the tests. Coupling constraints were employed between the reference point and corresponding surfaces. Top and bottom reference points were fixed against all translational and rotational degrees of freedom except the longitudinal translation at the loaded end and the rotational about examined buckling axis. Due to simplicity, CFRP warps were not modelled in this study, however, potential local failures at the ends were prevented by applying the coupling constraints between each reference point and each end of the specimens (Zhou and Young, 2012). The axial compressive uniform load was applied at the top reference point by specifying a displacement to replicate the loading condition used in the tests. Figure 4.7 presents the FE model of a typical CFAT column.

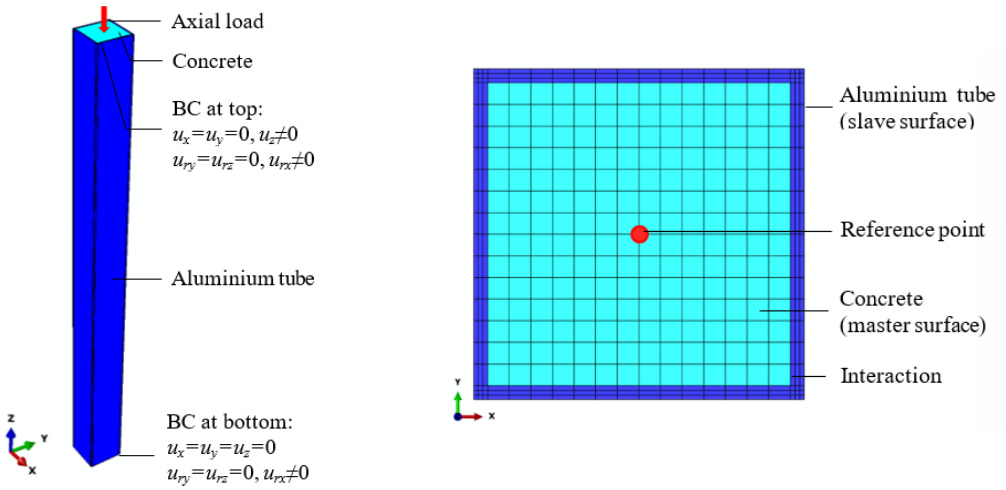

Figure 4.8: FE model of a typical CFAT column specimen.

4.4.2 FE model validation

The accuracy of the FE models was evaluated by comparing the experimental and numerical results in terms of the ultimate capacities, load versus mid-height lateral displacement curves and failure modes. Table 4.5 presents the ratios of numerical to experimental ultimate loads for varying imperfection levels. It is observed from the table that, mean values of $N_{u,FE}/N_{u,Test}$ for the L_{eff}/1500, L_{eff}/2000 and measured amplitude are 1.02, 1.08 and 1.02 which indicates that these global imperfection amplitudes slightly overestimated the strength of the columns. On the other hand, the global amplitude of L_{eff}/1000 provided the most accurate predictions of ultimate capacities with the mean value of $N_{u,FE}/N_{u,Test}$ equal to 0.99 and the corresponding coefficient of variation (COV) equal to 0.068. The comparison between test and FE load versus mid-height lateral displacement curves is depicted in Figure 4.8. It can be seen

that the elastic part FE curves of specimens 50.8×50.8×3.3 (Figure 4.8(a)) and 76.2×38.1×3.3 (Figure 4.8(b)) is slightly higher compared to the corresponding test curve. This may happen if the material properties obtained from the coupon tests are higher than the actual ones of the respective specimens. During measuring the geometry of the coupons, errors may be occurred when recording the values in decimal places. Hence, the estimated cross-section area of the gauge section may have been different than the actual area, resulting in different tensile stress values compared to the real values. Except this the developed FE models closely replicate the experimental load versus mid-height lateral displacement curves. Moreover, the failure modes resulting from both experimental and numerical studies, illustrated in Figure 4.9, also show excellent agreement as the simulated local (Figure 4.9(a)) and global buckling (Figure 4.9(b)) failures of specimens match with the corresponding test observations. The failure modes and test and FE load versus mid-height lateral displacement curves of all specimens are provided in Figures A.1, A.2 in Appendix A and Figures B.1, B.2 in Appendix B, respectively. Overall, it can be concluded that the developed FE models are capable of accurately predicting the structural response of CFAT and BAT columns.

Table 4.5: Comparison of test and FE results for varying imperfection amplitudes.

Specimen	$N_{u,FE}/N_{u,Test}$			
	Global imperfection amplitude			
	Measured	L_{eff} /1000	L_{eff} /1500	L_{eff} /2000
50.8×50.8×1.6	1.02	0.95	0.98	1.00
50.8×50.8×1.6-C	0.87	0.83	0.85	0.87
50.8×50.8×3.3	0.94	0.96	1.00	1.02
50.8×50.8×3.3-C	1.02	1.02	1.05	1.06
50.8×50.8×4.8	0.90	0.95	0.98	0.99
50.8×50.8×4.8-C	0.87	0.90	0.92	0.94
76.2×76.2×3.3	0.94	0.95	0.97	0.98
76.2×76.2×3.3-C	1.19	1.08	1.12	1.43
76.2×76.2×4.8	1.00	0.99	1.02	1.03
76.2×76.2×4.8-C	1.07	1.04	1.07	1.09
76.2×76.2×6.4	1.01	0.97	0.98	1.01
76.2×76.2×6.4-C	1.20	1.06	1.14	1.47
76.2×38.1×3.3	1.04	1.04	1.05	1.06
76.2×38.1×3.3-C	1.12	1.00	1.03	1.11
76.2×50.8×3.3	0.91	1.10	1.13	1.16
76.2×50.8×3.3-C	1.02	0.93	0.94	0.97
101.6×50.8×3.3	1.04	1.01	1.02	1.02
101.6×50.8×3.3-C	1.25	1.05	1.12	1.14
Mean	1.02	0.99	1.02	1.08
COV	0.109	0.068	0.077	0.143

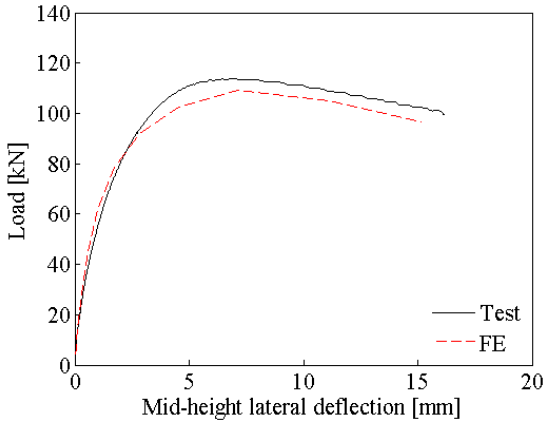

(a) 50.8×50.8×3.3

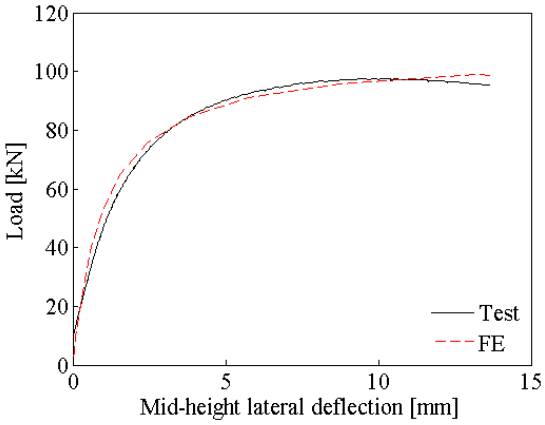

(b) 76.2×38.1×3.3

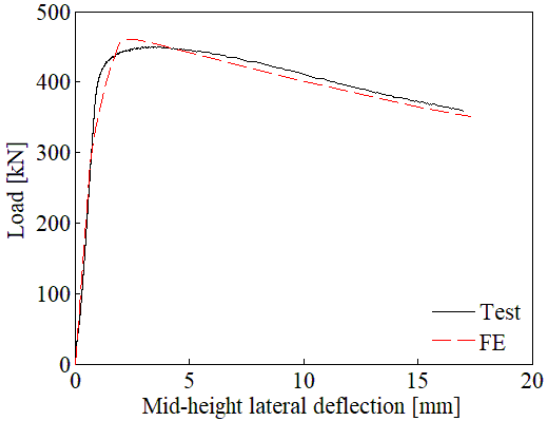

(c) 76.2×76.2×4.8-C

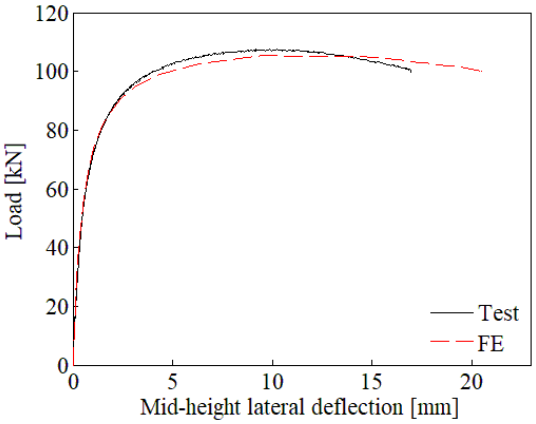

(d) 76.2×38.1×3.3-C

Figure 4.9: Test and FE load versus mid-height lateral deflection curves.

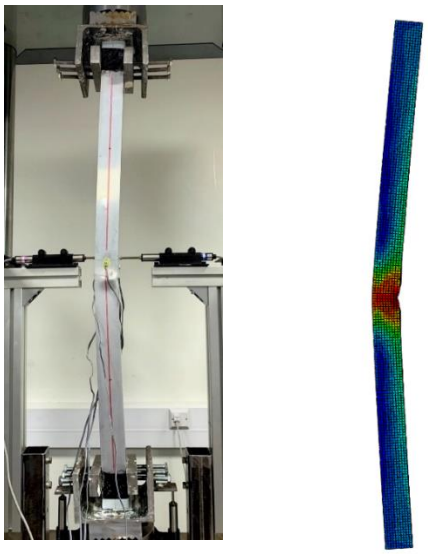

(a) 50.8×50.8×1.6

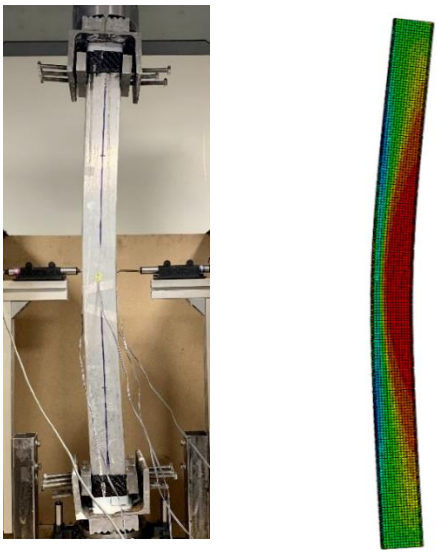

(b) 76.2×76.2×4.8-C

Figure 4.10: Test and FE failure modes.

4.4.3 Parametric study

Based on the validated FE models, a parametric study was undertaken to investigate the effect of different parameters, i.e., cross-sectional dimension, member relative slenderness and concrete strength on the capacities of the columns. In total, 108 CFAT and BAT columns were modelled in this study. Square hollow section (SHS) specimens with cross-section dimensions of 50×50 (D×B) and wall thicknesses 1, 3 and 5 mm and rectangular hollow section (RHS) specimens of 100×50 (D×B) section dimensions with 2, 6 and 10 mm plate thickness, allowing rotation about the weak axis (100×50W) and around the strong axis (100×50S) were studied. The letters 'W' and 'S' are used to indicate the rotation of specimens about the weak and strong axis, respectively. The specimen lengths were taken from 150 to 3000 mm and 500 to 2300 mm for BAT and CFAT columns, respectively, to cover a wide range of member relative slenderness. Three different concrete cube strengths of 30, 50 and 70 MPa were considered for CFAT columns. Average measured stress-strain curves were employed in the parametric study. The initial global imperfection amplitude of L_{eff} /1000 and the combination of initial local and global amplitudes of t/10 and L_{eff} /1000 were adopted for CFAT and BAT columns, respectively. The geometric dimensions and ultimate strength of all specimens considered in this parametric study are provided in Table C.1 in Appendix C.

4.5 Numerical observations

4.5.1 Effect of member slenderness ($\bar{\lambda}$)

The member slenderness ($\bar{\lambda}$) is one of the key factors that affect the flexural buckling behaviour of columns. In this numerical simulation, the influence of $\bar{\lambda}$ on the column performance was evaluated by changing the length of specimens from 150 to 300 mm for BAT and 500 to 2300 mm for CFAT columns. Figure 4.10 illustrates the axial compressive loads as a function of mid-height lateral displacements for constant cross-section (i.e., constant β/ε) and varying $\bar{\lambda}$ of BAT and CFAT (f_c = 30 MPa) columns. It can be seen that both initial stiffness and peak load are significantly reduced with the increase of $\bar{\lambda}$ (i.e., longer specimen), as the column becomes more prone to flexural buckling.

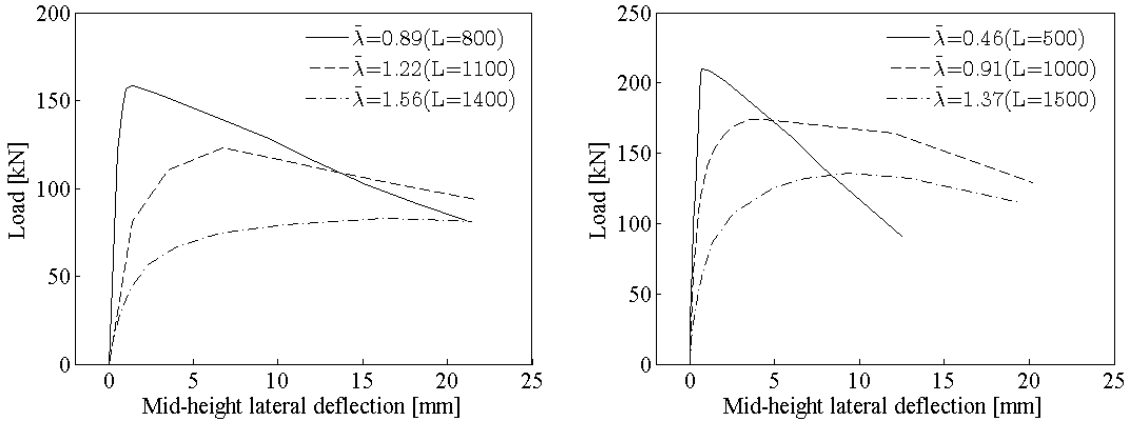

(a) 50×50×3 (b) 100×50×2W-C30

Figure 4.11: Load versus mid-height lateral displacement curves of columns with various member slenderness ratios.

4.5.2 Effect of cross-sectional slenderness (β/ε)

The effect of cross-sectional slenderness (β/ε) on the response of the columns was determined by changing the thickness of the aluminium tube. Figure 4.11 presents the relationship between ultimate capacity and β/ε of BAT and CFAT columns. It is found that the ultimate strength of the column is improved remarkably with the increase of thickness of the aluminium tube, i.e., the decrease of β/ε while keeping other dimensions unchanged. For example, the ultimate load of the specimen 100×50×10S, L=1300 is improved by 66.6% compared to the specimen 100×50×6S, L=1300 as the thickness of the hollow tube of the former specimen is increased from 6 mm to 10 mm. Similarly, when the thickness of hollow tube is increased from 2 mm to 10 mm, the ultimate capacity of the specimen 100×50×10S-C30, L=1000 is increased by 202.9% compared to the capacity of the specimen 100×50×2S-C30, L=1000. The main reason for this strength improvement is the larger thickness of the hollow tube which provides higher flexural rigidity. Moreover, the increased thickness slows down the formation of local buckling of hollow section and therefore hollow section offers more efficient confinement to the concrete core.

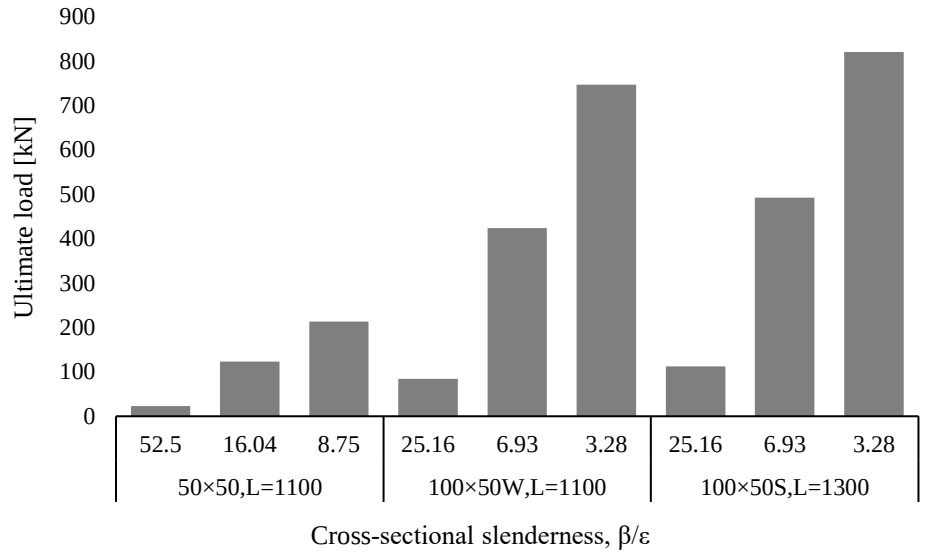

(a) BAT columns

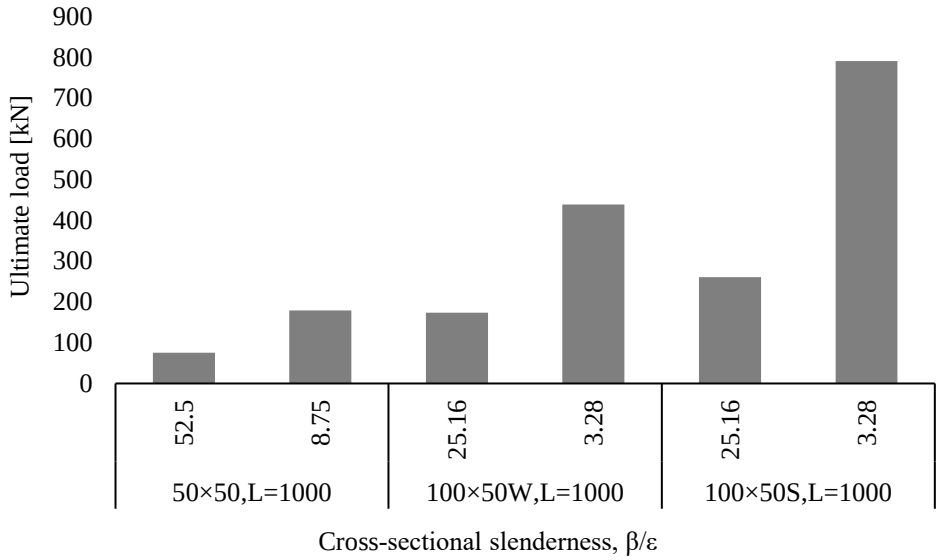

(b) CFAT columns (f_c = 30 MPa)

Figure 4.12: Ultimate loads of columns with various cross-sectional slenderness ratios.

4.5.3 Effects of concrete compressive strength (f_c)

In this parametric study, the effect of concrete compressive strength (f_c) on the ultimate load of CFAT columns was analysed by varying the strengths from 30 to 70 MPa with an increment of 20 MPa. Figure 4.12 presents the percentage increase of ultimate capacity when the concrete strengths increased from 30 to 50 and 70 MPa of CFAT columns with the same length and different cross-sectional dimensions. It is observed that the column buckling resistance increases with the increase of concrete strength as

expected. It can be also seen that the increase is more pronounced in columns with thinner tubular members, i.e., higher β/ε. Figure 4.13 depicts the percentage increase of peak loads of CFAT columns due to increase in length and concrete strengths from 30 to 50 and 70 MPa. It is demonstrated that the influence of concrete strengths decreases with the increase of column length, i.e., higher $\bar{\lambda}$.

It should be noted that in this study the tested CFAT columns were prepared by using concrete with normal compressive strength of 31.6 MPa. In sub-section 4.4.2 it is shown that the mean and COV values of $N_{u,FE}/N_{u,Test}$ for these columns are 0.99 and 0.08, respectively which indicates that the developed FE model can accurately predict the ultimate load of CFAT columns fabricated by normal strength concrete. Based on this validated FE model, this parametric study was conducted to investigate the effect of normal grade concrete on the column strength by selecting two normal concrete compressive strengths, i.e., 30 MPa and 50 MPa. To get a preliminary idea of the effect of high strength concrete on the column strength a higher grade concrete with compressive strength of 70 MPa was considered. However, the accuracy of this generated FE data was not able to be determined due to the absence of test data related to high strength concrete. Hence, future experimental studies in this direction are required to gain a better understanding of the performance of CFAT columns constructed with high strength concrete.

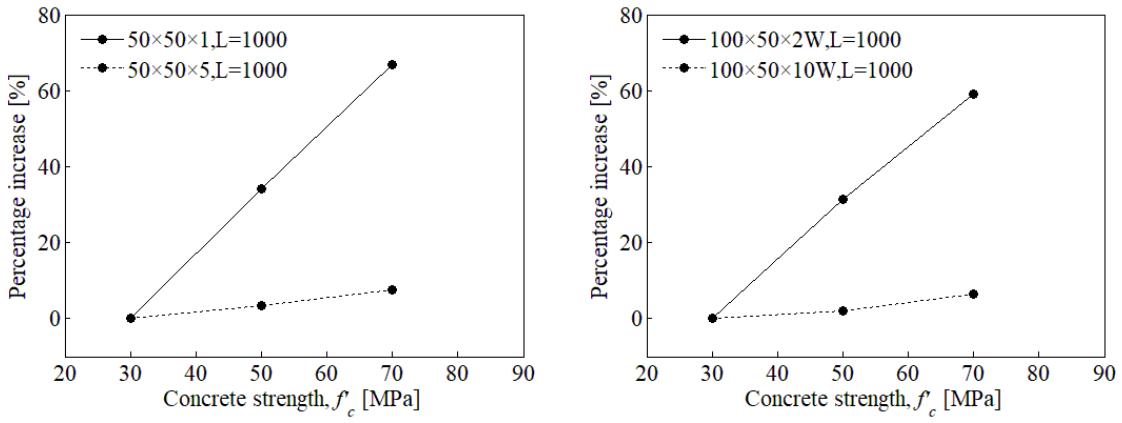

(a) SHS (b) RHS

Figure 4.13: Percentage increase of ultimate capacity due to increase of concrete strengths from 30 to 50 and 70 MPa of CFAT columns with the same length and different cross-sections.

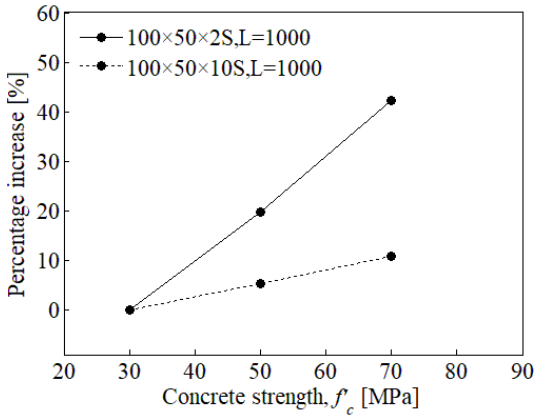

(c) RHS

Figure 4.12 (continued): Percentage increase of ultimate capacity due to increase of concrete strengths from 30 to 50 and 70 MPa of CFAT columns with the same length and different cross-sections.

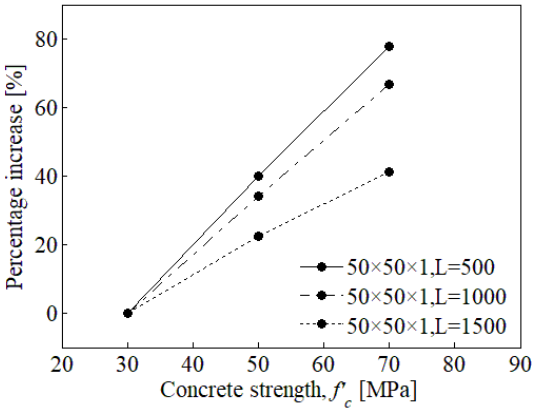

(a) SHS

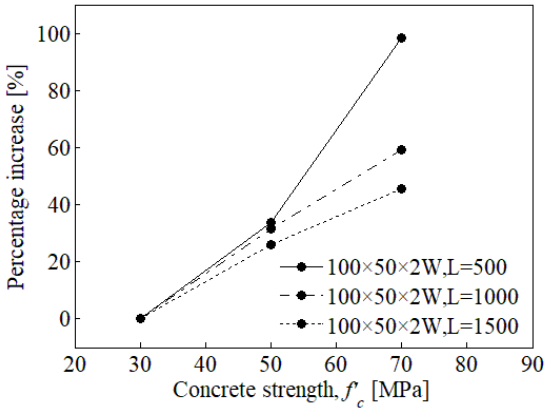

(b) RHS

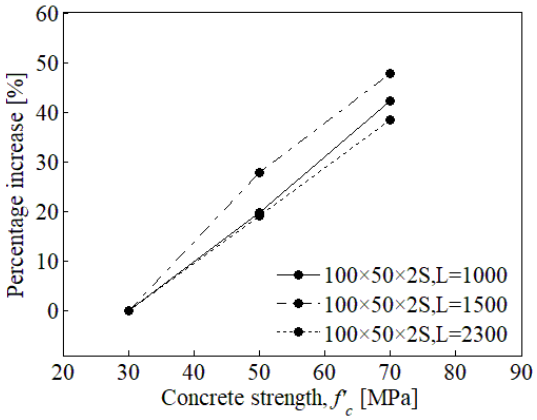

(c) RHS

Figure 4.14: Percentage increase of ultimate capacity due to increase of concrete strengths from 30 to 50 and 70 MPa of CFAT columns with the same cross-section and different lengths.

4.6 Design recommendations

In this section, the experimental and FE results are used to assess the ultimate load predictions of Eurocode 9 (2007) for BAT columns. Moreover, based on design provisions for steel-concrete composite columns provided by Eurocode 4 (2004), design recommendations are provided for predicting the ultimate load of CFAT columns. It should be noted that in the design equations the material partial safety factors were considered equal to unity.

4.6.1 BAT columns

The results obtained herein are used to assess the accuracy of Eurocode 9 (2007). According to Eurocode 9 (2007) aluminium structural members subjected to axial compression could fail by flexural buckling or local buckling. The effective thickness method (Eurocode 9, 2007) is adopted to consider the local buckling effect to the ultimate strength. The design strengths ($N_{u,EC9}$) of BAT square and rectangular columns are determined by the design equation given in Eurocode 9 (2007):

$$N_{u,EC9} = min\left(N_C, N_{pl}\right) \tag{4.4}$$

where N_c is the design resistance for uniform compression and N_{pl} is the design resistance for buckling. The design resistance for uniform compression is calculated by Equation (4.5):

$$N_c = Af_{0.2}/\gamma_{M1} \tag{4.5}$$

where A is the gross area for class 1, 2 and 3 cross-section sections or A_{eff} is the effective area for class 4 cross-sections (i.e., sections prone to local buckling), $f_{0.2}$ is the yield or proof stress and γ_{M1} is the safety factor for ultimate limit states which is considered equal to 1 herein. Note that the classification of cross-sections is linked to the values of the cross-sectional slenderness ratio (β/ε) as follows (Eurocode 9, 2007):

$$\beta/\varepsilon < 11\text{: Class 1}$$

$$\beta/\varepsilon < 16\text{: Class 2}$$

$$\beta/\varepsilon < 22\text{ : Class 3}$$

otherwise, the cross-section is considered Class 4.

The A_{eff} can be obtained by employing a coefficient ρ_c to factor down the component thickness, which is estimated by Equation (4.6):

$$\rho_c = \frac{32}{(\beta/\varepsilon)} - \frac{220}{(\beta/\varepsilon)^2} \tag{4.6}$$

The design buckling resistance of a compression member without welding can be obtained by the following equation:

$$N_{u,EC9} = N_{pl} = \chi A f_{0.2} / \gamma_{M1} \tag{4.7}$$

where χ is the reduction factor to allow the influence of the flexural buckling phenomenon on the capacity of the specimens. This factor is evaluated by Equation (4.8):

$$\chi = \frac{1}{\phi + \left[\phi^2 - \bar{\lambda}^2\right]^{0.5}} \leq 1.0 \tag{4.8}$$

where $\bar{\lambda}$ is the relative slenderness and ϕ is a parameter which is calculated by Equation (4.9):

$$\phi = 0.5\left[1 + \alpha_1\left(\bar{\lambda} - \bar{\lambda}_0\right) + \bar{\lambda}^2\right] \tag{4.9}$$

where α_1 is the imperfection factor that corresponds to the relevant buckling curve which is recommended as 0.2 for Class A aluminium alloy and $\bar{\lambda}_0$ is the limit of the horizontal plateau which is suggested as 0.1 by Eurocode 9 (2007).

In order to assess the accuracy of Eurocode 9 (2007) to predict the ultimate load of aluminium alloy columns, Figure 4.14 depicts the ultimate loads (N_u) obtained from the experiments and the FE study normalised by the plastic resistance (N_{pl}) and plotted against the member slenderness $\bar{\lambda}$. The Eurocode buckling design curve (EC9) is also included in this figure. It can be seen that both the experimental and FE data are above the design curve, which signifies that the design predictions by the Eurocode 9 (2007) are conservative.

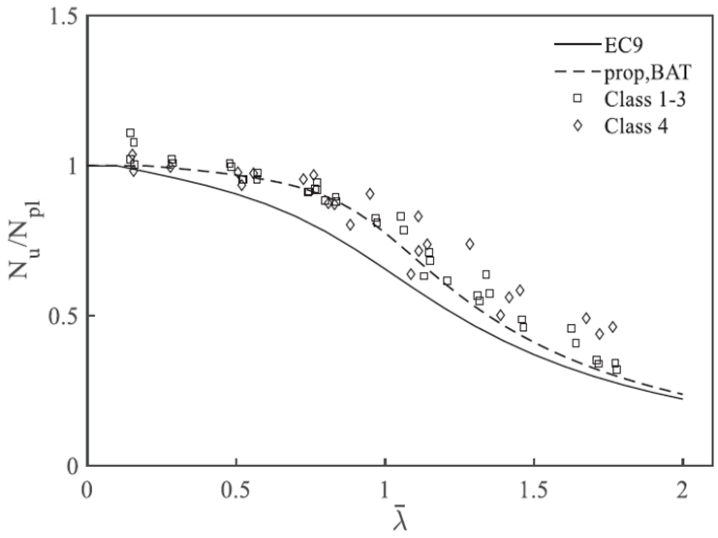

Figure 4.15: Comparison of normalised test and FE ultimate capacities of BAT columns study with the Eurocode 9 (2007) buckling curve.

Table 4.6 lists the $N_u/N_{u,EC9}$ ratios together with the corresponding member slenderness, $\bar{\lambda}$, and the cross-sectional Class of the examined columns. Based on both the FE and test data, the mean value of $N_u/N_{u,EC9}$ ratio is 1.20 indicating that Eurocode 9 (2007) underestimates the actual buckling strength of bare columns. In Figure 4.15 the test and FE results are plotted against the ultimate loads predicted by Eurocode 9 (2007). It can be observed from the figure that most of the predicted data deviate from the diagonal line (i.e., $N_u/N_{u,EC9} = 1$).

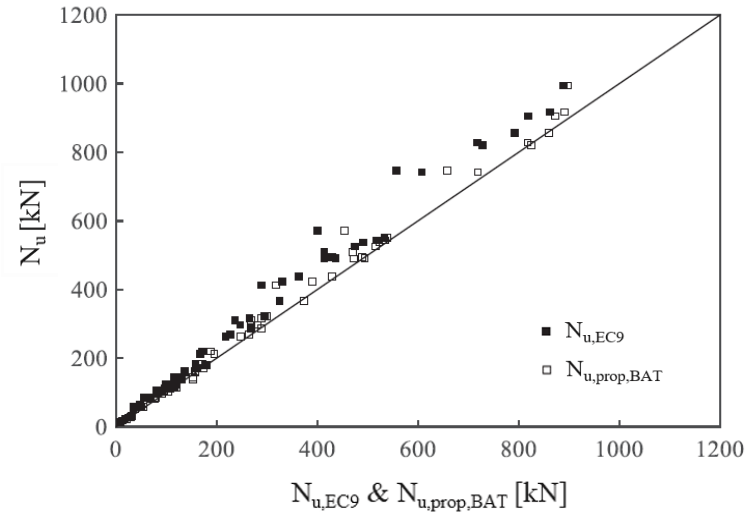

Figure 4.16: Comparison of test and FE ultimate capacities with design strengths based on Eurocode 9 (2007) and proposed equations for BAT columns.

Aiming to improve the accuracy of the current design rules for BAT slender columns, a revised buckling curve is suggested. Based on the obtained test and FE results, Equation (4.10) is proposed for the calculation of parameter ϕ for Class A aluminium alloys. This equation uses a revised imperfection factor (α_1), which is equal to 0.08 and a revised limit of the horizontal plateau ($\bar{\lambda}_0$), which is equal to 0.2. The revised values of α_1 and $\bar{\lambda}_0$ were determined by a iteration process which was conducted until the revised buckling curve shown in Figure 4.13 fit to the test and FE data.

$$\phi = 0.5\left[1 + 0.08\left(\bar{\lambda} - 0.2\right) + \bar{\lambda}^2\right] \tag{4.10}$$

The proposed buckling curve is shown in Figure 4.13, whilst the corresponding $N_u/N_{u,prop,BAT}$ ratios are included in Table 4.6. $N_{u,prop,BAT}$ is considered the predicted ultimate capacity found from Equation (4.7), using a value of ϕ that is calculated by the proposed Equation (4.10). It can be seen that the proposed curve improves the accuracy of the predicted strength as the mean value of $N_u/N_{u,prop,BAT}$ is reduced to 1.08 than the mean value of $N_u/N_{u,EC9}$ which is 1.20. The same observations can be drawn from Figure 4.14, where the ultimate loads (N_u) are plotted versus the predicted ultimate capacity ($N_{u,prop,BAT}$), showing that the proposed curve provides better strength predictions (i.e., closer to the diagonal line, $N_u/N_{u,prop,BAT}$ = 1) compared to those of Eurocode 9 (2007).

Table 4.6: Comparison of test and FE results with design strengths for BAT columns.

Specimen	No	Class	$\bar{\lambda}$	$N_u/N_{u,EC9}$	$N_u/N_{u,prop,BAT}$
50.8×50.8×1.6	1	4	1.11	1.43	1.22
50.8×50.8×3.3	1	2	1.13	1.11	0.95
50.8×50.8×4.8	1	1	1.21	1.18	1.03
76.2×76.2×3.3	1	4	0.76	1.21	1.06
76.2×76.2×4.8	1	2	0.80	1.13	0.98
76.2×76.2×6.4	1	2	0.77	1.18	1.04
76.2×38.1×3.3	1	4	1.39	1.19	1.06
76.2×50.8×3.3	1	4	1.09	1.07	0.91
101.6×50.8×3.3	1	4	0.88	1.10	0.94
Test			Mean	1.18	1.02
			COV	0.08	0.08
FE	36	1-3	0.14-1.78	1.13	1.06
	18	4	0.15-1.76	1.25	1.12
			Mean (all)	1.20	1.08
			COV (all)	0.12	0.11

4.6.2 CFAT columns

In absence of design provisions for the aluminium-concrete composite columns, the present study adopts the design formulae for steel-concrete composite members available in Eurocode 4 (2004) for the prediction of the ultimate capacities of CFAT columns, with the material properties of steel replaced by that for the aluminium alloy appropriately. Both the experimental and FE results are analysed to determine the applicability of this design code to design aluminium-concrete slender columns. According to Eurocode 4 (2004), the plastic resistance of CFAT square and rectangular columns subjected to compressive force is determined by Equation (4.11):

$$N_{pl} = Af_{0.2} + \alpha_c A_c f_c \tag{4.11}$$

where A_c and f_c are the cross-sectional area and the compressive cylinder strength of the concrete infill, respectively. It is noted that in the above equation the gross cross-sectional area of aluminium tube (A) should be replaced by the effective cross-sectional area (A_{eff}) for Class 4 sections. It is assumed that the concrete reaches its full f_c because of the confinement provided by the hollow tubes. Therefore, the concrete coefficient α_c is taken as 1 (Wang *et al.*, 2020a; 2020b).

In Figure 4.15 the ultimate loads (N_u) obtained from the experiments and the FE study normalised by the plastic resistance (N_{pl}) from Equation (4.11) are plotted against the member slenderness $\bar{\lambda}$. In addition, a buckling design curve is proposed following the Eurocode 9 (2007) methodology. However, the imperfection factor and limit of the horizontal plateau are calibrated on the basis of the obtained data according to Equation (4.12). The proposed buckling design curve is also shown in Figure 4.15.

$$\phi = 0.5\left[1 + 0.18\left(\bar{\lambda} - 0.2\right) + \bar{\lambda}^2\right] \tag{4.12}$$

Based on Figure 4.16, it can also be observed that the Class 4 (slender) and Class 1-3 aluminium cross-sections follow a different trend, particularly for increasing member slenderness. This is related to the fact that the strength increase is higher for most slender cross-sections as the concrete infill effectively prevents the occurrence of local buckling and delays the formation of global buckling of the hollow tube. This observation mirrors the conclusion derived from the test and parametric study results.

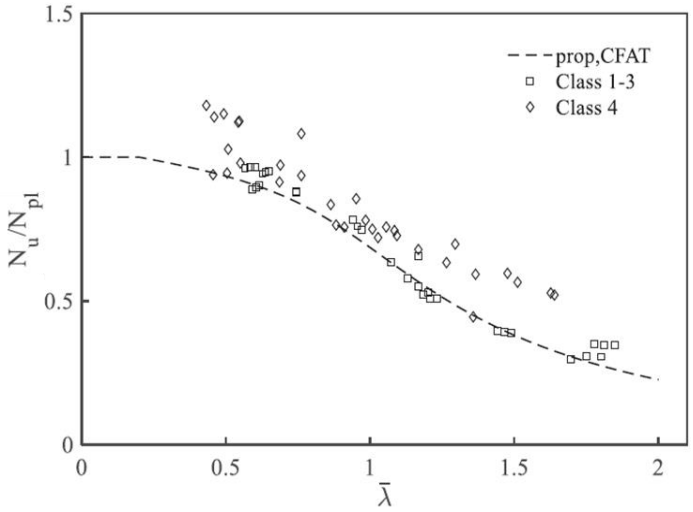

Figure 4.17: Proposed design buckling curve for CFAT columns.

Using the Equation (4.11) the ultimate capacity of CFAT columns ($N_{u,prop,CFAT}$) is calculated and the values of the ratios of $N_u/N_{u,prop,CFAT}$ are summarised in Table 4.7. The resulting overall mean value is 1.13, whilst the strength is more accurately predicted Class 1-3 cross-sections (mean value of $N_u/N_{u,prop,CFAT}$ equal to 1.05). These values indicate that the combined design formulae proposed herein provide good predictions with reasonable consistency. The same findings can be found in Figure 4.17 where the examined $N_{u,prop,CFAT}$ values deviate slightly from the diagonal line.

Table 4.7: Comparison of test and FE results with design strengths for CFAT columns.

Specimen	No	Class	$\bar{\lambda}$	$N_u/N_{u,prop,CFAT}$	
				Class 1-3	Class 4
50.8×50.8×1.6-C	1	4	0.98	-	1.19
50.8×50.8×3.3-C	1	2	1.09	1.00	-
50.8×50.8×4.8-C	1	1	1.18	1.16	-
76.2×76.2×3.3-C	1	4	0.70	-	1.05
76.2×76.2×4.8-C	1	2	0.76	1.04	-
76.2×76.2×6.4-C	1	2	0.75	1.04	-
76.2×38.1×3.3-C	1	4	1.38	-	0.99
76.2×50.8×3.3-C	1	4	1.05	-	1.08
101.6×50.8×3.3-C	1	4	0.91		1.00
Test			Mean	1.06	1.06
			COV	0.06	0.07
FE (mean)	31	1-3	0.57-1.85	1.08	-
	32	4	0.43-1.64	-	1.05
			Mean (all)	1.13	
			COV (all)	0.14	

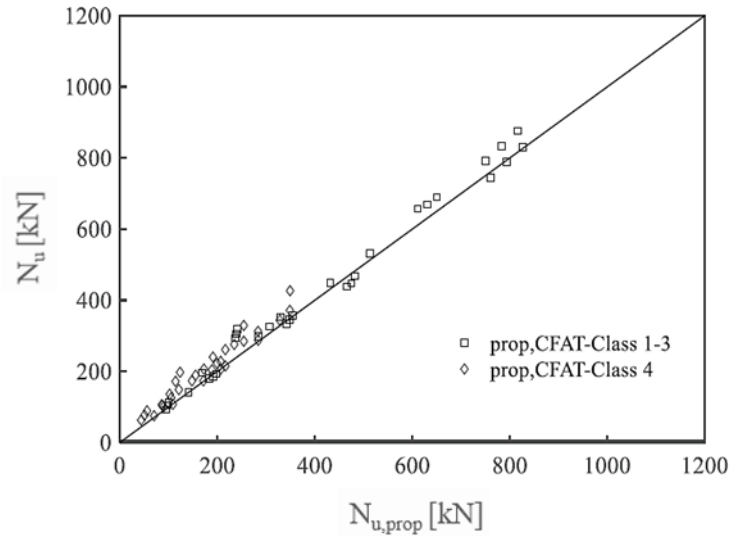

Figure 4.18: Comparison of test and FE ultimate capacities with proposed design strengths for CFAT columns.

4.7 Conclusions

A comprehensive experimental and numerical study was carried out to investigate the flexural buckling performance of BAT and CFAT columns, reaching the following conclusions:

- The ultimate capacity of CFAT columns improved remarkably compared to the BAT columns. This is attributed to the efficiency of concrete infill.

- The experimental results showed that the strength increase owing to the concrete infill for constant member length was more significant in the case of slender cross-sections. The highest increase, which was equal to 72%, has been observed for the slenderest cross-section and can be attributed to the delay in the local buckling offered by the concrete infill.

- It was demonstrated that the developed FE models with a global imperfection magnitude of L_{eff}/1000 could accurately capture the structural response of CFAT and BAT columns. Hence, a parametric study, including 108 columns was performed.

- The FE parametric study revealed that the buckling resistance of CFAT columns increases with the increase of thickness of aluminium tube (i.e., the decrease of cross-sectional slenderness) and the concrete strength. However, the ultimate

capacity decreased noticeably with the increase of member slenderness.

- The comparison between the Eurocode 9 and the experimental and FE results for BAT slender columns showed that the current codified equations underestimate the actual strength of BAT slender columns.

- A revised buckling curve was proposed for BAT columns which was able to improve the strength prediction of square and rectangular Class A aluminium tubes compared to that of Eurocode 9.

- In absence of design provisions for aluminium-concrete composite columns, the present study proposed adopting the Eurocode 4 design formulae for composite steel-concrete members with the material properties of steel replaced by those of aluminium alloy. A new buckling design curve was proposed on the basis of the experimental and numerical data and used in conjunction with European standards. The proposal was found to be suitable for the design of CFAT columns providing reasonably accurate and consistent strength predictions.

CHAPTER 5 : BAT AND CFAT MEMBERS IN BENDING

5.1 Introduction

This chapter presents experimental and numerical investigations on the behaviour of BAT and CFAT members under in-plane bending. The experimental observations are reported in terms of failure mode, flexural strength, flexural stiffness, ductility and bending moment versus mid-span deflection curve. FE models of BAT and CFAT beams are developed and validated against test results. The validated models are used in the subsequent parametric study. The results obtained from experiments and numerical analysis for BAT members are used to assess the flexural capacity predictions and the applicability of the slenderness limits provided in Eurocode 9. Moreover, design recommendations for CFAT flexural members are provided based on Eurocode 4.

5.2 Experimental programme

5.2.1 Test specimens and material properties

In total 20 beams, including 10 CFAT and 10 BAT specimens with square and rectangular sections, are tested under pure in-plane bending. The hollow tubes consisted of different cross-sections, with nominal outer width (B) varied from 25.4 to 76.2 mm, nominal outer depth (D) varied from 76.2 to 101.6 mm and nominal thickness (t) varied from 1.6 to 6.4 mm. All beams were 1000 mm long and the span (L_s) between the pinned supports was 900 mm. Table 5.1 provides the measured dimensions of all test specimens. The specimens are labelled based on the dimensions of their cross-section and the existence or absence of the concrete infill. For example, the designation '76.2×25.4×3.3' denotes a specimen with a nominal outer height, width and thickness of 76.2 mm, 25.4 mm and 3.3 mm, respectively. The symbol '-C' denotes that the specimen is CFAT, i.e., it has concrete infill, and the absence of '-C' indicates that it is a BAT specimen. The initial local geometric imperfections of all specimens were measured before the experiment and their magnitudes are also presented in Table 5.1.

Table 5.1: Geometric dimensions and initial local geometric imperfections of test specimens.

Specimen	D (mm)	B (mm)	t (mm)	D/B	B/t	L (mm)	ω_l (mm)
76.2×76.2×1.6	76.3	76.2	1.54	1.00	49.48	900	0.36
76.2×76.2×1.6-C	76.3	76.2	1.54		49.48	900	0.55
76.2×76.2×3.3	76.2	76.2	3.21	1.00	23.74	900	0.12
76.2×76.2×3.3-C	76.2	76.2	3.21		23.74	900	1.15
76.2×76.2×4.8	76.2	76.1	4.71	1.00	16.16	900	0.20
76.2×76.2×4.8-C	76.2	76.1	4.71		16.16	900	0.71
76.2×76.2×6.4	76.2	76.2	6.21	1.00	12.27	900	0.26
76.2×76.2×6.4-C	76.2	76.2	6.21		12.27	900	0.12
76.2×25.4×3.3	76.3	25.5	3.33	2.99	7.66	900	0.11
76.2×25.4×3.3-C	76.3	25.5	3.32		7.68	900	0.65
76.2×38.1×3.3	76.2	38.3	3.26	1.99	11.75	900	0.10
76.2×38.1×3.3-C	76.2	38.3	3.26		11.75	900	0.40
76.2×50.8×3.3	76.1	50.7	3.15	1.50	16.10	900	0.14
76.2×50.8×3.3-C	76.1	50.7	3.15		16.10	900	0.52
101.6×25.4×3.3	101.6	25.4	3.21	4.00	7.91	900	0.31
101.6×25.4×3.3-C	101.6	25.4	3.20		7.94	900	0.20
101.6×50.8×3.3	101.9	51.4	3.44	1.98	14.94	900	0.32
101.6×50.8×3.3-C	101.9	51.4	3.41		15.07	900	0.16
101.6×76.2×3.3	101.5	76.3	3.14	1.33	24.30	900	0.28
101.6×76.2×3.3-C	101.5	76.3	3.14		24.30	900	0.17

The mechanical properties of the aluminium alloy and concrete are reported in Tables 5.2 and 5.3, respectively. Figure 5.1 presents the typical failure modes of the tensile coupons and the experimental stress-strain curve of specimen 76.2×76.2×3 together with the curve reproduced using the Ramberg-Osgood expressions.

Table 5.2: Mechanical properties of aluminium alloy.

Specimen	E_a (GPa)	$f_{0.1}$ (MPa)	$f_{0.2}$ (MPa)	f_u (MPa)	ε_f (mm/mm)	ε_u (mm/mm)	n
76.2×76.2×1.6	67.9	288.4	292.9	316	6.9	8.4	44.8
76.2×76.2×3.3	66.2	295.2	299.1	321	7.5	10.5	52.8
76.2×76.2×4.8	64.7	303.7	306.1	316	6.3	9.7	88.1
76.2×76.2×6.4	69.3	290.4	295.3	326	8.8	15.3	41.4
76.2×25.4×3.3	68.9	271.8	277.9	316	8.8	14.3	31.2
76.2×38.1×3.3	68.5	270.4	276.8	315	7.8	9.3	29.6
76.2×50.8×3.3	67.5	285.9	289.5	312	7.1	9.1	55.4
101.6×25.4×3.3	63.9	234.7	242.5	290	7.6	13.2	21.2
101.6×50.8×3.3	71.6	166.9	175.1	204	7.4	12.1	14.4
101.6×76.2×3.3	72.8	303.5	306.7	320	5.6	6.9	66.1

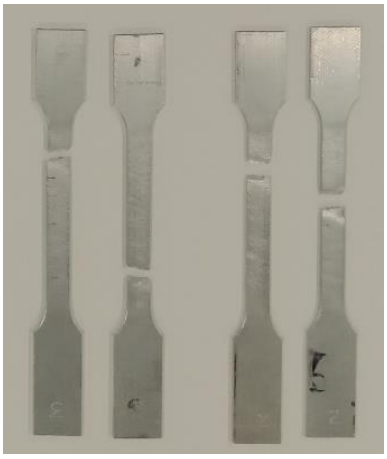

(a)

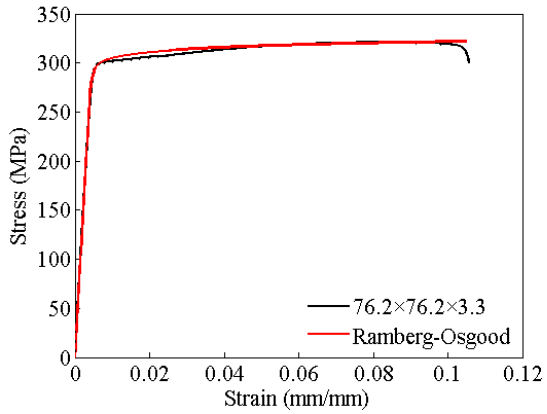

(b)

Figure 5.1: (a) Failure modes of typical coupons, (b) Comparison of measured and Ramberg-Osgood curves of specimen 76.2×76.2×3.3.

Table 5.3: Measured compressive strength of concrete cylinder.

Compressive strength of cylinder (MPa)	Mean (MPa)
24.2 25.6 28.6	26.1

5.2.2 Four-point bending tests

The CFAT and BAT beams were tested under a four-point bending configuration. Here, four-point bending configuration is used to spread out the maximum stress over the span between the two loading points for avoiding premature failure of the specimens. The ratio of shear span to depth was considerably higher than 0.5 for all the specimens to prevent shear failure of the specimens (Xu *et al.*, 2009). In line with previous studies (Wang *et al.*, 2016; Gkantou *et al.*, 2019), a 20 mm thick steel plate was used at each loading point to avoid stress concentration. Moreover, wooden blocks were placed at supports and loading points inside the BAT specimens to distribute the loads along the cross-sections. Three LVDTs were used to obtain the vertical deflection profile of the extreme tensile fibre of all specimens, in which one was installed at the mid-span and the other two were located at the two loading points. Two strain gauges were instrumented at the outer surface of the mid-span of the top and bottom flange to record the longitudinal strain of all specimens. The photograph of the test set-up is presented in Figure 5.2.

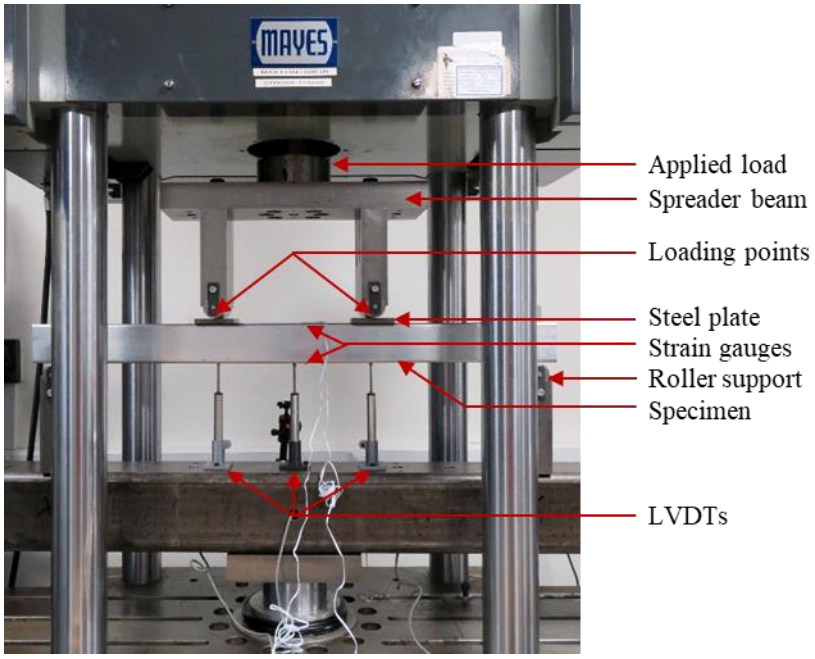

Figure 5.2: Test set-up and instrumentation for the four-point bending tests.

5.3 Experimental observations

5.3.1 Failure mode

The typical modes of failure of BAT and CFAT specimens obtained from four-point bending tests are illustrated in Figure 5.3 and summarised in Table 5.4. The specimens failed by yielding (Y), local buckling (LB) or a combination of these failure modes. Figure 5.3(a) shows the flexural deformation of a typical specimen that failed by yielding. Most of the BAT specimens failed by yielding, except specimens 76.2×76.2×1.6, 76.2×76.2×3.3 and 101.6×76.2×3.3 which have thinner cross-section (i.e., higher *B*/*t* ratio) failed by local buckling only. Besides yielding, almost all BAT specimens experienced inward and outward bulging near the loading points or the mid-span on the compression side of the specimens, including the flange and the part of the web in compression (Figure 5.3(b)). For all CFAT specimens, the main failure mode was yielding. In addition to yielding, local buckling was observed in the majority of the CFAT specimens whereas the inward bulging was absent and the outward bulging was smaller in comparison with the BAT specimens. It is believed that the concrete infill effectively restrained the development of inward buckling and delayed the formation of outward buckling. However, no local buckling was identified in BAT specimens 76.2×25.4×3.3 and 76.2×38.1×3.3 and CFAT specimens 76.2×76.2×6.4-C, 76.2×25.4×3.3-C and 76.2×38.1×3.3-C as they have thicker cross-section (i.e., lower *B*/*t*

ratio). Moreover, in specimens 101.6×50.8×3.3, 76.2×76.2×1.6-C, 76.2×76.2×3.3-C, 101.6×50.8×3.3-C and 101.6×76.2×3.3-C, a fracture was observed at the tensile zone of the aluminium tube after attainment of maximum load (Figure 5.4(a)).

To examine the failure of infilled concrete, the aluminium alloy tubes were partly removed after the tests. Figure 5.4(b) shows the typical failure modes of concrete. Several parallel flexural cracks were observed between two loading points within the tension zone of the concrete. These cracks were uniformly distributed and extended from tension to compression zone for the specimens failed by yielding. No diagonal cracks were observed in any specimen, indicating that shear force did not develop between the two loading points of CFAT specimens.

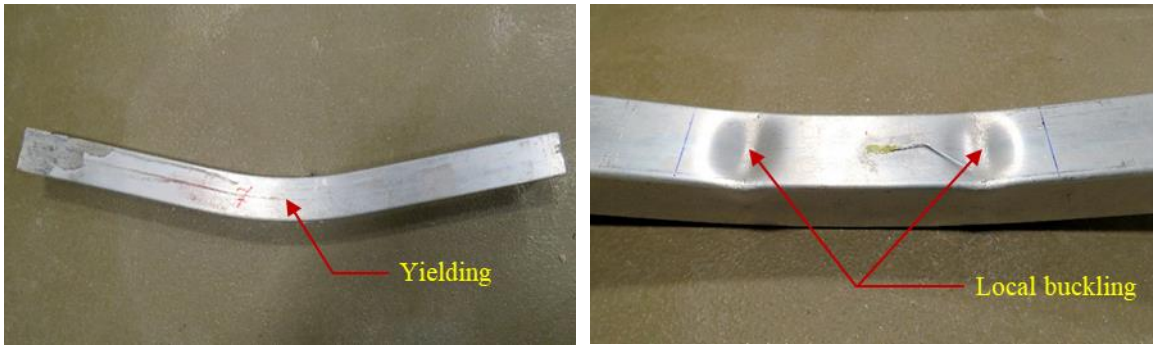

(a) 76.2×76.2×4.8-C (b) 76.2×76.2×4.8

Figure 5.3: Typical failure modes: (a) Yielding, (b) Local buckling.

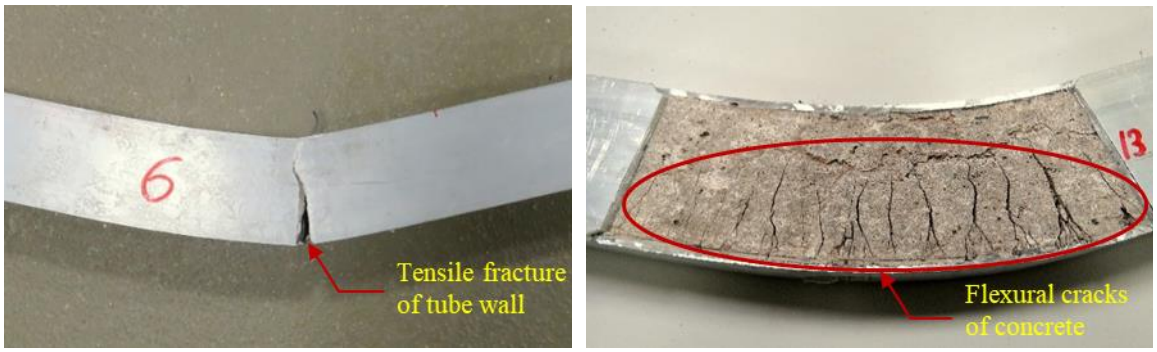

(a) 76.2×76.2×3.3-C (b) 101.6×50.8×3.3-C

Figure 5.4: (a) Tensile fracture of tube wall, (b) Typical failure modes of concrete.

Table 5.4: Observed failure modes of test specimens.

Specimen	Failure mode	Specimen	Failure mode
76.2×76.2×1.6	LB	76.2×76.2×1.6-C	Y+LB
76.2×76.2×3.3	LB	76.2×76.2×3.3-C	Y+LB
76.2×76.2×4.8	Y+LB	76.2×76.2×4.8-C	Y+LB
76.2×76.2×6.4	Y+LB	76.2×76.2×6.4-C	Y
76.2×25.4×3.3	Y	76.2×25.4×3.3-C	Y
76.2×38.1×3.3	Y	76.2×38.1×3.3-C	Y
76.2×50.8×3.3	Y+LB	76.2×50.8×3.3-C	Y+LB
101.6×25.4×3.3	Y+LB	101.6×25.4×3.3-C	Y+ LB
101.6×50.8×3.3	Y+LB	101.6×50.8×3.3-C	Y+LB
101.6×76.2×3.3	LB	101.6×76.2×3.3-C	Y+LB
Note: Y = Yielding, LB = Local buckling			

5.3.2 Bending moment versus mid-span deflection curve

Based on the load-deformation paths recorded during the tests, bending moment versus mid-span deflection curves of BAT and CFAT flexural members are obtained and shown in Figure 5.5. For these plots, bending moments for the specimens are calculated using Equation (5.1):

$$M = \frac{PL}{6} \tag{5.1}$$

where P is the applied load over the specimen and L is the span. A closer look at Figure 5.5 reveals that, at the initial stage of the curves, the mid-span deflection increased linearly and gradually with the increase in bending moment. This linearity implies that the material of specimens was in the elastic stage. It is found that in this region the slope of the curve for the CFAT specimens is higher than that of BAT specimens, indicating an improvement in flexural stiffness due to the concrete infill. The presence of elastic-plastic region is evidenced by deviation from the initial linearity within these curves. At post-yielding, all curves of CFAT specimens and most curves of BAT specimens exhibited a fairly flat plastic plateau with a steady bending moment for increasing deformation. The maximum recorded bending moment was considered as the flexural strength of the respective specimen. In most of the CFAT specimens and some BAT specimens, no softening part or failure was observed at the elastic-plastic region as the post-yield plateau extended with increasing deformation. Owing to the limited displacement capacity of the test rig, the tests of these specimens had to be discontinued

at mid-span vertical displacement of $L/15$. The bending moment recorded at this displacement was considered as the ultimate bending moment (M_u) of the respective specimen. It is noteworthy that a similar strategy was applied in many recent studies (Li *et al.*, 2017; Lu *et al.*, 2017; Al Zand *et al.*, 2020), where the researchers used different mid-span vertical displacement limits to define the flexural strength of CFST beams. As shown in Figure 5.5, some of the specimens (e.g., Figure 5.5(j)) denoted a clear maximum bending moment followed by a softening curve, whilst others (e.g., Figure 5.5(e)) exhibited a rather flat post-yield response for increasing deformation. Overall, in all cases, it can be seen that due to the presence of concrete infill the CFAT specimens achieved higher bending moment capacity compared to their BAT counterparts.

On the basis of experimental data, the flexural stiffness and ductility of BAT and CFAT specimens have also been determined and listed in Table 5.5. For these calculations, the initial and serviceability limit state flexural stiffness are calculated using Equations (5.2) and (5.3) (Chen *et al.*, 2017), respectively.

$$K_i = \frac{0.2M_u L^2}{\pi^2 \delta_i} \tag{5.2}$$

$$K_s = \frac{0.6M_u L^2}{\pi^2 \delta_s} \tag{5.3}$$

Here K_i and K_s represent the initial flexural stiffness and that at the serviceability limit state, respectively. Notations δ_i and δ_s denote the vertical displacement at the mid-span corresponding to $0.2M_u$ and $0.6M_u$, respectively.

As an indicator of the post-elastic ductility exhibited by the CFAT and BAT specimens, a ductility index μ is calculated using Equation (5.4) and reported in Table 5.6.

$$\mu = \frac{\delta_u}{\delta_y} \tag{5.4}$$

where δ_y represents the mid-span displacement at the yield bending moment and δ_u denotes the mid-span displacement at the ultimate bending moment. It can be seen from Table 5.5 that the initial and serviceability limit state flexural stiffness as well as the ductility of BAT specimens increased noticeably due to the concrete infill. The increase in the flexural stiffness is more pronounced for the specimens with thinner cross-

sections (i.e., higher B/t ratio). However, the increase of flexural stiffness at the serviceability limit state is relatively lower compared to that of initial flexural stiffness. This could be attributed to the development of cracks in concrete within the tension zone of the specimens. It is also noteworthy that the BAT specimens 76.2×76.2×1.6, 76.2×76.2×3.3 and 101.6×76.2×3.3 (Figures 5.5 (a), 5.5 (b) and 5.5 (j), respectively) failed by local buckling, whereas the CFAT specimens with identical cross-section behaved in a more ductile manner as the ductility index of the specimens increased by 168.20%, 203.48% and 47.22%, respectively than the BAT counterparts.

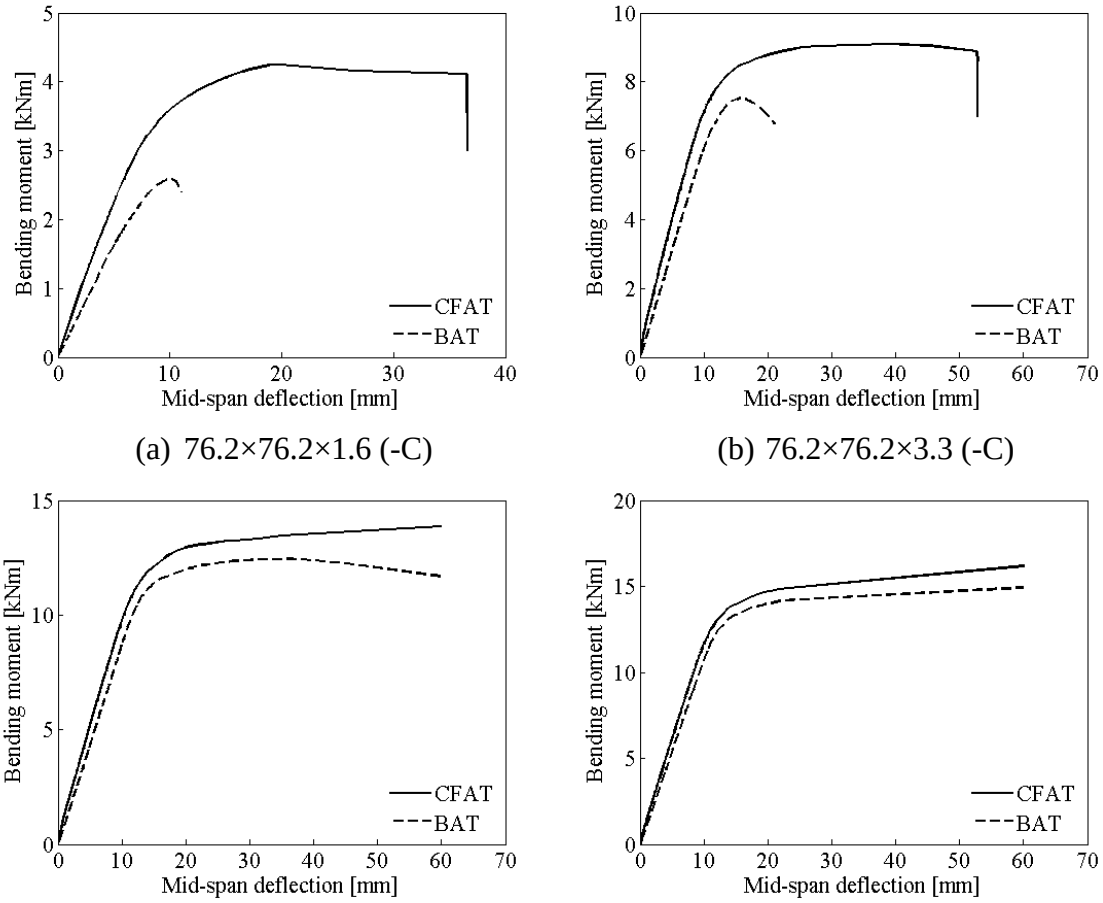

(a) 76.2×76.2×1.6 (-C) (b) 76.2×76.2×3.3 (-C)

(c) 76.2×76.2×4.8 (-C) (d) 76.2×76.2×6.4 (-C)

Figure 5.5: Bending moment versus mid-span deflection curves of test specimens.

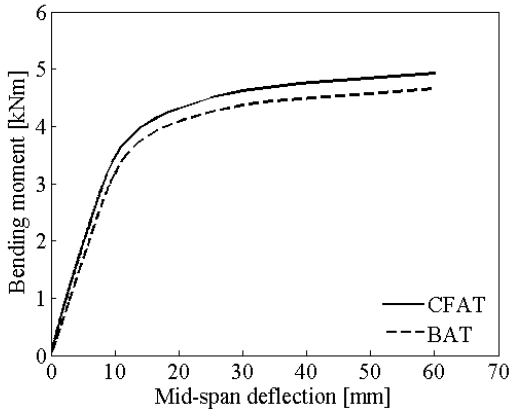

(e) 76.2×25.4×3.3 (-C)

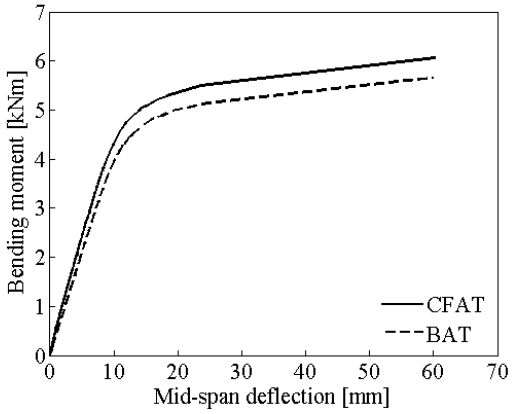

(f) 76.2×38.1×3.3 (-C)

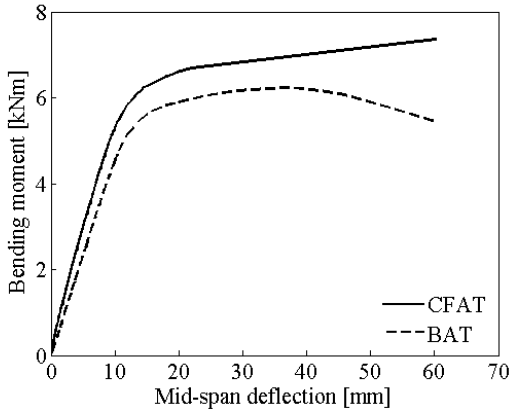

(g) 76.2×50.8×3.3 (-C)

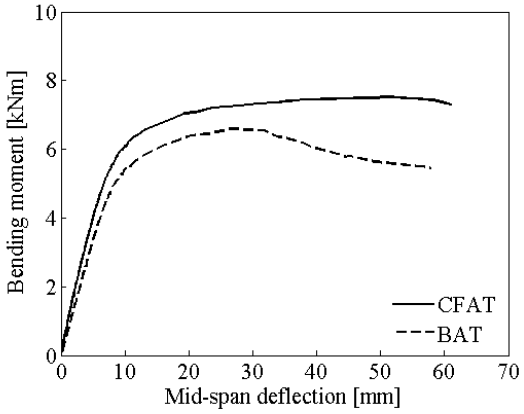

(h) 101.6×25.4×3.3 (-C)

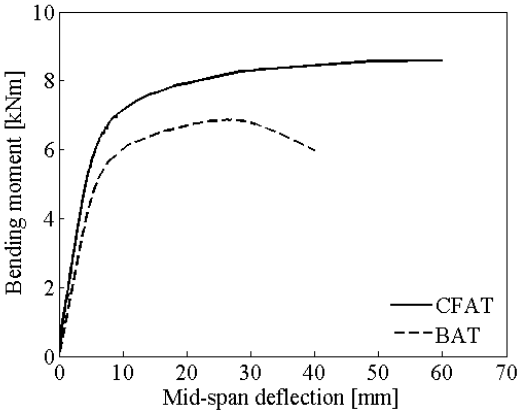

(i) 101.6×50.8×3.3 (-C)

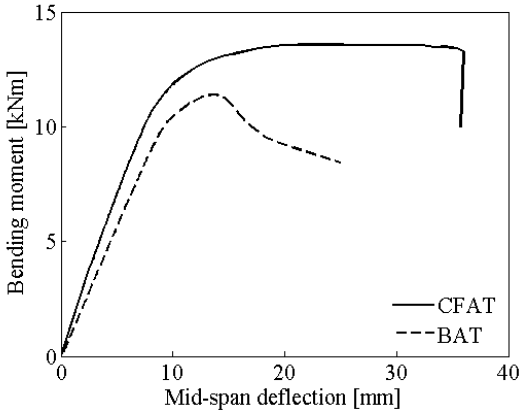

(j) 101.6×76.2×3.3 (-C)

Figure 5.6 (continued): Bending moment versus mid-span deflection curves of test specimens.

Table 5.5: Flexural stiffness and ductility of the test specimens.

Specimen	K_i (kN m^2)	$K_{i,CFAT}$ / $K_{i,BAT}$	K_s (kN m^2)	$K_{s,CFAT}$ / $K_{s,BAT}$	δ_y (mm)	δ_u (mm)	μ	μ_{CFAT} / μ_{BAT}
76.2×76.2×1.6	29.95	55.63	26.99	33.72	4.72	11.30	2.39	167.90
76.2×76.2×1.6-C	46.61		36.09		5.80	37.20	6.41	
76.2×76.2×3.3	51.85	40.60	50.57	30.26	7.32	21.01	2.87	203.45
76.2×76.2×3.3-C	72.90		65.87		6.89	60.01	8.71	
76.2×76.2×4.8	72.50	23.79	71.37	14.41	8.60	60.00	6.97	2.83
76.2×76.2×4.8-C	89.75		81.66		8.37	60.02	7.17	
76.2×76.2×6.4	90.02	16.25	88.60	10.72	8.36	59.98	7.17	3.04
76.2×76.2×6.4-C	104.65		98.10		8.12	60.03	7.39	
76.2×25.4×3.3	28.23	22.14	27.10	11.07	8.47	60.01	7.09	4.30
76.2×25.4×3.3-C	34.48		30.10		8.13	60.08	7.39	
76.2×38.1×3.3	34.21	23.71	33.70	12.23	8.29	60.01	7.24	4.95
76.2×38.1×3.3-C	42.32		37.82		7.90	60.02	7.60	
76.2×50.8×3.3	36.87	45.49	34.14	42.38	8.14	60.03	7.38	9.16
76.2×50.8×3.3-C	53.64		48.61		7.48	60.24	8.05	
101.6×25.4×3.3	55.17	35.94	53.90	17.70	6.07	57.77	9.52	6.87
101.6×25.4×3.3-C	75.00		63.44		5.90	60.01	10.17	
101.6×50.8×3.3	77.61	47.39	76.12	25.39	4.49	34.16	7.61	76.07
101.6×50.8×3.3-C	114.39		95.45		4.48	60.01	13.40	
101.6×76.2×3.3	91.21	44.56	90.20	26.82	6.05	24.98	4.13	47.37
101.6×76.2×3.3-C	131.80		114.39		5.91	35.96	6.08	

5.3.3 Flexural strength

The ultimate bending moment recorded during testing was considered as the flexural strength of BAT and CFAT members and the obtained values are reported in Table 5.5. It can be seen that the flexural strengths for the square and rectangular CFAT specimens were remarkably improved due to the presence of concrete infill compared to the corresponding BAT specimens. To examine the contribution of concrete infill, the percentage increase of ultimate strength due to the concrete infill is presented in Table 5.6. The highest increase is noticed for specimen 76.2×76.2×1.6-C, which is equal to 64.17%. The lowest enhancement is observed for specimen 76.2×76.2×6.4-C, which is equal to 6.61%. For the same thickness of the section, it is observed that the percentage improvement in flexural strength is higher for members with larger width and depth. This could be related to the fact that larger aluminium cross-sections offer more moment of inertia, which results in enhanced flexural strength.

Table 5.6: Flexural strength of test specimens.

Specimen	$M_{u,Test}$ (kNm)	$M_{u,Test}$ increase (%)
76.2×76.2×1.6	2.59	64.17%
76.2×76.2×1.6-C	4.25	
76.2×76.2×3.3	7.52	19.84%
76.2×76.2×3.3-C	9.01	
76.2×76.2×4.8	12.47	11.25%
76.2×76.2×4.8-C	13.87	
76.2×76.2×6.4	15.04	7.56%
76.2×76.2×6.4-C	16.18	
76.2×25.4×3.3	4.66	6.61%
76.2×25.4×3.3-C	4.97	
76.2×38.1×3.3	5.67	6.96%
76.2×38.1×3.3-C	6.07	
76.2×50.8×3.3	6.27	17.75%
76.2×50.8×3.3-C	7.38	
101.6×25.4×3.3	6.64	14.52%
101.6×25.4×3.3-C	7.60	
101.6×50.8×3.3	6.89	25.96%
101.6×50.8×3.3-C	8.68	
101.6×76.2×3.3	11.39	20.54%
101.6×76.2×3.3-C	13.73	

5.4 Numerical investigation

5.4.1 FE modelling

FE models of CFAT and BAT beams were developed based on the assumptions stated in Chapter 3. The measured geometry and material properties of aluminium alloy tubes and concrete reported in Tables 5.1, 5.2 and 5.3 were used to build the models. Four-node quadrilateral shell elements with reduced integration (S4R) were used to simulate the aluminium tubes, whereas eight-node hexahedral solid elements with reduced integration (C3D8R) were adopted to model the concrete core. According to the mesh sensitivity study presented in Chapter 3, 5 mm mesh size (L_{eff}/200) was assigned to both aluminium tube and concrete core using the structured meshing technique. After meshing, typical BAT and CFAT beams contain over 7500 and 18500 elements, respectively. The elastic and plastic responses of aluminium alloy and concrete were modelled according to the procedure mentioned in Chapter 3. The contact behaviour between the aluminium tube and the concrete infill was modelled by the surface-to-surface. The existence of initial local geometric imperfections of all specimens was taken into account in the FE models. The amplitudes of initial geometric imperfection

listed in Table 5.1 were used in the models. To replicate the boundary conditions, the rotation about the bending axis (X direction) and displacement in the axial direction of the specimen (Z direction) were left unrestrained. At loading points, the load was applied along the vertical direction (Y direction) using a displacement control approach. Figure 5.6 illustrates a FE model of a typical CFAT beam.

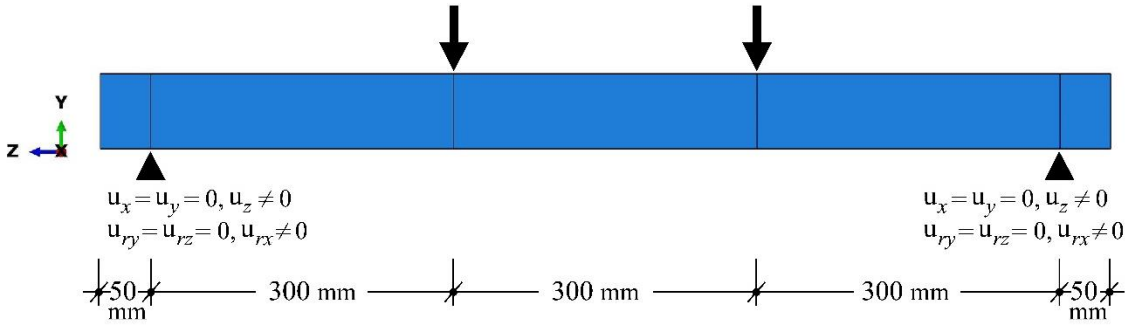

(a)

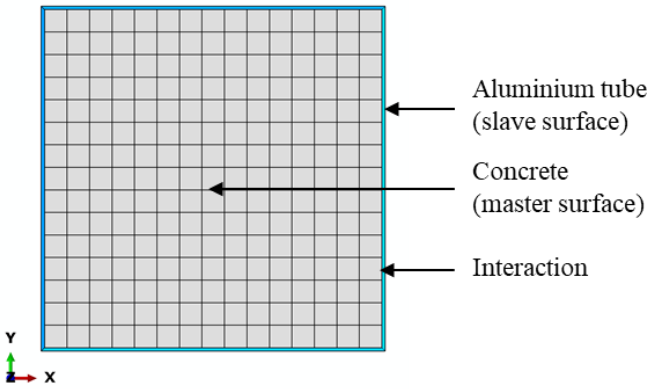

(b)

Figure 5.7: FE model of a typical CFAT beam: (a) geometry, loading and boundary conditions, (b) cross-section

5.4.2 FE model validation

The precision of the developed FE models was evaluated by comparing the experimental flexural strengths, bending moment versus mid-span deflection curves and failure modes with the corresponding FE results. The ratios of the FE over the experimental flexural strength ($M_{u,FE}/M_{u,Test}$) of all specimens are reported in Table 5.7. Close agreement is noticed between the experimental data and the FE results with a mean value of the $M_{u,FE}/M_{u,Test}$ ratio equal to 0.98 and a coefficient of variation (COV) equal to 0.05. Figure 5.7 shows the comparison between the experimental and FE bending moment versus mid-span deflection curves of some representative specimens.

It is observed that the developed FE models simulate the experimental curves very accurately. In addition, the experimental and FE failure modes of typical specimens are presented in Figure 5.8. It is demonstrated that the FE models fairly reproduce the deformed shapes and failure modes of the tested specimens. The failure modes and bending moment versus mid-span deflection curves of all specimens are provided in Figures A.3, A.4 in Appendix A and Figures B.3, B.4 in Appendix B, respectively. Overall, the developed FE models can satisfactorily predict the flexural behaviour of BAT and CFAT beams.

Table 5.7: Comparison of experimental and FE flexural strengths.

Specimen	$M_{u,FE}/M_{u,Test}$
76.2×76.2×1.6	1.10
76.2×76.2×1.6-C	0.96
76.2×76.2×3.3	1.01
76.2×76.2×3.3-C	1.02
76.2×76.2×4.8	0.91
76.2×76.2×4.8-C	0.94
76.2×76.2×6.4	0.95
76.2×76.2×6.4-C	0.94
76.2×25.4×3.3	0.99
76.2×25.4×3.3-C	0.98
76.2×38.1×3.3	0.98
76.2×38.1×3.3-C	0.99
76.2×50.8×3.3	0.94
76.2×50.8×3.3-C	0.92
101.6×25.4×3.3	1.05
101.6×25.4×3.3-C	1.04
101.6×50.8×3.3	0.96
101.6×50.8×3.3-C	0.94
101.6×76.2×3.3	0.94
101.6×76.2×3.3-C	0.94
Mean	0.98
COV	0.05

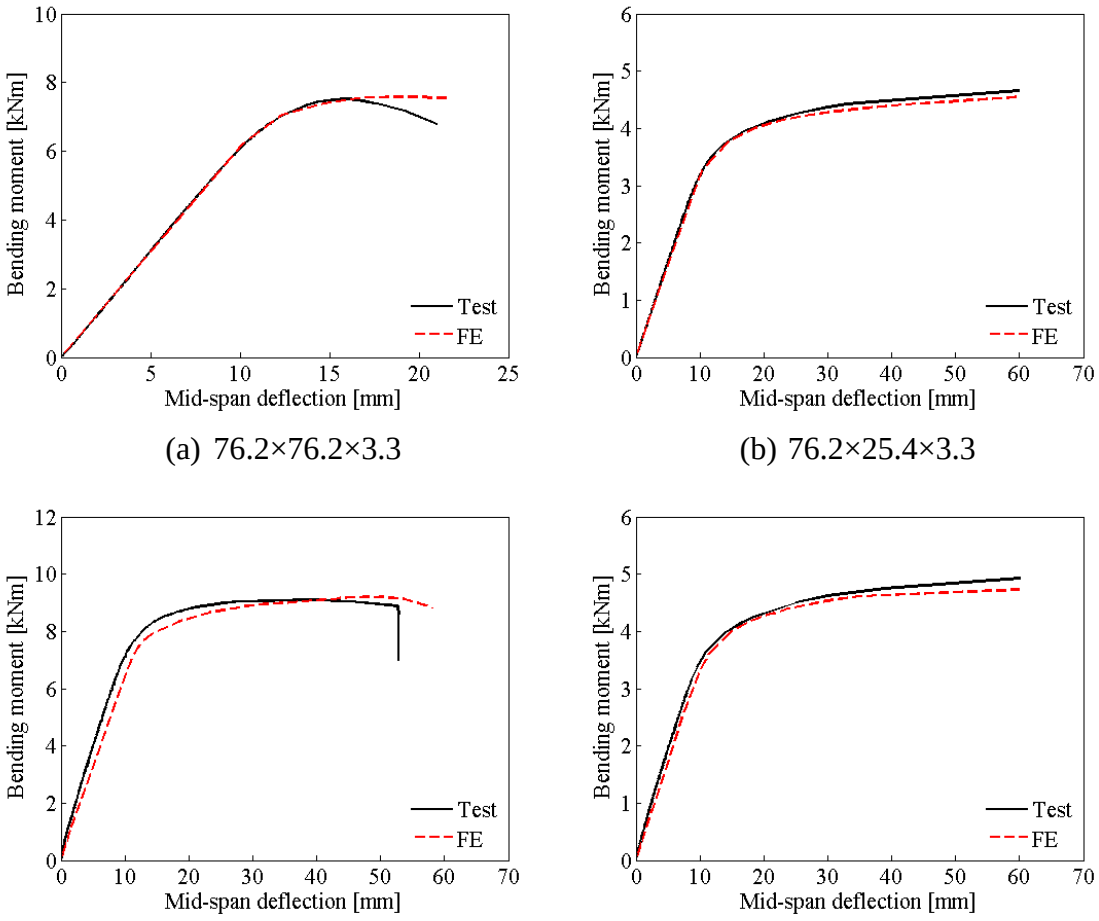

(a) 76.2×76.2×3.3 (b) 76.2×25.4×3.3

(c) 76.2×76.2×3.3 (-C) (d) 76.2×25.4×3.3 (-C)

Figure 5.8: Experimental and numerical bending moment versus mid-span deflection curves.

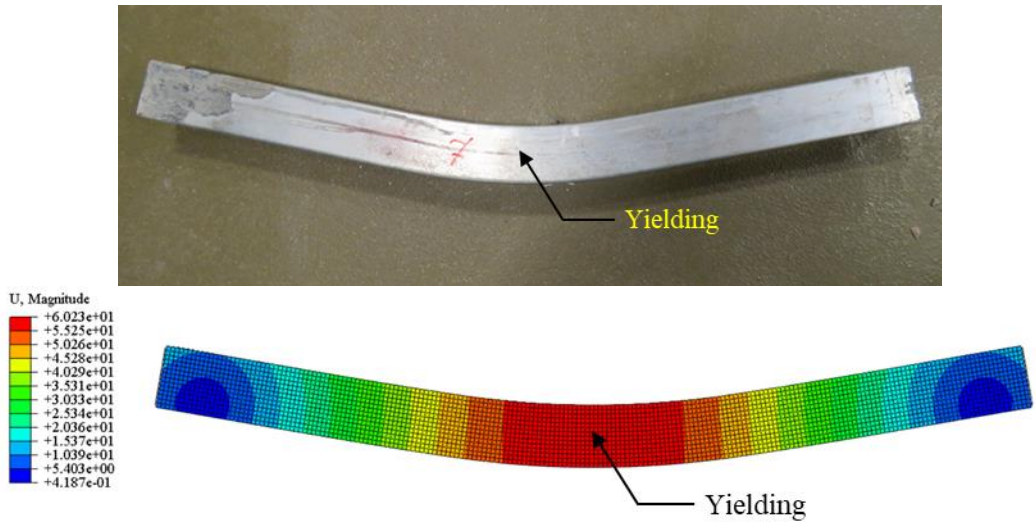

(a) 76.2×76.2×4.8 (-C)

Figure 5.9: Experimental and FE failure modes of typical specimens.

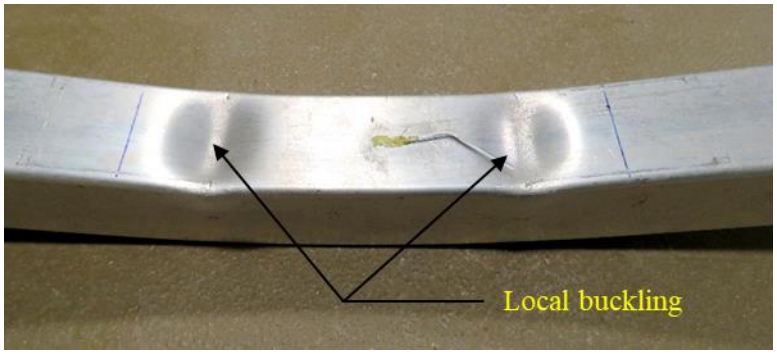

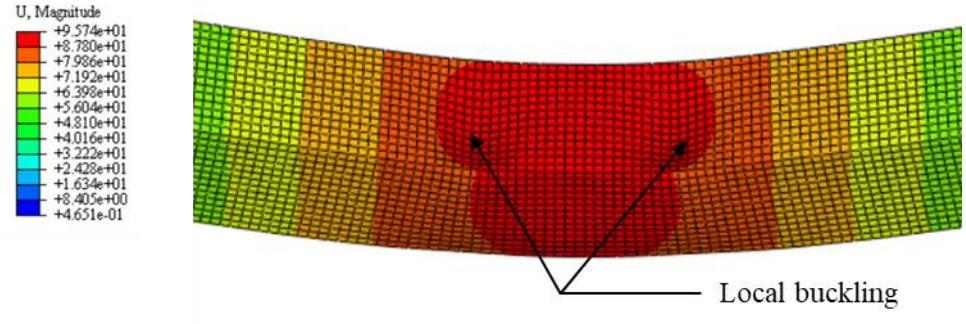

(b) 76.2×76.2×4.8

Figure 5.10 (continued): Experimental and FE failure modes of typical specimens.

5.4.3 Parametric study

A parametric study considering different cross-sections, slenderness and concrete grades was carried out based on the validated FE models. An average stress-strain curve acquired from the coupon tests was used for the aluminium tube. The average measured initial local imperfection value of $t/20$ was applied throughout. In this study, a total of 76 beams were modelled including 40 CFAT and 36 BAT specimens. Three cross-sectional aspect ratios (D/B), i.e., 1.0, 1.5 and 2 and the wall thickness varied from 1 mm to 10 mm were considered which are available in the UK market for structural applications. In this study, the wider range of cross-sectional aspect ratio and wall thickness were chosen to generate a sufficient amount of data for suggesting design recommendations. It is believed that the use wider range of cross-sectional dimensions in the parametric study compared to test specimens does not reduce the level of reliability of generated data as the failure pattern of the specimen with larger cross-sections considered in the parametric study is similar to that of test specimens having larger cross-sections. Moreover, three different normal strengths of concrete, i.e., 30, 40 and 50 MPa were selected to study the effect of concrete grade on the behaviour of CFAT beams. Here, high strength concrete was not considered as the developed FE

model was validated against only the test data related to the normal strength of concrete. The geometric dimensions and flexural strengths of the specimens considered in this parametric study are listed in Appendix C, Table C.2.

5.5 Numerical observations

Typical results of the numerically obtained moment-deformation behaviour are presented in Figure 5.9. Figures 5.9(a) and (b) illustrate the effect of the cross-sectional aspect ratio on the bending moment versus mid-span deflection curve of square and rectangular BAT and CFAT beams, respectively. The flexural strength of the BAT and CFAT members increases with the increase of D/B when the thickness is constant. In Figures 5.9(c) and (d) the FE flexural response of BAT and CFAT beams with different wall thicknesses is illustrated, respectively, showing the higher flexural capacity for lower cross-section slenderness (i.e., largest wall thickness).

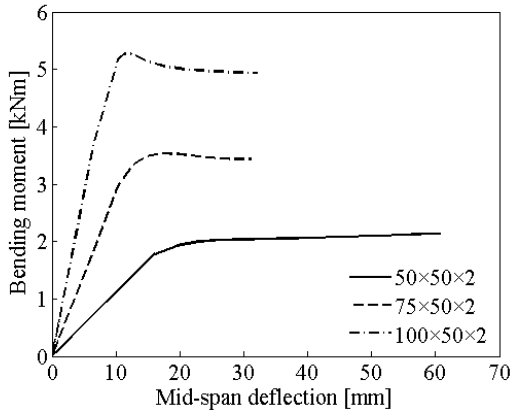

(a) BAT beams-effect of aspect ratio

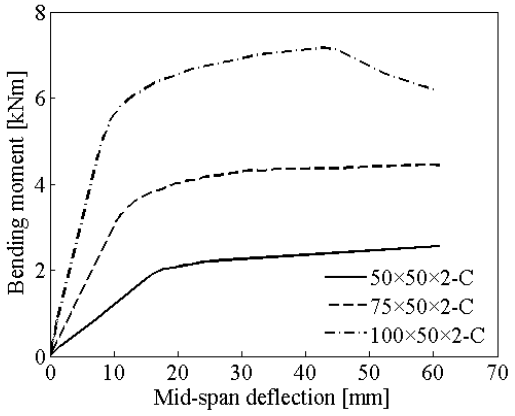

(b) CFAT beams-effect of aspect ratio

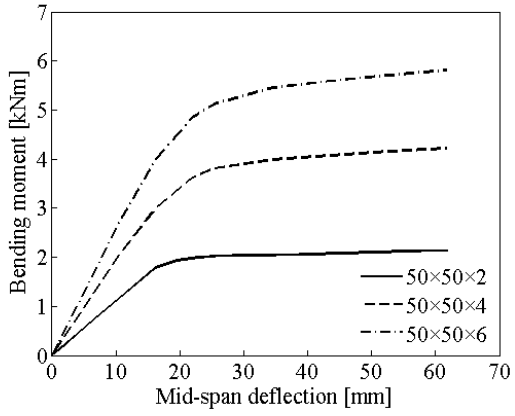

(c) BAT beams-effect of thickness

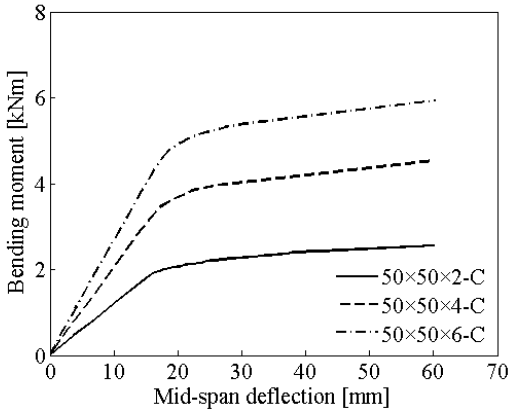

(d) CFAT beams-effect of thickness

Figure 5.11: Typical bending moment versus mid-span deflection curves from the parametric study.

Figure 5.10 presents the percentage increase in flexural strength due to higher concrete grade having as reference the flexural strength of 30 MPa for typical CFAT specimens. It is found that with the increase in compressive strength of concrete the flexural strength of CFAT members enhanced up to 6.9% for 40 MPa and up to 12.6% for 50 MPa. Moreover, it is also observed that the percentage increase of flexural strength is higher for CFAT beams with thinner cross-sections compared to thicker ones. This indicates that the higher-grade concrete offers more enhancement to the bending resistance of slender sections as the higher-grade concrete provides stronger support against the development of local buckling of slender sections.

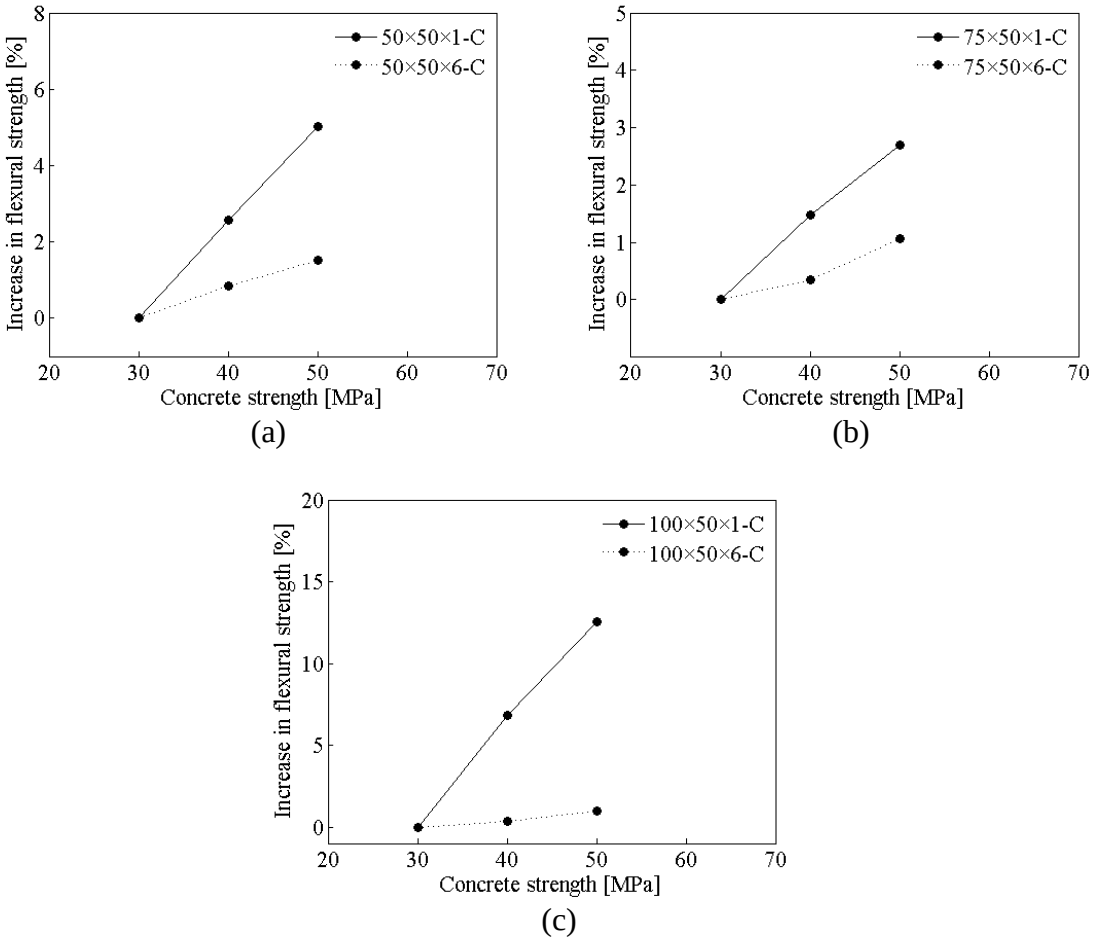

Figure 5.12: Effect of concrete compressive strength on the flexural strength of CFAT specimens.

5.6 Design Recommendations

In this section, the obtained experimental data and numerical results are used to assess the flexural strength predictions and the applicability of the slenderness limits provided

by Eurocode 9 (2007) for BAT beams. Moreover, based on codified rules for steel-concrete composite beams provided by Eurocode 4 (2004), design recommendations are made for the flexural strength predictions and the cross-sectional slenderness limits for the CFAT cross-sections. Note that the partial factors of safety were set equal to unity for the design code assessment.

5.6.1 Design provisions for BAT beams

In Eurocode 9 (2007), cross-sections are categorized into four classes, i.e., Class 1, 2, 3 and 4. According to Eurocode 9 (2007), the design flexural capacity of a square and rectangular hollow aluminium section can be calculated by Equation (5.5).

$$M_{u,EC9} = \alpha_s W_{el} f_{0.2} \tag{5.5}$$

In the above equation, α_s is the shape factor which is defined according to the cross-section classification as follows:

$$\alpha_s = \begin{cases} W_{pl}/W_{el} & \textit{(for Class 1 \& 2)} \\ 1 & \textit{(for Class 3)} \\ W_{eff}/W_{el} & \textit{(for Class 4)} \end{cases} \tag{5.6}$$

where W_{el} and W_{pl} represent the elastic modulus and plastic modulus of the gross section, respectively and W_{eff} denotes the effective modulus of the gross section.

5.6.2 Assessment of Eurocode 9 flexural strength prediction

The flexural strength, M_u, of BAT beams determined from experiments and FE analysis was compared with the flexural strengths calculated by Eurocode 9 (2007), $M_{u,EC9}$. The moment ratios, $M_u/M_{u,EC9}$, and their corresponding mean and COV values are presented in Table 5.8. Figure 5.11 shows a comparison between flexural strength obtained from experiments and FE analysis and the corresponding predicted design strengths. Based on the above comparisons, it can be seen that Eurocode 9 (2007) provides good predictions of flexural strengths with a mean value of $M_u/M_{u,EC9}$ equal to 1.06. However, the COV value reported in Table 5.8 indicates relatively scattered predictions.

Table 5.8: Comparison of experimental and FE flexural strengths with design strengths for BAT beams.

	Specimen	No	Class	$M_u/M_{u,EC9}$
Test	76.2×76.2×1.6	1	3	0.79
	76.2×76.2×3.3	1	1	0.98
	76.2×76.2×4.8	1	1	1.13
	76.2×76.2×6.4	1	1	1.11
	76.2×25.4×3.3	1	1	1.17
	76.2×38.1×3.3	1	1	1.20
	76.2×50.8×3.3	1	1	1.12
	101.6×25.4×3.3	1	2	1.21
	101.6×50.8×3.3	1	1	1.14
	101.6×76.2×3.3	1	2	0.98
			Mean	1.08
			COV	0.11
FE (mean)		36	1-4	1.05
			Mean (all)	1.06
			COV (all)	0.07

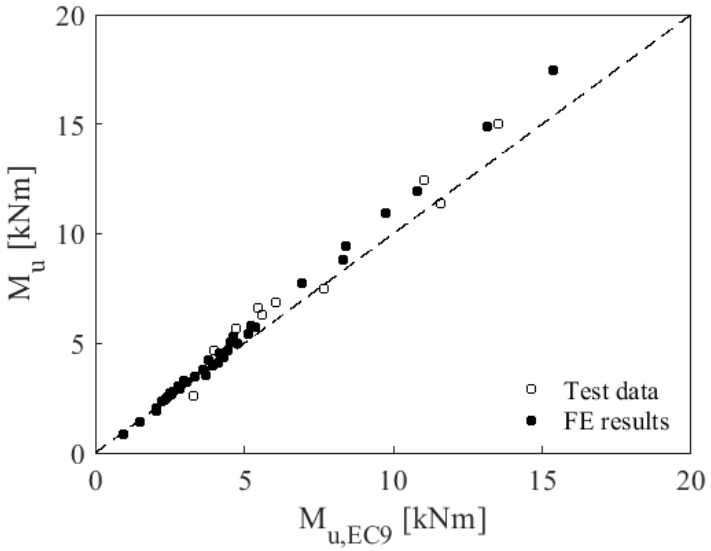

Figure 5.13: Comparison of test and FE flexural strengths with strengths calculated by Eurocode 9 (2007) for BAT beams.

5.6.3 Assessment of Eurocode 9 Class 1 limit

According to Eurocode 9 (2007), a Class 1 cross-section can achieve and sustain its full plastic moment capacity with sufficient deformation under uniaxial bending. In contrast, a Class 2 cross-section can reach full plastic capacity but cannot maintain it due to the

development of inelastic local buckling. The Class 1 and Class 2 cross-sections can be distinguished based on their rotation capacity R that is defined in Equation (5.7) (Moen *et al.*, 1999):

$$R = \frac{\kappa_u}{\kappa_{pl}} - 1 \tag{5.7}$$

where κ_{pl} is the curvature of a beam at which the moment first reaches the plastic moment capacity of the member, $M_{pl,m}$, and κ_u is the curvature of a beam at which the moment drops back to $M_{pl,m}$ after reaching the peak flexural strength, M_u. κ_{pl} and κ_u are calculated by Equations (5.8) and (5.9), respectively.

$$\kappa_{pl} = \frac{M_{pl,m}}{EI} \tag{5.8}$$

$$\kappa_u = \frac{8\left(\delta - \delta_{av}\right)}{4\left(\delta - \delta_{av}\right)^2 + L_l^{\,2}} \tag{5.9}$$

where I is the moment of inertia of the cross-section, δ and δ_{av} are the mid-span displacement and average vertical displacement at two loading points corresponding to the moment which reaches $M_{pl,m}$ again after the M_u and L_l is the distance between two loading points. For the specimens not showing any softening part in their moment-mid-span deflection curves, δ is taken as the maximum mid-span displacement δ_u. A rotation capacity of 3 is required for the plastic design of steel structures (Eurocode 3, 2005; AISC, 2010). In line with a past study (Su *et al.*, 2017), this value is considered herein for BAT flexural members.

To assess Class 1 limit for internal elements in compression of Class A materials, the rotation capacity of BAT beams obtained from the experiments and numerical analysis is plotted against the flange slenderness parameter β/ε in Figure 5.12. The term β is equal to b/t (where b is the flat part of the width and t is the thickness of the cross-section) and ε is the material factor which is equal to $\sqrt{250/f_{0.2}}$. The corresponding Class 1 slenderness limit given in Eurocode 9 is shown in Figure 5.12 along with the rotation capacity limit of 3 (Su *et al.*, 2017). It can be observed that the rotation capacities of aluminium alloy flexural members are scattered which is related to the effects of material properties as well as the interaction of constituent plates (Su *et al.*,

2017). Regardless the scatteredness of data, a decreasing trend of rotation capacity with increasing member slenderness is clear. It is found that the Eurocode 9 Class 1 limit of β/ε =11 for Class A aluminium alloy is conservative, as the number of cross-sections beyond this limit have higher rotational capacity than the minimum value of 3 specified in the design standard (Eurocode 3, 2005; AISC, 2010). For this reason, a new vertical line of β/ε =15 is proposed which separates the Class 1 cross-sections that have the rotational capacity equal to or higher than the specified value (i.e., $R \geq 3$). The proposed limit is aligned with the limit suggested by Su *et al.* (2017).

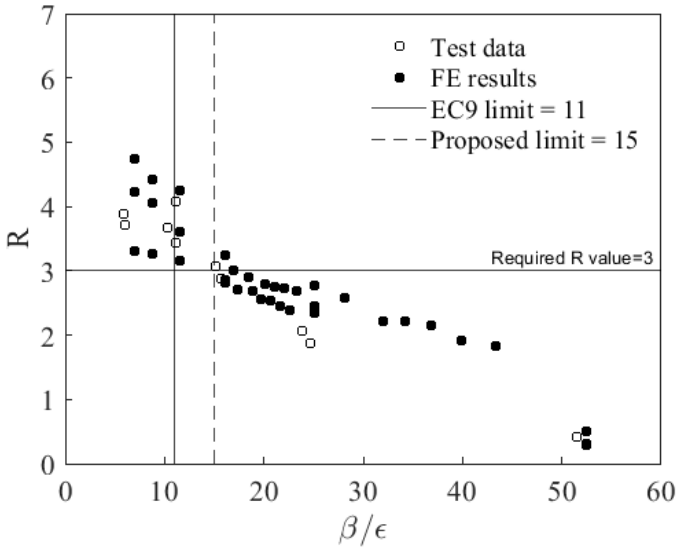

Figure 5.14: Assessment of Class 1 slenderness limits for internal elements of Class A materials given by Eurocode 9 (2007).

5.6.4 Assessment of Eurocode 9 Class 2 limit

According to Eurocode 9 (2007), the design flexural capacity of a Class 2 cross-section is the plastic moment capacity $M_{pl,cr}$ of the cross-section, which is determined by Equation (5.10) where W_{pl} is the plastic section modulus of the cross-section and $f_{0.2}$ is the yield stress of the material. Hence, to assess the Class 2 limit for internal elements suggested by Eurocode 9, the flexural strength M_u determined from the experiments and FE analysis is normalised by $M_{pl,cr}$ and plotted against the slenderness parameter β/ε of the flange in Figure 5.13. Here, the reason for normalizing the M_u by $M_{pl,cr}$ is to find the Class 2 cross-sections which can achieve their full plastic moment capacity.

$$M_{pl,cr} = W_{pl} f_{0.2} \tag{5.10}$$

An expected trend of decreasing normalised flexural strength, $M_u/M_{pl,cr}$ with increasing flange slenderness can be observed in Figure 5.13. The horizontal line at $M_u/M_{pl,cr}$ equal to unity separates Class 2 (i.e., having $M_u/M_{pl,cr} \geq 1$) from Class 3 (i.e., having $M_u/M_{pl,cr} < 1$) cross-sections. Based on this demarcation, it can be observed from Figure 5.13 that the Eurocode 9 slenderness limit of $\beta/\varepsilon = 16$ appears to be strict since many sections with values of β/ε larger than this limit have $M_u/M_{pl,cr} \geq 1$ and can be classified as Class 2 cross-sections. Based on the experimental and numerical data of this work, a new limit of $\beta/\varepsilon = 22$ is proposed that is more appropriate as a Class 2 limit, as it includes all the sections of Figure 5.13 that have $M_u/M_{pl,cr} \geq 1$.

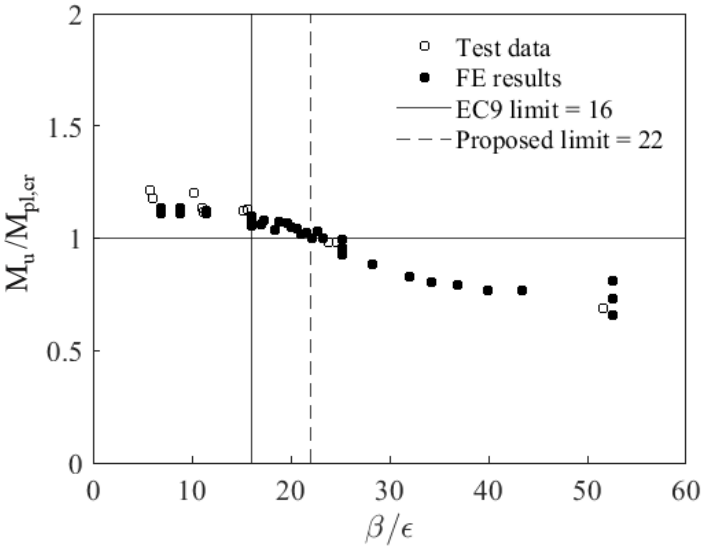

Figure 5.15: Assessment of Class 2 slenderness limits for internal elements of Class A materials given by Eurocode 9 (2007).

5.6.5 Assessment of Eurocode 9 Class 3 limit

In Eurocode 9 (2007), the cross-sections that can achieve the elastic moment capacity (i.e., moment related to the first yielding), but experience local buckling before reaching the plastic moment capacity are defined as Class 3 cross-sections. On the other hand, Class 4 sections fail by local buckling before reaching the elastic moment capacity. In Figure 5.14, the ultimate bending strength M_u normalised by elastic moment capacity of cross-section M_{el} ($W_{el} f_{0.2}$) are plotted against flange slenderness β/ε to assess EC9 Class 3 limit for internal elements in compression. Similar to Figure 5.13, the horizontal line

in Figure 5.14 at M_u/M_{el} equal to unity separates Class 3 cross-sections (i.e., having $M_u/M_{el} \geq 1$) and Class 4 cross-sections (i.e., having $M_u/M_{el} < 1.0$). It can be observed from this figure that the slenderness limit of $\beta/\varepsilon = 22$ specified in Eurocode 9 is conservative for the internal elements of Class 3 aluminium sections, as some cross-sections beyond this limit achieve flexural capacity higher than the elastic moment capacity, i.e., $M_u/M_{el} \geq 1$. Thus, a Class 3 limit of $\beta/\varepsilon = 31$ is suggested, as it seems to be more suitable on the basis of the experimental and numerical findings of this study.

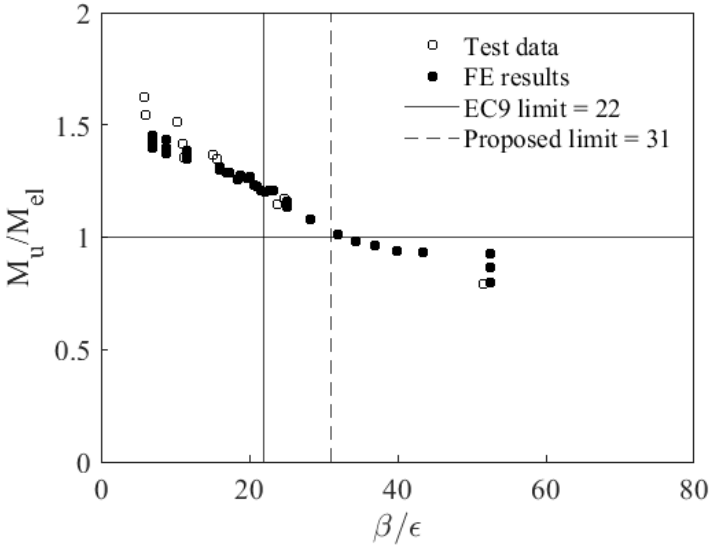

Figure 5.16: Assessment of Class 3 slenderness limits for internal elements of Class A materials given by Eurocode 9 (2007).

5.6.6 Design methodology for CFAT beams

In the absence of design specifications for CFAT flexural members, design recommendations for evaluating the flexural strength of CFAT beams are provided in this section based on Eurocode 4 (2004) where the steel's material properties are replaced with those of aluminium alloy. Based on Eurocode 4 (2004), the design bending capacity of square and rectangular CFAT cross-section can be obtained using the following design formula:

$$M_{pl,cr} = \left(W_{pla} - W_{pla,n}\right) f_{0.2} + 0.5\left(W_{plc} - W_{plc,n}\right) f_c \tag{5.11}$$

where W_{pla} and W_{plc} are the plastic section moduli of the aluminium tube and concrete, respectively, which are determined by Equations (5.12) and (5.13), respectively. $W_{pla,n}$

and $W_{plc,n}$ are the plastic section moduli of the aluminium tube and concrete from $2h_n$, respectively, which are calculated by Equations (5.14) and (5.15), respectively. The term h_n is the location of the neutral axis determined by Equation (5.16), where A_c and f_c are the area and compressive strength of concrete, respectively. In Equations (5.12) and (5.13), r_{int} represents the internal corner radius of the hollow tube which is taken zero herein. The cross-sections of aluminium tubes of CFAT specimens are classified based on the criteria provided by Eurocode 9 (2007) and the revised slenderness limits proposed in the previous section.

$$W_{pla} = \frac{BH^2}{4} - \frac{2}{3}\left(r_{int}+t\right)^3 - \left(r_{int}+t\right)^2\left(4-\pi\right)\left(\frac{H}{2}-t-r_{int}\right) - W_{plc} \tag{5.12}$$

$$W_{plc} = \frac{\left(B-2t\right)\left(H-2t\right)^2}{4} - \frac{2}{3}{r_{int}}^3 - {r_{int}}^2\left(4-\pi\right)\left(\frac{H}{2}-t-r_{int}\right) \tag{5.13}$$

$$W_{pla,n} = B{h_n}^2 - W_{plc,n} \tag{5.14}$$

$$W_{plc,n} = \left(B-2t\right){h_n}^2 \tag{5.15}$$

$$h_n = \frac{A_c f_c}{2Bf_c + 4t\left(2f_{0.2} - f_c\right)} \tag{5.16}$$

5.6.7 Flexural strength prediction for CFAT beams

To assess the applicability of the design methodology mentioned in the previous section, Table 5.9 presents the moment ratio of $M_u/M_{pl,cr}$ along with the mean and COV values. The mean value of $M_u/M_{pl,cr}$ is 1.04, indicating that the design rules of Eurocode 4 (2004) offer good predictions. In Figure 5.15, the flexural strengths obtained from tests and FE analysis are plotted against the ultimate bending moments calculated by Eurocode 4 (2004). It can be observed from the figure that Eurocode 4 (2004) is quite accurate as most of the points are close to the diagonal line (i.e., $M_u/M_{pl,cr} = 1$). Overall, it can be concluded that Eurocode 4 (2004) can be applied to predict the flexural capacity of CFAT beams by replacing steel's material properties with those of aluminium alloy.

Table 5.9: Comparison of test and FE flexural strengths with design strengths for CFAT beams.

	Specimen	No	Class	$M_u/M_{pl,cr}$
Test	76.2×76.2×1.6-C	1	3	0.93
	76.2×76.2×3.3-C	1	1	1.06
	76.2×76.2×4.8-C	1	1	1.17
	76.2×76.2×6.4-C	1	1	1.14
	76.2×25.4×3.3-C	1	1	1.17
	76.2×38.1×3.3-C	1	1	1.18
	76.2×50.8×3.3-C	1	1	1.20
	101.6×25.4×3.3-C	1	2	1.28
	101.6×50.8×3.3-C	1	1	1.24
	101.6×76.2×3.3-C	1	2	1.04
			Mean	1.14
			COV	0.09
FE (mean)		40	1-4	1.02
			Mean (all)	1.04
			COV (all)	0.09

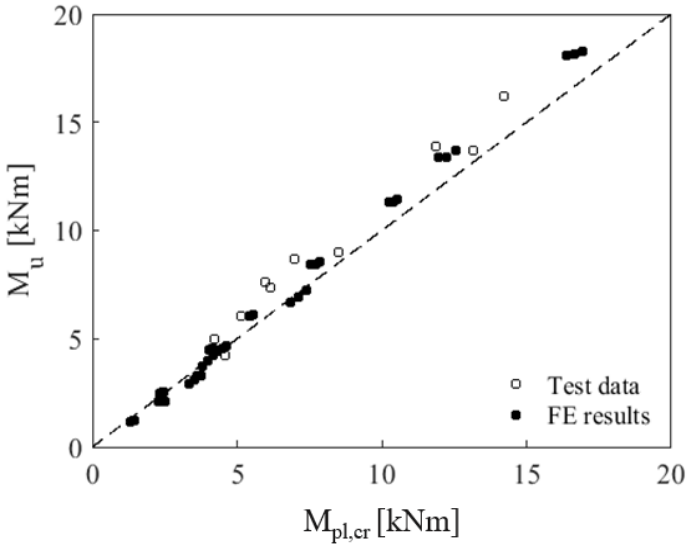

Figure 5.17: Comparison of test and FE flexural strengths with strengths calculated by the proposed design methodology for CFAT beams.

5.6.8 Slenderness limit for CFAT cross-sections

According to Eurocode 4 (2004), the effect of local buckling can be neglected for composite cross-sections if the slenderness value, β_1/ε of these sections does not exceed 52. These composite cross-sections are considered as compact sections. In β_1/ε, $\beta_1=D/t$,

D is the depth of the cross-section and $\varepsilon=\sqrt{250/f_{0.2}}$. To obtain a slenderness limit for compact sections of CFAT flexural members, the moment ratio $M_u/M_{pl,cr}$ determined from experimental and FE results are plotted against the β_1/ε in Figure 5.16. Here the material factor ε for aluminium alloy is considered $\sqrt{250/f_{0.2}}$ based on Eurocode 9 (2007). The horizontal line of $M_u/M_{pl,cr}$ = 1 separates the cross-sections that have flexural strength equal to or higher than their plastic flexural strength (i.e., $M_u/M_{pl,cr} \geq 1$) from the cross-sections having lower flexural strength than their plastic flexural strength (i.e., $M_u/M_{pl,cr} < 1$). Based on this demarcation, it can be seen that the proposed vertical line of 46 separates the CFAT cross-sections having normalised flexural strength greater than or equal to unity (i.e., $M_u/M_{pl,cr} \geq 1$). Thus, according to the test and FE data of this study, the cross-section slenderness limits of β_1/ε = 46 is proposed for CFAT cross-sections.

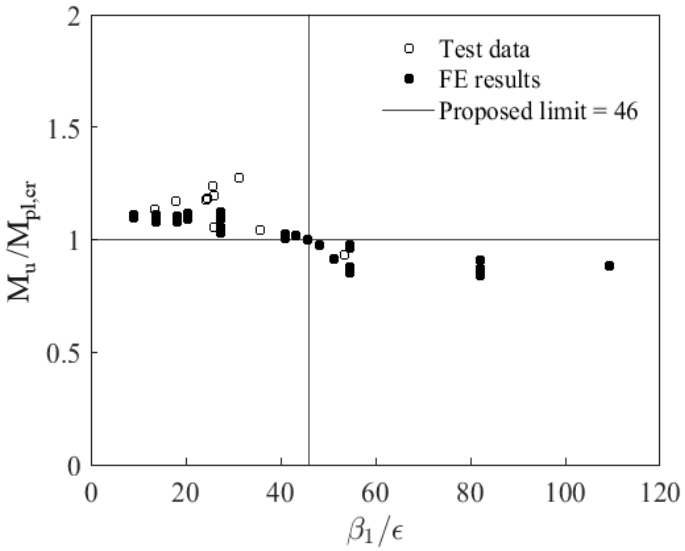

Figure 5.18: Proposed slenderness limit for CFAT cross-sections.

5.7 Conclusions

This study presented experimental and numerical investigations on the performance of BAT and CFAT members under in-plane bending. In total 20 beams, including 10 CFAT and 10 BAT specimens, were tested. FE models of BAT and CFAT specimens were developed and used to conduct a parametric study. Based on the observed experimental and numerical results the following conclusions can be drawn:

- The flexural strength, flexural stiffness and ductility of CFAT specimens were significantly higher than those of BAT specimens with identical cross-sections. This signifies the effectiveness of concrete infill in reducing the possibility and extent of local buckling of bare aluminium sections.
- It was also shown that the strength increase because of the concrete infill was more prominent for slender cross-sections. This is attributed to the delay in the onset of local buckling in the slender plate elements offered by the concrete infill, resulting in an additional increase in the ultimate strength.
- It was demonstrated that the developed FE models can closely predict the flexural behaviour of BAT and CFAT beams. Hence, a parametric study was performed, including 76 beams (40 CFAT beams and 36 BAT beams) with a broad range of cross-sections and different concrete grades.
- The FE results have shown that the flexural strength of the BAT and CFAT members increases with the increase of D/B when the thickness is constant. Moreover, based on the flexural response of BAT and CFAT beams with different wall thicknesses, it was shown that a higher flexural capacity was observed for sections with lower cross-section slenderness.
- Based on the FE results, it was shown that the flexural strength of CFAT members is generally enhanced with the increase of concrete compressive strength and this enhancement is prominent for the thinner cross-sections.
- The applicability of the slenderness limits provided by Eurocode 9 was assessed based on the experimental and numerical results. It was demonstrated that the current slenderness limits in Eurocode 9 are conservative for Class A aluminium sections. Hence, revised Class 1, Class 2 and Class 3 limits are proposed which appear to be better applicable to Class A aluminium alloys.
- In the absence of design specifications for CFAT flexural members, the design rules for CFST flexural members provided by Eurocode 4 are adopted by replacing the steel's material properties with those of aluminium alloy. It was shown that the design methodology based on Eurocode 4 can sufficiently predict the flexural strength of CFAT members.
- A slenderness limit for CFAT cross-sections was proposed based on Eurocode 4 framework.

CHAPTER 6 : CFDSAT MEMBERS IN COMPRESSION

6.1 Introduction

This chapter reports experimental and numerical investigations on the flexural buckling behaviour of CFDSAT columns under axial compression. The results obtained from the tests are presented in terms of failure modes, ultimate load and load versus mid-height lateral displacement curves. Non-linear FE models of the CFDSAT columns are established and validated against test results. Using the validated FE models, a numerical parametric study is conducted to investigate the influence of hollow ratio, member slenderness, cross-sectional slenderness of hollow tubes and concrete strength on the structural behaviour of CFDSAT columns. Finally, a design methodology is proposed with a design buckling curve to predict the ultimate load of CFDSAT columns according to Eurocode 4 framework.

6.2 Experimental programme

6.2.1 Test specimens and material properties

A total of 8 CFDSAT columns were tested under axial compression, in which 6 specimens comprised of square outer and inner tubes and 2 specimens made with square outer and circular inner tubes. Figure 6.1 shows the photographs of typical cross-sections of the specimens and Table 6.1 presents the measured geometric dimensions of all specimens, including depth/diameter (D), width (B) and thickness (t), where the subscripts 'o' and 'i' denote the outer and inner tubes, respectively. In this study, a total 8 hollow sections were taken, where three large sections with measured depth/diameter to thickness ratio (D_o/t_o) varying from 16.45 to 20.81 were utilized as the outer profiles and five small sections with measured depth/diameter to thickness ratio (D_i/t_i) ranging from 6.09 to 16.74 were utilized as the inner profiles. All specimens were 1000 mm long. The nominal effective length (L_{eff}) of the specimens, including pin-ended supports, was 1064 mm. The specimens were labelled considering the geometric dimensions of the outer and inner tubes. For example, the label 'S63.4×3.2-C19.2×3.2' indicates a CFDSAT specimen consisting of 'S63.4×3.2' outer section and 'C19.2×3.2' inner section. In the notation 'S63.4×3.2', the letter 'S' signifies that the hollow section is a square shape with nominal depth and width of 63.4 mm and thickness of 3.2 mm. In the notation 'C19.2×3.2', the letter 'C' represents a circular hollow section which has

nominal diameter of 19.2 mm and thickness of 3.2 mm. The measured initial global geometric imperfection (ω_g) of all specimens is listed in Table 6.1. Prior to the tests, the initial loading eccentricity (e_0) of all specimens was determined by Equation (3.3) presented in Chapter 3 and the values are also listed in Table 6.1. Figure 6.1 shows photos of the typical cross-sections of the specimens.

Table 6.1: Measured dimensions and initial geometric imperfection and loading eccentricity of CFDSAT specimens.

Specimen	D_o (mm)	B_o (mm)	t_o (mm)	D_o/t_o	D_i (mm)	B_i (mm)	t_i (mm)	D_i/t_i	ω_g (mm)	e_0 (mm)
S50.8×3.2-S19.2×1.6	50.83	50.83	3.09	16.45	19.05	19.05	1.53	12.45	0.27	0.52
S63.4×3.2-S19.2×1.6	63.48	63.48	3.05	20.81	19.06	19.06	1.53	12.46	0.15	0.89
S63.4×3.2-S25.4×3.2	63.48	63.48	3.06	20.75	25.38	25.38	3.28	7.74	0.39	0.68
S76.2×4.8-S19.2×1.6	76.09	76.09	4.61	16.51	19.05	19.05	1.57	12.13	0.11	0.81
S76.2×4.8-S25.4×1.6	76.09	76.09	4.58	16.61	25.27	25.27	1.51	16.74	0.04	0.93
S76.2×4.8-S25.4×3.2	76.09	76.09	4.61	16.51	25.42	25.42	3.30	7.70	0.07	0.66
S63.4×3.2-C19.2×3.2	63.54	63.45	3.10	20.50	18.88	-	3.10	6.09	0.12	0.64
S63.4×3.2-C25.4×3.2	63.48	63.45	3.08	20.61	25.41	-	3.37	7.54	0.30	0.60

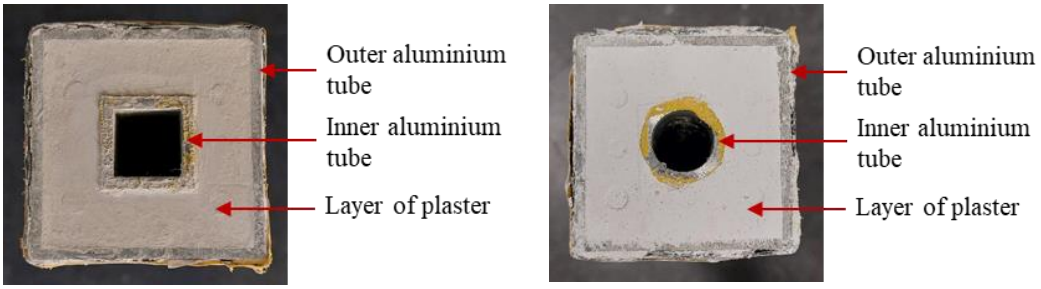

(a) CFDSAT specimen with square outer and inner tubes

(b) CFDSAT specimen with square outer and circular inner tubes

Figure 6.1: Photographs of typical cross-sections of CFDSAT specimens.

The material properties of aluminium alloy hollow tubes and concrete are summarized in Tables 6.2 and 6.3, respectively. Figure 6.2 shows the typical failure modes of tensile coupon specimens and some experimental stress-strain curves along with the respective Ramberg-Osgood curves.

Table 6.2: Material properties of the aluminium alloy tubes.

Specimen	E (GPa)	$f_{0.1}$ (MPa)	$f_{0.2}$ (MPa)	f_u (MPa)	ε_u (%) (mm/mm)	ε_f (%) (mm/mm)	n
S19.2×1.6	72500	185	189	215	4.57	5.45	28.83
S25.4×1.6	68700	192	197	229	6.43	11.40	27.55
S25.4×3.2	70000	276	283	328	7.66	16.00	28.06
S50.8×3.2	68300	257	264	304	7.49	14.70	28.19
S63.5×3.2	69900	157	164	212	6.69	15.60	21.94
S76.2×4.8	70700	305	311	338	5.97	11.70	33.91
C19.2×3.2	72800	303	306	320	5.18	8.94	36.53
C25.4×3.2	71900	283	289	327	8.50	13.00	29.58

(a)

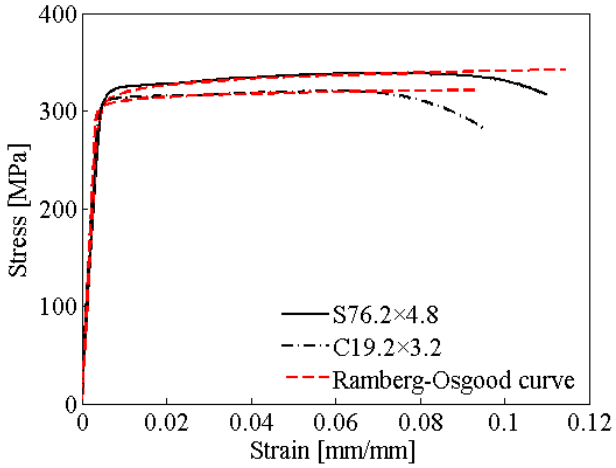

(b)

Figure 6.2: (a) Failure modes of typical coupons, (b) Experimental and respective Ramberg-Osgood stress-strain curves of S76.2×4.8 and C19.2×3.2 material coupons.

Table 6.3: Measured compressive strength of concrete cubes.

Compressive strength of cubes (MPa)	Mean (MPa)
37.2 35.7 36.8 36.5	36.5

6.2.2 Flexural buckling tests

The axial compression tests were conducted to investigate the flexural buckling behaviour and determine the ultimate load of CFDSAT specimens. The pin-ended boundary condition described in Chapter 3 were used for the tests. During the tests, LVDTs were used, in which two were positioned at the mid-length to measure the

lateral displacement and two were placed at the bottom channel to record the rotation of the specimens. Two strain gauges were attached at the mid-height of two faces parallel to the bending axis of a specimen to measure the in-plane axial strains. Figure 6.3 presents a photograph of the test set-up.

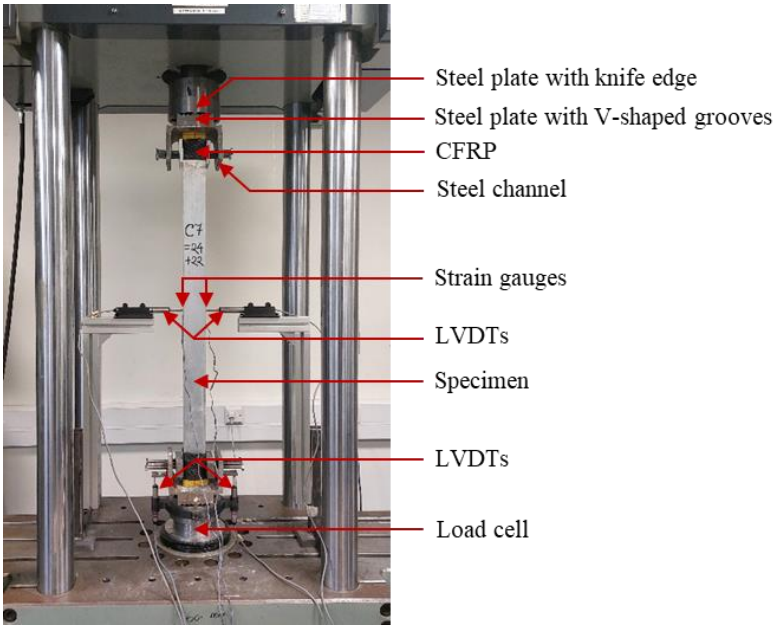

Figure 6.3: Photograph and schematic diagram of the axial compression test.

6.3 Experimental observations

6.3.1 Failure mode

The failure mode of all CFDSAT columns was examined after the axial compression tests. Figure 6.4 illustrates the typical failure mode of the tested specimens. It was observed that the predominant failure mode of all specimens was flexural buckling (Figure 6.4(a)) as the pin-ended set-up allowed the specimens to rotate about the buckling axis. No inward or outward local buckling was identified at the outer tube of the CFDSAT specimens. This is attributed to the concrete infill that effectively prevented the occurrence of inward buckling and delayed the formation of outward buckling of the outer tube. Moreover, no fracture was noticed in the outer tube of any specimen. For investigating the failure pattern of the inner components, the outer tube and concrete infill of some specimens were partly cut and detached after the tests. The failure pattern of the inner tube and the concrete infill of a typical specimen is presented in Figure 6.4(b) and 6.5, respectively. Figure 6.4(b) shows that, same as the outer tube, the inner tube displayed obvious flexural buckling. However, any inward or outward

bulging or fracture was not found in the inner tube of the inspected specimens. It can be seen from Figure 6.5 that some small horizontal cracks in concrete appeared at the tension region near the mid-height of the specimen as tension stresses are higher in this region. The failure mode of all specimens is listed in Table 6.4.

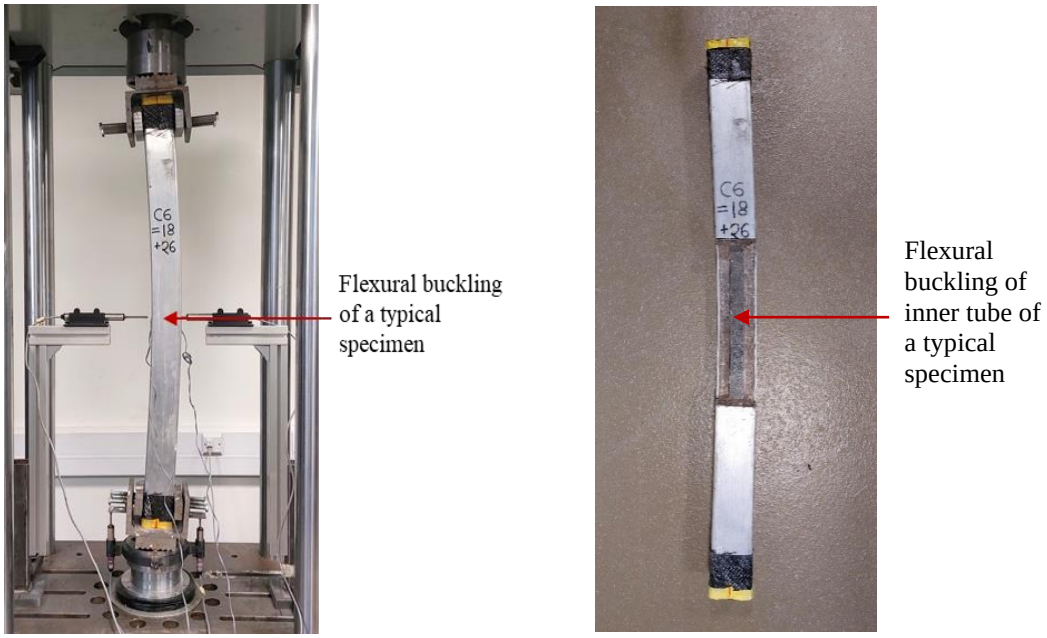

(a) S76.2×4.8-S25.4×3.2 (b) S76.2×4.8-S25.4×3.2

Figure 6.4: Flexural buckling of (a) a typical CFDSAT specimen, (b) inner tube of a typical CFDSAT specimen.

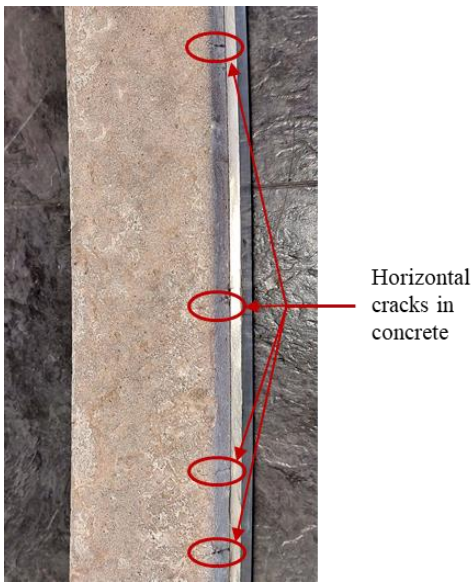

(a) S76.2×4.8-S19.2×1.6

Figure 6.5: Horizontal cracks in the concrete infill of a typical CFDSAT specimen.

Table 6.4: Failure mode, ultimate load and ductility of CFDSAT specimens.

Specimen	Failure mode	$N_{u,Test}$ (kN)	μ
S50.8×3.2-S19.2×1.6	FB	143.30	14.61
S63.4×3.2-S19.2×1.6	FB	179.83	13.18
S63.4×3.2-S25.4×3.2	FB	216.85	26.34
S76.2×4.8-S19.2×1.6	FB	464.47	23.54
S76.2×4.8-S25.4×1.6	FB	455.64	18.33
S76.2×4.8-S25.4×3.2	FB	466.51	17.15
S63.4×3.2-C19.2×3.2	FB	210.67	22.47
S63.4×3.2-C25.4×3.2	FB	198.51	14.81

FB = Flexural buckling

6.3.2 Load versus mid-height lateral displacement curve

Figure 6.6 presents the axial load versus mid-height lateral displacement curves of all specimens. The curves are plotted using the compressive load and lateral displacement data recorded from the load cell of the machine and the LVDT located at the mid-height of the specimens, respectively. It is found from the figure that, initially the relationship between axial load and mid-height lateral displacement is linear which indicates that the materials of composite specimens were in the elastic stage. At the end of the elastic stage, all curves diverge from linear to nonlinear response as the growth of load decreases compare to the lateral displacement. This is the evidence of the elastic-plastic stage which exists up to the ultimate load. After reaching the ultimate load, a softening part appears in the curves as the load started to fall gradually with the development of lateral displacement. It can be observed from the figure that, a certain ductility is visible in all curves, attributing to the beneficial composite response of the three elements of CFDSAT columns. The ultimate load and ductility of all specimens obtained from the tests are provided in Table 6.4. It is found that the ultimate load of the specimens improved by increasing the dimensions of the outer sections. The influence of outer and inner sections on the ultimate load is further studied by the FE analysis and discussed in the following section.

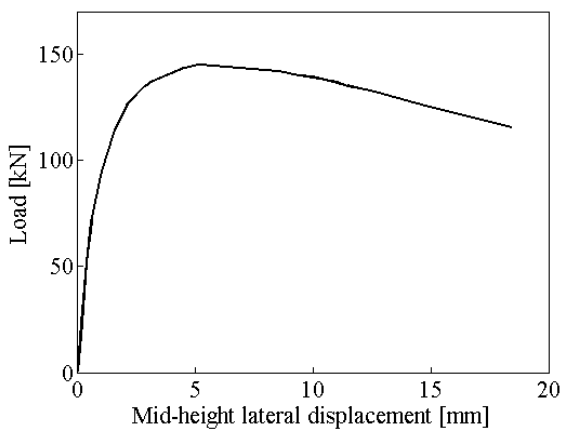

(a) S50.8×3.2-S19.2×1.6

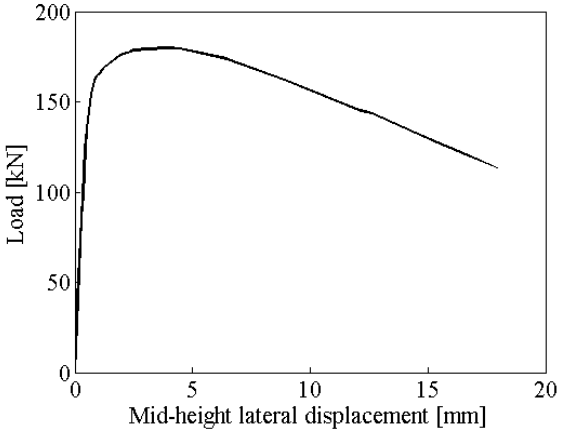

(b) S63.4×3.2-S19.2×1.6

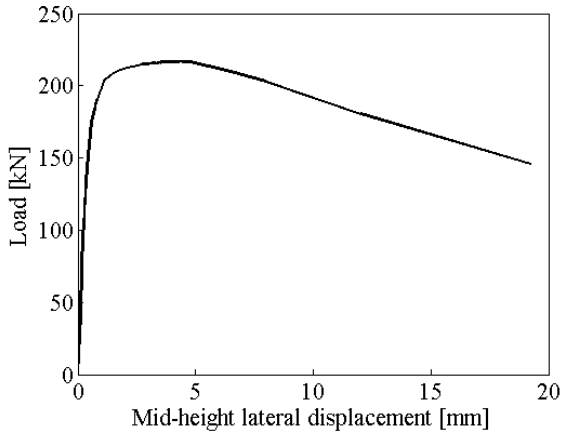

(c) S63.4×3.2-S25.4×3.2

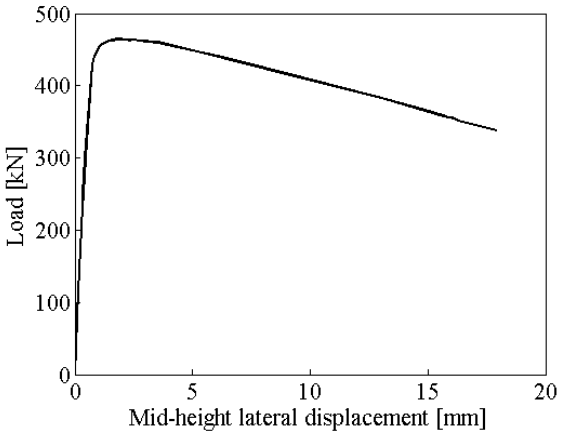

(d) S76.2×4.8-S19.2×1.6

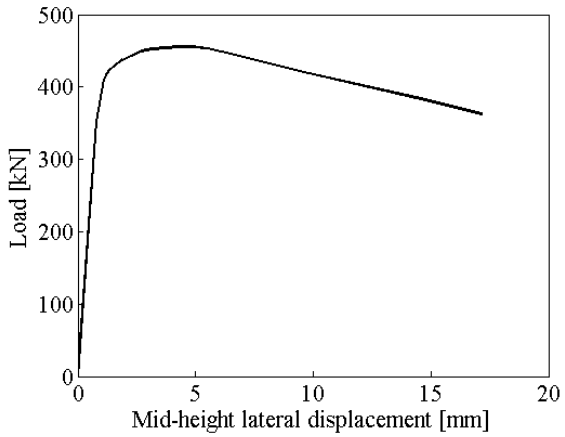

(e) S76.2×4.8-S25.4×1.6

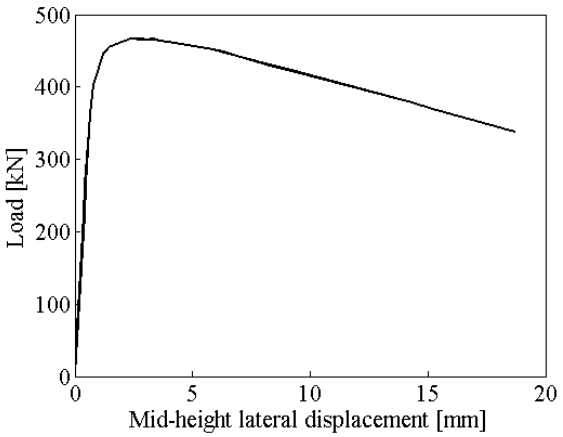

(f) S76.2×4.8-S25.4×3.2

Figure 6.6: Axial load versus mid-height lateral displacement curves of CFDSAT specimens.

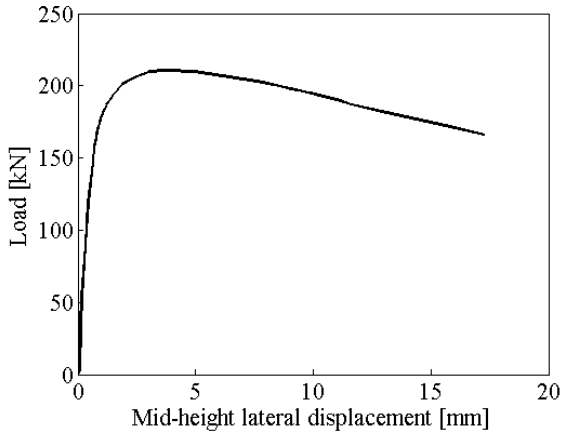

(g) S63.4×3.2-C19.2×3.2

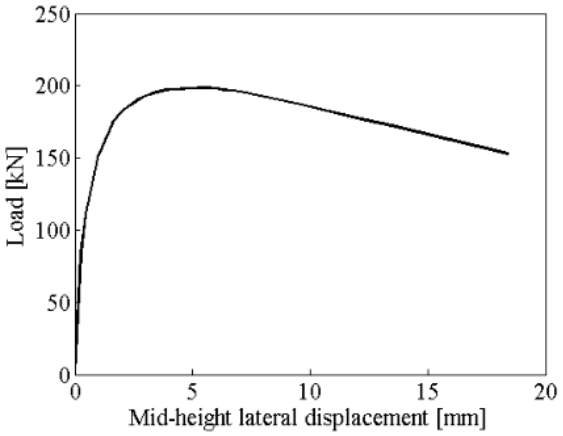

(h) S63.4×3.2-C25.4×3.2

Figure 6.7 (continued): Axial load versus mid-height lateral displacement curves of CFDSAT specimens.

6.4 Numerical investigation

6.4.1 FE modelling

All CFDSAT columns were modelled according to the measured cross-sectional dimensions and material properties reported in Tables 6.1, 6.2 and 6.3. 8-node hexahedral solid elements with reduced integration (C3D8R) were used to simulate the hollow tubes and the concrete infill. 5 mm element size obtained from the mesh sensitivity study described in Chapter 4 is used for the FE models. The thickness of the hollow sections was discretised at least into three elements to capture the nonlinear response of the sections (Milan *et al.*, 2019). The mechanical behaviours of aluminium alloy tubes and concrete were simulated by following the procedure discussed in Chapter 3. The built-in surface-to-surface contact option in ABAQUS was used to simulate the interaction between the concrete and the hollow tubes. The amplitude of global imperfection of a specimen was calculated by adding the value of ω_g with the respective value of e_0. The pin-end supports were simulated by applying the boundary conditions on the reference points which were created on the centroid of the top and bottom ends of the specimens. The distance between the two reference points was the same as the specimens' effective length. The reference points were fixed against all degrees of freedom, except the displacement at the loaded end (Z direction) and the rotation around the buckling axis (X direction). The axial compressive load was employed at the top reference point using a displacement control approach. Figure 6.7 shows the loading direction, boundary conditions and cross-section of a typical model.

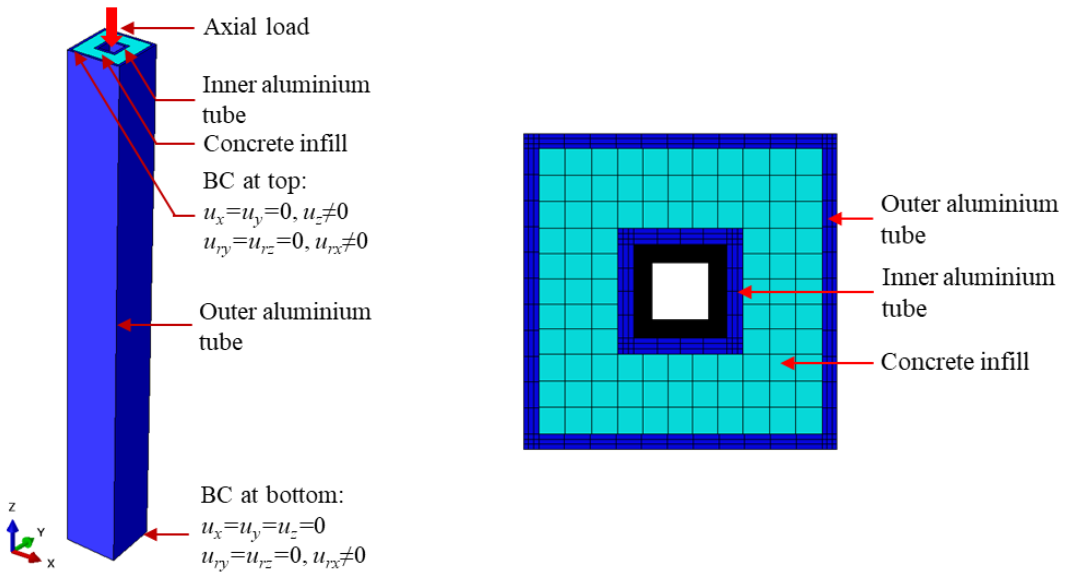

(a) (b)

Figure 6.8: FE model of a typical CFDSAT specimen: (a) loading direction and boundary conditions, (b) cross-section.

6.4.2 FE model validation

The developed FE model was validated by comparing the FE ultimate load, load versus mid-height lateral displacement and failure mode with corresponding test results. An imperfection sensitivity study was carried out to evaluate an appropriate global imperfection amplitude for using in the numerical parametric study. In this study, four global imperfection amplitudes were considered including the measured amplitudes (i.e., summation of ω_g and e_0) and three values of fractions of the effective length, i.e., $L_{eff}/1000$, $L_{eff}/1500$ and $L_{eff}/2000$. Table 6.5 reports the ratios of FE over the test ultimate load ($N_{u,FE}/N_{u,Test}$) for four global imperfection amplitudes. It can be observed that the global imperfection amplitude of $L_{eff}/1000$ offers a good prediction of ultimate load with a mean value of $N_{u,FE}/N_{u,Test}$ is 1.02 and the corresponding coefficient of variation (COV) is 0.04. Figure 6.8 presents the comparison between FE (for global imperfection magnitude of $L_e/1000$) and test axial load versus mid-height lateral displacement curves of two specimens. The figure illustrates that the developed FE model accurately simulates the axial load versus mid-height lateral displacement relationship of the specimens. Moreover, Figure 6.9 shows a good agreement between the failure mode observed from the test and the FE analysis of a typical specimen. The failure modes and test and FE load versus mid-height lateral displacement curves of all specimens are provided in Figure A.5 in Appendix A and Figure B.5 in Appendix B, respectively. All

the above comparisons demonstrate the accuracy of the developed FE model to replicate the structural behaviour of CFDSAT columns.

Table 6.5: Comparison of test and FE ultimate load.

Specimen	$N_{u,FE}/N_{u,Test}$			
	Global imperfection amplitude			
	Measured	L_{eff}/1000	L_{eff}/1500	L_{eff}/2000
S50.8×3.2-S19.2×1.6	1.04	1.00	1.07	1.11
S63.4×3.2-S19.2×1.6	1.09	1.10	1.14	1.15
S63.4×3.2-S25.4×3.2	0.98	0.99	1.03	1.05
S76.2×4.8-S19.2×1.6	1.02	1.02	1.04	1.05
S76.2×4.8-S25.4×1.6	1.02	1.03	1.06	1.07
S76.2×4.8-S25.4×3.2	1.07	1.04	1.07	1.08
S63.4×3.2-C19.2×3.2	0.98	0.96	0.99	1.00
S63.4×3.2-C25.4×3.2	1.02	1.01	1.04	1.07
Mean	1.03	1.02	1.05	1.07
COV	0.03	0.04	0.04	0.04

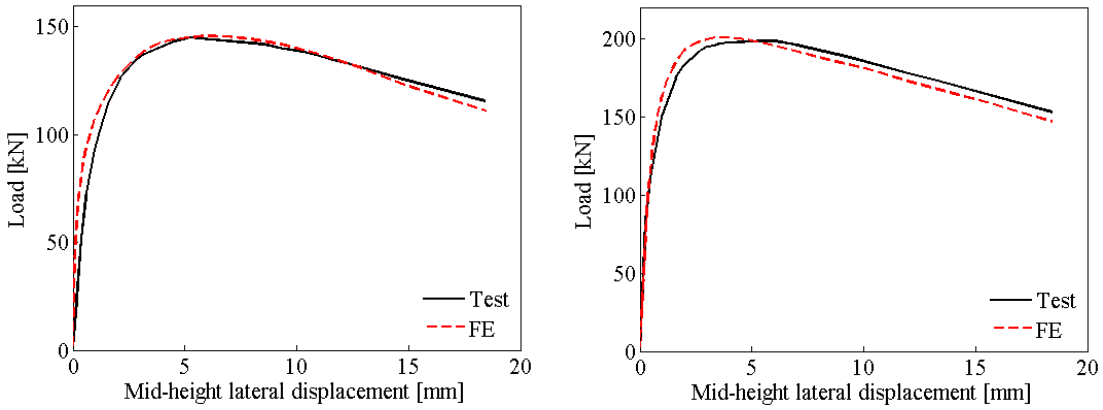

(a) S50.8×3.2-S19.2×1.6 (b) S63.4×3.2-C25.4×3.2

Figure 6.9: Comparison of test and FE axial load versus mid-height lateral displacement curves.

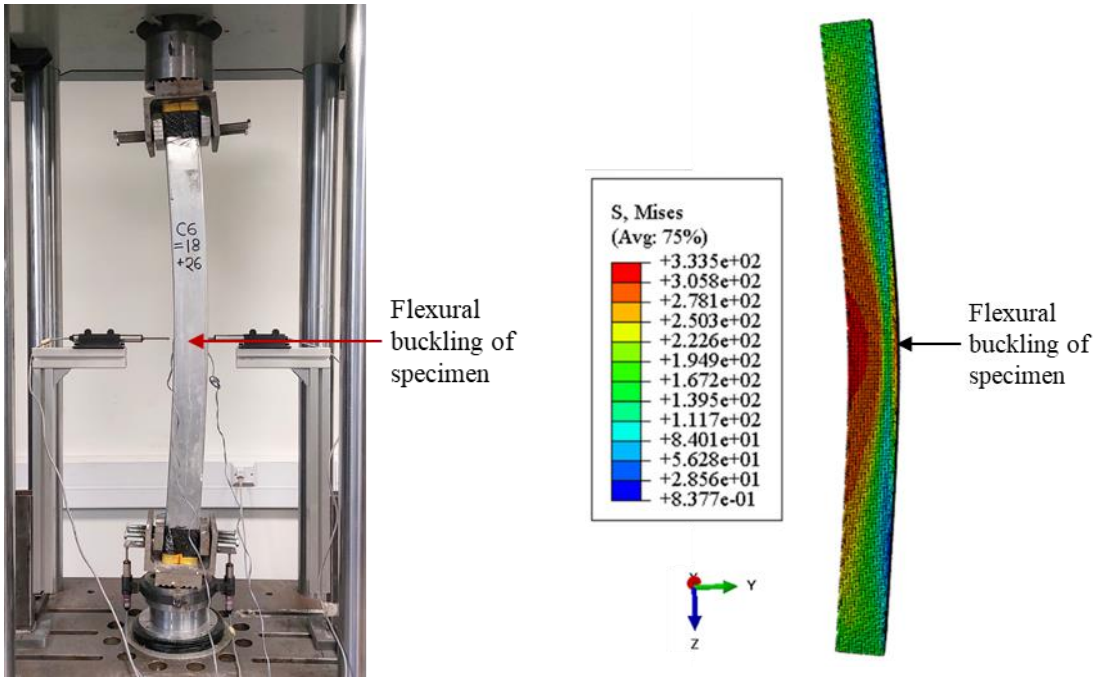

(a) Flexural buckling of S76.2×4.8-S25.4×3.2

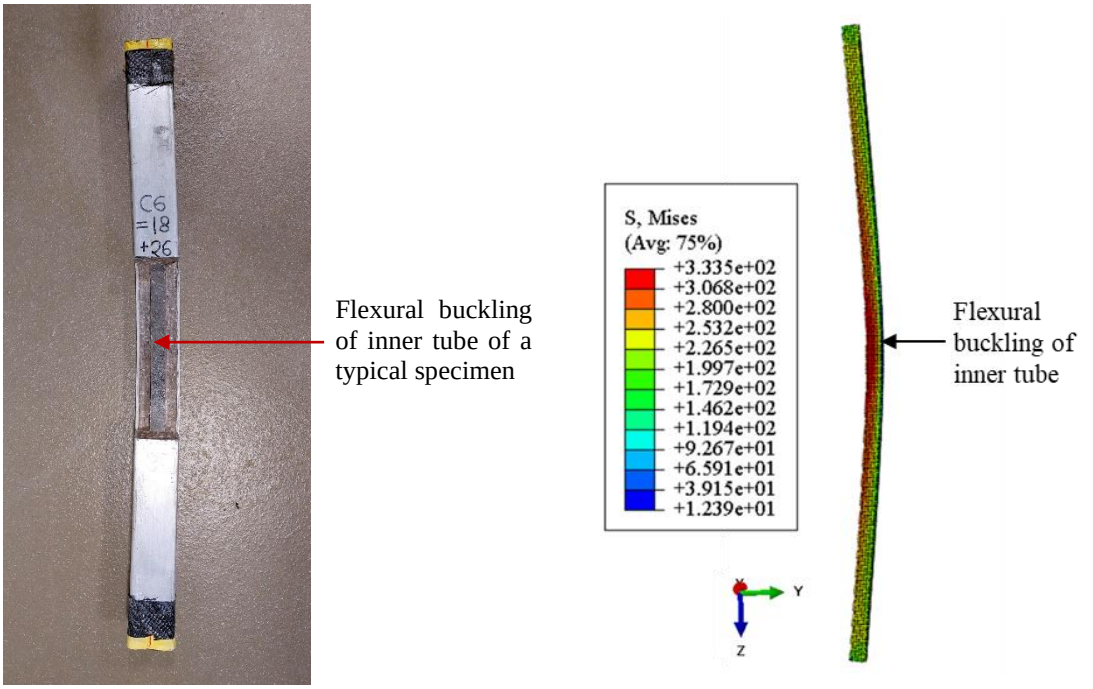

(b) Flexural buckling of inner tube of S76.2×4.8-S25.4×3.2

Figure 6.10: Comparison of test and FE failure mode of a typical CFDSAT specimen.

6.4.3 Parametric study

Using the validated FE model, a numerical parametric study was conducted to investigate the effect of hollow ratio, member slenderness, cross-section slenderness of

hollow tubes and concrete strength on the ultimate load of CFDSAT columns. The average material properties of flat and curved coupons were adopted for the square and circular aluminium sections, respectively. Total 81 CFDSAT columns were modelled considering different outer sections, i.e., 45×45, 60×60, 75×75, 100×100, 120×120 and 150×150 mm^2 with wall thickness varied from 1 to 8 mm and inner sections, i.e., 20×20, 25×25, 30×30 and 35×35 mm^2 with wall thickness ranged from 1 to 5 mm, two combinations of outer and inner cross-section shapes, i.e., square-square and square-circular, three different member height, i.e., 500, 1000 and 1500 mm and three different concrete cube compressive strength, i.e., 30, 40 and 50 MPa. The geometric dimensions and ultimate capacity of the specimens used in this parametric study are listed in Appendix C, Table C.3.

6.5 Numerical observations

6.5.1 Effect of hollow ratio

To investigate the effect of hollow ratio on the ultimate load of CFDSAT columns a wide range of depth/diameter of the outer and the inner cross-sections was considered in this study. The hollow ratio is calculated using Equation (6.1).

$$\alpha = \frac{D_i}{D_o - 2t_o} \tag{6.1}$$

where α is the hollow ratio which is varied from 0.14 to 0.86 by changing the depth/diameter of outer and inner tubes. The influence of α on the axial load versus mid-height lateral displacement curves of typical CFDSAT columns is illustrated in Figure 6.10. It can be seen from Figure 6.10(a) that the ultimate load of CFDSAT columns significantly improved with the decrease of α (i.e., increase of depth of the outer tube) when the inner section's dimensions remain the same. This is related to the fact that, by increasing the depth, the flexural rigidity of the outer tube increased along with the increase of concrete area, which contribute to the improvement of the ultimate load of the specimens. Figure 6.10(b) demonstrates that when the dimensions of the outer tube are constant, the ultimate load of CFDSAT columns is decreased slightly by enlarging the depth/diameter of the inner tube (i.e., increase of α). This is because the larger depth/diameter of the inner tube decreased the area of concrete, resulting in a reduction of ultimate load. This can be explained by Figure 6.11, which shows the

contribution of the outer tube, concrete infill and inner tube to the ultimate load of typical CFDSAT specimens. It can be observed from Figures 6.11(a) and (b) that, concrete infill provides the second-highest cross-sectional resistance to axial compression among the three components, whereas the contribution of the inner tube to the cross-sectional compressive resistance is least compared to the other components of CFDSAT columns. Therefore, the variation of the depth/diameter of the inner tube has a slight influence on the ultimate load of CFDSAT columns.

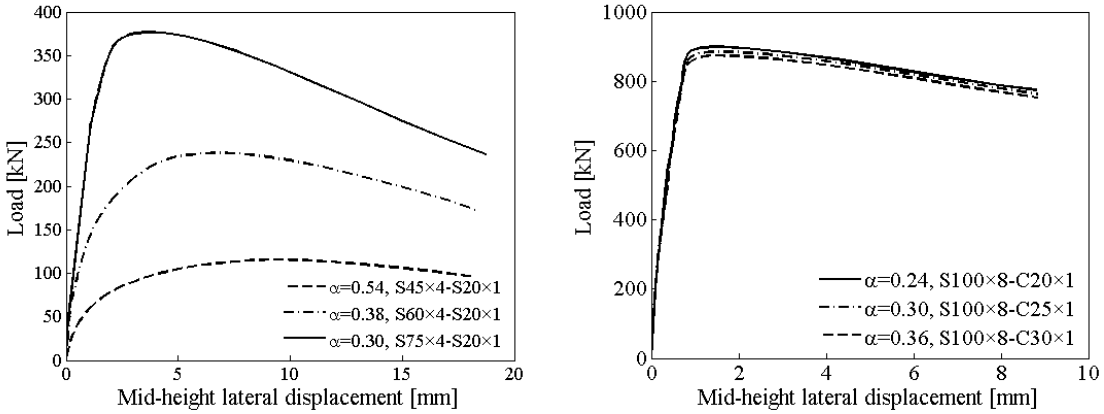

(a) CFDSAT specimens with constant inner tube (S20×1)

(b) CFDSAT specimens with constant outer tube (C100×8)

Figure 6.11: Effect of hollow ratio on the axial load versus mid-height lateral displacement of typical CFDSAT specimens.

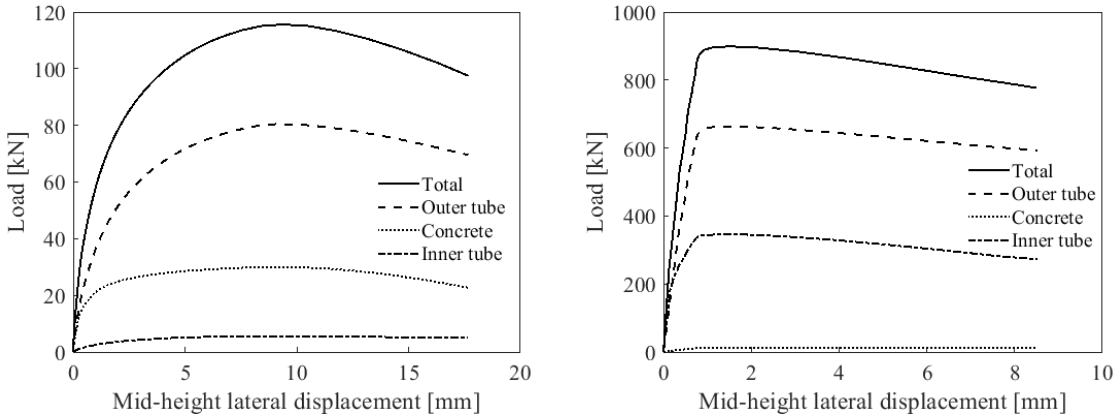

(a) S75×4-S20×1

(b) C100×8-C20×1

Figure 6.12: Contribution of the outer tube, concrete infill and inner tube on the ultimate load of typical CFDSAT specimens.

6.5.2 Effect of depth to thickness ratio of the outer tube

Figure 6.12 presents the effect of depth to thickness ratio of the outer tube (D_o/t_o) on the axial load versus mid-height lateral displacement of typical CFDSAT columns. The D_o/t_o ratio ranging from 6 to 150 was considered by altering the outer tube thickness from 1 mm to 8 mm. These selected thicknesses for the cross-sections are available in the UK market for structural applications. It is observed from the figure that the effect of D_o/t_o ratio is remarkable on the buckling behaviour of CFDSAT columns, as the ultimate load of the columns increased noticeably by decreasing D_o/t_o ratio (i.e., increase of thickness of outer tube). This is because the larger thickness provides higher flexural rigidity of the outer tube, which results in an improved ultimate load of the specimens.

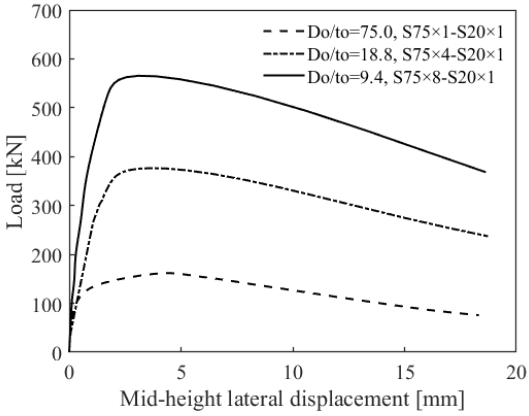

Figure 6.13: Effect of D_o/t_o ratio on the axial load versus mid-height lateral displacement curves of typical CFDSAT specimens.

6.5.3 Effect of depth/diameter to thickness ratio of the inner tube

Figure 6.13 illustrates the effect of the depth/diameter to thickness ratio of the inner tube (D_i/t_i) on the buckling behaviour of CFDSAT columns. The D_i/t_i ratios were considered from 4 to 35 by varying the thickness of square and circular inner sections. It can be seen from Figure 6.13 the ultimate load of specimen S100×4-C20×1 increased by 1.8% and 5.9%, respectively when the D_i/t_i ratio decreased from 20 (for t = 1 mm) to 10 (for t = 2 mm) and 4 (for t = 5 mm). This indicates that with the decrease of D_i/t_i ratio the ultimate load of the CFDSAT columns generally improved, as the smaller D_i/t_i ratio means a larger thickness of the inner tube which offers an addition in the load-carrying capacity of the specimens. However, the influence of D_i/t_i is minimal as the

maximum improvement of the ultimate load of the studied columns is noticed at around 6% when the inner tube thickness is increased from 1 mm to 5 mm. This is because the inner tube provides the least cross-sectional resistance among the three components of the CFDSAT columns (Figure 6.11).

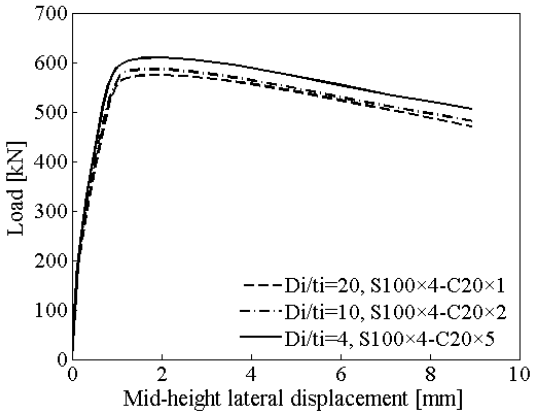

Figure 6.14: Effect of D_i/t_i ratio on the axial load versus mid-height lateral displacement curves of typical CFDSAT specimens.

6.5.4 Effect of member slenderness ($\bar{\lambda}$)

To examine the effect of member slenderness ($\bar{\lambda}$) on the capacity of CFDSAT columns, three different column lengths, i.e., 500, 1000 and 1500 mm were considered without changing the cross-sectional dimensions of the columns. The member's slenderness is determined according to Eurocode 4 (2004). Figure 6.14 presents the effect of $\bar{\lambda}$ on the axial load versus mid-height lateral displacement curves of a typical CFDSAT specimen S100×1.5-S20×1. It can be seen from the figure that when the member length increased from 500 mm ($\bar{\lambda}$ = 0.25) to 1000 mm ($\bar{\lambda}$ = 0.47) and 1500 mm ($\bar{\lambda}$ = 0.69) the ultimate capacity of the column is reduced by 5.2% and 15.3%, respectively. It can be explained that when the cross-sectional dimensions of the specimens are constant, the critical buckling load of columns decreases with the increase of the member length, which makes the columns prone to global buckling failure, resulting in a reduced ultimate load.

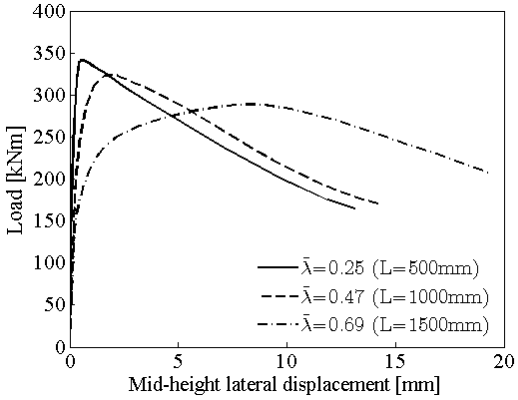

Figure 6.15: Effect of member slenderness ($\bar{\lambda}$) on the axial load versus mid-height lateral displacement curves of a typical CFDSAT specimen S100×1.5-S20×1.

6.5.5 Effect of concrete compressive strength

In the parametric study, three different compressive strengths of concrete cube (f_{cu}), i.e., 30, 40 and 50 MPa were adopted to study the effect of normal strength concrete grade on the ultimate load of CFDSAT columns. The effect of different concrete grades on the axial load versus mid-height lateral displacement of a typical CFDSAT column is shown in Figure 6.15. It can be observed from the figure that the concrete grade has a profound effect on the buckling behaviour of the CFDSAT columns, as the bearing capacity of the columns enhanced substantially with the increase of compressive strength of the concrete. This is related to the fact that concrete provides the second highest cross-sectional resistance among the three components of the CFDSAT columns and improves the load-carrying capacity of the outer tube by preventing the occurrence of inward buckling and slowing down the formation of outward buckling. Hence, the higher-grade concrete adds more cross-sectional resistance and offers stronger support against the local buckling effect of the outer tube.

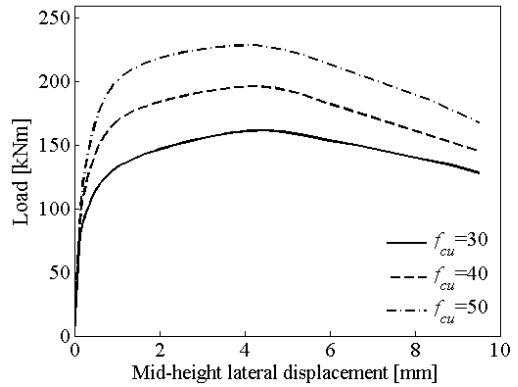

Figure 6.16: Effect of concrete cube compressive strength on the axial load versus mid-height lateral displacement curves of a typical CFDSAT specimen S75×1-S20×1.

6.6 Design Recommendations

The existing design code for composite structural members, i.e., Eurocode 4 (2004) provides guidelines for the design of fully concrete-filled carbon steel tubular columns. However, no design rules are available for the design of CFDSAT columns. Hence, in this study, a design methodology with a design buckling curve is proposed based on the Eurocode 4 (2004) framework for determining the ultimate load of CFDSAT columns. The accuracy of the proposed methodology is evaluated by comparing the design strengths with the corresponding test and FE data.

6.6.1 Design methodology for CFDSAT columns

In Eurocode 4 (2004), a design formula for calculating the ultimate load of fully concrete-filled carbon steel structural columns is provided by summing the plastic cross-sectional resistance of the outer tube and the concrete infill. To determine the ultimate load of CFDSAT columns, the formula is modified by substituting the material properties of carbon steel for the outer tube with those of aluminium alloy and considering the contribution of the inner tube by adding its plastic cross-sectional resistance function. Thus, the ultimate load of CFDSAT columns is calculated using Equation (6.2).

$$N_{pl} = A_o f_{0.2,o} + \alpha A_c f_c + A_i f_{0.2,i} \tag{6.2}$$

where A_o, A_c, and A_i are the cross-sectional areas of the outer tube, concrete infill and inner tube, respectively. $f_{0.2,o}$ and $f_{0.2,i}$ are the yield stresses of the outer and the inner tube, respectively. f_c is the compressive cylinder strength of concrete. It is assumed that the concrete reaches its full f_c due to the confinement provided by the outer and inner tubes. Therefore, the concrete coefficient α is considered 1 instead of 0.85 (Wang *et al.*, 2020).

The design strength of the CFDSAT section is converted to member strength by employing a reduction factor χ recommended by Eurocode 4 (2004).

$$N_{u,prop} = \chi N_{pl} \tag{6.3}$$

The expression of χ is given in Equation (6.4).

$$\chi = \left[\varphi + \sqrt{\phi^2 - \bar{\lambda}^2} \right]^{-1} \leq 1.0 \tag{6.4}$$

In the above equation, ϕ is a parameter and $\bar{\lambda}$ is the member slenderness. The $\bar{\lambda}$ is calculated by Equation (6.5).

$$\bar{\lambda} = \sqrt{N_{pl} / N_{cr}} \tag{6.5}$$

The N_{cr} denotes the Euler buckling load, which is defined by Equation (6.6).

$$N_{cr} = \pi^2 \left(EI \right)_{eff} / L_{eff}^{\ 2} \tag{6.6}$$

where $(EI)_{eff}$ represents the effective flexural rigidity of the composite section. The $(EI)_{eff}$ is calculated by Equation (6.7).

$$\left(EI \right)_{eff} = E_{a,o} I_{a,o} + k_e E_c I_c + E_{a,i} I_{a,i} \tag{6.7}$$

where $E_{a,o}$, E_c, and $E_{a,i}$ are the modulus of Elasticity of the outer tube, concrete infill and inner tube, respectively. $I_{a,o}$, I_c, and $I_{a,i}$ are the moment of inertia of the cross-section of the outer tube, concrete infill and inner tube, respectively. The symbol k_e denotes the correction factor for the concrete, which is taken as 0.6 according to Eurocode 4 (2004).

The ϕ is determined by Equation (6.8).

$$\phi = 0.5 \left[1 + \alpha_1 \left(\bar{\lambda} - \bar{\lambda_0} \right) + \bar{\lambda}^2 \right] \tag{6.8}$$

in which, α_1 is the imperfection factor and $\bar{\lambda}_0$ is the limit of horizontal plateau. The value of α_1 is taken equal to 0.34 which is suggested by Eurocode 4 (2004) for composite columns having a ratio of the cross-sectional area of the hollow tube over concrete infill greater than 3%. The value of $\bar{\lambda}_0$ is considered as 0.1 according to the recommendation provided by Eurocode 9 (2007) for Class A materials. It should be noted that in Eurocode 9 (2007) the aluminium alloys are categorized into two material classes, i.e., Class A and B and the 6082-T6 aluminium alloy used in this study is a Class A material. Figure 6.16 plots the test and FE ultimate load normalized by plastic capacity (i.e., N_u/N_{pl}) against the member slenderness $\bar{\lambda}$. Moreover, the proposed design

buckling curve considering the above-mentioned values of α_1 and $\bar{\lambda}_0$ is also presented in the same figure. From the figure, an anticipated decreasing trend of the normalised load can be observed with the increase of the member slenderness $\bar{\lambda}$. It can also be seen that most of the test and the FE data are above the buckling curve, which signifies that the proposed design curve is suitable for the design of CFDSAT columns providing safe capacity predictions.

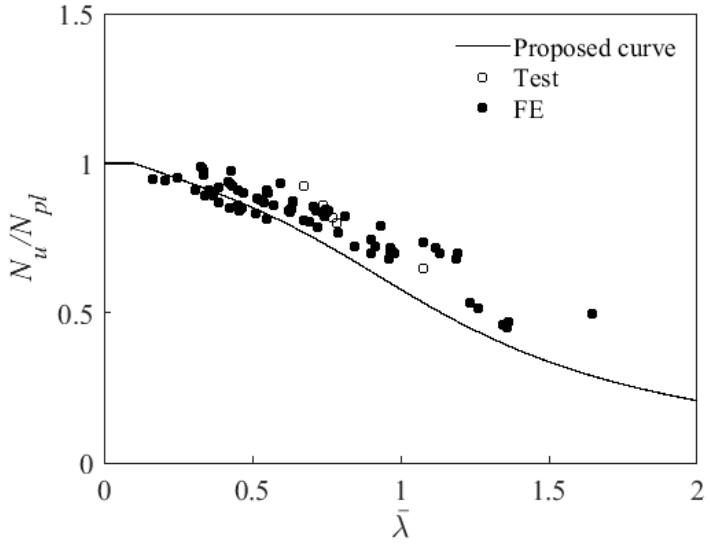

Figure 6.17: Proposed design buckling curve for CFDSAT columns.

6.6.2 Ultimate load prediction for CFDSAT columns

To evaluate the applicability of the proposed design methodology, the predicted ultimate load is compared with the corresponding ultimate load obtained from the test and FE analysis. Table 6.6 presents the ratios of test and FE ultimate load over the predicted design capacity ($N_u/N_{u,prop}$) along with the corresponding mean and COV values. The mean and COV values of $N_u/N_{u,prop}$ are 1.06 and 0.08, respectively, indicating that the proposed methodology is appropriate to predict the ultimate load of CFDSAT columns.

Table 6.6: Comparison of the design capacity with the corresponding test and FE ultimate load.

	Specimen	No	Class of outer section	Class of inner section	$N_u/N_{u,prop}$
Test	S50.8×3.2-S19.2×1.6	1	2	1	1.22
	S63.4×3.2-S19.2×1.6	1	2	1	1.20
	S63.4×3.2-S25.4×3.2	1	2	1	1.13
	S76.2×4.8-S19.2×1.6	1	3	1	1.16
	S76.2×4.8-S25.4×1.6	1	3	2	1.14
	S76.2×4.8-S25.4×3.2	1	2	1	1.17
	S63.4×3.2-C19.2×3.2	1	2	1	1.14
	S63.4×3.2-C25.4×3.2	1	2	1	1.14
				Mean	1.16
				COV	0.03
FE (mean)		81	1-4	1-4	1.05
				Mean (all)	1.06
				COV (all)	0.08

In Figure 6.17, the test and FE ultimate load are plotted against the predicted design capacity. It also illustrates the accuracy of the proposed methodology as most of the data in the figure are close to the diagonal line of $N_u = N_{u,prop}$. Overall, it can be concluded that the proposed design methodology can accurately predict the ultimate load of CFDSAT columns.

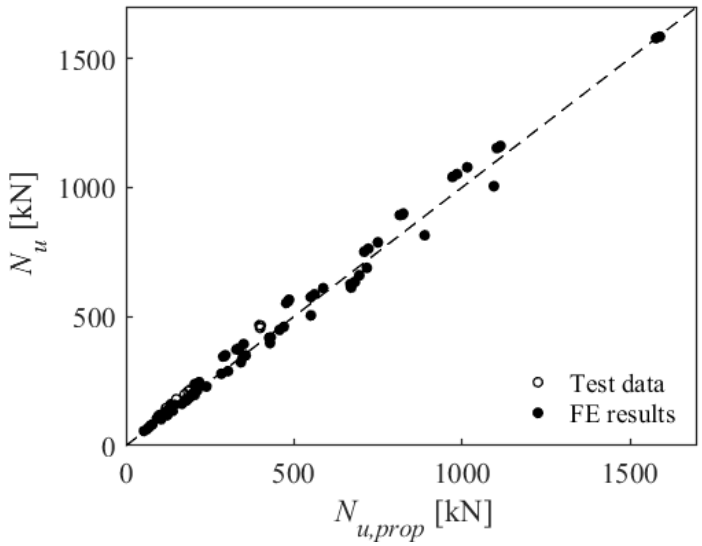

Figure 6.18: Comparison of the design capacity with the corresponding test and FE ultimate load.

6.7 Conclusions

This study reported experimental and numerical investigations on the flexural buckling behaviour of CFDSAT columns under axial compression. A total of 8 columns were tested and 81 columns were numerically modelled, considering two combinations of outer and inner cross-section shapes, i.e., square-square and square-circular, a wide range of cross-section slenderness, different member slenderness and concrete grades. Based on the observed results, the following points can be summarised:

- The predominant failure mode of all CFDSAT specimens was flexural buckling. No inward or outward local buckling was identified at the outer tube of any specimen. Overall, the concrete infill effectively prevented the occurrence of inward local buckling and delayed the formation of outward local buckling.
- The experimental axial load versus mid-height lateral displacement curves demonstrated good ductility of all CFDSAT specimens, attributing to the beneficial composite response of three elements of the CFDSAT cross-sections.
- It was shown that the developed FE model with a global imperfection amplitude of L_e/1000 accurately replicated the flexural buckling behaviour of CFDSAT columns. Hence, this model was adopted to conduct a numerical parametric study which included 81 specimens to investigate the effect of hollow ratio, member slenderness, cross-section slenderness of hollow tubes and concrete compressive strength on the ultimate load of CFDSAT specimens.
- The numerical parametric study results revealed that the cross-sectional dimensions of the outer tube, member slenderness and concrete compressive strength have significant influence on the ultimate load of CFDSAT columns. It was demonstrated that the larger cross-sectional dimensions of the outer tube and the higher concrete compressive strength substantially improved the load-carrying capacity of the composite members, while the load-carrying capacity reduced noticeably with the increase of member slenderness. However, the variation of cross-sectional dimensions of the inner tube has a slight effect on the ultimate load of the columns, as the inner tube provides the least buckling resistance among the three components of the composite cross-sections.

- In the absence of design standards for CFDSAT members, a design methodology is proposed with a design buckling curve to predict the ultimate load of CFDSAT columns according to the Eurocode 4 framework. It was shown that the proposed design methodology is appropriate for the design of CFDSAT columns as it accurately predicted the ultimate load of the composite columns.

CHAPTER 7 : CFDSAT MEMBERS IN BENDING

7.1 Introduction

This chapter presents experimental and numerical investigations on the flexural behaviour of CFDSAT members under in-plane bending. The failure modes, flexural strength and bending moment versus mid-span deflection curves obtained from the experiments are reported. FE models of the CFDSAT beams are developed and validated against the experimental results. The validated FE models are adopted to carry out a parametric study to examine the influence of cross-section slenderness of inner and outer tubes, hollow ratio, cross-section shape, composite action and concrete compressive strength on the flexural behaviour of CFDSAT beams. A design methodology based on the Eurocode 4 framework, is proposed to determine the flexural strength of square and circular CFDSAT members.

7.2 Experimental programme

7.2.1 Test specimens and material properties

A total of 10 CFDSAT members, including 3 specimens with square outer and inner tubes, 2 specimens with square outer and circular inner tubes and 5 specimens with circular outer and inner tubes, were tested under in-plane bending. The measured geometric dimensions of all specimens are reported in Table 7.1 in which D_o, B_o and t_o are the depth/diameter, width and thickness of outer tube, respectively and D_i, B_i and t_i are the depth/diameter, width and thickness of inner tube, respectively. The hollow tubes consisted of eight different cross-sections, of which four large sections were used for outer tube with measured depth/diameter to thickness ratio (D_o/t_o) ranging from 12.08 to 59.07 and four small sections were used for inner tube with measured depth/diameter to thickness ratio (D_i/t_i) varied from 6.04 to 24.22. The length of all specimens was 1000 mm. The distance between the two supports (L_s) was 900 mm. A labelleing system was considered for all specimens based on the key features of outer and inner cross-sections. For example, the label ‘S76.2×6.4-C38.2×1.6’ denotes a CFDSAT specimen with an outer tube of ‘S76.2×6.4’ and an inner tube of ‘C38.2×1.6’. The notation ‘S76.2×6.4’ shows that the section is square (‘S’) with nominal depth and width of 76.2 mm and thickness of 6.4 mm. ‘C38.2×1.6’ stands for a circular section (‘C’) with nominal diameter of 38.2 mm and thickness of 1.6 mm. The recorded values

of initial local geometric imperfection (ω_l) of all specimens are also listed in Table 7.1. Figure 7.1 presents photographs of the three different types of cross-sections of test specimens.

Table 7.1: Measured geometric dimensions of CFDSAT beams.

Specimen	D_o (mm)	B_o (mm)	t_o (mm)	D_o/t_o	D_i (mm)	B_i (mm)	t_i (mm)	D_i/t_i	ω_l
S76.2×6.4-S19.2×1.6	76.24	76.30	6.31	12.08	19.07	19.07	1.60	11.92	0.18
S76.2×6.4-S25.4×3.2	76.23	76.30	6.26	12.18	25.39	25.39	3.24	7.84	0.14
S76.2×4.8-S25.4×3.2	76.10	76.30	4.57	16.65	25.39	25.39	3.24	7.84	0.08
S76.2×6.4-C25.4×3.2	76.17	76.30	6.22	12.25	25.41	-	3.36	7.56	0.12
S76.2×6.4-C38.2×1.6	76.20	76.30	6.29	12.11	38.03	-	1.64	23.19	0.18
C88.6×1.6-C19.2×3.2	88.69	-	1.55	57.22	18.86	-	3.12	6.04	0.11
C88.6×1.6-C25.4×3.2	88.66	-	1.60	55.41	25.41	-	3.39	7.50	0.17
C88.6×1.6-C38.2×1.6	88.61	-	1.50	59.07	38.03	-	1.57	24.22	0.30
C76.2×3.2-C25.4×3.2	76.15	-	3.22	23.65	25.36	-	3.34	7.59	0.14
C76.2×3.2-C38.2×1.6	76.19	-	3.31	23.02	38.00	-	1.59	23.90	0.44

(a) CFDSAT specimen with square outer and inner tubes

(b) CFDSAT specimen with square outer and circular inner tubes

(c) CFDSAT specimen with circular outer and inner tubes

Figure 7.1: Photographs of typical cross-sections of CFDSAT specimens.

The measured material properties of the aluminium alloy are listed in Table 7.2. It should be noted that the CFDSAT columns and beams are cast from the same batch of concrete mix. Hence, the compressive strength of concrete cubes presented in Table 6.3

in the previous chapter is used herein. Typical failure patterns of tensile coupons and typical stress-strain curves along with the corresponding Ramberg-Osgood curves of the S25.4×3.2 and C19.2×3.2 material coupons are presented in Figure 7.2.

Table 7.2: Tensile coupon test results.

Specimen	E (GPa)	$f_{0.1}$ (MPa)	$f_{0.2}$ (MPa)	f_u (MPa)	ε_u (%) (mm/mm)	ε_f (%) (mm/mm)	n
S19.2×1.6	72500	185	189	215	4.57	5.45	28.83
S25.4×3.2	70000	276	283	328	7.66	16.00	28.06
S76.2×4.8	70700	305	311	338	5.97	11.70	33.91
S76.2×6.4	68400	293	298	329	7.62	18.00	34.80
C25.4×3.2	71900	283	289	327	8.50	13.00	29.58
C19.2×3.2	72800	303	306	320	5.18	8.94	36.53
C38.2×1.6	72700	289	295	311	4.40	7.22	35.48
C76.2×3.2	69500	264	270	313	7.87	13.30	28.92
C88.6×1.6	68300	199	203	233	6.98	12.40	29.02

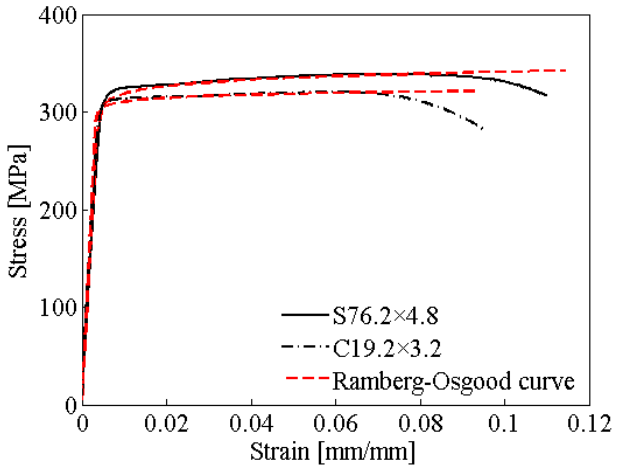

(a) (b)

Figure 7.2: (a) Typical failure modes of tensile coupons, (b) Experimental and respective Ramberg-Osgood stress-strain curves of S76.2×4.8 and C19.2×3.2 material coupons.

7.2.2 Four-point bending tests

The CFDSAT specimens were tested in four-point bending arrangement. The shear span over depth ratio of all specimens was greater than 0.5 to avoid shear failure of the specimens (Xu *et al.*, 2009). At the loading points, steel plates were employed for the

square specimens and half-circle steel blocks were used for the circular specimens to avoid any localised failure due to load concentration (Wang *et al.*, 2021). During the tests, three 50 mm-stroke linear variable displacement transducers (LVDTs) were applied to record the vertical movement of the specimens, among them one was placed at mid-length and two were positioned under the loading points. At the mid-length of the top and bottom flanges, two strain gauges were used to measure the compressive and tensile strains of the specimens. Figure 7.3 presents photographs of the experimental set-up.

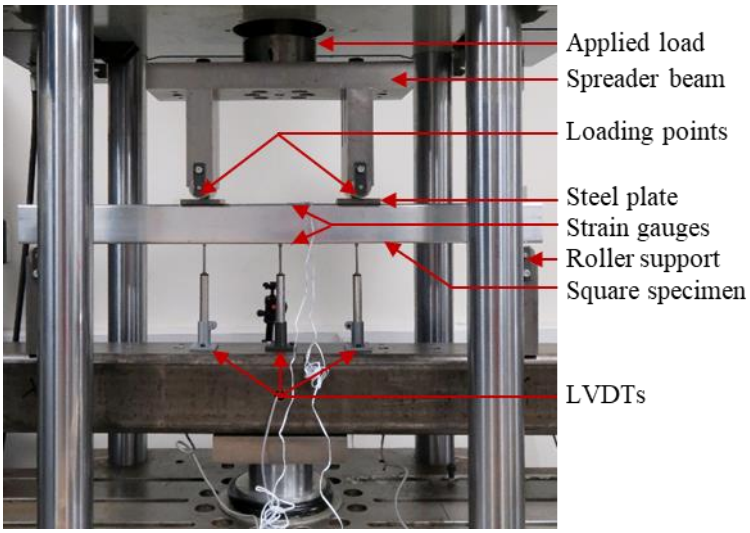

(a) Square CFDSAT specimen test set-up

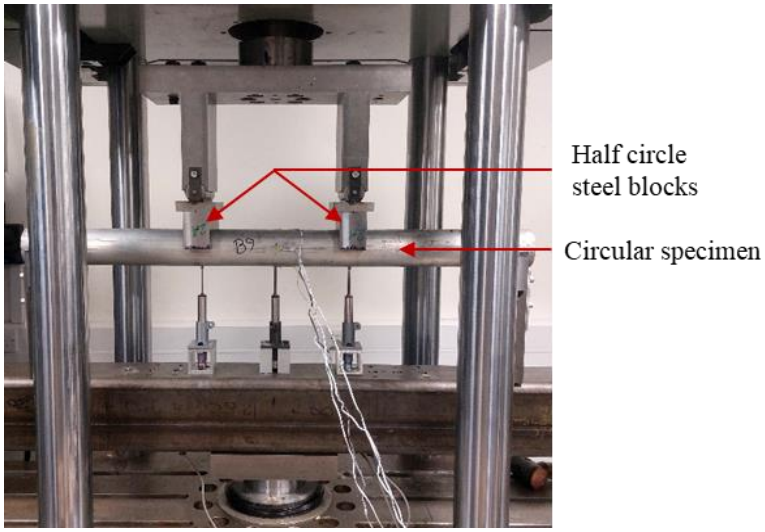

(b) Circular CFDSAT specimen test set-up

Figure 7.3: Photographs of the experimental set-up.

7.3 Experimental observations

7.3.1 Failure mode

Typical failure modes of CFDSAT specimens observed from the bending tests are presented in Figures 7.4 and 7.5 and reported in Table 7.3. The predominant observed failure mode was yielding (Figure 7.4(a)). Besides yielding, some circular specimens, i.e., C88.6×1.6-C19.2×3.2, C88.6×1.6-C25.4×3.2 and C88.6×1.6-C38.2×1.6 experienced small outward local buckling at the top face of the outer tube within the two loading points (Figure 7.4(b)). The local buckling appeared when the outer tube exceeded its yield strain. However, no inward bulging was observed at the outer tube of any specimen which is attributed to the infilled concrete that efficiently delayed the occurrence of outward buckling and prevented the formation of inward buckling. Moreover, in some circular specimens, i.e., C88.6×1.6-C19.2×3.2, C88.6×1.6-C25.4×3.2 and C88.6×1.6-C38.2×1.6, fracture of the outer tube was noticed at the tension side after they reached their flexural capacity (Figure 7.5(a)).

To investigate the failure pattern of the concrete infill and the inner profile, the outer profile and concrete infill were partly removed after the bending test. Figures 7.4(c) and 7.5(b) illustrate the failure pattern of the inner tube and concrete infill of a typical specimen, respectively. It can be found from Figure 7.4(c) that similarly to the outer tube the inner tube exhibited obvious bending deformation. However, no tensile fracture or local buckling was noticed at the inner tube of the examined specimens. Figure 7.5(b) shows that a number of flexural cracks occurred parallelly in the tension region of concrete along the moment span. The cracks developed uniformly and propagated from tension to the compression region. In the moment span, no diagonal crack of concrete is noticed, which indicates that shear force was not developed during the tests.

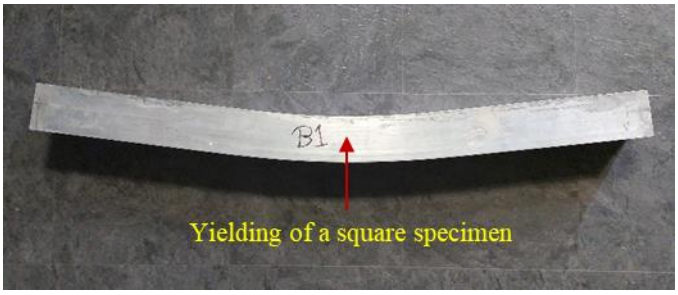

(a) S76.2×6.4-S25.4×3.2

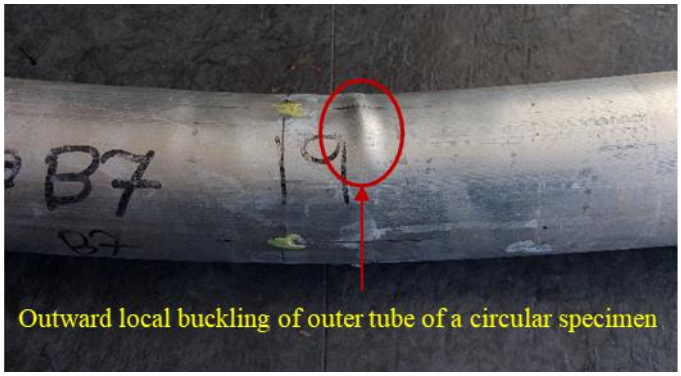

(b) C88.6×1.6-C25.4×3.2

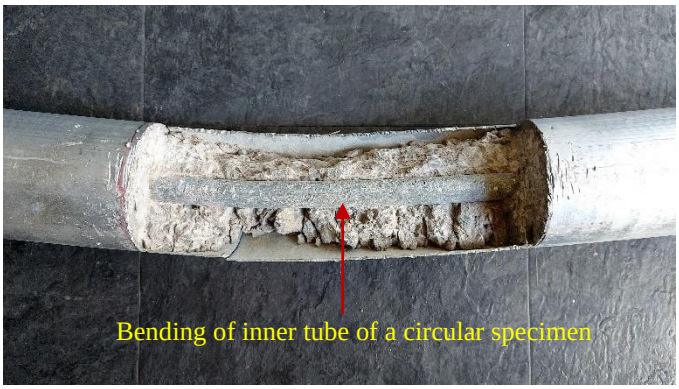

(c) C88.6×1.6-C19.2×3.2

Figure 7.4: Typical failure modes: (a) yielding of a square specimen, (b) local outward buckling of the outer tube of a circular specimen, (c) bending of the inner tube of a circular specimen.

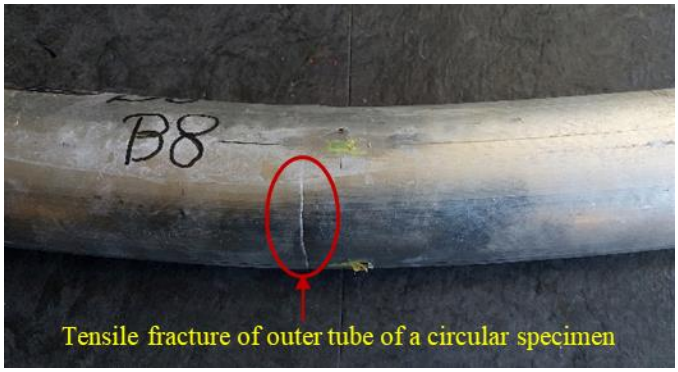

(a) C88.6×1.6-C38.2×1.6

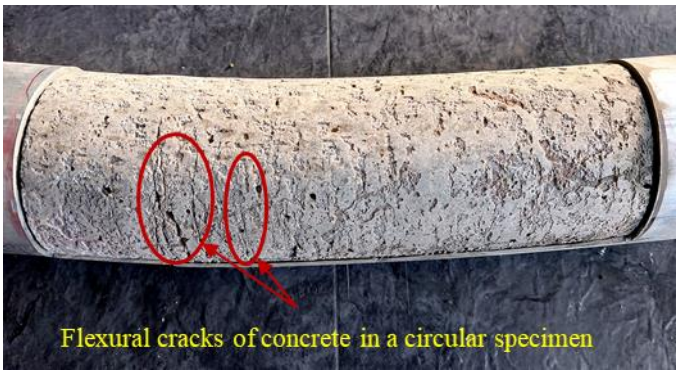

(b) C88.6×1.6-C19.2×3.2

Figure 7.5: (a) tensile fracture of the outer tube of a circular specimen, (b) flexural cracks of concrete in a circular specimen.

Table 7.3: Failure modes, flexural strength and ductility of CFDSAT specimens.

Specimen	Failure mode	$M_{u,Test}$ (kNm)	μ
S76.2×6.4-S19.2×1.6	Y	17.37	4.80
S76.2×6.4-S25.4×3.2	Y	18.35	4.96
S76.2×4.8-S25.4×3.2	Y	14.88	4.81
S76.2×6.4-C25.4×3.2	Y	18.18	5.03
S76.2×6.4-C38.2×1.6	Y	18.25	5.45
C88.6×1.6-C19.2×3.2	Y+LB+TF	4.74	6.86
C88.6×1.6-C25.4×3.2	Y+LB+TF	5.02	7.79
C88.6×1.6-C38.2×1.6	Y+LB+TF	4.84	5.87
C76.2×3.2-C25.4×3.2	Y	7.62	6.32
C76.2×3.2-C38.2×1.6	Y	7.71	6.34
Note: Y = Yielding, LB =Local buckling of outer tube, TF = Tensile fracture			

7.3.2 Bending moment versus mid-span deflection/strain curve

A typical bending moment versus mid-span deflection/longitudinal strain curve of the specimens is shown in Figure 7.6 indicating different stages appeared during the test.

The deflection and longitudinal strain data recorded from the LVDT and strain gauge positioned at the mid-span of the bottom flange were used for the curve. Note that the locations of initiation of the tensile cracks in concrete infill and outward local buckling of outer tube in the curve were identified using FE analysis (FEA) (Figures 7.6(b) and (c)). The yielding point of the aluminium alloy is indicated by the yield strain measured during the tensile test of the respective coupons. The bending moment of all the specimens was determined using Equation (5.1) presented in Chapter 5.

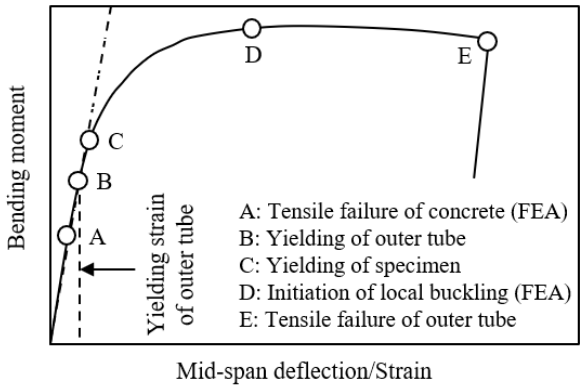

(a) Typical bending moment versus mid-span deflection/longitudinal strain curve

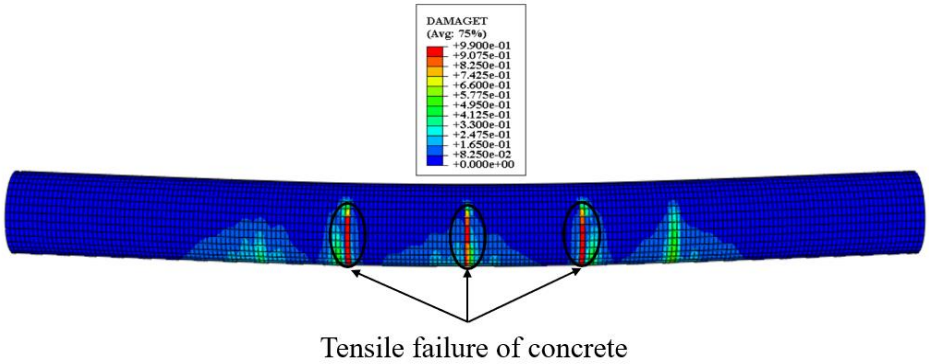

(b) Point A: Tensile failure of concrete

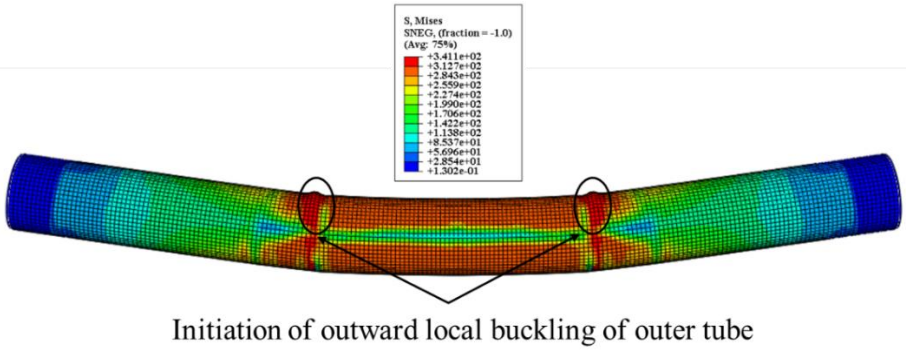

(c) Point C: Initiation of local buckling of outer tube

Figure 7.6: Typical bending moment versus mid-span deflection/longitudinal strain curve indicating different stages appeared during the test shown with the FE models.

Figure 7.7 presents the bending moment versus mid-span deflection/bottom longitudinal strain curves of all specimens. The figure illustrates that initially all curves exhibit a linear relationship between mid-span deflection/longitudinal strain and bending moment, indicating that the material of CFDSAT sections was in the elastic stage. At this stage, the cracks of concrete infill appear at the tensile region and the aluminium alloy starts to yield when the moment reaches points A and B, respectively. After this stage, the curves deviate from the initial linearity and start to exhibit nonlinear behaviour as they enter the elastic-plastic stage. At the plastic stage, the curves of all specimens show an almost flat yield plateau with increasing displacement. In this region, specimens C88.6×1.6-C19.2×3.2, C88.6×1.6-C25.4×3.2 and C88.6×1.6-C38.2×1.6 experienced outward local buckling at the outer tubes as they fall in Class 4 category according to Eurocode 9 (2007). Point C shows the location in the curve where the local buckling starts to appear. It can be observed that the small outward local buckling appeared at the plastic stage before the bending moment reached the flexural strength of these specimens. However, the effect of local buckling was minimised as the concrete infill restrained the formation of inward buckling and delayed the development of outward buckling. Moreover, at this stage, these specimens failed due to tensile fracture of the outer tube which is indicated by point D. No softening branch or sudden drop appears in the curve of other specimens in the plastic region. In these cases, the tests were terminated at a large vertical displacement of 60 mm (i.e., L_s/15) and the recorded bending moment at that displacement was taken as the flexural strength of the corresponding specimens. It can be observed from Figure 7.7 that all CFDSAT specimens demonstrated good ductile response which is attributed to the beneficial composite behaviour of the three components of the CFDSAT sections. The flexural strength ($M_{u,Test}$) and ductility of all test specimens are reported in Table 7.3. It can be observed from this table that the flexural strength of CFDSAT specimens increased significantly with the increase of thickness of the outer tube when the inner tube dimensions remain the same. For example, the flexural strength of specimen S76.2×6.4-S25.4×3.2 enhanced by 23.3% compared to specimen S76.2×4.8-S25.4×3.2 as the thickness of the outer tube of the former one increased from 4.8 mm to 6.4 mm. Moreover, it is also noticed that the flexural strength of CFDSAT specimens improved due to the increase of dimensions of the inner tube when the outer tube dimensions are constant, however, the enhancement is not prominent. For example, when the outer diameter of the inner tube increased from 19.2 mm to 25.4 mm, the flexural strength of

specimen C88.6×1.6-C19.2×3.2 improved moderately, i.e., around 5% compared to the strength of specimen C88.6×1.6-C25.4×3.2. The effect of cross-sectional dimensions of the outer and inner tubes on the flexural capacity of CFDSAT specimens is further investigated by FE analyses and discussed in the following section.

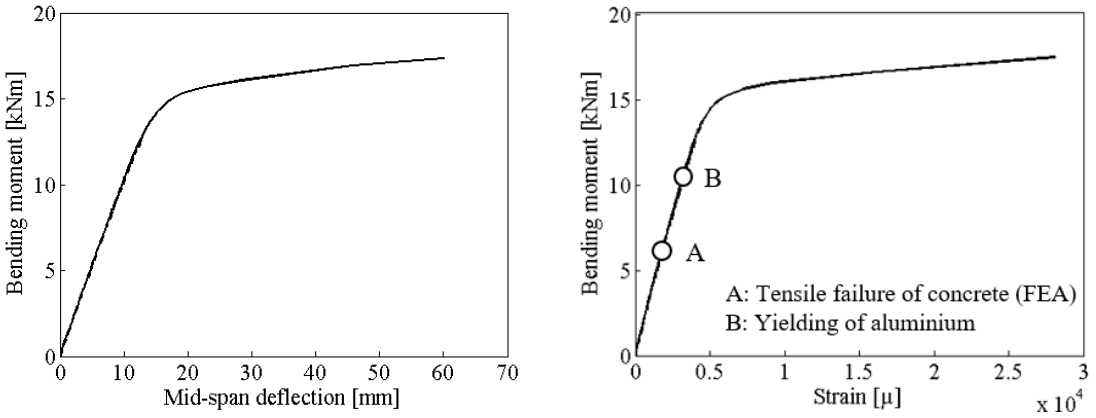

(a) 76.2×6.4-S19.2×1.6

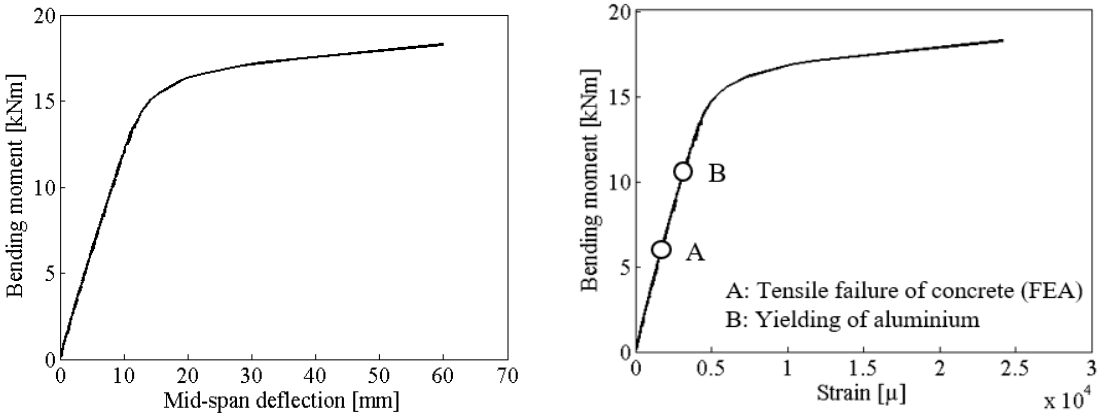

(b) S76.2×6.4-S25.4×3.2

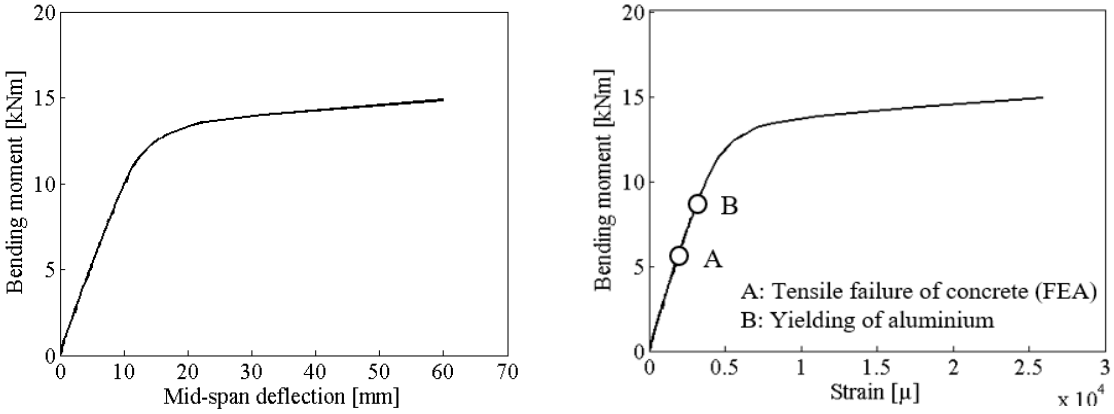

(c) S76.2×4.8-S25.4×3.2

Figure 7.7: Bending moment versus mid-span deflection/longitudinal strain curves of CFDSAT specimens indicating different stages.

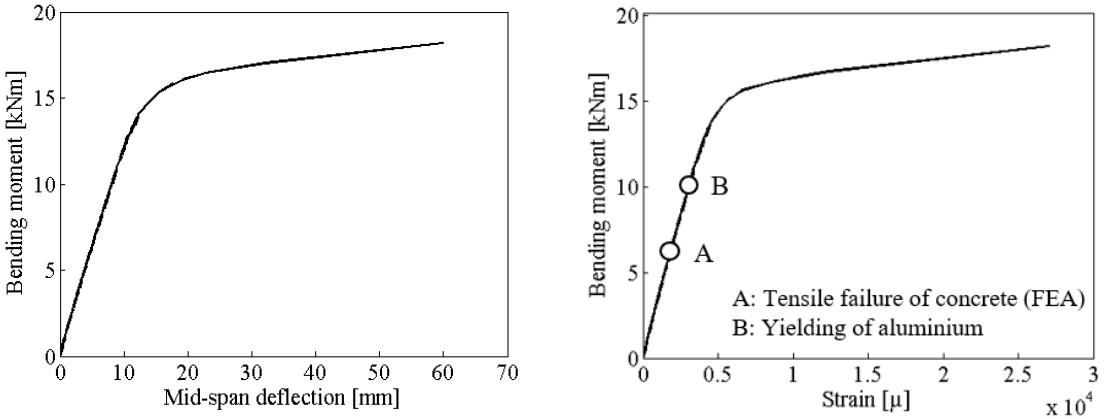

(d) S76.2×6.4-C25.4×3.2

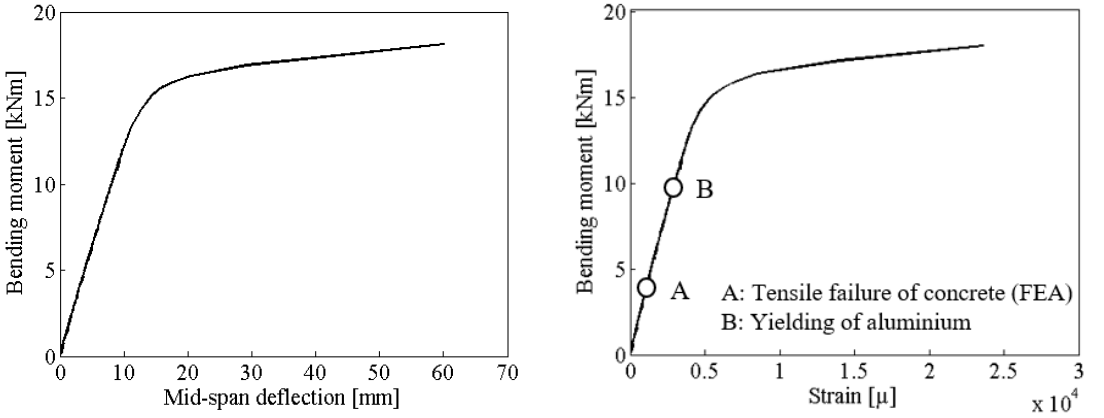

(e) S76.2×6.4-C38.2×1.6

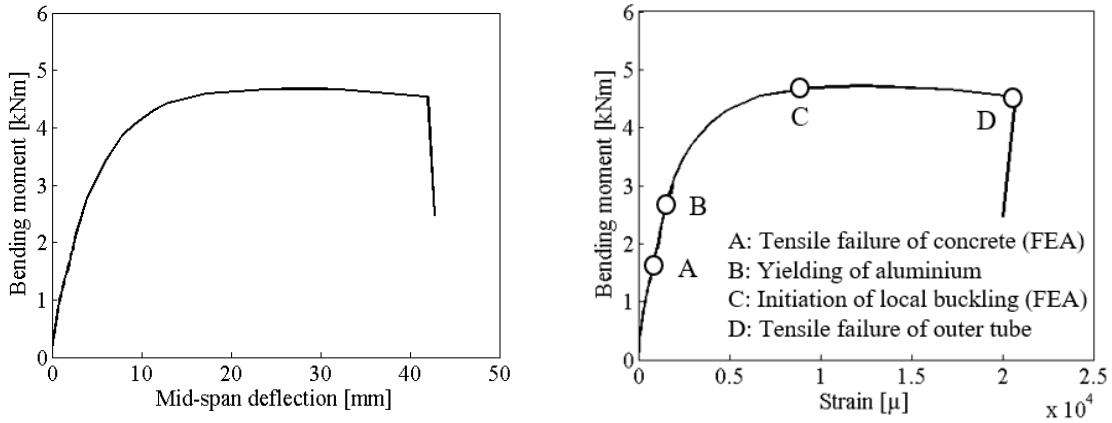

(f) C88.6×1.6-C19.2×3.2

Figure 7.8 (continued): Bending moment versus mid-span deflection/longitudinal strain curves of CFDSAT specimens indicating different stages.

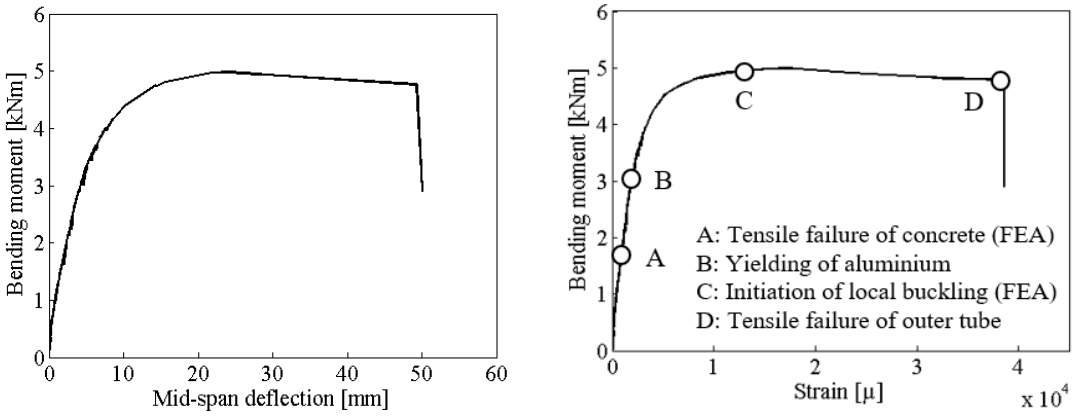

(g) C88.6×1.6-C25.4×3.2

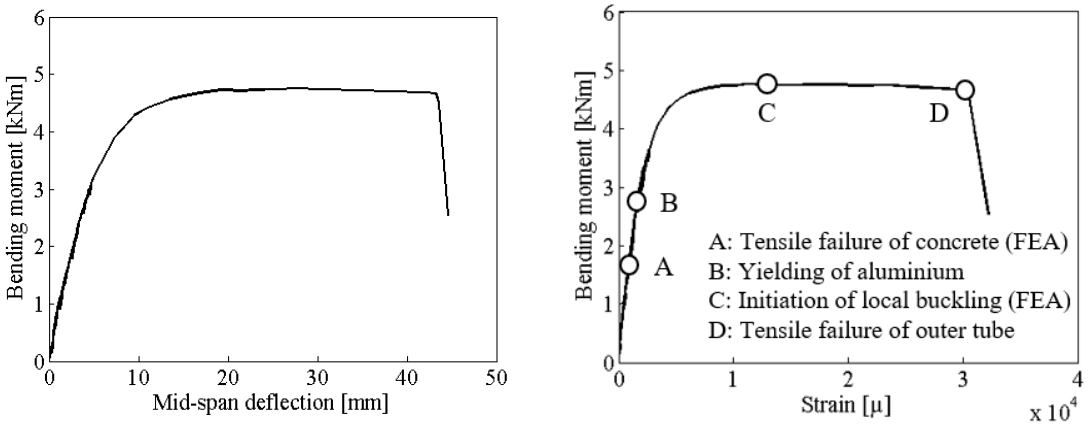

(h) C88.6×1.6-C38.2×1.6

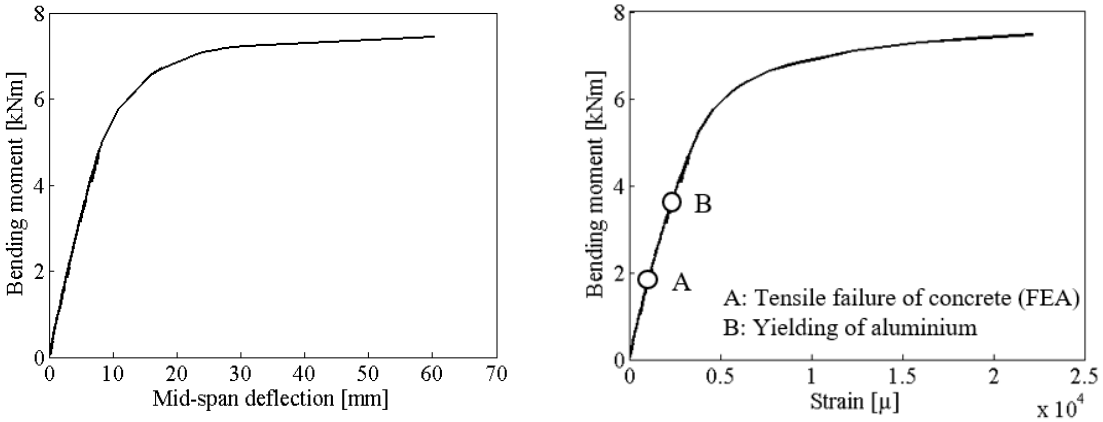

(i) C76.2×3.2-C25.4×3.2

Figure 7.9 (continued): Bending moment versus mid-span deflection/longitudinal strain curves of CFDSAT specimens indicating different stages.

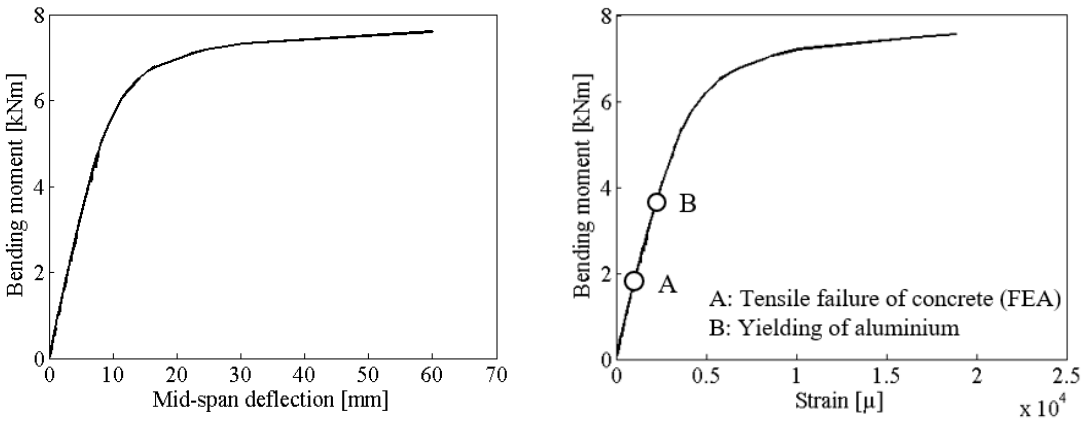

(j) C76.2×3.2-C38.2×1.6

Figure 7.10 (continued): Bending moment versus mid-span deflection/longitudinal strain curves of CFDSAT specimens indicating different stages.

7.4 Numerical investigation

7.4.1 FE modelling

FE models were developed utilizing the measured geometric dimensions and material proprieties listed in Tables 7.1, 7.2 and 6.3 (Chapter 6). The outer and inner tubes were modelled using 4-node shell elements (S4R) and the concrete infill was simulated considering 8-node solid elements (C3D8R). Based on the mesh sensitivity study result presented in Chapter 4, 5 mm element size was used to discretize the models. The elastic and plastic behaviours of aluminium alloy tubes and concrete were simulated by following the procedure discussed in Chapter 3. The interaction between the aluminium hollow sections and concrete infill was considered using surface-to-surface contact in ABAQUS. The initial local geometric imperfection has no considerable influence on the flexural behaviour of concrete-filled double skin metal sections because of the existence of concrete infill (Wang *et al.*, 2021). Therefore, the influence of initial local geometric imperfection was not taken into account in the FE analyses. The pinned support conditions were modelled by considering rotation around the bending axis (X direction) and translation in the longitudinal direction of the beam (Z direction). The load was applied along the vertical direction (Y direction) at the loading points using the displacement control technique. Figure 7.8 presents the geometry, boundary and loading conditions of a typical FE model.

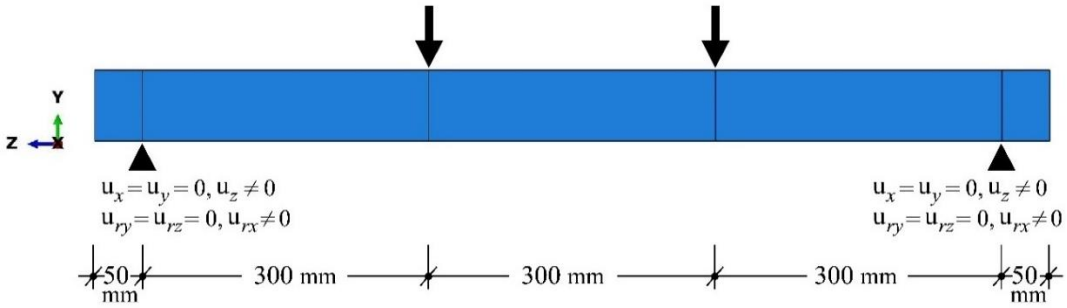

(a)

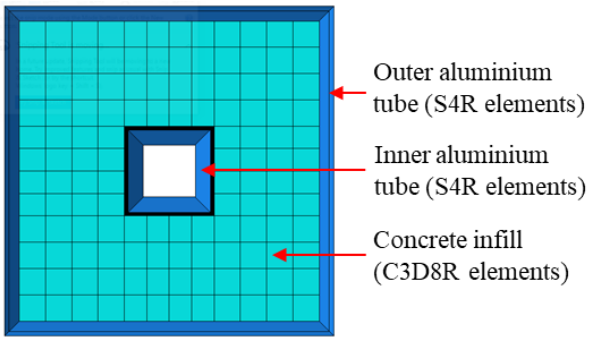

(b)

Figure 7.11: FE model: (a) boundary conditions at supports and loading direction, (b) cross-section.

7.4.2 FE model validation

FE model was validated by comparing the FE flexural strength, bending moment versus mid-span deflection relationship and failure modes with the corresponding results obtained from the experiments. Table 7.4 presents the ratios of the flexural strength of all specimens obtained from the FE analyses over the corresponding ones from the bending tests ($M_{u,FE}/M_{u,Test}$). It is found that the developed FE model correctly determines the flexural capacity of the CFDSAT specimens with mean and coefficient of variation (COV) of $M_{u,FE}/M_{u,Test}$ equal to 1.01 and 0.05, respectively. In Figure 7.9, FE and experimental bending moment versus mid-span deflection curves are compared for two typical specimens, where good agreement is observed between the curves. Figure 7.10 illustrates the comparison of failure modes of some specimens observed from the bending tests and FE analyses, again showing accurate replication of the deformation profile and failure modes of CFDSAT specimens. The failure modes and bending moment versus mid-span deflection curves of all specimens are provided in Figure A.6 in Appendix A and Figure B.6 in Appendix B, respectively. On the basis of

the above observations, it can be concluded that the developed FE models can accurately capture the structural response of CFDSAT beams.

Table 7.4: Comparison of the FE flexural strength with the corresponding test flexural strength.

Specimen	$M_{u,FE}/M_{u,Test}$
S76.2×6.4-S19.2×1.6	0.98
S76.2×6.4-S25.4×3.2	0.95
S76.2×4.8-S25.4×3.2	0.96
S76.2×6.4-C25.4×3.2	0.94
S76.2×6.4-C38.2×1.6	0.99
C88.6×1.6-C19.2×3.2	1.04
C88.6×1.6-C25.4×3.2	1.06
C88.6×1.6-C38.2×1.6	1.09
C76.2×3.2-C25.4×3.2	1.01
C76.2×3.2-C38.2×1.6	1.05
Mean	1.01
COV	0.05

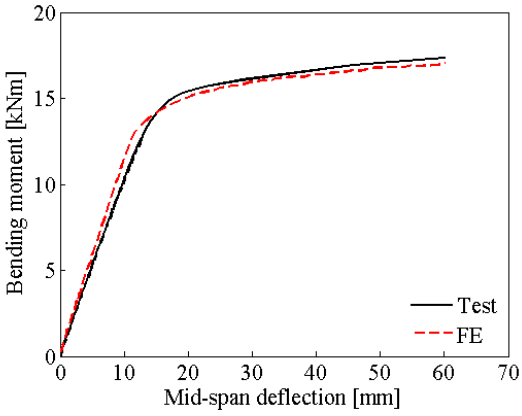

(a) S76.2×6.4-S19.2×1.6

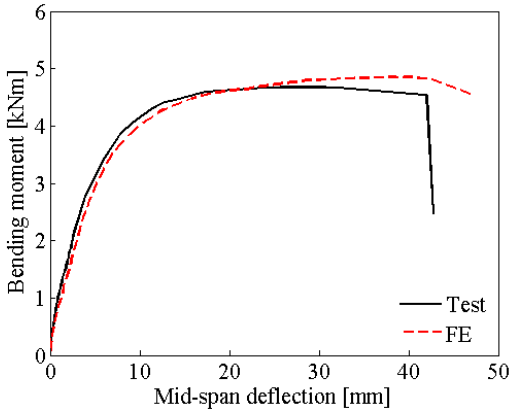

(b) C88.6×1.6-C19.2×3.2

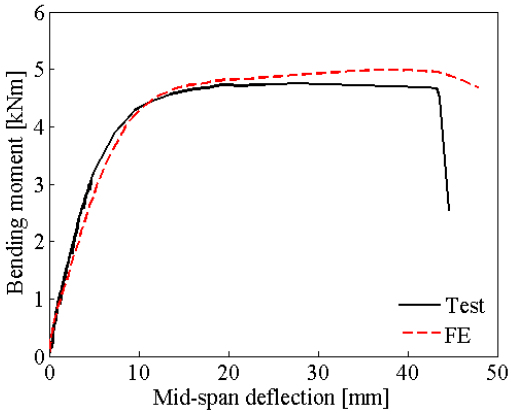

(c) C88.6×1.6-C38.2×1.6

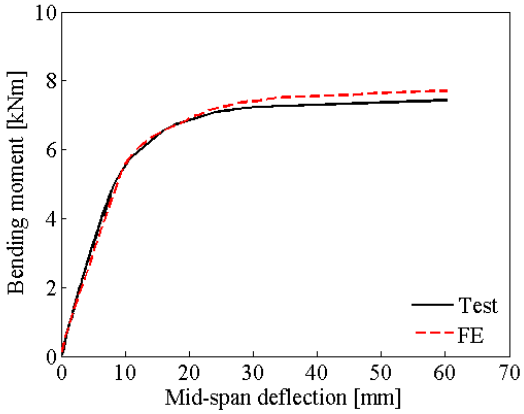

(d) C76.2×3.2-C25.4×3.2

Figure 7.12: Comparison of test and FE bending moment-midspan deflection curves.

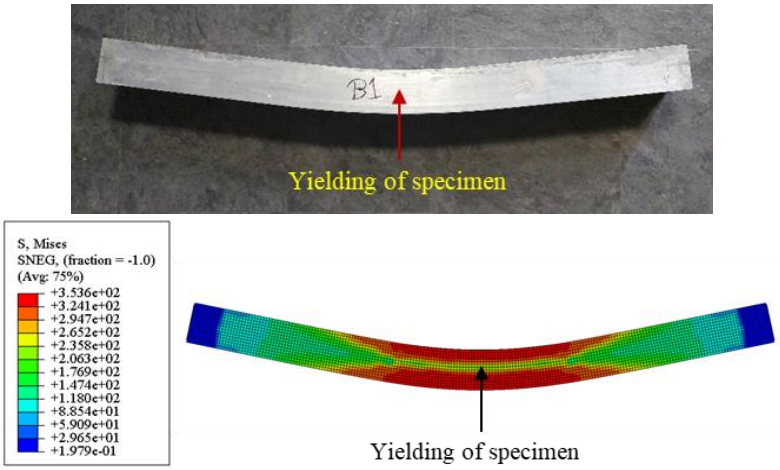

(a) S76.2×6.4-S19.2×1.6

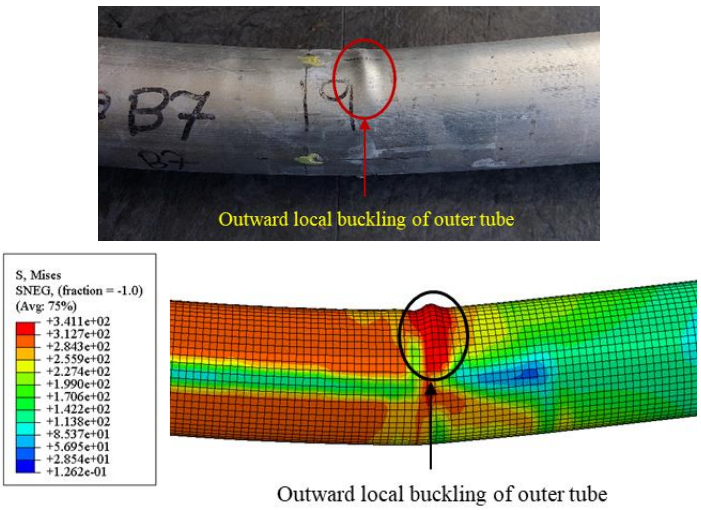

(b) C88.6×1.6-C25.4×3.2

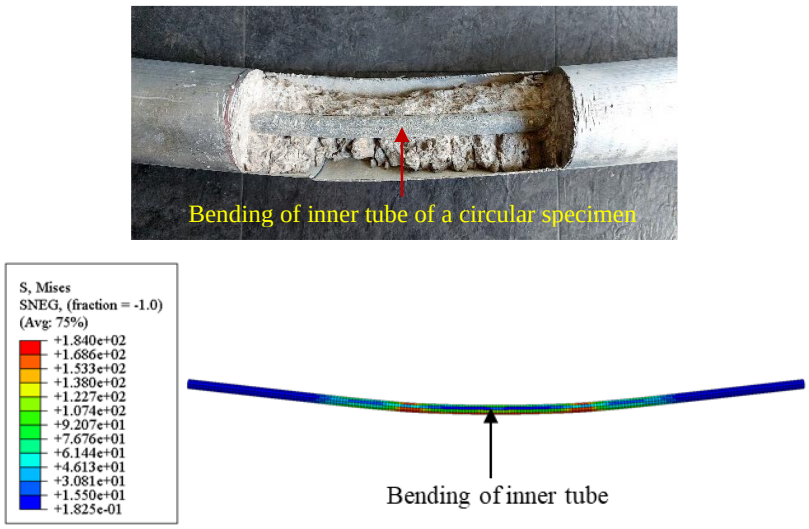

(c) C88.6×1.6-C19.2×3.2

Figure 7.13: Comparison of test and FE failure modes.

7.4.3 Parametric study

The validated FE model was adopted to conduct a parametric study for examining the influence of hollow ratio, cross-section slenderness of the outer and inner sections, concrete strength, cross-section shape and confinement effect on the flexural behaviour of CFDSAT specimens. The average material properties found from flat and curved coupons were used for square and circular aluminium tubes, respectively. In total 94 CFDSAT specimens were modelled, considering different combinations of outer and inner cross-section shapes, i.e., square-square, square-circular, circular-circular and circular-square. Outer tubes with cross-sectional dimensions of 60×60, 75×75, 100×100 and 120×120 mm^2 for square sections and diameters of 60, 75, 100 and 120 mm for circular sections were considered with wall thicknesses varied from 1 to 8 mm. Inner tubes with cross-sectional dimensions of 20×20, 25×25, 30×30 and 35×35 mm^2 for square sections and diameters of 20, 25, 30 and 35 mm for circular sections were considered with wall thicknesses ranging from 1 to 5 mm. Three different concrete cube compressive strengths of 30, 40 and 50 MPa were considered in this study. The geometric dimensions and the flexural strength of the specimens considered in this parametric study are reported in Appendix C, Table C.4.

7.5 Numerical observations

7.5.1 Effect of hollow ratio

The influence of hollow ratio on the flexural behaviour CFDSAT specimen was investigated by changing the depth/diameter of inner and outer tube. The hollow ratio is determined by Equation (6.1) of Chapter 6. Hollow ratios (α) varying from 0.17 to 0.80 were considered for both square and circular CFDSAT specimens. Figure 7.11 presents the effect of α on the bending moment versus midspan deflection curves of typical CFDSAT specimens. From Figure 7.11(a) it is found that the flexural strength of the specimen S75×4-S20×1 having α=30 increased by 62.9% compared to the specimen S60×4-S20×1 having α=38. Similarly, the increment is 89.9% for specimen S100×4-S20×1 having α=22 than specimen S75×4-S20×1 having α=30. It indicates that the flexural strength of CFDSAT specimens remarkably increased with the decrease of α (i.e., increase of depth/diameter of outer tube), which mirrors the test observation. This can be attributed to the fact the larger depth/diameter of outer tube offers higher moment of inertia of the outer tube as well as larger concrete area, which lead to the

enhancement of the bending capacity. The flexural strength of CFDSAT specimens also improved with the increase of inner tube depth/diameter by maintaining same outer tube (i.e., increase of α) (Figure 7.11(b)). From Figure 7.11(b) it can be seen that the flexural strengths of the specimens C100×8-C20×1 (α=24), C100×8-C25×1 (α=30) and C100×8-C30×1 (α=34) are 24.53 kNm, 24.61 kNm and 24.84 kNm, respectively. It indicates that the improvement is not prominent which is less than 1%. This finding matches the experimental observation. This is because the influence of inner tube is less on the overall flexural strength of CFDSAT specimens. This is demonstrated for typical specimens in Figures 7.12(a) and (b), where the moment contribution of each of the three sections (outer and inner aluminium tubes and concrete infill) is presented, showing a smaller contribution of the inner tube compared to the outer one and concrete infill. A similar observation is presented in a previous study on the structural response of CFDSST beams (Wang *et al.*, 2021).

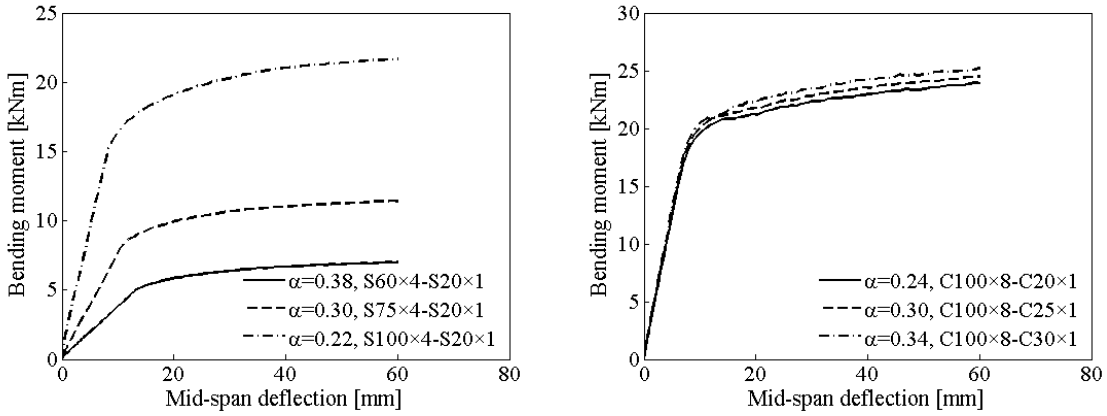

(a) Square CFDSAT specimens - constant inner tube (S20×1)

(b) Circular CFDSAT specimens - constant outer tube (C100×8)

Figure 7.14: Effect of hollow ratio on the bending moment-midspan deflection curves of typical CFDSAT specimens.

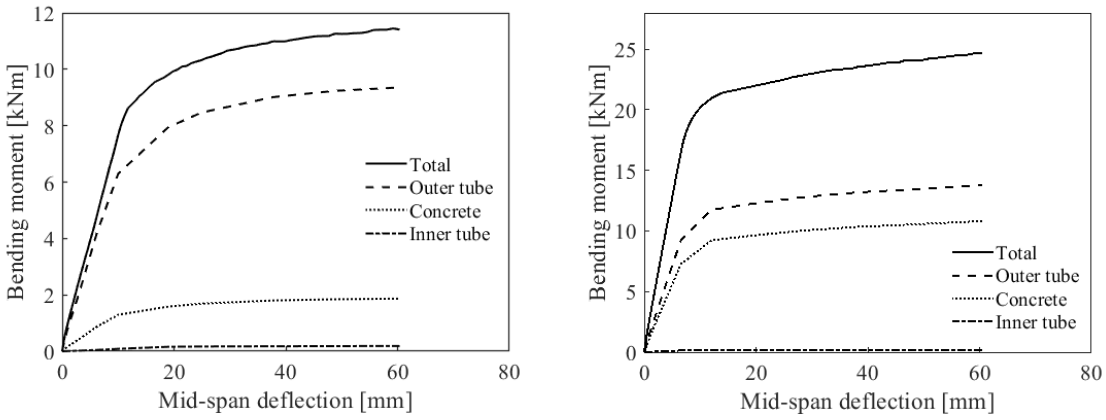

(a) S75×4-S20×1 (b) C100×8-C20×1

Figure 7.15: Moment contribution of outer tube, concrete infill and inner tube of typical CFDSAT specimens.

7.5.2 Effect of depth to thickness ratio of the outer tube

Figure 7.13 presents the effect of depth/diameter to thickness ratio of the outer tube (D_o/t_o) on the bending moment versus midspan deflection curves of typical CFDSAT beams. D_o/t_o values ranging from 7.5 to 120 for both square and circular sections were considered by altering the thickness of the outer tube. It can be observed from the figure that the D_o/t_o ratio has considerable influence on the flexural strength of CFDSAT specimens as decreasing D_o/t_o ratio noticeably increased the flexural strength of the specimens. For example, the flexural strength of the specimen S75×4-S20×1 improved by 159.6% compared to the specimen S75×1.5-S20×1 as the thickness of the outer tube of the former specimen is increased from 1.5 mm to 4 mm. Similarly when the thickness of the outer tube of this specimen is increased from 4 mm to 8 mm, the ultimate capacity is increased by 73.1%. This can be attributed to the fact that by decreasing D_o/t_o ratio (i.e., larger thickness) the moment of inertia of the outer section increases, enhancing the overall flexural resistance of the specimens.

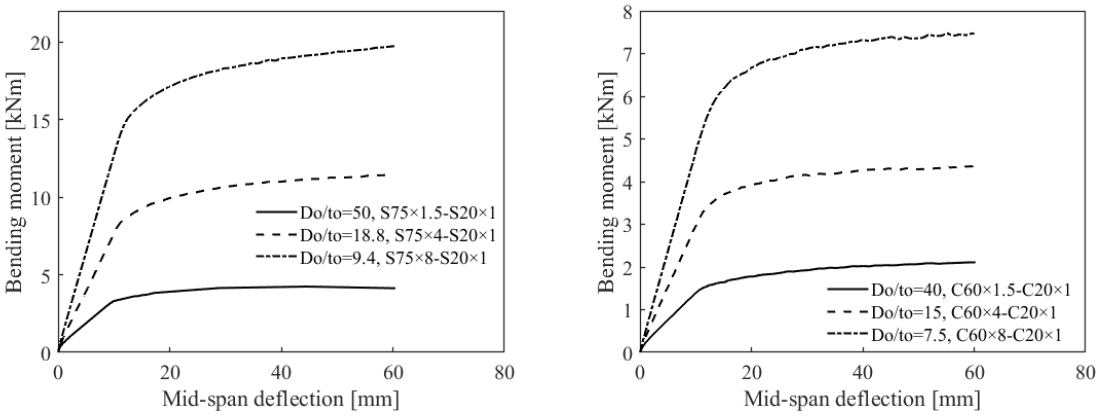

(a) Square CFDSAT specimens (b) Circular CFDSAT specimens

Figure 7.16: Effect of D_o/t_o ratio on the bending moment-midspan deflection curves of typical CFDSAT specimens.

7.5.3 Effect of depth/diameter to thickness ratio of the inner tube

The effect of depth/diameter to thickness ratio of the inner tube (D_i/t_i) on the flexural behaviour of CFDSAT specimens is presented in Figure 7.14. The D_i/t_i ratio varied from 4 to 35 and this was achieved by changing the thickness of the inner section of square and circular specimens. Figure 7.14 illustrates that by decreasing the D_i/t_i ratio the flexural strength of the CFDSAT specimens enhanced slightly. For example, the flexural strength of specimen C75×4-C20×1 increased by 1.5% and 2.4%, respectively when the D_i/t_i ratio decreased from 20 (for t = 1 mm) to 10 (for t = 2 mm) and 4 (for t = 5 mm). This is because the inner tube provides the least bending resistance among the three components of CFDSAT specimens (Figure 7.12(a) and (b)).

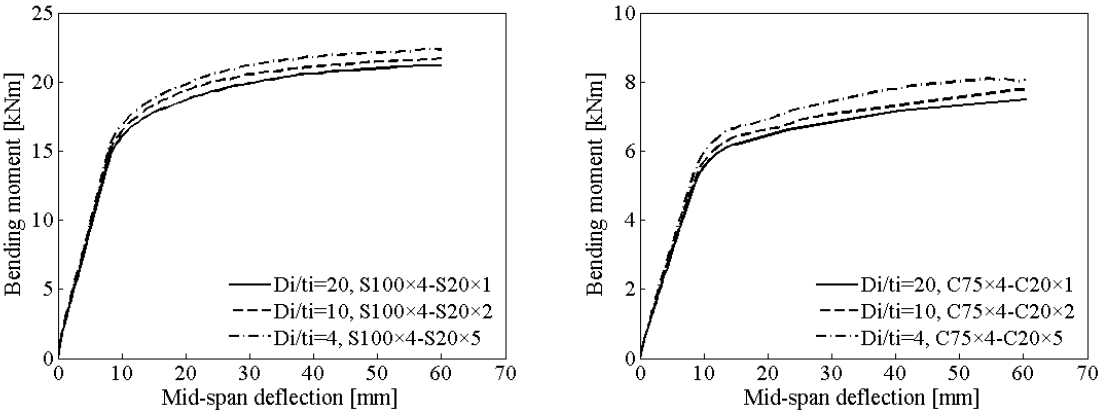

(a) Square CFDSAT specimens (b) Circular CFDSAT specimens

Figure 7.17: Effect of D_i/t_i ratio on the bending moment-midspan deflection curves.

7.5.4 Effect of concrete compressive strength

To investigate the effect of the concrete grade on the flexural strength of CFDSAT specimens, three different concrete cube compressive strengths (f_{cu}), i.e., 30, 40 and 50 MPa, were considered in the parametric study. Figure 7.15 shows the effect of the concrete grade on the bending moment versus midspan deflection curves of typical CFDSAT specimens. It is found from the figure that by increasing the concrete strength, the flexural strength of the specimens increased very moderately. For example, it can be seen from Figure 7.15(a) and (b) that the flexural strength of specimen S120×1-C20×1 and C120×1-S20×1 improved by 2.3% and 4.9%, respectively when concrete strength is increased from 30 MPa to 50 MPa. This is related to the fact that under in-plane bending the concrete beneath the neutral axis is in tension and the higher concrete grade offers minor contribution to the enhancement of the tensile strength of concrete. Therefore, increasing concrete strength has less influence on the improvement of flexural strength of the CFDSAT specimens.

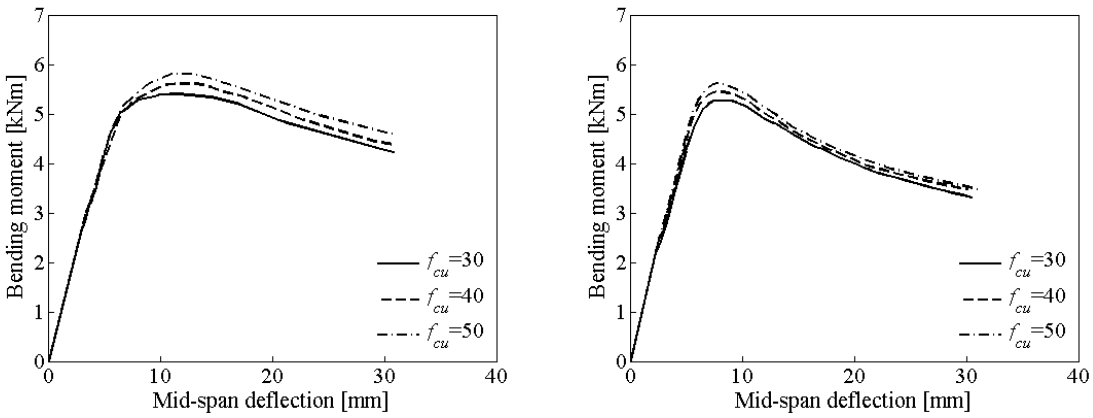

(a) Square CFDSAT (S120×1-C20×1) (b) Circular CFDSAT (C120×1-S20×1)

Figure 7.18: Effect of concrete cube compressive strength on the bending moment-midspan deflection curves of typical specimens.

7.5.5 Effect of cross-section shape

The effect of cross-section shape on bending moment versus midspan deflection curve is presented in Figure 7.16. A square and a circular CFDSAT specimen with the same cross-section area were considered to study the cross-section shape effect on the flexural strength of the composite beams. It can be noticed from Figure 7.16 that the flexural strength of the circular specimen improved slightly which is 2.3% than the square one, thus indicating that the circular cross-section offers relatively stronger confinement compared to the square cross-section.

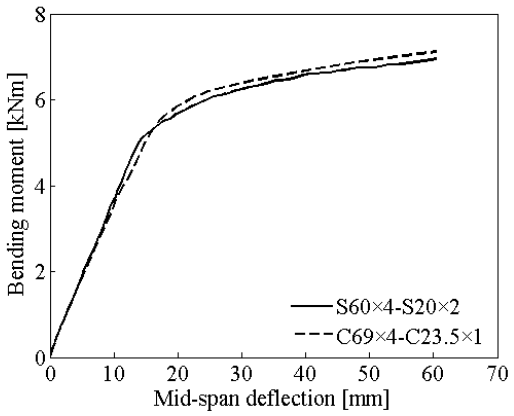

Figure 7.19: Effect of cross-section shape on the bending moment-midspan deflection curves of typical specimens.

7.5.6 Interaction of aluminium tubes and concrete

In order to study the composite action between aluminium and concrete, Figure 7.17 presents the contact stresses generated at different locations of the mid-span cross-section of typical specimens. It can be observed that initially the contact stress is small which is less than 1 MPa at 10 mm mid-span displacement for both specimens in Figure 7.17. This is because Poisson's ratios of the hollow tubes and the concrete infill are different. With the increase of the bending moment and the corresponding increase of the specimen's deflection, the contact stresses between the concrete infill and hollow tubes increase as well and the concrete interacts with the hollow tubes. It is clear from the figure that the confining pressure provided by the outer section (points 1 and 4) is higher than the inner section (points 2 and 3) as the outer tube exerts more resistance to the lateral strain of concrete compared to the inner one. Moreover, it is also noticed from the figure that point 4 experiences maximum contact stress which is 2.1 MPa for specimen S76.2×4.8-S25.4×3.2 (Figure 7.17(a)) and 10.5 MPa for specimen C76.2×3.2-C38.2×1.6 (Figure 7.17(b)) corresponding to 70 mm mid-span displacement. The cause of this high stress at the point is the development of large deformation of concrete at the tension zone which results in additional pressure between the two materials.

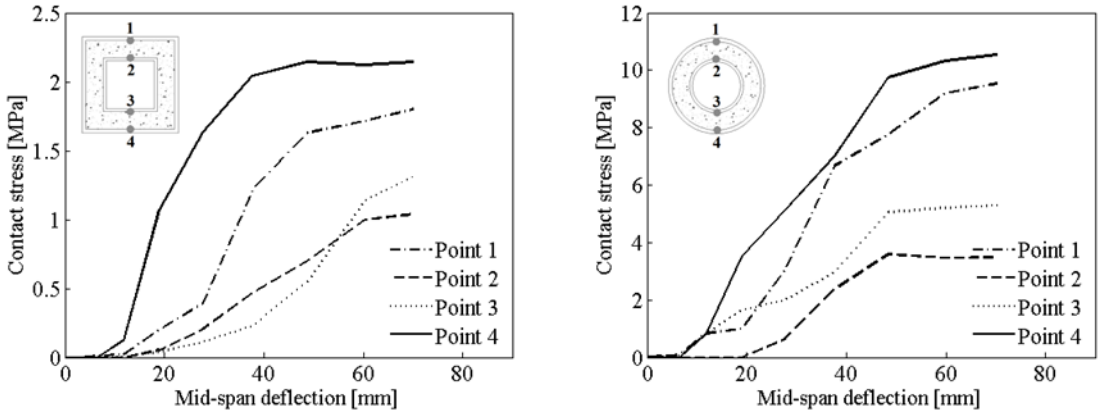

(a) S76.2×4.8-S25.4×3.2 (b) C76.2×3.2-C38.2×1.6

Figure 7.20: Contact stresses at mid-span cross-section of typical specimens.

7.6 Design Recommendations

The existing European standards for composite structures, i.e., Eurocode 4 (EC4) (2004) strictly provide design guidelines for fully concrete-filled carbon steel composite flexural members. However, no design rules are available for the design of CFDSAT flexural members. Therefore, in this section, a design methodology for determining the flexural strength of square and circular CFDSAT beams is proposed based on Eurocode 4.

7.6.1 Design methodology for CFDSAT beams

In Eurocode 4 (2004), the design equation for determining the plastic moment resistance of CFST members is provided based on the plastic stress distribution method (PSDM). In this study, the PSDM was adopted to calculate the plastic moment resistance (M_{pl}) which is considered the theoretical flexural strength ($M_{u,prop}$) of square and circular CFDSAT specimens. Figure 7.18 illustrates the plastic stress distribution of outer and inner aluminium sections and the concrete infill of a CFDSAT section. It is assumed that under compression and tension both outer and inner aluminium sections are able to achieve their yield stress, which are denoted as $f_{0.2,o}$ and $f_{0.2,i}$, respectively. The same assumption is considered in the previous study (Feng *et al.*, 2017) and Eurocode 9 (2007). In the compression zone, it is assumed that concrete can reach its full compressive cylinder strength because of the confinement provided by the hollow tubes. However, in the tension zone, the contribution of concrete infill is ignored.

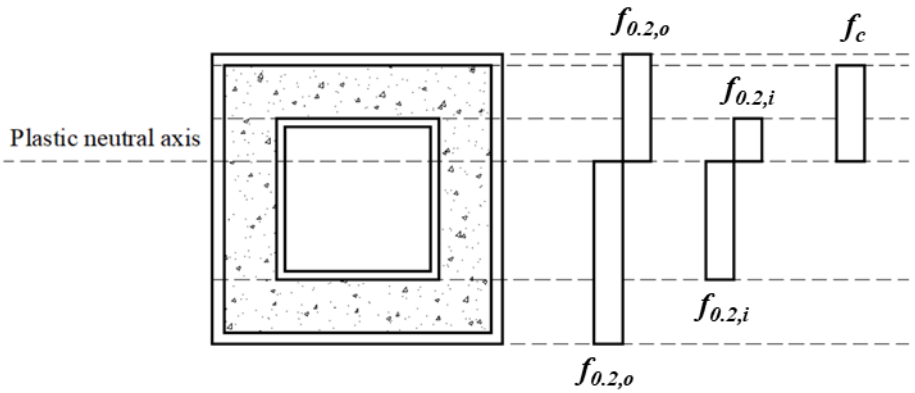

Figure 7.21: Plastic stress distribution of a CFDSAT section.

Using the PSDM, the following equation was derived to determine the flexural strength of square and circular CFDSAT sections.

$$M_{u,prop} = M_{pl} = \left(W_{pla_o} - W_{pla_o,n}\right) f_{0.2,o} + \left(W_{pla_i} - W_{pla_i,n}\right) f_{0.2,i} + 0.5\left(W_{plc} - W_{plc,n}\right) f_c \qquad (7.1)$$

Where W_{pla_o}, W_{pla_i} and W_{plc} are the plastic moduli of the outer and inner aluminium sections and concrete infill, respectively. $W_{pla_o,n}$, $W_{pla_i,n}$ and W_{plc} denote the plastic moduli of the outer and inner aluminium sections and concrete infill at $2h_n$, respectively. The term h_n represents the distance of plastic neutral axis from the centre line of the cross-section. The h_n was calculated by considering the equilibrium condition of axial forces in the CFDSAT section. For square sections, the following equations were used to determine the values of the terms used in Equation (7.1).

$$W_{pla_o} = \frac{B_o D_o^{\,2}}{4} - \frac{\left(B_o - 2t_o\right)\left(D_o - 2t_o\right)^2}{4} \qquad (7.2)$$

$$W_{pla_i} = \frac{B_i D_i^{\,2}}{4} - \frac{\left(B_i - 2t_i\right)\left(D_i - 2t_i\right)^2}{4} \qquad (7.3)$$

$$W_{plc} = \frac{\left(B_o - 2t_o\right)\left(D_o - 2t_o\right)^2}{4} - \frac{B_i D_i^{\,2}}{4} \qquad (7.4)$$

$$W_{pla_o,n} = B_o h_n^{\,2} - \left(B_o - 2t_o\right) h_n^{\,2} \qquad (7.5)$$

$$W_{pla_i,n} = B_i h_n^{\,2} - \left(B_i - 2t_i\right) h_n^{\,2} \qquad (7.6)$$

$$W_{plc,n} = \left(B_o - 2t_o - B_i\right) h_n^{\,2} \qquad (7.7)$$

$$h_n = \frac{A_c f_c}{2\left(B_o - B_i\right) f_c + 4t_o\left(2f_{0.2,o} - f_c\right) + 4t_i\left(2f_{0.2,i}\right)} \tag{7.8}$$

where A_c is area of concrete and f_c is the compressive cylinder strength of concrete, which is considered 80% of compressive cube strength of concrete, f_{cu}.

For circular sections, the following equations were applied to calculate the values of the terms used in Equation (7.1).

$$W_{pla_o} = \frac{D_o^{\,3}}{6} - \frac{\left(D_o - 2t_o\right)^3}{6} \tag{7.9}$$

$$W_{pla_i} = \frac{D_i^3}{6} - \frac{\left(D_i - 2t_i\right)^3}{6} \tag{7.10}$$

$$W_{plc} = \frac{\left(D_o - 2t_o\right)^3}{6} - \frac{D_i^3}{6} \tag{7.11}$$

$$W_{pla_o,n} = D_o h_n^{\,2} - \left(D_o - 2t_o\right) h_n^{\,2} \tag{7.12}$$

$$W_{pla_i,n} = D_i h_n^{\,2} - \left(D_i - 2t_i\right) h_n^{\,2} \tag{7.13}$$

$$W_{plc,n} = \left(D_o - 2t_o - D_i\right) h_n^{\,2} \tag{7.14}$$

$$h_n = \frac{A_c f_c}{2\left(D_o - D_i\right) f_c + 4t_o\left(2f_{0.2,o} - f_c\right) + 4t_i\left(2f_{0.2,i}\right)} \tag{7.15}$$

7.6.2 Flexural strength predictions for CFDSAT beams

The applicability of the proposed design rule is evaluated by comparing the predicted design flexural strength ($M_{u,prop}$) with the flexural strength obtained from the test and FE results (M_u). The ratios of the test and FE flexural strength over the predicted flexural strength ($M_u/M_{u,prop}$) along with their mean and COV values are listed in Table 7.5. The mean and COV values of $M_u/M_{u,prop}$ obtained from test data are 1.12 and 0.06, respectively, whereas the values calculated using both test and FE data are 1.05 and 0.08, respectively. This implies that the proposed methodology based on Eurocode 4 provides a close and safe prediction of the flexural strength of CFDSAT specimens. Figure 7.19 presents the comparisons between the predicted strength and strength obtained from the tests and FE analyses. It is also demonstrated that the proposed methodology is good as almost all the points are close to the diagonal line, i.e., $M_u/M_{u,prop}$ equal to unity. On the basis of the above comparisons, it can be concluded

that the proposed design methodology closely predicts the flexural strength of CFDSAT sections.

Table 7.5: Comparison of the design flexural strength with the corresponding test and FE flexural strength.

	Specimen	No	Class of outer section	Class of inner section	$M_u/M_{u,prop}$
Test	S76.2×6.4-S19.2×1.6	1	1	1	1.13
	S76.2×6.4-S25.4×3.2	1	1	1	1.16
	S76.2×4.8-S25.4×3.2	1	1	1	1.19
	S76.2×6.4-C25.4×3.2	1	1	1	1.17
	S76.2×6.4-C38.2×1.6	1	1	1	1.16
	C88.6×1.6-C19.2×3.2	1	4	1	1.03
	C88.6×1.6-C25.4×3.2	1	4	1	1.02
	C88.6×1.6-C38.2×1.6	1	4	1	1.02
	C76.2×3.2-C25.4×3.2	1	1	1	1.18
	C76.2×3.2-C38.2×1.6	1	1	1	1.15
				Mean	1.12
				COV	0.06
FE (mean)		94	1-4	1-4	1.04
				Mean (all)	1.05
				COV (all)	0.08

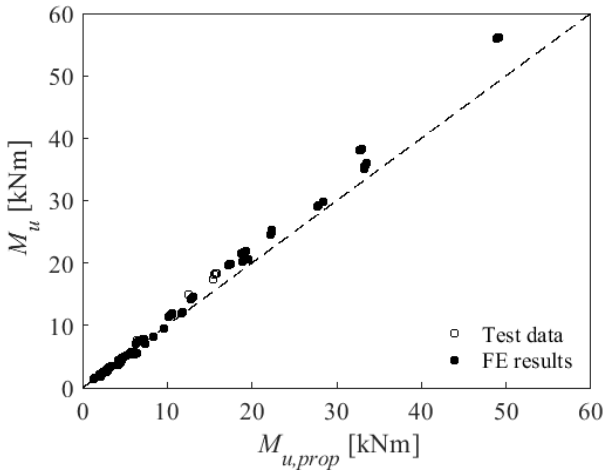

Figure 7.22: Comparison of the design flexural strength with the corresponding test and FE flexural strength.

7.6.3 Slenderness limits for CFDSAT cross-sections

In Eurocode 4 (2004), slenderness limits are provided for CFST cross-sections and it is suggested that the effect of local buckling needs to be accounted for those sections which exceed these limits. The maximum permitted value of the cross-sectional

slenderness is $52\sqrt{235/f_{0.2}}$ for square sections and $90(235/f_{0.2})$ for circular sections. However, no slenderness limits are available for CFDSAT cross-sections due to lack of data. Hence, in this section, slenderness limits for square and circular CFDSAT cross-sections are proposed based on the test and FE results. To obtain these limits, the ratio of experimentally/numerically obtained flexural strength (M_u) over the plastic moment capacity (M_{pl}), is plotted against the cross-section slenderness parameter β/ε in Figure 7.20(a) for square CFDSAT sections and against β/ε^2 in Figure 7.20(b) for circular CFDSAT sections. The symbol β represents the ratio of B_o/t_o for square sections and D_o/t_o for circular sections and ε denotes the material factor, which is taken equal to $\sqrt{250/f_{0.2}}$ for aluminium alloy, according to Eurocode 9 (2007).

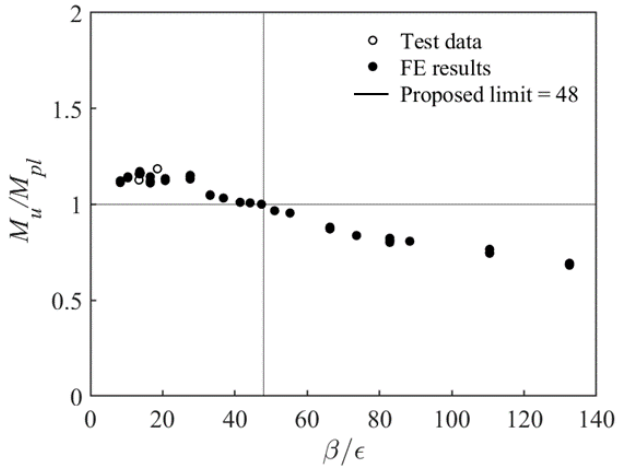

(a) Square CFDSAT specimens

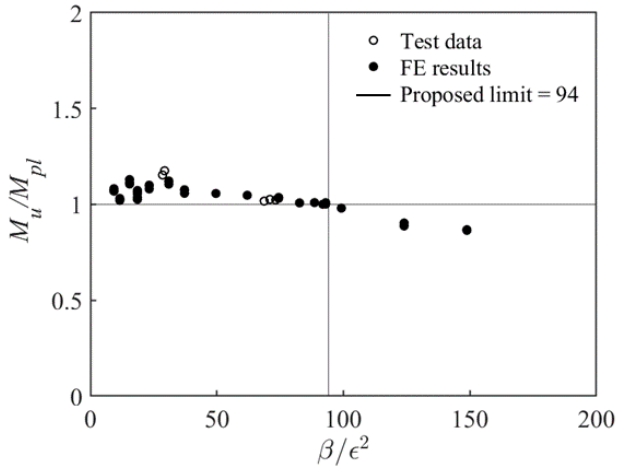

(b) Circular CFDSAT specimens

Figure 7.23: Proposed slenderness limits for CFDSAT cross-sections.

From Figures 7.20(a) and (b), a decreasing trend of normalised flexural strength M_u/M_{pl}

can be observed with the increase of the cross-section slenderness parameter for both square and circular specimens. The horizontal line of M_u/M_{pl} =1 separates the cross-sections that have flexural strength equal to or greater than their plastic flexural strength (i.e., $M_u/M_{pl} \geq 1$) from the cross-sections having lower flexural strength than their plastic flexural strength (i.e., $M_u/M_{pl} < 1$). On the basis of this demarcation, it can be seen that the proposed vertical limit lines of 48 and 94 for square and circular CFDSAT cross-sections respectively, separate the sections with normalised flexural strength larger or smaller than unity. Thus, based on the test and FE results of this study, the cross-section slenderness limits of β/ε=48 and β/ε^2=94 are proposed for square and circular CFDSAT cross-sections.

7.7 Conclusions

This study experimentally and numerically investigated the behaviour of CFDSAT beams under in-plane bending. A total 10 specimens was tested and 94 specimens were modelled considering different combinations of outer and inner cross-section shapes, i.e., square-square, square-circular, circular-circular and circular-square, over a range of cross-section slenderness and three different concrete cube compressive strengths. The following conclusions can be drawn based on the observed results:

- The predominant failure mode of all CFDSAT specimens was yielding. Besides yielding, some circular specimens experienced small outward local buckling at the top face of the outer tube and others presented fracture of the outer tube at the tension side upon reaching their flexural capacity. Overall, the concrete infill efficiently prevented the formation of inward local buckling and delayed the occurrence of outward local buckling of the outer tube.

- The experimental bending moment versus mid-span deflection curves demonstrated that all CFDSAT specimens achieved good ductility, which is attributed to the beneficial composite action of the three components of the CFDSAT sections.

- The developed FE model accurately captured the structural response of the CFDSAT beams. Based on this model, a FE parametric study including 94 CFDSAT beams was conducted to study the effect of hollow ratio, cross-section slenderness of outer and inner tubes and concrete strength on the flexural behaviour of CFDSAT specimens.

- The parametric study results showed that the cross-sectional dimensions of the outer tube have a substantial effect on the flexural response of CFDSAT beams. It was demonstrated that the larger cross-sectional dimensions of the outer tube remarkably increased the flexural strength of the beams.

- The flexural strength of CFDSAT beams generally improved by increasing the dimensions of the inner tube and the concrete compressive strength, however, the improvement is less significant.

- In the absence of design rules, a design methodology is proposed to determine the flexural strength of square and circular CFDSAT beams based on the Eurocode 4 framework. It was demonstrated that the proposed methodology closely predicts the flexural strength of these composite members.

- Cross-section slenderness limits of β/ε=48 and β/ε^2=94 for square and circular CFDSAT cross-sections are proposed based on the data obtained from the experiments and FE analyses.

CHAPTER 8 : SUSTAINABILITY OF CFAT AND CFDSAT MEMBERS

8.1 Introduction

This chapter assesses the sustainability of CFAT and CFDSAT columns and compared the results with those of conventional a CFST column. Life-cycle assessment (LCA) and life-cycle cost analysis (LCCA) are carried out to evaluate the long-term environmental impact and cost of these design alternatives. Moreover, the self-weight of these columns is calculated to determine the lighter design solution among the three structural members.

8.2 Investigated columns

In this study, a comparison of sustainability has been made among three different forms of composite columns, i.e., CFST, CFAT and CFDSAT by LCA and LCCA methods. The service life of these columns was considered 50 years. The columns were designed based on a one-story building configuration. The slab of the building was considered a composite panel consisting of a profiled steel sheet filled with concrete. The dimensions of the panel were taken as 10 m × 20 m. The appropriate dead and live loads for the panel were considered according to Eurocode 1 (2002). The calculated compressive load on a column was 1065 kN. The length of the columns was taken equal to 3 m. Figure 8.1 presents the cross-sections of three different column forms.

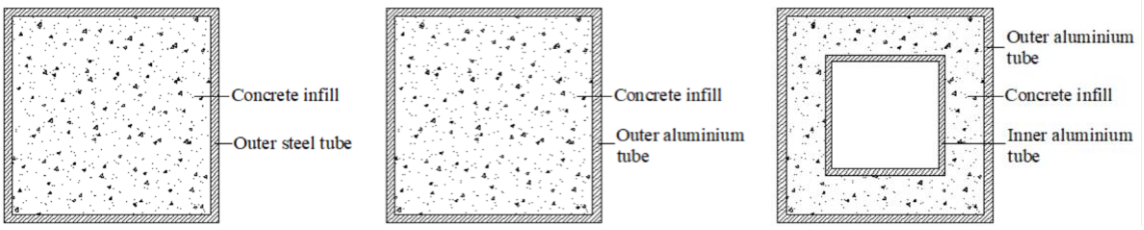

(a) CFST (b) CFAT (c) CFDSAT

Figure 8.1: Cross-sections of three different columns.

8.2.1 Material properties

The material properties of the components of composite columns are listed in Table 8.1. The material properties of steel and aluminium hollow sections are taken from the

coupon test results of the previous study (Tao *et al.*, 2004) and Chapter 4, respectively. It should be noted that the yield stress of the steel tube is taken equal to the yield stress of aluminium tube. The nominal compressive cylinder strength of concrete is considered equal to 30 MPa. The same concrete mix ratio of this study is used to calculate the amount of cement, fine aggregates, coarse aggregates and water for the concrete of composite columns.

Table 8.1: Material properties of the components of composite columns.

Column	Component	Material property			
		E (GPa)	$f_{0.1}$ (MPa)	$f_{0.2}$ (MPa)	f_c (MPa)
CFST	Steel tube (Tao *et al.*, 2004)	200	276	Not available	-
	Concrete	32837	-	-	30
CFAT	Aluminium tube	69	276	315	-
	Concrete	32837	-	-	30
CFDSAT	Outer aluminium tube	69	276	315	-
	Inner aluminium tube	69	276	315	-
	Concrete	32837	-	-	30

8.2.2 Structural design

In this study, Eurocode 4 (2004) is used to design the CFST column. However, due to the absence of design guidelines for the aluminium alloy concrete-composite tubular members, the design methodologies proposed in Chapter 4 and Chapter 6 are applied to design the CFAT and CFDSAT columns, respectively. The ultimate capacity of the composite columns is determined by summing the plastic resistance of hollow tube/tubes and concrete infill. The composite columns were designed to carry the nominal axial compressive load of 1065 kN. An iteration process was used to obtain the cross-sectional dimensions of the columns. During this process, the outer depth and width of the outer tube of the columns were kept the same, while the thickness of the outer tube was varied to achieve the targeted ultimate capacity. The cross-sectional dimensions of the composite columns obtained from the iteration process are listed in Table 8.2. The calculated ultimate capacity of CFST, CFAT and CFDSAT columns are 1065.9, 1065.5 and 1065.6 kN, respectively.

Table 8.2: Dimensions of the composite columns.

Column	D_o (mm)	B_o (mm)	t_o (mm)	D_i (mm)	B_i (mm)	t_i (mm)	L (mm)
CFST	150	150	4	-	-	-	3000
CFAT	150	150	6.75	-	-	-	3000
CFDSAT	150	150	6.75	100	100	3.61	3000

8.2.3 Comparison of self-weight of columns

In this section, the comparison of the self-weight of the composite columns is presented. For this purpose, the volume of the components of the columns was calculated and the calculated values were multiplied by the density of the respective components. The density of the steel, aluminium alloy and concrete were taken equal to 7850, 2700 and 2400 kg/m^3, respectively. Finally, the self-weight of the columns was determined by summing up the self-weight of their components. Table 8.3 reports the self-weight of the composite columns along with the density, volume and weight of their different components.

Table 8.3: Material quantities of the composite columns.

Material	Density (kg/m^3)	CFST		CFAT		CFDSAT	
		Volume (m^3)	Weight (kg)	Volume (m^3)	Weight (kg)	Volume (m^3)	Weight (kg)
Concrete	2400	0.06	145.18	0.06	134.13	0.026	62.13
Steel tube	7850	0.01	55.01	-	-	-	-
Outer aluminium tube	2700	-	-	0.01	31.35	0.012	31.35
Inner aluminium tube	2700	-	-	-	-	0.004	11.26
		Sum	200.19		165.48		104.75

It can be observed that when the outer depth and width are constant, the self-weight of the CFST, CFAT and CFDSAT columns are 200.19, 165.48 and 104.75 kg, respectively. It is indicated that the self-weight of the CFST column reduced by around 17% when the steel tube is replaced by an aluminium alloy tube having similar outer depth and width. Moreover, the self-weight of the CFST column decreased further which is around 47% when the double skin technique is adopted using aluminium alloy tubes (i.e., CFDSAT column), where the outer tube's outer dimensions are constant and the inner tube's outer depth/width ratio is 33% smaller than the outer tube one.

Compared to the CFAT column the self-weight of the CFDSAT column is around 36% lower due to the absence of inner concrete. Therefore, it can be concluded that the weight of the single skin concrete-filled tubular column can be reduced significantly by using aluminium alloy tube instead of steel one. Moreover, the composite columns become lighter when the double skin technique is adopted incorporating aluminium alloy tubes.

8.3 Life-cycle model

In this section the studied life-cycle model is discussed. Material quantities of each composite column presented in the previous section are used to evaluate the long-term environmental impact and cost of the columns. The goal and scope of this study are set by specifying the functional unit and system boundary. A deterioration model is considered for the composite columns to define a maintenance schedule during its service life (Wang *et al.*, 2014). In this study, the service life of the columns is considered 50 years.

8.3.1 Goal and scope definition

The functional unit chosen in this study is three different composite column forms, i.e., CFST, CFAT and CFDSAT. As mentioned earlier that the columns are designed to carry the same axial load which is equal to 1065 kN. The height of each column is considered 3 m which is the typical column height of a residential building. In this study, the cradle-to-grave system boundary is chosen which covers all aspects of the life span ranging from raw material extrusion to disposal or recycling process at the end of life. According to this approach, the life cycle of the composite columns is split into five main stages, including the production of structural components, transportation, column construction, maintenance and end-of-life stages. The first stage considered the production of structural components which includes, the extrusion of sand and stone chips and the production of cement, steel and aluminium hollow sections. In the second stage, the transportation of the produced structural components from the production plants to the construction site is taken into account. In the third stage, on-site construction of the composite columns is considered. In the fourth stage, a maintenance plan is taken into account to ensure a certain loss of mechanical performance during the life span of the columns. At the end-of-life stage, demolishment of the product and waste disposal or recycling are considered. Figure 8.2 presents the schematic diagram of

the framework of the cradle-to-grave system boundary considered in this study.

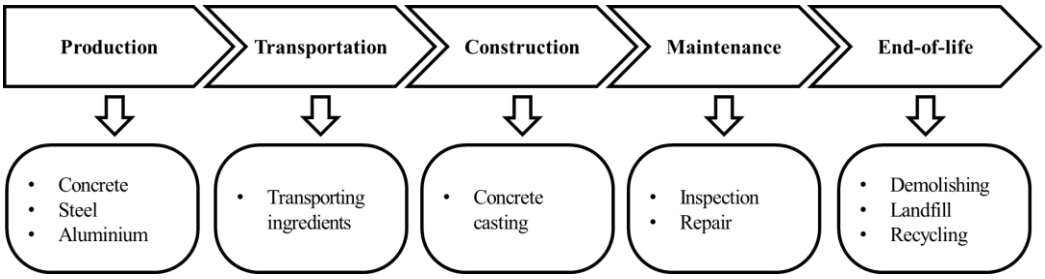

Figure 8.2: Schematic diagram of the studied life-cycle stages (Zhao *et al.*, 2021).

8.3.2 Maintenance plan

This study adopted a previously established deterioration model for the CFST column to set a maintenance plan. The maintenance work is essential when a structural member loses a certain level of mechanical performance. Based on the time-dependent corrosion model suggested in the previous study (Wang *et al.*, 2014), a CFST column can lose 10% performance in around 10 years under axial compression and harsh environment. Zhao *et al.* (2021) considered that for the CFST column, maintenance action is required after every 10 years and each time 10% of the original material needs to be replaced. This simplified maintenance plan is applied in this study. As aluminium alloy has excellent corrosion resistance, no expense related to the maintenance work of CFAT and CFDSAT columns is considered in this study. The same assumption is also considered in the past study (Gardner *et al.*, 2007).

8.3.3 Life-cycle unit processes

The ingredients of concrete and hollow metal tubes are purchased from local suppliers and transported to the construction site. The environmental impact and unit price of these structural ingredients are collected from previous research studies, reports, open literature and local supplier. During the construction stage, an electric concrete mixer and a vibrating table are used to cast the composite columns. The production, transportation and construction stages are combinedly considered as the initial stage. The maintenance schedule for the composite columns discussed in the previous section is used to determine their environmental impact or cost related to maintenance work.

At the end-of-life stage, it is considered that the structural elements will be demolished and the demolished materials will be disposed of properly. Several disposal ways, such

as landfill, recycling and incineration are commonly used in the construction sector. In this study, it is assumed that 100% steel and aluminium alloy will be recycled at the end-of-life stage. Concrete can be disposed of by landfilling and recycling. Recycled concrete is a good source of aggregates and can be used for new concrete (Aslani *et al.*, 2018). However due to quality inconsistency, the use of these aggregates is limited (Silva *et al.*, 2017). Therefore, it is assumed that after demolition concrete wastes will be transported to the nearest landfill plant. The environmental and economic impact associated with all these stages are determined in terms of CO_2 emission and cost, respectively.

8.4 LCA results

In this section, the environmental impact of composite columns is evaluated in terms of CO_2 emission during their life cycle. The unit CO_2 emissions during the production of cement, fine/coarse aggregates, steel and aluminium alloy hollow sections are taken as 0.951 kg CO_2/kg, 1.06×10^{-3} kg CO_2/kg (Müller *et al.*, 2014), 1.802 kg CO_2/kg (Zhao *et al.*, 2021) and 2.68 kg CO_2/kg (One Click LCA, 2020), respectively. It should be noted that the aluminium alloy considered in this study is low-carbon aluminium. The low-carbon aluminium alloy is manufactured using 100% renewable energy. Because of using 100% renewable energy, low-carbon aluminium emits around 60% less CO_2 during its production process (One Click LCA, 2020) which is 2.68 kg CO_2/kg than the conventional aluminium which emits 6.70 kg CO_2/kg (European Aluminium (EA), 2018). It is considered that the ingredients of concrete, steel and aluminium hollow sections are transported by medium diesel truck from local suppliers to the construction site. A medium diesel truck usually generates 0.166 kgCO_2 to carry one-tonne material for one kilometre (Xu *et al.*, 2021). The driving distances between local suppliers and the construction site are taken from Google map. Carbon emissions in the construction stage are related to the energy consumption of different equipment, such as concrete mixture, compacting equipment, crane and so on. In this study, the value of CO_2 emission is taken as 0.016 kg for casting 1 kg concrete (Fib, 2004). In the previous study, steel installation time was considered half of the time required for concrete casting (Zhao *et al.*, 2021). Therefore, it is assumed that half amount of CO_2 emits during steel installation, i.e., 0.008 kg per kg steel compared to concrete casting (Zhao *et al.*, 2021). Similar assumption is considered for CFAT and CFDSAT columns construction. The CO_2 emission for concrete landfilling is taken as 0.007 kg CO_2/kg

based on the previous study (Cho and Chae, 2016). During the recycling process, 1.63 kg CO_2 emits for 1 kg steel scrap (Worldsteel Association (WA), 2021). However, the value of CO_2 emission for 1 kg aluminium alloy recycling is 0.438 kg, as the recycling process of aluminium needs around 95% less energy than the primary production (European Aluminium (EA), 2021). Here, it is assumed that 100% steel and aluminium will be recycled at the end-of-life stage. Table 8.4 lists the amount of components of three different forms of composite columns along with their environmental impact in terms of CO_2 emission during different stages of the life-cycle. The amount of CO_2 emission for each type of column is calculated by Equation (8.1).

$$E_{Total} = E_P + E_T + E_C + E_M + E_E \tag{8.1}$$

where E_{Total} is the total CO_2 emitted during the life-cycle, E_p, E_T, E_c, E_M and E_E are CO_2 generated at production, transportation, construction, maintenance and end-of-life stages, respectively.

Figure 8.3 presents the compression of CO_2 emissions during the life-cycle of three different composite columns. It can be observed from the table and figure that, the CFAT column emits around 55% and 14% less CO_2 than the CFST and CFDSAT columns, respectively. While the carbon footprint of the CFDSAT column is around 48% lower than that CFST column. At the initial stage, the CFST column leads to around 15% more environmental impact than the CFAT column, however, the value is marginally higher which is less than 1% compared to the CFDSAT column. Due to the excellent corrosion resistance property of aluminium alloy no maintenance work is required for CFAT and CFDSAT columns, hence no CO_2 is emitted at the maintenance stage of these columns. The recycling process of aluminium alloy requires only 5% energy of the production of the original metal. Therefore, at the end-of-life, the emission of CO_2 of CFAT and CFDSAT columns is around 83% and 79% less, respectively compared to the carbon emission of the CFST column. Therefore, it can be concluded that the CFAT column provides the lowest environmental impact compared to the other composite columns.

Table 8.4: Life-cycle environmental impact assessment.

Column	Life-cycle stage	Consumed material	Amount	Unit	GWP coefficient	Unit	Reference	GWP ($kgCO_2$)
CFST	Production	Cement	26.62	kg	0.951	$kgCO_2$ /kg	Müller *et al.* (2014)	25.31
		Fine aggregate	38.71	kg	0.001	$kgCO_2$ /kg	Müller *et al.* (2014)	0.04
		Coarse aggregate	65.63	kg	0.001	$kgCO_2$ /kg	Müller *et al.* (2014)	0.07
		Steel tube	55.01	kg	1.802	$kgCO_2$ /kg	Zhao *et al.* (2021)	99.13
		Sum						**124.56**
	Transportation	Materials for concrete	0.75	t.km	0.166	$kgCO_2$ /t.km	Xu *et al.* (2021)	0.12
		Steel tube	1.79	t.km	0.166	$kgCO_2$ /t.km	Xu *et al.* (2021)	0.30
		Sum						**0.42**
	Construction	Concrete	145.18	kg	0.016	$kgCO_2$ /kg	Fib (2004)	2.32
		Steel tube	55.01	kg	0.008	$kgCO_2$ /kg	Zhao *et al.* (2021)	0.44
		Sum						**2.76**
	Maintenance	**Sum**					Zhao *et al.* (2021)	**63.87**
	End-of-life	Concrete-landfill	145.18	kg	0.007	$kgCO_2$ /kg	Cho, Chae (2016)	1.02
		Steel tube-100% recycled	55.01	kg	1.630	$kgCO_2$ /kg	WA (2021)	89.67
		Sum						**90.69**
	Total							**282.30**
CFAT	Production	Cement	24.59	kg	0.951	$kgCO_2$ /kg	Müller *et al.* (2014)	23.39
		Fine aggregate	35.77	kg	0.001	$kgCO_2$ /kg	Müller *et al.* (2014)	0.04
		Coarse aggregate	60.65	kg	0.001	$kgCO_2$ /kg	Müller *et al.* (2014)	0.06
		Aluminium tube	31.33	kg	2.68	$kgCO_2$ /kg	LCA (2020)	83.96
		Sum						**107.45**
	Transportation	Materials for concrete	0.69	t-km	0.166	$kgCO_2$ /t.km	Xu *et al.* (2021)	0.11
		Aluminium tube	1.03	t-km	0.166	$kgCO_2$ /t.km	Xu *et al.* (2021)	0.17
		Sum						**0.29**
	Construction	Concrete	134.15	kg	0.016	$kgCO_2$ /kg	Fib (2004)	2.15
		Aluminium tube	31.33	kg	0.008	$kgCO_2$ /kg		0.25
		Sum						**2.40**
	Maintenance							**0.00**
	End-of-life	Concrete-landfill	134.13	kg	0.007	$kgCO_2$ /kg	Cho, Chae (2016)	0.94
		Aluminium tube -100% recycled	31.33	kg	0.438	$kgCO_2$ /kg	EA (2021)	13.72
		Sum						**14.66**
	Total							**124.79**

Table 8.5 (continued): Life-cycle environmental impact assessment.

CFDSAT	Production	Cement	11.39	kg	0.951	$kgCO_2$ /kg	Müller *et al.* (2014)	10.83
		Fine aggregate	16.57	kg	0.001	$kgCO_2$ /kg	Müller *et al.* (2014)	0.02
		Coarse aggregate	28.10	kg	0.001	$kgCO_2$ /kg	Müller *et al.* (2014)	0.03
		Aluminium outer tube	31.33	kg	2.68	$kgCO_2$ /kg	LCA (2020)	83.96
		Aluminium inner tube	11.26	kg	2.68	$kgCO_2$ /kg	LCA (2020)	30.19
		Sum						**125.03**
	Transportation	Materials for concrete	0.32	t-km	0.166	$kgCO_2$ /t.km	Xu *et al.* (2021)	0.05
		Aluminium tube	1.40	t-km	0.166	$kgCO_2$ /t.km	Xu *et al.* (2021)	0.23
		Sum						**0.29**
	Construction	Concrete	62.13	kg	0.016	$kgCO_2$ /kg	Fib (2004)	0.99
		Aluminium tube	42.59	kg	0.008	$kgCO_2$ /kg		0.34
		Sum						**1.33**
	Maintenance							**0.00**
	End-of-life	Concrete-landfill	62.13	kg	0.007	$kgCO_2$ /kg	Cho, Chae (2016)	0.43
		Aluminium tube -100% recycled	42.59	kg	0.438	$kgCO_2$ /kg	EA (2021)	18.66
		Sum						**19.09**
	Total							**145.74**

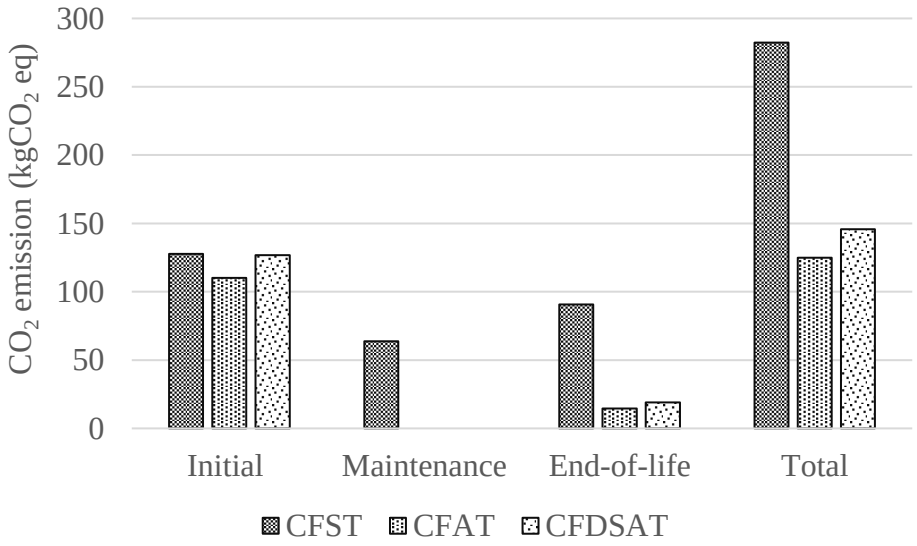

Figure 8.3: Comparison of CO_2 emissions at different stages of the composite columns.

8.5 LCCA results

In this section, the total cost associated with the entire life of composite columns is determined. The individual cost of different components of composite columns is presented in Table 8.5. The unit price of cement, coarse aggregates and fine aggregates are 0.30 £/kg (Blue Circle, 2023), 0.59 £/kg (Resapol, 2023) and 0.07 £/kg (Wickes, 2023), respectively. The price of metal hollow tubes varies depending on the dimensions of the cross-section. The unit price of 150 mm × 150 mm × 4 mm steel hollow section is 6.95 £/kg (Metalsupermarkets, 2023). The cost of 150 mm × 150 mm × 6.75 mm and 100 mm × 100 mm × 3.61 mm aluminium hollow sections are 8.62 £/kg and 9.51 £/kg, respectively (Simmal, 2023). The transportation cost is considered by adding the delivery charge required to transport the raw materials from the local supplier to the construction site. In the construction stage, the cost is related to labour used for erection, concrete casting, installation, etc. For determining the construction cost, the labour constant is introduced by considering the amount of work can do a labour per unit of time. Based on the previous study (Chan and Aibinu, 2012) labour constants for concrete and steel are taken equal to 5 m^3/hour and 0.02 tones/hour, respectively. In UK the average labour rate is £12.88 per hour (Linear Recruitment (LR), 2021). The maintenance cost of the column forms is calculated according to the maintenance plan mentioned earlier. At the end-of-life stage, money needs to spend on demolition and disposal of the materials. The unit cost of demolition and landfill of concrete are taken from the previous study (Zhao *et al.*, 2021). However, the money can earn by selling scrap steel and aluminium alloy. This amount is deducted from the total cost of the end-of-life stage. The local scrap metal selling rate is considered for both steel and aluminium alloy (Scrapmetalpricesuk, 2023). The unit cost associated with maintenance and end-of-life stage are discounted to present value. The total life-cycle cost of three different composite columns is determined and converted to present value using Equation (8.2) (Younis *et al.*, 2018).

$$LCC = \sum_{t=0}^{T} \frac{C_t}{(1+r)^t} \tag{8.2}$$

where t is the time (years) of incurred cost, T is the total studied period, C_t is the cost incurred at time t and r is the discount rate. The C_t is calculated by Equation (8.3).

$$C_t = C_P + C_T + C_C + C_M + C_E \tag{8.3}$$

where C_P is the production cost, C_T is the transportation cost, C_C is the construction cost, C_M is the maintenance cost and C_E is the end-of-life cost at the time *t*. The discount rate refers to the time value of money. It is applied to determine the future value by accounting for the nominal interest rate and inflation rate. In this study, the discount rate is considered equal to 3.3% (Zhao *et al.*, 2021). The discount rate is not taken into account at the initial stage, i.e., production, transportation and construction. However, the discount rate is applied for the future cost associated with the maintenance and end-of-life stages.

Figure 8.4 shows the comparison of life-cycle costs at different stages of the composite columns. It can be observed from the table and figure that compared to the CFST column the CFAT and CFDSAT columns are around 30% and 15% less expensive, respectively. The initial cost of CFAT and CFDSAT columns is around 22% and 5% lower than the CFST column. According to the maintenance plan stated earlier, each maintenance action for CFST column requires 10% cost of the initial stage cost, whereas the amount is zero for CFAT and CFDSAT columns. Due to the high scrap value of aluminium alloy, the total cost at the end-of-life stage of CFAT and CFDSAT columns can be offset compared to CFST column. In summary, the CFAT column is estimated to be the less expensive solution compared to other composite columns. However, due to the application of double hollow tube the cost of CFDSAT column slightly increased which is around 22% compared to the CFAT section.

Table 8.6 : Life-cycle cost analysis.

Column	Life-cycle stage	Consumed material	Amount/ Hour	Unit	Unit Cost	Unit	Reference	Cost (£)
CFST	Production	Cement	26.62	kg	0.30	£/kg	Blue Circle (2023)	7.98
		Fine aggregate	38.71	kg	0.59	£/kg	Wickes (2023)	22.84
		Coarse aggregate	65.63	kg	0.07	£/kg	Resapol (2023)	4.59
		Steel tube	55.01	kg	6.95	£/kg	Metalsupermarkets (2023)	382.34
		Sum						**417.76**
	Transportation	Materials for concrete						30.00
		Steel tube						21.50
		Sum						**51.50**
	Construction	Concrete	1.00	hr	12.88	£/hr	LR (2021)	12.88
		Steel tube	2.50	hr	12.88	£/hr	LR (2021)	32.20
		Sum						**45.08**
	Maintenance	**Sum**						**257.17**
	End-of-life	Concrete - demolition	0.06	m^3	98.00	£/m^3	Zhao *et al.* (2021)	5.93
		Concrete-landfill	145.18	kg	0.07	£/kg	Zhao *et al.* (2021)	10.31
		Steel tube-100% recycled	55.01	kg	0.06	£/kg	Scrapmetalpricesuk (2023)	3.30
		Sum						**12.94**
	Total				3.30	%	Zhao *et al.* (2021)	**567.61**
CFAT	Production	Cement	24.59	kg	0.30	£/kg	Blue Circle (2023)	7.38
		Fine aggregate	35.77	kg	0.59	£/kg	Wickes (2023)	21.10
		Coarse aggregate	60.65	kg	0.07	£/kg	Resapol (2023)	4.25
		Aluminium tube	31.33	kg	8.62	£/kg	Simmal (2023)	270.05
		Sum						**302.78**
	Transportation	Materials for concrete						30.00
		Aluminium tube						21.50
		Sum						**51.50**
	Construction	Concrete	1.00	hr	12.88	£/hr	LR (2021)	12.88
		Aluminium tube	2.50	hr	12.88	£/hr	LR (2021)	32.20
		Sum						**45.08**
	Maintenance							**0.00**
	End-of-life	Concrete - demolition	0.06	m^3	98.00	£/m^3	Zhao *et al.* (2021)	5.48
		Concrete-landfill	134.15	kg	0.07	£/kg	Zhao *et al.* (2021)	9.52
		Aluminium tube-100% recycled	31.33	kg	0.60	£/kg	Scrapmetalpricesuk (2023)	18.80
		Sum						**-3.80**
	Total				3.30	%	Zhao *et al.* (2021)	**398.61**

Table 8.7 (continued): Life-cycle cost analysis.

CFDSAT	Production	Cement	11.39	kg	0.30	£/kg	Blue Circle (2023)	3.42
		Fine aggregate	16.57	kg	0.59	£/kg	Wickes (2023)	9.78
		Coarse aggregate	28.10	kg	0.07	£/kg	Resapol (2023)	1.97
		Aluminium outer tube	31.33	kg	8.62	£/kg	Simmal (2023)	270.05
		Aluminium inner tube	11.26	kg	9.51	£/kg	Simmal (2023)	107.12
		Sum						**392.33**
	Transportation	Materials for concrete						30.00
		Aluminium tube						21.50
		Sum						**51.50**
	Construction	Concrete	1.00	hr	12.88	£/hr	LR (2021)	12.88
		Aluminium tube	2.50	hr	12.88	£/hr	LR (2021)	32.20
		Sum						**45.08**
	Maintenance							**0.00**
	End-of-life	Concrete - demolition	0.03	m^3	98.00	£/m^3	Zhao *et al.* (2021)	2.54
		Concrete-landfill	62.15	kg	0.07	£/kg	Zhao *et al.* (2021)	4.41
		Aluminium tube-100% recycled	42.59	kg	0.60	£/kg	Scrapmetalpricesuk (2023)	25.56
		Sum						**-18.61**
	Total				3.30	%	Zhao *et al.* (2021)	**485.24**

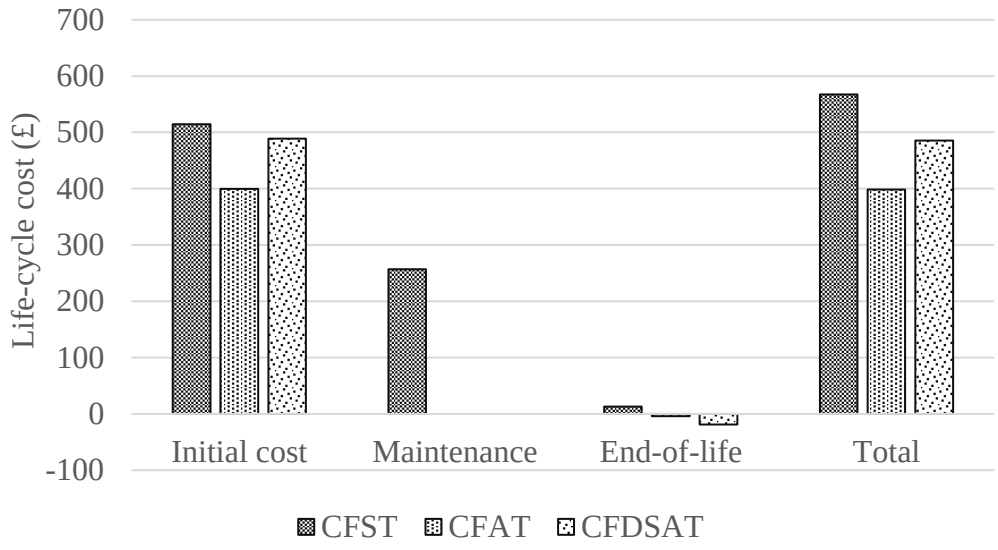

Figure 8.4: Comparison of life-cycle costs at different stages of the composite columns.

8.6 Conclusions

In this study, the sustainability of CFAT and CFDAT columns was assessed in terms of CO_2 emission and cost associated with their life span and the results were compared with those of a conventional CFST column. To determine the lighter solution the self-weight of these columns was calculated and compared with each other. Based on the findings of the study the following points can be summarized:

- It is found that the self-weight of the studied CFAT and CFDSAT columns is around 17% and 47% lower than that of the CFST column. Therefore, it can be concluded that the self-weight of the single skin concrete-filled tubular column can be reduced significantly by using aluminium alloy tube instead of steel one. Moreover, the composite columns become lighter when the double skin form is applied incorporating aluminium alloy tubes.

- It can be observed from the LCA that, CFAT column emits less CO_2 which is around 55% and 14% compared to the CFST and CFDSAT columns, respectively. While the carbon footprint of CFDSAT column is around 48% lower than that CFST columns. Therefore, it can be concluded that the CFAT column provides the lowest environmental impact among the three design alternatives.

- The LCCA results showed that the total cost associated with the life cycle of CFAT and CFDSAT columns is around 30% and 15% lower, respectively than the CFST one. It is indicated that the CFAT column is a less expensive solution compared to other composite columns.

CHAPTER 9 : CONCLUSIONS AND FUTURE RESEARCH

This chapter provides the key findings and overall conclusions of this research study. Moreover, some recommendations for future study are also discussed at the end of this chapter.

9.1 Concluding remarks

The present study experimentally and numerically investigated the structural behaviour of CFAT and CFDSAT structural members subjected to axial compression and bending. The hollow tubes used in this study were fabricated by 6082-T6 high-strength aluminium alloy. Chapters 4 and 5 studied the compressive and flexural response of CFAT structural members. Chapters 6 and 7 investigated the structural behaviours of CFDSAT columns and beams. Chapter 8 evaluated the sustainability of CFAT and CFDSAT columns and compared the results with those of conventional a CFST column.

In the experimental programme of CFAT structural members, a total of 18 columns, including 9 CFAT and 9 BAT specimens and 20 beams, including 10 CFAT and 10 BAT specimens were tested. The BAT structural members were tested for reference purposes and to assess the applicability of Eurocode 9 design standard. The experimental investigation of CFDSAT structural members included 8 columns and 10 beams. The material properties of aluminium alloy were obtained from tensile coupon tests. It was observed that the aluminium alloy exhibits a rounded stress-strain relationship, which can be accurately captured by the Ramberg-Osgood model. The compressive strength of concrete was determined by compression tests of concrete cubes and cylinders. As the initial geometric imperfections have a significant influence on the behaviour of the structural members, the magnitudes of initial local and global imprecations were measured experimentally. The column tests were conducted using a pin-ended set-up for allowing the specimens to rotate around the buckling axis. The flexural members were tested under a four-point bending configuration. The experimental results were presented in terms of failure mode, ultimate strength and load/moment versus mid-length lateral displacement curves. Based on the observed experimental results the following conclusions can be reached:

- The predominant failure mode of the composite columns and beams was flexural

buckling and member yielding, respectively. However, no inward local buckling was identified at the outer tube of any members. This signifies the effectiveness of concrete infill in preventing the occurrence of inward local buckling.

- The ultimate capacity, stiffness and ductility of CFAT structural members were remarkably improved compared to the BAT counterparts. This is attributed to the beneficial composite action between hollow tube and concrete infill of the composite cross-sections.

- For CFAT members, the strength increase was more prominent for slender cross-sections. This is due to the delay in the onset of local buckling in the slender plate elements offered by the concrete infill, resulting in an additional increase in the ultimate strength.

Numerical investigation on the structural response of bare and composite members was performed by developing FE models of BAT, CFAT and CFDSAT specimens with the consideration of geometry and material nonlinearities. The experimentally measured geometric dimensions and material properties of the specimens were used for developing the models. The compressive behaviour of concrete infill was considered according to the confined-concrete model proposed in the previous study (Tao *et al.*, 2013), while the tensile response was taken into account by a stress-crack opening displacement relationship based on fracture energy. The suitable mesh size for the FE models was selected from a mesh sensitivity study. The experimentally measured initial geometric imperfection values were considered in the FE models by defining the lowest buckling mode obtained from the eigenvalue analysis. Appropriate contact interaction between aluminium tube and concrete infill and proper boundary conditions were applied in the models to simulate the test conditions. The FE models were validated against the experimental results. It was demonstrated that the developed FE models can accurately predict the structural behaviour of BAT, CFAT and CFDSAT structural members. The validated models were used in the parametric studies to study the effect of different design parameters, such as cross-sectional aspect ratio, cross-sectional slenderness, member slenderness, concrete strength and hollow ratio of outer and inner tubes on the behaviour of the structural members. A geometric imperfection sensitivity study was conducted for each type of structural member, to choose suitable initial geometric imperfection values for the parametric investigation. In the parametric

studies, total 108 CFAT and BAT columns, 76 CFAT and BAT flexural members, 81 CFDSAT columns and 94 CFDSAT flexural members were modelled. The FE results reveal that the member slenderness, cross-sectional dimensions of outer tube and concrete compressive strength have a significant influence on the ultimate capacity of CFAT and CFDSAT columns. The following conclusions can be drawn based on the observed numerical results:

- For CFAT and CFDSAT columns, the ultimate capacity reduced noticeably with the increase of member slenderness (i.e., increase of member length). This can be clarified by the fact that when the cross-sectional dimensions of the specimens are constant, the critical buckling load of columns decreases with the increase of the member length, which makes the columns prone to global buckling failure, resulting in a reduced ultimate load.

- For CFAT and CFDSAT columns, the bearing capacity of the members enhanced substantially with the increase of cross-sectional dimensions of the outer tube and compressive strength of concrete. This is because the larger cross-sectional dimensions provide higher flexural rigidity of the outer tube, which offers higher buckling resistance to composite section. Moreover, concrete provides significant cross-sectional resistance to the composite columns and improves the capacity of the hollow tube (outer tube for CFDSAT members) by preventing the occurrence of inward buckling and slowing down the formation of outward buckling. Hence, the higher grade of concrete adds more cross-sectional resistance and offers stronger support against the local buckling of the outer profile. Furthermore, it is also found that the improvement of ultimate capacity due to higher concrete grade is higher for the columns with bigger cross-sections than the smaller ones. It indicates that the bigger cross-section contains a larger concrete area which provides more cross-sectional resistance against the axial compression for higher concrete grades.

- For CFAT and CFDSAT flexural members, the larger cross-sectional dimensions of the hollow tube (outer tube for CFDSAT members) remarkably increased the flexural strength of the members. This can be attributed to the fact that the larger cross-sectional dimensions offer a higher moment of inertia of the outer tube as well as a larger concrete area, which leads to the enhancement of the bending capacity. However, it was observed that concrete compressive strength has a less significant

influence on the improvement of the flexural strength of composite beams. This is related to the fact that under in-plane bending, the concrete beneath the neutral axis, is in tension and the higher concrete grade offers a minor contribution to the enhancement of the tensile strength of concrete.

- For both CFDSAT columns and beam, the cross-sectional dimensions of the inner tube have a negligible effect on the ultimate capacity or bending strength of the members, as the inner tube provides the least buckling/bending resistance among the three components of the composite cross-sections.

The results obtained from experiments and numerical analysis of BAT members were used to assess the ultimate capacity predictions and the applicability of the cross-sectional slenderness limits provided in Eurocode 9 (2007). In the absence of design specifications for CFAT and CFDSAT structural members, design methodologies are proposed to predict the ultimate capacity of these composite members based on Eurocode 4 (2004) framework. Based on the comparison between the predicted ultimate capacities and the corresponding ones obtained from the experiments and FE analyses, the following design recommendations are proposed:

- The ultimate capacity predicting methodology for BAT columns and slenderness limits for Class A aluminium cross-sections provided by Eurocode 9 (2007) are conservative. Hence, a revised buckling curve and Class 1, Class 2 and Class 3 limits are proposed which appear to be better applicable to Class A aluminium alloy tubular sections.

- For the design of CFAT and CFDSAT columns, design buckling curves are proposed according to the obtained experimental and FE results. It was shown that the proposed methodologies can sufficiently predict the ultimate capacity of CFAT and CFDSAT structural members.

- Slenderness limits for CFAT and CFDSAT cross-sections are also proposed based on the data obtained from the experiments and FE analyses.

The sustainability of CFAT and CFDSAT columns was evaluated in terms of CO_2 emission and cost associated with their entire life using life-cycle assessment (LCA) and life-cycle cost analysis (LCCA), respectively. The environmental and economic

aspects of these structural members were compared with those of a conventional CFST column. For a fair comparison, the members were designed to have the same ultimate capacity. The cradle-to-grave system boundary was considered for the analysis. Moreover, to determine the lighter composite column the self-weight of these members was calculated and compared with each other. Based on the self-weight comparison and the findings of the sustainability study the following points can be summarised:

- The self-weight of the CFST column decreased by around 17% by replacing the steel tube with an aluminium alloy tube (i.e., CFAT column) when the outer depth and width are constant. Moreover, the self-weight of the CFST column reduced further which is around 47% when the double skin technique is adopted using aluminium alloy tubes (i.e., CFDSAT column).

- The LCA shows that CFAT column provides the lowest environmental impact, i.e., emits less CO_2 which is around 55% and 14% compared to the CFST and CFDSAT columns, respectively. While the carbon footprint of CFDSAT column is around 48% lower than that CFST column.

- The LCCA results indicate that the CFAT and CFDSAT columns are around 30% and 15% less expensive, respectively than the CFST one.

9.2 Recommendations for future research

The present study experimentally and numerically investigated the structural behaviour of aluminium alloy concrete-composite structural members subjected to concentric axial compression and pure bending. However, in most practical applications, compression structural members are subjected to a combination of axial compression force and bending moment, where flexure develops because of unavoidable eccentricities of axial force. For the design of such structural members bending moment versus axial load interaction curves are required, which are constructed by knowing the resistance of the members against pure compression, eccentric compression and pure bending. Therefore, further study is required to know the structural response of these composite members subjected to eccentric compression.

Fire safety is one of the major concerns in the design of aluminium alloy concrete-composite structural members, as the aluminium alloy can heat up quickly in the event

of a fire and suffer degradation in load-carrying capacity. In most cases, fire is extinguished before it spreads to the whole structure. Therefore, it is necessary to investigate the damage and examine the residual load-carrying capacity of the structural members after exposure to fire. To date, no research study exists that investigates the structural behaviour of CFAT and CFDSAT structural members at elevated temperatures or after exposure to fire. Hence, the material properties of aluminium alloy tubes, damage of concrete infill and residual load-carrying capacity of these structural members after exposure to elevated temperatures need to be investigated.

Aluminium alloys' excellent corrosion resistance property is mainly responsible for their popularity in the construction industry. Aluminium alloys contain a natural oxide layer which helps them to maintain their durability. However, under certain conditions, they are susceptible to corrosion. Previous studies (Wright, 1955; Monfore and Borje, 1965; McGeary, 1966) showed that aluminium alloys corroded severely when they were embedded in reinforced concrete that carries calcium chloride. This is because aluminium and steel form a galvanic cell when they are embedded in concrete. In this situation, aluminium and steel work as the anode and cathode, respectively, whereas concrete acts as the good electrolyte as it remains wet for many days after casting. As a result, a current starts to flow which causes corrosion of aluminium. This situation gets more worst when calcium chloride is added in the concrete to enhance its performance. Chloride breaks the protective oxide layer of aluminium, resulting in acceleration of its corrosion. Moreover, corrosive phenomena can rise when aluminium alloy contact with Portland cement concrete contains alkali hydroxide, which is not reported as being as severe as galvanic corrosion (Concrete Construction Magazine, 1965). To protect aluminium from being exposed to corrosive environments, some researchers suggested to use protective coating, such as bituminous or asphaltic or methacrylate resin paints (Monfore and Borje, 1965; McGeary, 1966; Woods, 1966). From the above discussion, it is clear that under different conditions, i.e., the presence of chloride and steel and the level of alkalinity aluminium can suffer corrosion. Therefore, more research is needed to know the corrosive behaviour of aluminium alloy used in composite structural members exposed to different unfavourable environments, particularly when different chemical additives are used in concrete.

Due to less self-weight aluminium alloy concrete-composite structural members can

provide better seismic performance to structural systems. By reviewing the literature presented in Chapter 2 it is found that all past studies are focused on the static behaviour of aluminium alloy concrete-composite structural members. However, the dynamic behaviour of these structural members is still unexplored. Hence, research studies are essential to have information about the structural behaviour of these composite members subjected to cyclic loading.

References

Aluminum Association (AA) (1967) ‘Aluminum construction manual: Specifications for aluminum structures’, *Washington, D.C., USA.*

Aluminum Association (AA) (1994) ‘Aluminum design manual’, *Washington, D.C., USA.*

Aluminum Association (AA) (2010) ‘Aluminum design manual’, *Washington, D.C., USA.*

Aluminum Association (AA) (2020) ‘Aluminum design manual’, *Washington, D.C., USA.*

Aluminum Company of America (AlCOA) (1958) ‘Alcoa structural handbook: A design manual for aluminum’, *Aluminum Company of America, Pittsburgh, Pennsylvania, USA.*

Architectural Institute of Japan (AIJ) (1997) ‘Recommendations for Design and Construction of Concrete Filled Steel Tubular Structures.’, *Architectural Institute of Japan, Tokyo, Japan*.

American Institute of Steel Construction (AISC) (2010) ‘Specification for structural steel buildings’, *ANSI/AISC 360-16, Chicago-Illinois, USA*.

ASCE Committee on Metals (1962) ‘Suggested specifications for structures of aluminum alloys 6061-T6 and 6062-T6’, *Journal of the Structural Division, ASCE*, 88(6), pp. 1-45.

ASCE Committee on Metals (1962) ‘Suggested specifications for structures of aluminum alloys 6063-T5 and 6063-T6’, *Journal of the Structural Division, ASCE*, 88(6), pp. 47-95.

Australian/New Zealand Standard (AS/NZS) (1997) ‘Aluminum structures part 1: Limit state design, AS/NZS 1664.1:1997’, *Standards Australia, Sydney, Australia*.

ABAQUS (2018) ‘ABAQUS Standard User’s Manual’, *Version 6.14. Providence, RI (USA): Dassault Systemes Corp*.

Abed, F., AlHamaydeh, M. and Abdalla, S. (2013) ‘Experimental and numerical investigations of the compressive behavior of concrete filled steel tubes (CFSTs)’, *Journal of Constructional Steel Research*, 80, pp. 429–439.

Abed, F.H., Abdelmageed, Y.I. and Ilgun, A.K. (2018) ‘Flexural response of concrete-filled seamless steel tubes’, *Journal of Constructional Steel Research*, 149, pp. 53–63.

Adeoti, Fan, F., Wang, Y.J. and Zhai, X.M. (2015) ‘Stability of 6082-T6 aluminum alloy columns with H-section and rectangular hollow sections’, *Thin-Walled Structures*, 89, pp. 1–16.

Ahmed, M., Liang, Q.Q., Hamoda, A. and Arashpour, M. (2022) ‘Behavior and design of thin-walled double-skin concrete-filled rectangular steel tubular short and slender columns with external stainless-steel tube incorporating local buckling effects’, *Thin-Walled Structures*, 170(108552).

Alqawzai, S., Chen, K., Shen, L., Ding, M. and Yang, B. (2020) ‘Elchalakani M. Behavior of octagonal concrete-filled double-skin steel tube stub columns under axial

compression', *Journal of Constructional Steel Research*, 170(106115).

Al Zand, A.W., Badaruzzaman, W.H.W., Al-Shaikhli, M.S., Ali, M.M. (2020) 'Flexural performance of square concrete-filled steel tube beams stiffened with V-shaped grooves', *Journal of Constructional Steel Research*, 166(105930).

Aslani, F., Ma, G., Wan, D.L.Y. and Muselin, G. (2018) 'Development of high-performance self compacting concrete using waste recycled concrete aggregates and rubber granules', *Journal of Cleaner Production*, 182, pp. 553–66.

Aslani, F., Uy, B., Hur, J. and Carino, P. (2017) 'Behaviour and design of hollow and concrete-filled spiral welded steel tube columns subjected to axial compression', *Journal of Constructional Steel Research*, 128, pp. 261–288.

Baehre, R. (1966) 'Compression between structural behaviour of elastoplastic materials', *Tekn. Dr Arne Johnson Ingenjosbyra, Report No. 16.*

Bathe, K.J. (1982) 'Finite Element Procedures for Solids and Structures - Linear Analysis', *Finite Element Procedures*, pp. 148–214.

Bathe, K.J. and Wilson, E.L. (1973) 'Solution methods for eigenvalue problems in structural mechanics', *International Journal for Numerical Methods in Engineering*, 6(2), pp. 213–226.

Bažant, Z. and Becq-Giraudon, E. (2002) 'Statistical prediction of fracture parameters of concrete and implications for choice of testing standard.', *Cement and Concrete Research*, 32(4), pp. 529–556.

Benson, P. (1990) 'Local and flexural buckling of eccentrically loaded square, thinwalled aluminum alloy columns', Royal Inst.

Bernard, A. and Frey, F. (1971) 'Research on the behaviour of aluminum columns against buckling', *University of Liège, Laboratories for testing materials and stability of constructions*, Liège, Bel.

Beton, F.I.D. (2004) 'Environmental design: state-of-the-art report: International federation for structural concrete (fib)'.

Blue Circle (2023) *Blue Circle Multipurpose Cement, 25kg Bag*. Available at: https://www.diy.com/departments/blue-circle-multipurpose-cement-25kg-bag/35715_BQ.prd.

BS 5400-5 (2005) 'Steel, Concrete and Composite Bridges— Part 5: Code of Practice for the Design of Composite Bridges', *British Standards Institution (BSI), London, UK*.

Brungraber, R.J. and Clark, J.W. (1962) 'Strength of welded aluminum columns', *Jouranl of Structural Division, ASCE*, 127.

BS EN 12390-3 (2009) 'Testing hardened concrete. Compressive strength of test specimens', *European Committee for Standardization (CEN), Brussels*.

BS EN ISO 14040 (2006) 'Environmental management - Life cycle assessment - Principles and framework', *European Committee for Standardization (CEN), Brussels*.

BS EN ISO 6892-1 (2009) 'Metallic Materials – Tensile Testing – Part 1: Method of Test at Room Temperature', *European Committee for Standardization (CEN), Brussels*.

Chan, T. and Aibinu, A. (2012) 'A comparison of construction cost and technology choice', *Economics*, pp. 61–72.

Chang, Y., Liu, M. and Wang, P. (2016) 'Interacted buckling failure of thin-walled irregular-shaped aluminum alloy column under axial compression', *Thin-Walled Structures*, 107, pp. 627–647.

Chang, Y. Liu, M., Wang, P. and Li, X. (2017) 'Behaviors and design method for distortional buckling of thin-walled irregular-shaped aluminum alloy struts under axial compression', *Engineering Structures*, 153, pp. 118–135.

Chen, J. and Chan, T.M. (2019) 'Experimental assessment of the flexural behaviour of concrete-filled steel tubular beams with octagonal sections', *Engineering Structures*, 199(109604).

Chen, J., Wang, J., Xie, F. and Jin, W.L. (2016) 'Behavior of thin-walled dodecagonal section double skin concrete-filled steel tubes under bending', *Thin-Walled Structures*, 98, pp. 293–300.

Chen, S., Zhang, R., Jia, L.J., Wang, J.Y. and Gu, P. (2018) 'Structural behavior of UHPC filled steel tube columns under axial loading', *Thin-Walled Structures*, 130, pp. 550–563.

Chen, Y., Feng, R. and Wang, L. (2017) 'Flexural behaviour of concrete-filled stainless steel SHS and RHS tubes', *Engineering Structures*, 134, pp. 159–171.

Chen, Y., Feng, R. and Gong, W. (2018) 'Flexural behavior of concrete-filled aluminum alloy circular hollow section tubes', *Construction and Building Materials*, 165, pp. 295–319.

Chen, Y., Feng, R. and Xu, J. (2017) 'Flexural behaviour of CFRP strengthened concrete-filled aluminium alloy CHS tubes', *Construction and Building Materials*, 142, pp. 295–319.

Chen, Y., Wang. K., Feng. R., He, K. and Wang, L. (2017) 'Flexural behaviour of concrete-filled stainless steel CHS subjected to static loading', *Journal of Constructional Steel Research*, 139, pp. 30–43.

Cho, S.H. and Chae, C.U. (2016) 'A Study on Life Cycle CO2 Emissions of Low-Carbon Building in South Korea', *Sustainability*, 8.

Chopra, A.K. (2017) 'Dynamics of structures: theory and applications to earthquake engineering', *5th edition, Prentice Hall, Englewood Cliffs*, New Jersey, USA.

Concrete Construction Magazine (1965) 'The aluminum and concrete controversy', *The Aberdeen Group*.

Clark, J.W. (1955) 'Eccentrically loaded aluminum columns', *ASCE Trans.*, 120, pp. 1116–1132.

Clark, J.W. and Jombock, J.R. (1957) 'Lateral Buckling of I-beams Subjected to Unequal End Moments', *Journal of the Engineering Mechanics Division, ASCE*, 83.

Clark, J.W., Richard, L. and Rolf, A.M. (1966) 'Buckling of Aluminium Columns, Plates, and Beams', *Journal of Structural Division*, 92(3), pp. 17–38.

Dai, X. and Lam, D. (2010) 'Numerical modelling of the axial compressive behavior of short concrete-filled elliptical steel columns', *Journal of Constructional Steel Research*, 66(7), pp. 931–942.

Davis, J.R. (2001) 'Alloying: Understanding the Basics', *ASM International*, pp. 351–416.

Duarte, A.P.C., Silvestre, N., Brito, J.D., Júlio, E. and Silvestre, J.D. (2018) 'On the sustainability of rubberized concrete filled square steel tubular columns', *Journal of Cleaner Production*, 170, pp. 510–521.

Earij, A., Alfano, G., Cashell, K. and Zhou, X. (2017) 'Nonlinear three–dimensional finite–element modelling of reinforced-concrete beams: Computational challenges and experimental validation', *Engineering Failure Analysis*, 82, pp. 92–115.

Elchalakani, M., Ayough, P. and Yang, B. (2022) 'Single Skin and Double Skin Concrete Filled Tubular Structures', *Woodhead Publishing Series in Civil and Structural Engineering*, *Elsevier*, pp. 29–166.

Elchalakani, M., Zhao, X.L. and Grzebieta, R. (2002) 'Tests on concrete filled double-skin (CHS outer and SHS inner) composite short columns under axial compression', *Thin-Walled Structures*, 40, pp. 415–441.

Ellobody, E.; Young, B. (2006) 'Nonlinear analysis of concrete-filled steel SHS and RHS columns', *Thin-Walled Structures*, 44, pp. 919–930.

Eom, S-S., Vu, Q-V., Choi, J-H., Park, H-H. and Kim, S.-E. (2019) 'Flexural behavior of concrete-filled double skin steel tubes with a joint', *Journal of Constructional Steel Research*, 155, pp. 260–272.

Eurocode 1 (EC1) (2002) 'Eurocode 1: Actions on structures - Part 1-1: General actions - Densities, self-weight, imposed loads for buildings', *European Committee for Standardisation (CEN)*, EN 1991-1-1.

Eurocode 3 (EC3) (2005) 'Eurocode 3: Design of steel structures - Part 1-1: General rules and rules for buildings', *European Committee for Standardisation (CEN)*, EN 1993-1-1.

Eurocode 4 (EC4) (2004) 'Eurocode 4: Design of Composite Steel and Concrete Structures. Part 1-1: General Rules and Rules for Buildings', *European Committee for Standardisation (CEN)*, EN 1994-1-1.

Eurocode 9 (EC9) (2007) 'Eurocode 9: Design of Aluminium Structures - Part 1-1 : General Structural Rules. EN-1991-1-1', *European Committee for Standardisation (CEN)*, EN 1999-1-1.

European Aluminium (EA) (2018), 'Environmental profile report: Life-Cycle inventory data for aluminium production and transformation processes in Europe', *Executive Summary*.

European Aluminium (EA) (2021), 'Environmental profile report: for the aluminium refining industry', *Executive Summary*.

Faella, C. Mazzolani, F.M., Piluso, V. and Rizzano, G. (2000) 'Local Buckling of Aluminum Members: Testing and Classification', *Journal of Structural Engineering*, ASCE, 126(3), pp. 353–360.

Fam, A., Qie, F.S. and Rizkalla, S. (2004) 'Concrete-filled steel tubes subjected to axial compression and lateral cyclic loads', *Jouranl of Structural Engineering, ASCE*, 130, pp. 631–640.

Feng, R., Chen, Y. and Gong, W. (2017) 'Flexural behaviour of concrete-filled aluminium alloy thin-walled SHS and RHS tubes', *Engineering Structures*, 137, pp. 33–49.

Feng, R. and Liu, J. (2019) 'Numerical investigation and design of perforated

aluminium alloy SHS and RHS columns', *Engineering Structures*, 199, p. 109591.

Feng, R., Mou, X., Chen, A. and Ma, Y. (2016) 'Tests of aluminium alloy CHS columns with circular openings', *Thin-Walled Structures*, 109, pp. 113–131.

Feng, R., Mou, X., Chen, Z., Roy, K., Chen, B. and Lim, J.B.P. (2020) 'Finite-element modelling and design guidelines for axial compressive capacity of aluminium alloy circular hollow sections with holes', *Thin-Walled Structures*, 157(107027).

Feng, R., Sun, W., Shen, C. and Zhu, J. (2017) 'Experimental investigation of aluminum square and rectangular beams with circular perforations', *Engineering Structures*, 151, pp. 613–632. doi:10.1016/j.engstruct.2017.08.053.

Feng, R. and Young, B. (2015) 'Experimental Investigation of Aluminum Alloy Stub Columns with Circular Openings', *J. Struct. Eng. ASCE*, 141(11), p. 04015031.

Feng, R., Zhu, W., Wan, H., Chen, A. and Chen, Y. (2018) 'Tests of perforated aluminium alloy SHSs and RHSs under axial compression', *Thin-Walled Structures*, 130, pp. 194–212.

FIP (1993) 'Ceb-Fip Model Code 1990', *Ceb-Fip Model Code 1990* [Preprint]. doi:10.1680/ceb-fipmc1990.35430.

Furlong, R.W. (1967) 'Strength of steel-encased concrete beam-columns', *Jouranl of Structural Division, ASCE*, 93(ST5), pp. 113–124.

Gardner, N.J. and Jacobson, E.R. (1967) 'Structural behavior of concrete filled steel tubes', *Journal of the American Concrete Institute*, 64, pp. 404–413.

Gardner, L., Cruise, R.B., Sok, C.P., Krishnan, K. and Ministro, J. (2007) 'Life cycle costing of metallic structures', *Proceedings of the Institution of Civil Engineers - Engineering Sustainability*, 160(4), pp. 167–177.

Gardner, L., Talja, A. and Baddoo, N. (2006) 'Structural design of high-strength austenitic stainless steel', *Thin-Walled Structures*, 44(5), pp. 517–528.

Gendy, B.L. and Hanna, M.T. (2017) 'Effect of geometric imperfections on the ultimate moment capacity of cold-formed sigma-shape sections', *HBRC Journal*, 13, pp. 163–170.

Georgantzia, E., Gkantou, M. and Kamaris, G.S. (2021) 'Aluminium alloys as structural material: A review of research', *Engineering Structures*, 227, 111372.

Georgantzia, E., Gkantou, M., Kamaris, G.S. and Kansara, K.D. (2022) 'Ultimate response and plastic design of aluminium alloy continuous beams', *Structures*, 39, pp. 175–193.

Gkantou, M., Kokosis, G., Theofanous, M. and Dirar, S. (2019) 'Plastic design of stainless steel continuous beams', *Journal of Constructional Steel Research*, 152(68–80).

Gruber, B., Weißensteiner, I., Kremmer, T., Grabner, F., Falkinger, G., Schökel, A, Spieckermann, F., Schäublin, R., Uggowitzer, P.J. and Pogatscher, S. (2020) 'Mechanism of low temperature deformation in aluminium alloys', *Materials Science & Engineering A*, 795(139935).

Gunawardena, Y. and Aslani, F. (2020) 'Static flexural behaviour of concrete-filled spiral-weldedmild-steel tubes', *Journal of Constructional Steel Research*, 166(105915).

Gupta, P.K., Sarda, M.S. and Kumar, M.S. (2007) 'Experimental and computational

study of concrete filled steel tubular columns under axial loads', *Journal of Constructional Steel Research*, 63, pp. 182–193.

Han, L.H. (2004) 'Flexural behaviour of concrete-filled steel tubes', *Journal of Constructional Steel Research*, 60, pp. 313–337.

Han, L.H., Li, Y.J. and Lao, F.Y. (2011) 'Concrete-filled double skin steel tubular (CFDST) columns subjected to long-term sustained loading', *Thin-Walled Structures*, 49, pp. 1534–1543.

Han, L.H., Tao, Z., Huang, H. and Zhao, X.L. (2004) 'Concrete-filled double skin (SHS outer and CHS inner) steel tubular beam-columns', *Thin-Walled Structures*, 42, pp. 1329–1355.

Han, L.H., Yao, G.H. and Zhao, X.L. (2005) 'Tests and calculations for hollow structural steel (HSS) stub columns filled with self-consolidating concrete (SCC)', *Journal of Constructional Steel Research*, 61, pp. 1241–1269.

Hamunzala, B. and Teklemariam, D. (2016) 'Design of thick concrete beams using non-linear FEM', *Master of Science thesis*, KTH royal institute of technology. Stockholm, Sweden.

Hassanein, M.F. and Kharoob, O.F. (2014) 'Analysis of circular concrete-filled double skin tubular slender columns with external stainless steel tubes', *Thin-Walled Structures*, 79, pp. 23–37.

Hastak, M. and Halpin, D.W. (2000) 'Assessment of life-cycle benefit-cost of composites in construction', *J Compos Constr*, 4, pp. 103–111.

Hastak, M., Mirmiran, A. and Richard, D. (2003) 'A framework for life-cycle cost assessment of composites in construction', *Journal of Reinforced Plastic and Composites*, 22(15), pp. 1409–1430.

Hatzigeorgiou, G.D. (2008) 'Numerical model for the behavior and capacity of circular CFT columns, part I: theory', *Engineering Structures*, 30, pp. 1573–1578.

Hauschild, M.Z., Rosenbaum, R.K. and Olsen, S.I. (2018), 'Life Cycle Assessment: Theory and Practice', *Springer*.

Hibbitt, Karlsson & Sorensen and Inc. (2012) 'ABAQUS. ABAQUS/Standard User's Manual Volumes I–III and ABAQUS CAE Manual.', *Pawtucket, USA: Dassault Systèmes*.

Hill, H.N. (1942) 'The Lateral Instability of Unsymmetrical I Beams', *Journal of the Aeronautical Sciences*, 9.

Hill, H.N. (1944) 'Determination of stress-strain relations from the offset yield strength values', *Technical Note No. 927. National Advisory Committee for Aeronautics. Washington, D.C.*.

Hill, H.N. (1954) 'Lateral Buckling of Channels and Z-beams', *Transactions, A.S.C.E.*, 119.

Hill, H.N. and Clark, J.W. (1951) 'Lateral buckling of eccentrically loaded I-section columns', *ASCE Trans.*, 116, pp. 1179–1196.

Hill, H.N. and Clark, J.W. (1955) 'Straight-line column formulas for aluminum alloys', *Alcoa Technical Paper*, No. 12.

Hill, H.N., Hartmann, E.C. and Clark, J.W. (1956) 'Design of aluminum alloy beam-

columns', *ASCE Trans.*, 121, pp. 1–21.

Hopperstad, O.S., Langseth, M. and Tryland, T. (1999) 'Ultimate compressive strength of aluminum alloy outstands in compression: experiments and simplified analysis', *Thin-Walled Structures*, 34, pp. 279–294.

Hordijk, D. (1991) 'Local approach to fatigue of concrete', *PhD thesis*, Delft Univ. of Technology. Delft, Netherlands.

Hou, CC. and Han, L.H. (2018) 'Life-cycle performance of deteriorated concrete-filled steel tubular (CFST) structures subject to lateral impact', *Thin-Walled Structures*, 132, pp. 362–374.

Hou, C.C., Han, L.H., Wang, Q.L. and Hou, C. (2016) 'Flexural behavior of circular concrete filled steel tubes (CFST) under sustained load and chloride corrosion', *Thin-Walled Structures*, 107, pp. 182–196.

Hu, H.T., Huang, C.S., Wu, M.H. and Wu, Y.M. (2003) 'Nonlinear analysis of axially loaded concrete-filled tube columns with confinement effect', *Jouranl of Structural Engineering, ASCE*, 129, pp. 1322–1329.

Huang, C.S., Yeh, Y.K., Liu, G.Y., Hu, H.T., Tsai, K.C., Weng, Y.T., Wang, S.H. and Wu, M.H. (2002) 'Axial load behavior of stiffened concrete-filled steel columns', *Journal of structural engineering, ASCE*, 128, pp. 1222–1230.

Huang, H., Han, L.H., Tao, Z., Zhao, X.L. (2010) 'Analytical behaviour of concrete-filled double skin steel tubular (CFDST) stub columns', *Journal of Constructional Steel Research*, 66(4), pp. 542–555.

Ibañez, C., Hernández-Figueirido, D. and Piquer, A. (2018) 'Shape effect on axially loaded high strength CFST stub columns', *Journal of Constructional Steel Research*, 147, pp. 247–256.

Jiang, L., Wang, C., Fu, H., Shen, J., Zhang, Z. and Xie, J. (2022) 'Discovery of aluminum alloys with ultra-strength and high-toughness via a property-oriented design strategy', *Journal of Materials Science & Technology*, 98, pp. 33–43.

Johansson, M. and Gylltoft, K. (2002) 'Mechanical behavior of circular steel-concrete composite stub columns', *Jouranl of Structural Engineering, ASCE*, 128, pp. 1073–1081.

Kato, B. (1995) 'Compressive strength and deformation capacity of concrete-filled tubular stub columns (strength and rotation capacity of concrete-filled tubular columns, part 1)', *Journal of Structural and Construction Engineering, AIJ*, 468, pp. 183–191.

Kaufman, J.G. (2000) 'Introduction to aluminum alloys and tempers', *ASM International*, pp. 9–22.

Kim, Y. and Peköz, P. (2010) 'Ultimate flexural strength of aluminum sections', *Thin-Walled Structures*, 48(10–11), pp. 857–865.

Kissell, J. and Ferry, R.L. (2002) 'Aluminum structures: a guide to their specifications and design', *2nd edition, New York: John Wiley & Sons*.

Knowles, R.B. and Park, R. (1969) 'Strength of concrete filled steel tubular columns', *Journal of the Structural Division, ASCE*, 95, pp. 2565–2587.

Lai, Y.F.W. and Nethercot, D.A. (1992) 'Strength of aluminum members containing local transverse welds', *Engineering Structures*, 14(4), pp. 241–254.

Lam, D. and Wong, K. (2005) 'Axial capacity of concrete filled stainless steel columns', *ASCE Journal of Structures*, pp. 1107–1120.

Li, D., Uy, B., Aslani, F. and Hou, C. (2019) 'Behaviour and design of spiral-welded stainless steel tubes subjected to axial compression', *Journal of Constructional Steel Research*, 154, pp. 67–83.

Li, G., Liu, D., Yang, Z. and Zhang, C. (2017) 'Flexural behavior of high strength concrete filled high strength square steel tube', *Journal of Constructional Steel Research*, 128, pp. 732–744.

Li, W., Ren, Q.X., Han, L.H. and Zhao, X.L. (2012) 'Behaviour of tapered concrete-filled double skin steel tubular (CFDST) stub columns', *Thin-Walled Structures*, 57, pp. 37–48.

Liao, F.Y., Hou, C., Zhang, W.J. and Ren, J. (2019) 'Experimental investigation on sea sand concrete-filled stainless steel tubular stub columns', *Journal of Constructional Steel Research*, 155, pp. 46–61.

Linear Recruitment (LR) (2021) *Highest paying construction jobs in the UK*. Available at: https://www.linearrecruitment.co.uk/news/highest-paying-construction-jobs-uk.

Liu, H, Xiong, Y., Chen, Z., Ouyang, Y. and Mashrah, W.A.H. (2022) 'Compressive performance of H-shaped aluminium alloy members with web openings', *Engineering Structures*, 266(114595).

Liu, M., Zhang, L., Wang, P. and Chang, Y. (2015a) 'Buckling behaviors of irregular section aluminum alloy columns under axial compression', *Engineering Structures*, 95, pp. 127–137.

Liu, M. Zhang, L., Wang, P. and Chang, Y. (2015b) 'Experimental investigation on local buckling behaviors of stiffened closed-section thin-walled aluminum alloy columns under compression', *Thin-Walled Structures*, 94, pp. 188–198.

Liu, Z., Lu, Y., Li, S., Zong, S. and Yi, S. (2020) 'Flexural behavior of steel fiber reinforced self-stressing recycled aggregate concrete-filled steel tube', *Journal of Cleaner Production*, 274(122724).

Lu, F.W., Li, S.P., Li, D.W. and Sun, G.J. (2007) 'Flexural behavior of concrete filled non-uni-thickness walled rectangular steel tube', *Journal of Constructional Steel Research*, 63(8), pp. 1051–1057.

Lu, Y., Liu, Z., Li, S. andLi, W. (2017) 'Behavior of steel fibers reinforced self-stressing and self-compacting concrete-filled steel tube subjected to bending', *Construction and Building Materials*, 156, pp. 639–651.

Lu, Y.Q. and Kennedy, D.J.L. (1994) 'The flexural behaviour of concrete-filled hollow structural sections', *Canadian Journal of Civil Engineering*, 21(1), pp. 111–130.

Marin, J. (1947) 'Creep deflections in columns', *Journal of Applied Physics*, 18(1), pp. 103–109.

Matteis, G.D., Moen, L.A., Langseth, M., Landolfo, R., Hopperstad, O.S. and Mazzolani, F.M. (2001) 'Cross-sectional classification for aluminium beams - parametric study', *Journal of Structural Engineering, ASCE*, 127(3), pp. 271–279.

Mazzolani, F.M. (1972) 'Characterization of the σ-ε law and buckling of aluminium columns', *Construction Metallic, No.3*.

Mazzolani, F.M. (1975) ‘Residual Stress Tests Alu-Alloy Austrian Profiles’, *ECCS Committee, Brussels, Technical Report, Doc*, Doc 16-75.

Mazzolani, F.M. (1995) ‘Aluminium alloy structures’, *2nd ed. London: Chapman & Hall*.

McAteer, P., Bonacci, J.F. and Lachemi, M. (2004) ‘Composite response of high-strength concrete confined by circular steel tube’, *ACI Structural Journal*, 101, pp. 466–474.

McGeary, F. (1966) ‘Performance of aluminum in concrete containing chlorides’, *Journal of the American Concrete Institute*, 63(9), pp. 247–265.

McLennan, J.F. (2004) ‘The Philosophy of Sustainable Design’, *Bainbridge Island, WA: Ecotone Publishing Company LLC*.

Metalsupermarkets (2023) *Mild Steel Square Tube S235/S275*. Available at: https://www.metalsupermarkets.co.uk/product/mild-steel-square-tube-s235-s275/.

Milan, C.C., Albareda-Valls, A., Carreras, J.M. (2019) ‘Evaluation of structural performance between active and passive preloading systems in circular concrete-filled steel tubes (CFST)’, *Engineering Structures*, 194(207–219).

Milan, C.C., Albareda-Valls, A. and Carreras, J.M. (2019) ‘Evaluation of structural performance between active and passive preloading systems in circular concrete-filled steel tubes (CFST)’, *Engineering Structures*, 194, pp. 207–219.

Mises, V. (1913) ‘Mechanik der festen Körper in plastisch-deformablen Zustand’, *Nachr. Ges. Wiss. Gottingen*, pp. 582–592.

Moen, L.A., Langseth, M. and Hopperstad, O.S. (1999a) ‘Rotational capacity of aluminium beams under moment gradient. I: experiments’, *Journal of Structural Engineering, ASCE*, 125(8), pp. 910–920.

Moen, L.A., De Matteis, G., Hopperstad, O.S., Langseth, M., Landolfo, R. and Mazzolani, M. (1999b) ‘Rotational capacity of aluminium beams under moment gradient II: numerical simulations’, *Journal of Structural Engineering, ASCE*, 125(8), pp. 921–929.

Monfore, G.E. and Borje, O. (1965) ‘Corrosion of aluminum conduit in concrete’, *Journal Portland Cement Assoc. Research and Development Laboratories*, 7(1), pp. 10–22.

Montuori, R. and Piluso, V. (2015) ‘Analysis and modeling of CFT members: moment curvature analysis’, *Thin-Walled Structures*, 86, pp. 157–166.

Morino, S. and Tsuda, K. (2002) ‘Design and construction of concrete-filled steel tube column system in Japan’, *Earthquake Engineering and Engineering Seismology*, 4(1), pp. 51–73.

Morino, S., Uchikoshi, M. and Yamaguchi, I. (2001) ‘Concrete-filled steel tube column system-its advantages’, *International Journal of Steel Structures*, 1(1), pp. 33–44.

Müller, H.S., Breiner, R., Moffatt, J.S. and Haist, M. (2014) ‘Design and properties of sustainable concrete’, *Procedia Engineering*, 95, pp. 290–304.

Nicolo, B.D., Pani, L. and Pozzo, E. (1994) ‘Strain of concrete at peak compressive stress for a wide range of compressive strengths’, *Materials and Structures*, 27(4), pp. 206–210.

One Click LCA (2020) ‘Low-carbon aluminium: solution for sustainable construction and renovation’, *Whitepaper - June 2020*.

Oliveira, W.L.A.D., Nardin, S.D., Debs, A.L.H.D.E. and Debs, M.K.E. (2010) ‘Evaluation of passive confinement in CFT columns’, *Journal of Constructional Steel Research*, 66, pp. 487–495.

Osgood, W. and Holt, M. (1939) ‘The Column Strength of Two Extruded Aluminium Alloy H-Sections’, *Report No. 656, National advisory committee for aeronautics*.

Panlilo, F. (1947) ‘The theory of limit design applied to magnesium alloy and aluminum alloy structures’, *Journal of the Aeronautical Society*, 51(438), pp. 534–571.

Papanikolaou, V. and Kappos, A. (2007) ‘Confinement-sensitive plasticity constitutive model for concrete in triaxial compression’, *International Journal of Solids and Structures*, 44(21), pp. 7021–7048.

Patel, V.I., Liang, Q. and Hadi, M.N. (2019) ‘Numerical study of circular double-skin concrete-filled aluminum tubular stub columns’, *Engineering Structures*, 197, 109418.

Patel, V.I., Liang, Q.Q. and Hadi, M.N. (2020) ‘Numerical simulations of circular high strength concrete-filled aluminum tubular short columns incorporating new concrete confinement model’, *Thin-Walled Structures*, 147, 106492.

Ramberg, W. and Osgood, W.R. (1943) ‘Description of stress-strain curves by three parameters’, *Washington, D.C: National Advisory Committee for Aer-onautics*, Technical.

Rasmussen, K.J.R. and Rondal, J. (2000) ‘Strength curves for aluminum alloy columns’, *Engineering Structures*, 23, pp. 1505–1517.

Resapol (2023) *Stone 10mm 25kg*. Available at: https://www.resapol.com/product/limestone-10mm-25kg/.

Rossi, B., Lukic, I., Iqbal, N., Du, G.L., Cregg, D., Borg, R.P. and Haller, P. (2011) ‘Life cycle impacts assessment of steel, composite, concrete and wooden columns’, in *International Conference; Final Conference of the COST Action C25*, pp. 277–284.

Russell-Smith, S.V. and Lepech, M.D. (2009) ‘Life cycle assessment of frp seismic retrofitting’, in *US-Japan workshop on life cycle assessment of sustainable infrastructure materials*.

Sakino, K., Nakahara, H., Morino, S. and Nishiyama, A. (2004) ‘Behavior of centrally loaded concrete-filled steel-tube short columns’, *Jouranl of Structural Engineering, ASCE*, 130, pp. 180–188.

Samani, A. and Attard, M. (2012) ‘A stress–strain model for uniaxial and confined concrete under compression’, *Engineering Structures*, 41, pp. 335–349.

Schneider, S.P. (1998) ‘Axially loaded concrete-filled steel tubes’, *Jouranl of Structural Division, ASCE*, 124, pp. 1125–1138.

Scrapmetalpricesuk (2023) *Scrap metal prices UK*. Available at: http://www.scrapmetalpricesuk.co.uk/.

Silva, R.V., De Brito, J. and Dhir, R.K. (2017) ‘Availability and processing of recycled aggregates within the construction and demolition supply chain: A review’, *Journal of Cleaner Production*, 143, pp. 598–614.

Simmal (2023) *Aluminium Square/Rectangular tube*. Available at:

https://www.simmal.com/product/aluminium-rectangular-tube/.

Starossek, U., Falah, N. and Lohning, T. (2010) 'Numerical analyses of the force transfer in concrete-filled steel tube columns', *Structural Engineering and Mechanics*, 35(2), pp. 241–256.

Su, M.N. (2014) 'Behaviour and design of aluminium alloy structural elements', *PhD thesis*, Joint Doctor of Philosophy at Imperial College London, UK and The University of Hong Kong, Hong Kong.

Su, M.N., Young, B. and Gardner, L. (2017) 'Classification of Aluminium Alloy Cross-sections', *Engineering Structures*, 141, pp. 29–40.

Su, M.N., Young, B. and Gardner, L. (2014a) 'Testing and design of aluminum alloy cross sections in compression', *J. Struct. Eng. ASCE*, 140(9), p. 04014047.

Su, M.N., Young, B. and Gardner, L. (2014b) 'Deformation-based design of aluminium alloy beams', *Engineering Structures*, 80, pp. 339–349.

Su, M.N., Young, B. and Gardner, L. (2015) 'Continuous beams of aluminum alloy tubular cross sections. I: tests and model validation', *Journal of Structural Engineering, ASCE*, 141(9), p. 04014232.

Su, M.N., Young, B. and Gardner, L. (2016) 'Flexural response of aluminium alloy SHS and RHS with internal stiffeners', *Engineering Structures*, 121, pp. 170–180.

Sulthana, U.M. and Jayachandran, S.A. (2017) 'Axial compression behaviour of long concrete filled double skinned steel tubular columns', *Structures*, 9, pp. 157–164.

Tao, Z. and Han, L.H. (2006) 'Behaviour of concrete-filled double skin rectangular steel tubular beam–columns', *Journal of Constructional Steel Research*, 62, pp. 631–646.

Tao, Z., Han, L.H. and Zhao, X.L. (2004) 'Behaviour of concrete-filled double skin (CHS inner and CHS outer) steel tubular stub columns and beam-columns', *Journal of Constructional Steel Research*, 60, pp. 1129–1158.

Tao, Z. Uy, B., Liao, F.Y. and Han, L.H. (2011) 'Nonlinear analysis of concrete-filled square stainless steel stub columns under axial compression', *Journal of Constructional Steel Research*, 67, pp. 1719–1732.

Tao, Z., Wang, Z.B. and Yu, Q. (2013) 'Finite element modelling of concrete-filled steel stub columns under axial compression', *Journal of Constructional Steel Research*, 89, pp. 121–131.

Templin, R.L., Strum, R.G., Hartman, E.C. and Holt, M. (1938) 'Column strength of various aluminum alloys', *Aluminum research laboratories, Pittsburgh, Aluminum Co. of America*, Technical.

Tsuruta, A., Sakurai, J. and Horikawa, K. (1972) 'Buckling strength of welded aluminium columns', *Trans. Jpn. Weld. Soc.*, 3(2), pp. 285–291.

Tziavos, N.I., Gkantou, M., Theofanous, M., Dirar, S. and Baniotopoulos, C. (2020) 'Behaviour of grout-filled double-skin tubular steel stub-columns: Numerical modelling and design considerations', *Structures*, 27, pp. 1623–1636.

Uenaka, K., Kitoh, H. and Sonoda, K. (2008) 'Concrete filled double skin tubular members subjected to bending', *Steel and Composite Structures*, 8(4), pp. 297–312.

Uenaka, K., Kitoh, H. and Sonoda, K. (2010) 'Concrete filled double skin circular stub columns under compression', *Thin-Walled Structures*, 48, pp. 19–24.

Valtinat, G. and Müller, R. (1977) 'Ultimate load of beam columns in aluminum alloys with longitudinal and transversal welds', *Second Int. Coll. Stability, Prelim. Rep.*, Liège, pp. 393–402.

Wang, F., Young, B. and Gardner, L. (2019) 'Compressive testing and numerical modelling of concrete-filled double skin CHS with austenitic stainless steel outer tubes', *Thin-Walled Structures*, 141, pp. 345–359.

Wang, F., Young, B. and Gardner, L. (2020a) 'CFDST sections with square stainless steel outer tubes under axial compression: Experimental investigation, numerical modelling and design', *Engineering Structures*, 207(110189).

Wang, F., Young, B. and Gardner, L. (2020b) 'Compressive behaviour and design of CFDST cross-sections with stainless steel outer tubes', *Journal of Constructional Steel Research*, 170(105942).

Wang, F., Young, B. and Gardner, L. (2021) 'Testing and numerical modelling of circular CFDST cross-sections with stainless steel outer tubes in bending', *Engineering Structures*, 247(113170).

Wang, F., Zhao, H. and Han, L. (2019) 'Analytical behavior of concrete-filled aluminum tubular stub columns under axial compression', *Thin-Walled Structures*, 140, pp. 21–30.

Wang, J., Afshan, S., Gkantou, M., Theofanous, M., Baniotopoulos, C. and Gardner, L. (2016) 'Flexural behaviour of hot-finished high strength steel square and rectangular hollow sections', *Journal of Constructional Steel Research*, 121, pp. 97–109.

Wang, Y, Cao, M-M. and Sun, H. (2014) 'Time-dependent reliability analysis of circular CFST stub columns under environment corrosion', *Pacific Science Review*, 16(3), pp. 201–206.

Wang, Y., Fan, F. and Lin, S.B. (2015) 'Experimental investigation on the stability of aluminum alloy 6082 circular tubes in axial compression', *Thin-Walled Structures*, 89, pp. 54–66.

Wang, Y., Lin, S., Feng, F., Zhai, X. and Qian, H. (2016) 'Numerical simulation of aluminum alloy 6082-T6 columns failing by overall buckling', *Advances in Structural Engineering*.

Wang, Y.Q., Wang, Z.X., Hu, X.G., Han, J.K. and Xing, H.J. (2016) 'Experimental study and parametric analysis on the stability behavior of 7A04high-strength aluminum alloy angle columns under axial compression', *Thin-Walled Structures*, 108, pp. 305–320.

Wang, Y.Q., Yuan, H.X., Chang, T., Du, X.X. and Yu, M. (2017) 'Compressive buckling strength of extruded aluminium alloy I-section columns with fixed-pinned end conditions', *Thin-Walled Structures*, 119, pp. 396–403.

Wang, Z.X., Wang, Y.Q., Sejeong, J. and Ouyang, Y.W. (2018) 'Experimental investigation and parametric analysis on overall buckling behavior of large-section aluminum alloy columns under axial compression', *Thin-Walled Structures*, 122, pp. 585–596.

Wickes (2023) *Building sand*. Available at: https://www.wickes.co.uk/Tarmac-Building-Sand---Jumbo-Bag/p/131889.

Worldsteel Association (WA) (2021) *Life cycle inventory (LCI) study, Seventh global*

LCI study for steel products.

Wright, T.E. (1955) ‘An unusual case of corrosion of aluminum conduit in concrete’, *The Engineering Journal*, 38(10), p. 1357-1362.

Xiong, M-X., Xiong, D-X. and Liew, J.Y.R. (2017) ‘Flexural performance of concrete filled tubes with high tensile steel and ultra-high strength concrete’, *Journal of Constructional Steel Research,* 132, pp. 191–202.

Xu, C., Haixiao, L. and Chengkui, H. (2009) ‘Experimental study on shear resistance of self-stressing concrete filled circular steel tubes’, *Journal of Constructional Steel Research,* 65, pp. 801–807.

Xu, K., Kang, H., Wang, W., Jiang, P. and Li, N. (2021) ‘Carbon emission estimation of assembled composite concrete beams during construction’, *energies,* 14(1810), pp. 1–14.

Yamamoto, T., Kawaguchi, J. and Morino, S. (2000) ‘Experimental study of scale effects on the compressive behavior of short concrete-filled steel tube columns’, *Composite Construction in Steel and Concrete IV, ASCE,* pp. 879–890.

Yan, X.F. and Zhao, Y.G. (2020) ‘Compressive strength of axially loaded circular concrete-filled double-skin steel tubular short columns’, *Journal of Constructional Steel Research,* 170(106114).

Yao, S., An, H., Yating, L. and Ou, Z. (2020) ‘Flexural buckling behaviour of highchromium stainless steel welded I-section columns’, *Thin-Walled Structures,* 154(106812).

Ye, Y., Wang, L., Zhang, S-J. and Zhang, C.Y. (2021) ‘Compressive behavior of concrete-filled aluminum alloy tube (CFAAT) stub column with inner carbon steel tube’, *Structures,* 32, pp. 701–712.

Younis, A., Ebead, U. and Judd, S. (2018) ‘Life cycle cost analysis of structural concrete using seawater, recycled concrete aggregate, and GFRP reinforcement’, *Construction and Building Materials,* 175, pp. 152–160.

Yu, T., Teng, J.G., Wong, Y.L. and Dong, S.L. (2010) ‘Finite element modeling of confined concrete-I: Drucker-Prager type plasticity model’, *Engineering Structures,* 32(3), pp. 665–679.

Yu, Q., Tao, Z. and Wu, Y.X. (2008) ‘Experimental behaviour of high performance concrete-filled steel tubular columns’, *Thin-Walled Structures,* 46, pp. 362–370.

Yu, Z.W., Ding, F.X. and Cai, C.S. (2007) ‘Experimental behavior of circular concrete-filled steel tube stub columns’, *Journal of Constructional Steel Research,* 63, pp. 165–174.

Zhai, X.M., Wang, Y.J., Wu, H. and Fan, F. (2010) ‘Research on stability of high strength aluminum alloy columns loaded by axial compressive load’, *Advanced Materials Research,* 168–170, pp. 1915–1920.

Zhang, T., Gong, Y., Ding, F., Liu, X. and Yu, Z. (2021) ‘Experimental and numerical investigation on the flexural behavior of concrete-filled elliptical steel tube (CFET)’, *Journal of Building Engineering,* 41(102412).

Zhang, W.H., Wang, R., Zhao, H., Lam, D. and Chen, P. (2022) ‘Axial-load response of CFST stub columns with external stainless steel and recycled aggregate concrete: Testing, mechanism analysis and design’, *Engineering Structures,* 256(113968).

Zhao, H., Wang, R., Lam, D., Hou, C-C. and Zhang, R. (2021) 'Behaviours of circular CFDST with stainless steel external tube: Slender columns and beams', *Thin-Walled Structures*, 158(107172).

Zhao, M., Doung, Y. and Guo, H. (2021) 'Comparative life cycle assessment of composite structures incorporating uncertainty and global sensitivity analysis', *Engineering Structures*, 242(112394).

Zhao, O., Gardner, L. and Young, B. (2016) 'Testing and numerical modelling of austenitic stainless steel CHS beam–columns', *Engineering Structures*, 111, pp. 263–274.

Zhao, X.L. and Grzebieta, R. (2002) 'Strength and ductility of concrete-filled double skin (SHS inner and SHS outer) tubes', *Thin-Walled Structures*, 40, pp. 199–213.

Zhao, X.L., Tong, L.W. and Wang, X.Y. (2010) 'CFDST stub columns subjected to large deformation axial loading', *Engineering Structures*, 32, pp. 692–703.

Zhao, Y., Zhai, X. and L. Sun (2016) 'Test and design method for the buckling behaviors of 6082-T6 aluminum alloy columns with box-type and L-type sections under eccentric compression', *Thin-Walled Structures*, 100, pp. 62–80.

Zhao, Y., Zhai, X. and Wang, J. (2019b) 'Buckling behaviors and ultimate strengths of 6082-T6 aluminum alloy columns under eccentric compression – Part I: Experiments and finite element modeling', *Thin-Walled Structures*, 143, p. 106207.

Zhao, Y., Zhai, X. and Wang, J. (2019a) 'Buckling behaviors and ultimate strength of 6082-T6 aluminum alloy columns with square and circular hollow sections under eccentric compression – Part II: Parametric study, design provisions and reliability analysis', *Thin-Walled Structures*, 143, p. 106208.

Zheng, Y., He, C. and Zheng, L. (2018) 'Experimental and numerical investigation of circular double-tube concrete-filled stainless steel tubular columns under cyclic loading', *Thin-Walled Structures*, 132, pp. 151–166.

Zhou, F. and Young, B. (2008) 'Tests of concrete-filled aluminum stub columns', *Thin-Walled Structures*, 46(6), pp. 573–583.

Zhou, F. and Young, B. (2009) 'Concrete-filled aluminum circular hollow section column tests', *Thin-Walled Structures*, 47(11), pp. 1272–1280.

Zhou, F. and Young, B. (2012) 'Numerical analysis and design of concrete-filled aluminum circular hollow section columns', *Thin-Walled Structures*, 50(1), pp. 45–55. doi:10.1016/j.tws.2011.10.002.

Zhou, F and Young, B. (2012) 'Numerical analysis and design of concrete-filled aluminum circular hollow section columns', *Thin-Walled Structures*, 50, pp. 45–55.

Zhou, F. and Young, B. (2018) 'Concrete- filled double-skin aluminum circular hollow section stub columns', *Thin-Walled Structures*, 133, pp. 141–52.

Zhou, F. and Young, B. (2019) 'Compressive strengths of concrete-filled double-skin (circular hollow section outer and square hollow section inner) aluminium tubular sections', *Advances in Structural Engineering*, pp. 1–17.

Zhu, J.H., Li, Z.Q., Su, M.N. and Young, B. (2019a) 'Behaviour of aluminium alloy plain and lipped channel columns', *Thin-Walled Structures*, 135, pp. 306–316.

Zhu, J.H., Li, Z.Q., Su, M.N. and Young, B. (2019b) 'Numerical study and design of

aluminium alloy channel section columns with welds', *Thin-Walled Structures*, (139), pp. 139–150.

Zhu, J.H. and Young, B. (2006) 'Experimental investigation of aluminum alloy circular hollow section columns', *Engineering Structures*, 28(2), pp. 207–215.

Zhu, J.H. and Young, B. (2009) 'Design of Aluminum alloy flexural members using direct strength method', *Journal of Structural Engineering, ASCE*, 135(5), pp. 558–566.

Zhu, J.Y. and Chan, T.M. (2018) 'Experimental investigation on octagonal concrete filled steel stub columns under uniaxial compression', *Journal of Constructional Steel Research*, 147, pp. 457–467.

Zhu, Y., Chen, Y., He, K., Feng, R., Zhang, X., Zhu, Q. and Tang, C. (2020) 'Flexural behavior of concrete-filled SHS and RHS aluminum alloy tubes strengthened with CFRP', *Composite Structures*, 238(111975).

Appendix A : Test and FE Failure modes

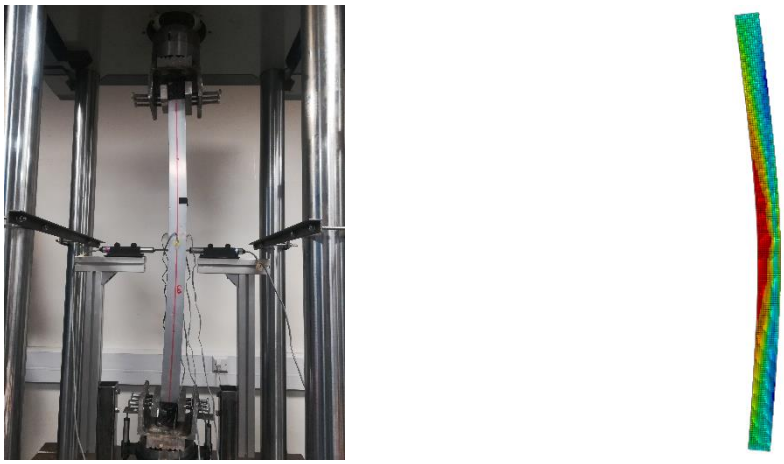

(a) 50.8×50.8×3.3

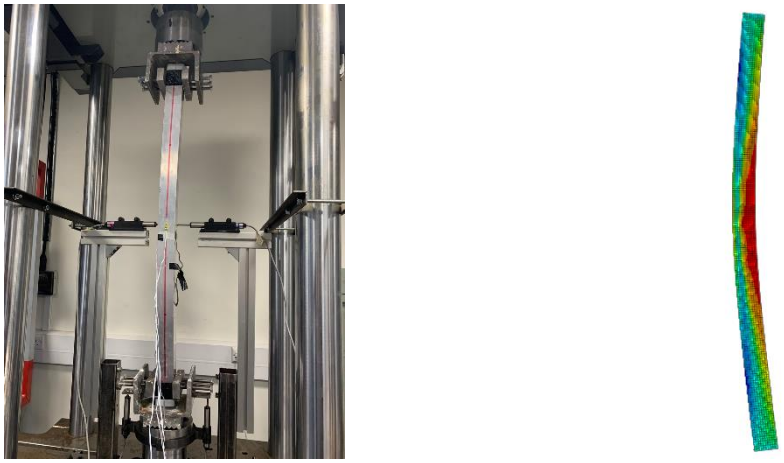

(b) 50.8×50.8×4.8

(c) 76.2×76.2×3.3

Figure A.1: Test and FE failure modes of BAT columns.

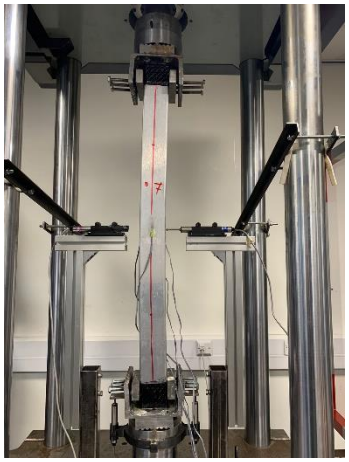

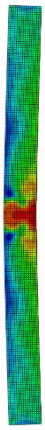

(d) 76.2×76.2×4.8

(e) 76.2×38.1×3.3

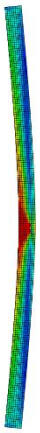

(f) 76.2×50.8×3.3

Figure A.1 (continued): Test and FE failure modes of BAT columns.

(g) 101.6×50.8×3.3

Figure A.1 (continued): Test and FE failure modes of BAT columns.

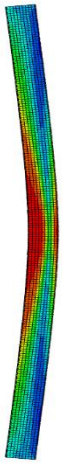

(a) 50.8×50.8×1.6-C

(b) 50.8×50.8×3.3-C

Figure A.2: Test and FE failure modes of CFAT columns.

(c) 50.8×50.8×4.8-C

(d) 76.2×76.2×3.3-C

(e) 76.2×76.2×6.4-C

Figure A.2 (continued): Test and FE failure modes of CFAT columns.

(f) 76.2×38.1×3.3-C

(g) 76.2×50.8×3.3-C

(h) 101.6×50.8×3.3-C

Figure A.2 (continued): Test and FE failure modes of CFAT columns.

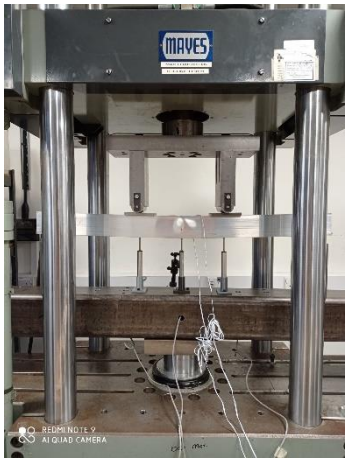

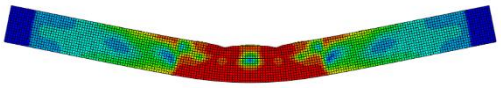

(a) 76.2×76.2×1.6

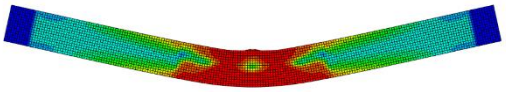

(b) 76.2×76.2×3.3

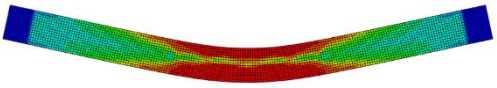

(c) 76.2×76.2×6.4

Figure A.3: Test and FE failure modes of BAT beams.

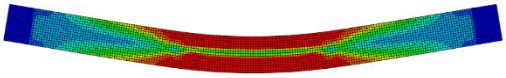

(d) 76.2×25.4×3.3

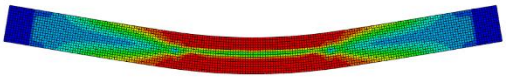

(e) 76.2×38.1×3.3

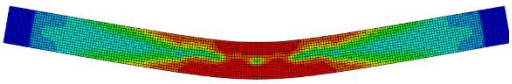

(f) 76.2×50.8×3.3

Figure A.3 (continued): Test and FE failure modes of BAT beams.

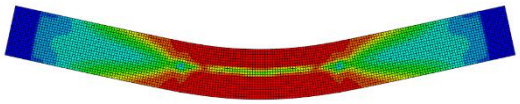

(g) 101.6×25.4×3.3

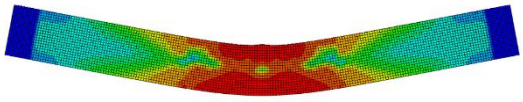

(h) 101.6×50.8×3.3

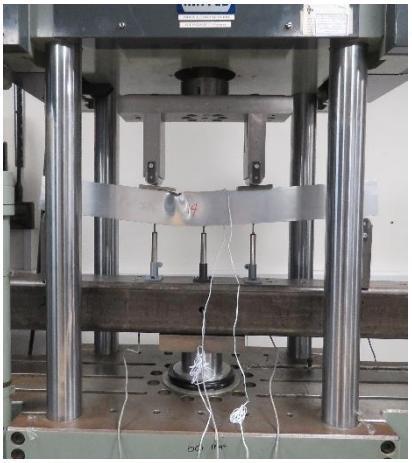

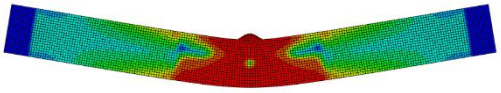

(i) 101.6×76.2×3.3

Figure A.3 (continued): Test and FE failure modes of BAT beams.

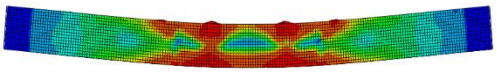

(a) 76.2×76.2×1.6-C

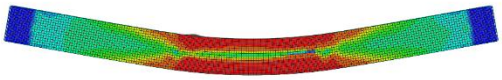

(b) 76.2×76.2×2.3-C

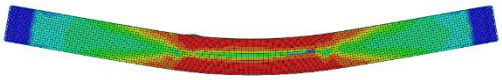

(c) 76.2×76.2×6.4-C

Figure A.4: Test and FE failure modes of CFAT beams.

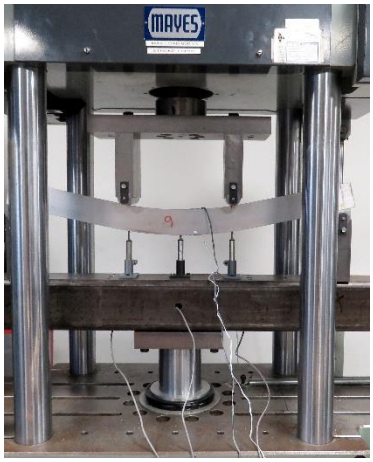

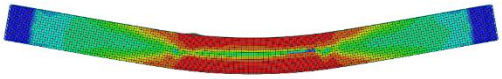

(d) 76.2×25.4×3.3-C

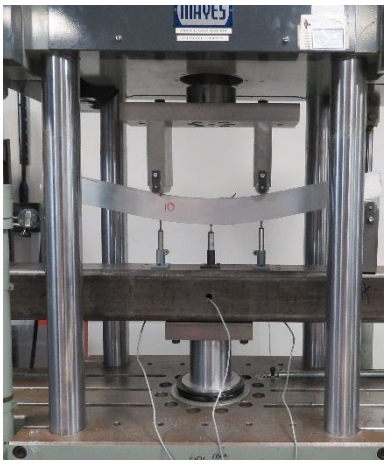

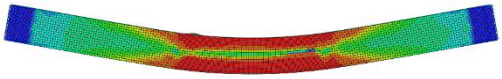

(e) 76.2×38.1×3.3-C

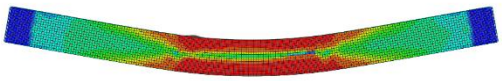

(f) 76.2×50.8×3.3-C

Figure A.4 (continued): Test and FE failure modes of CFAT beams.

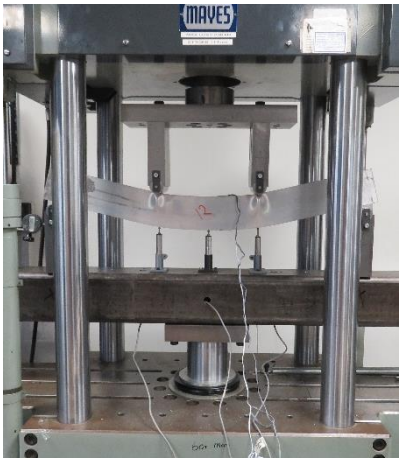

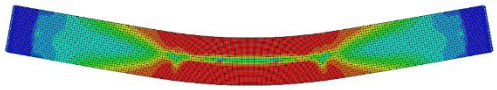

(g) 101.6×25.4×3.3-C

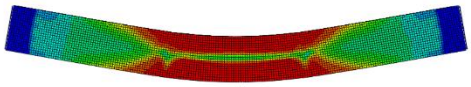

(h) 101.6×50.8×3.3-C

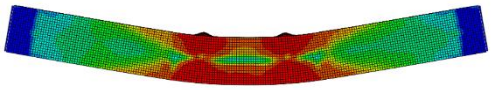

(i) 101.6×76.2×3.3-C

Figure A.4 (continued): Test and FE failure modes of CFAT beams.

(a) S50.8×3.2-S19.2×1.6

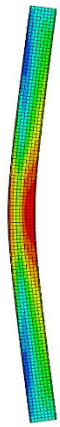

(b) S63.4×3.2-S19.2×1.6

(c) S63.4×3.2-S25.4×3.2

Figure A.5: Test and FE failure modes of CFDSAT columns.


(d) S76.2×4.8-S19.2×1.6

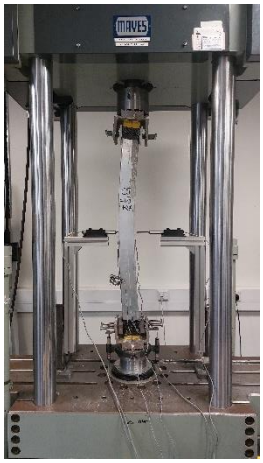


(e) S76.2×4.8-S25.4×1.6

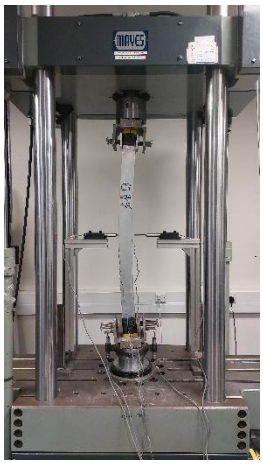


(f) S63.4×3.2-C19.2×3.2

Figure A.5 (continued): Test and FE failure modes of CFDSAT columns.

(g) S63.4×3.2-C25.4×3.2

Figure A.5 (continued): Test and FE failure modes of CFDSAT columns.

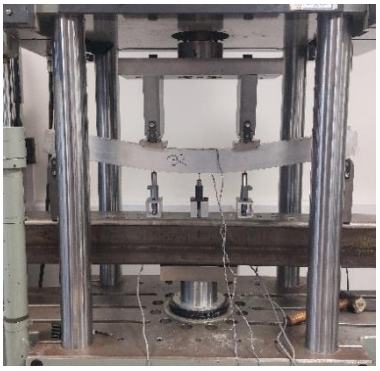

(a) S76.2×6.4-S25.4×3.2

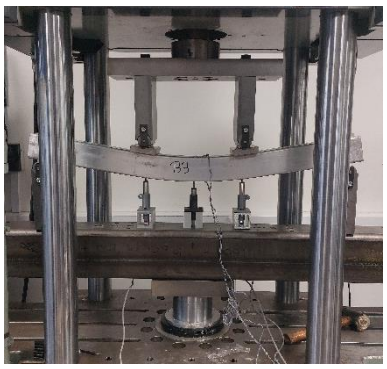

(b) S76.2×4.8-S25.4×3.2

Figure A.6: Test and FE failure modes of CFDSAT beams.

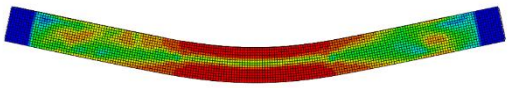

(c) S76.2×6.4-C25.4×3.2

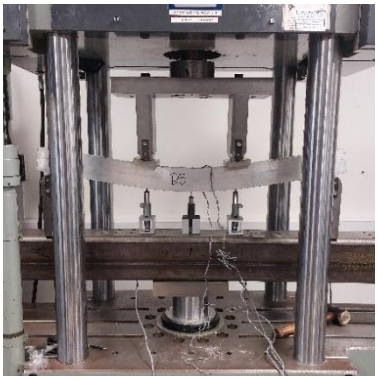

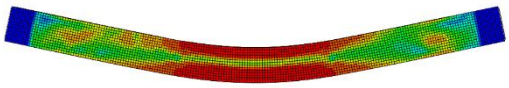

(d) S76.2×6.4-C38.2×1.6

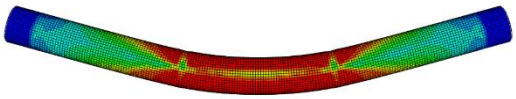

(e) C88.6×1.6-C38.2×1.6

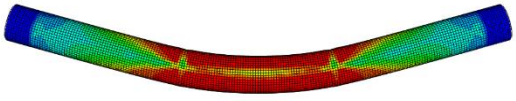

(f) C76.2×3.2-C25.4×3.2

Figure A.6 (continued): Test and FE failure modes of CFDSAT beams.

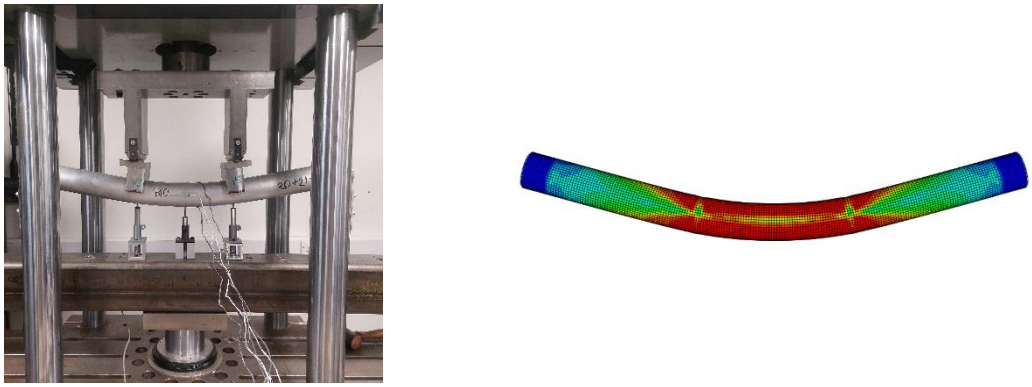

(g) C76.2×3.2-C38.2×1.6

Figure A.6 (continued): Test and FE failure modes of CFDSAT beams.

Appendix B :Test and FE curves

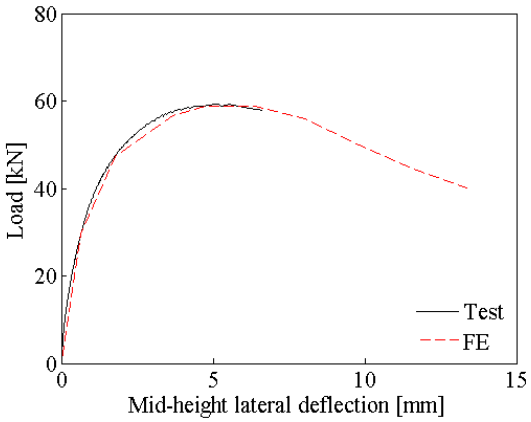

(i) 50.8×50.8×1.6

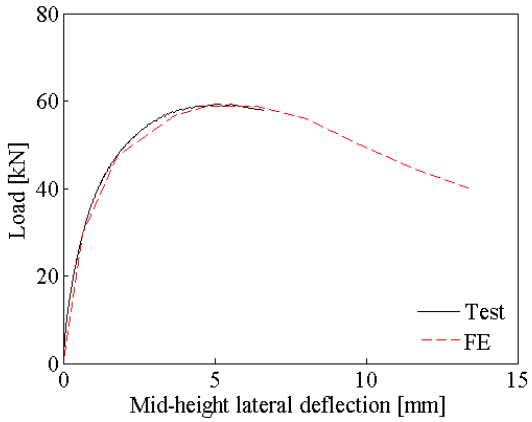

(j) 50.8×50.8×4.8

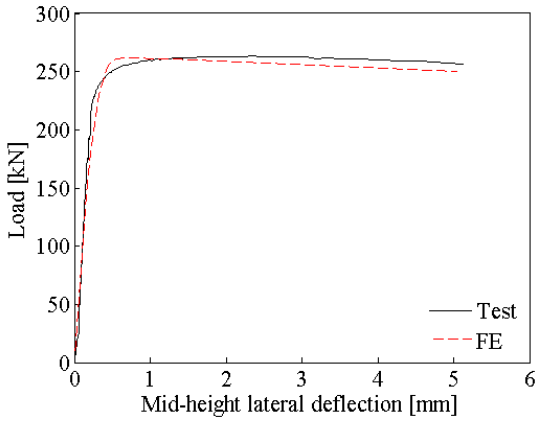

(k) 76.2×76.2×3.3

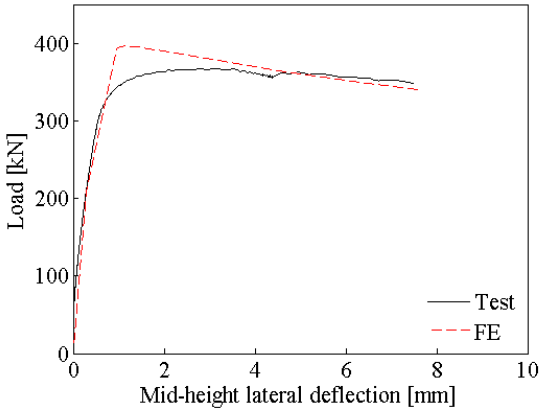

(l) 76.2×76.2×4.8

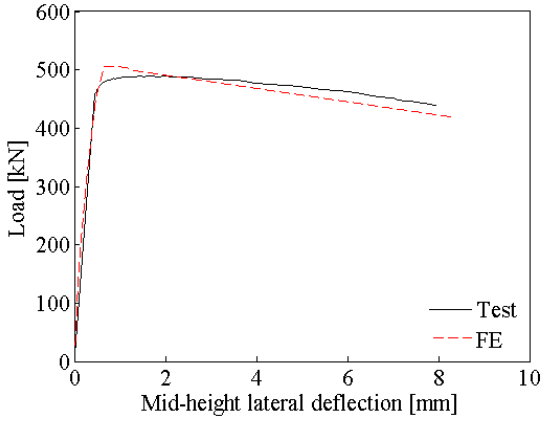

(m)76.2×76.2×6.4

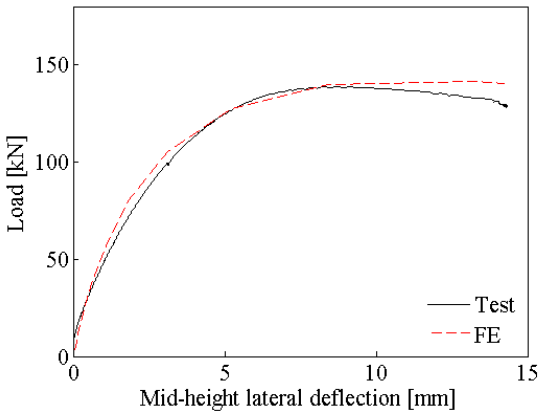

(n) 76.2×50.8×3.3

Figure B.1: Test and FE load versus mid-height lateral deflection curves of BAT columns.

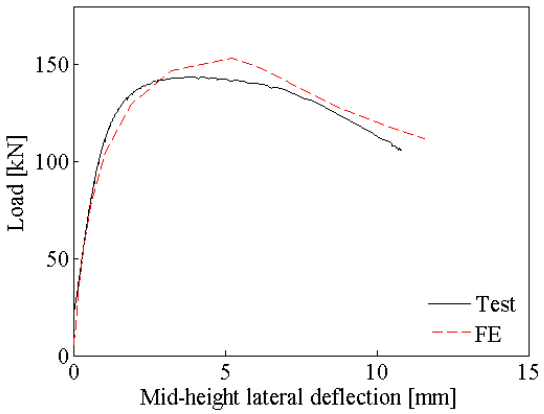

(o) 101.6×50.8×3.3

Figure B.1 (continued): Test and FE load versus mid-height lateral deflection curves of BAT columns.

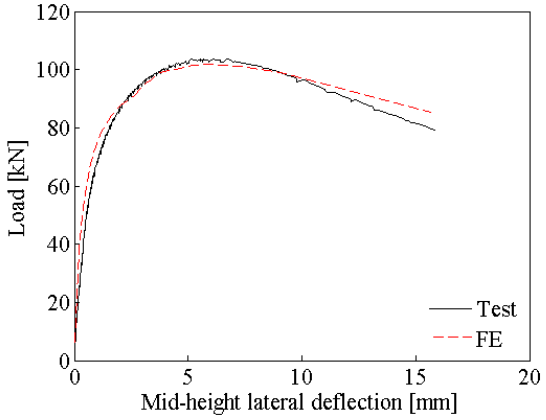

(a) 50.8×50.8×1.6-C

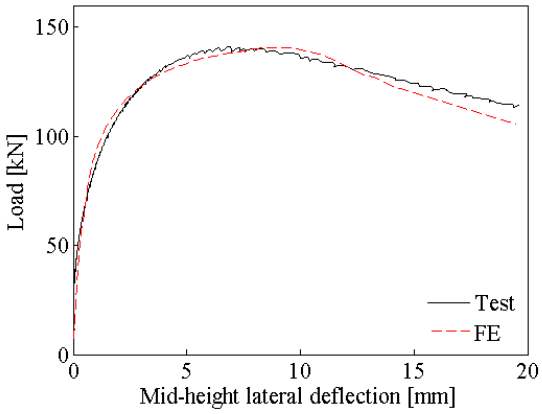

(b) 50.8×50.8×3.3-C

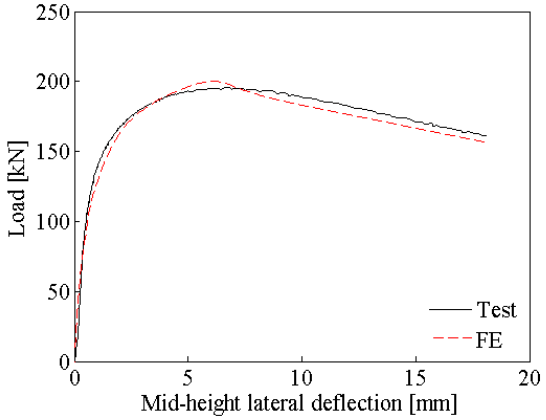

(c) 50.8×50.8×4.8-C

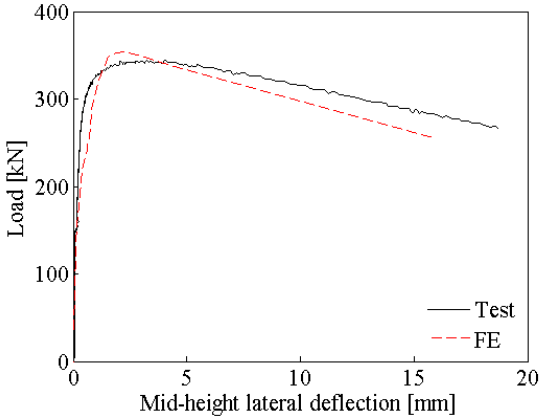

(d) 76.2×76.2×3.3-C

Figure B.2: Test and FE load versus mid-height lateral deflection curves of CFAT columns.

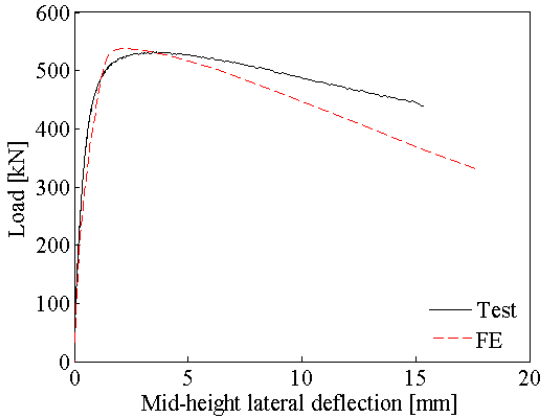

(e) 76.2×76.2×6.4-C

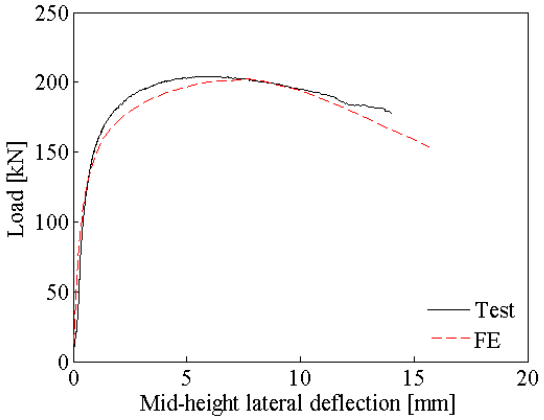

(f) 76.2×50.8×3.3-C

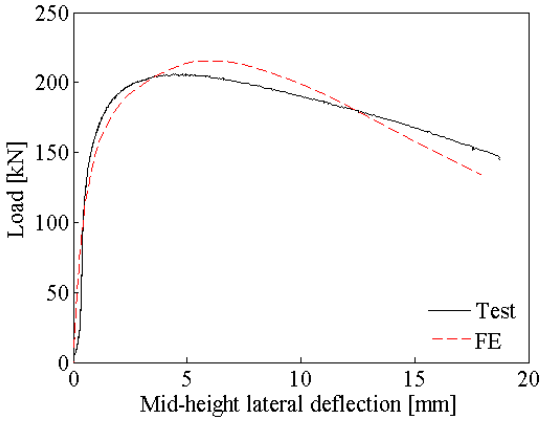

(g) 101.6×50.8×3.3-C

Figure B.2 (continued): Test and FE load versus mid-height lateral deflection curves of CFAT columns.

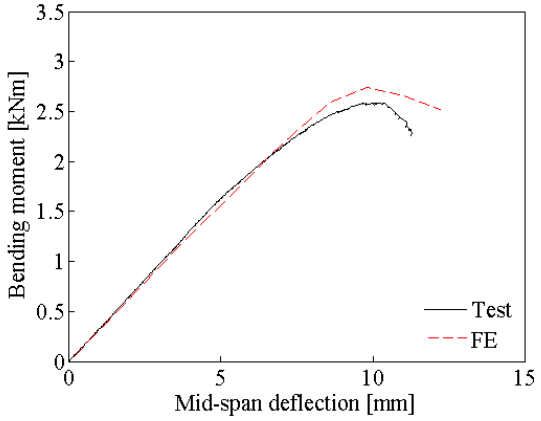

(a) 76.2×76.2×1.6

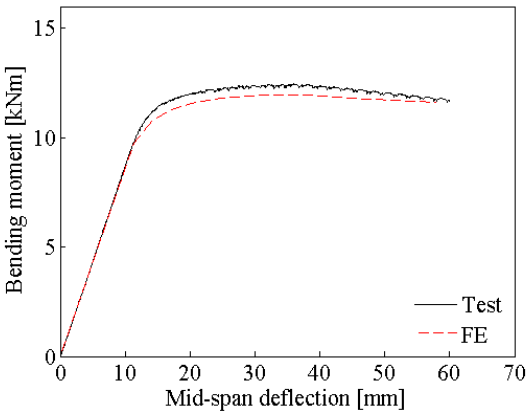

(b) 76.2×76.2×4.8

Figure B.3: Test and FE moment versus mid-span lateral deflection curves of BAT beams.

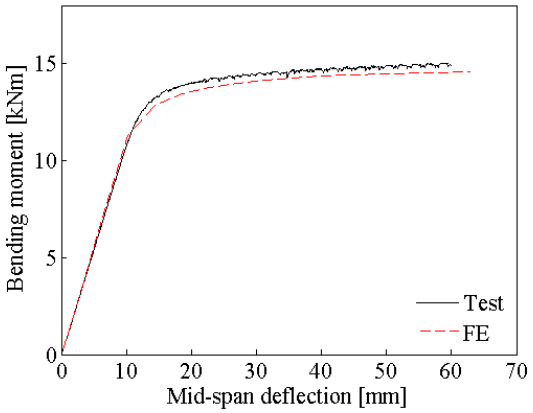

(c) 76.2×76.2×6.4

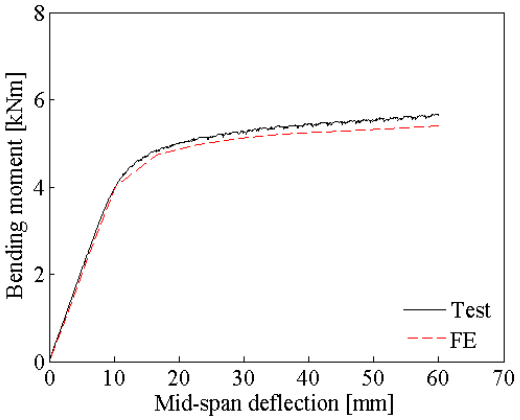

(d) 76.2×38.1×3.3

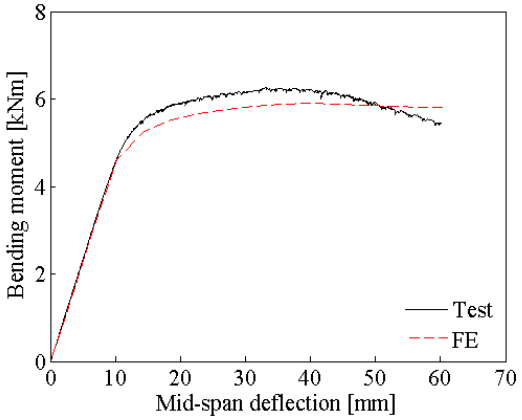

(e) 76.2×50.8×3.3

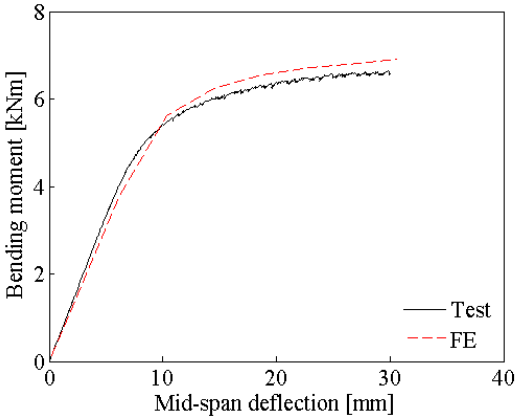

(f) 101.6×25.4×3.3

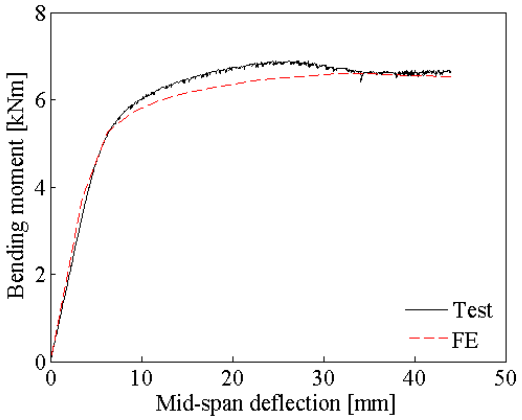

(g) 101.6×50.8×3.3

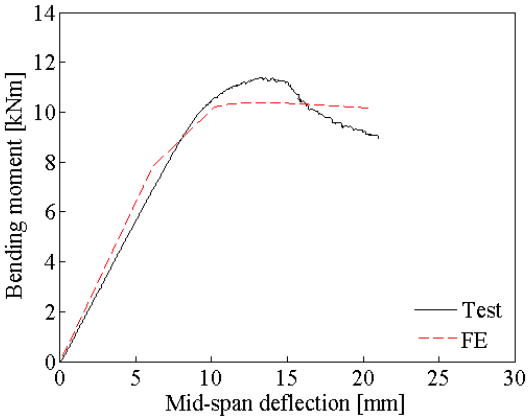

(h) 101.6×76.2×3.3

Figure B.3 (continued): Test and FE moment versus mid-span lateral deflection curves of BAT beams.

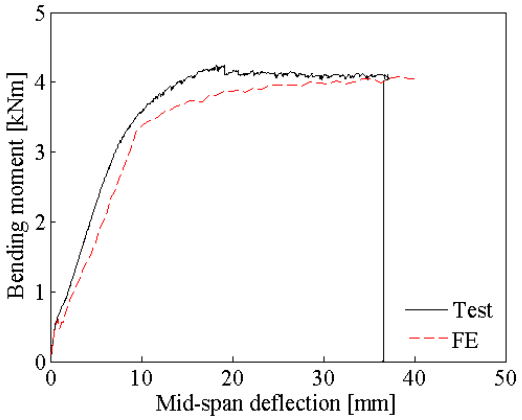

(a) 76.2×76.2×1.6-C

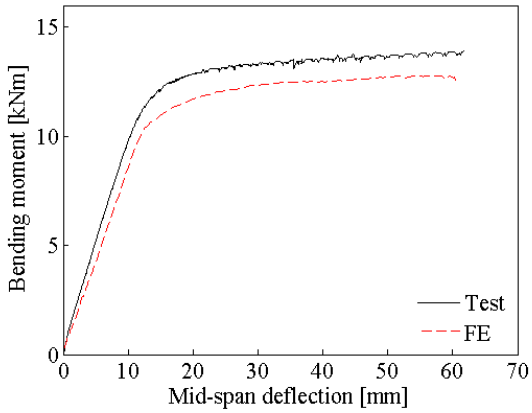

(b) 76.2×76.2×4.8-C

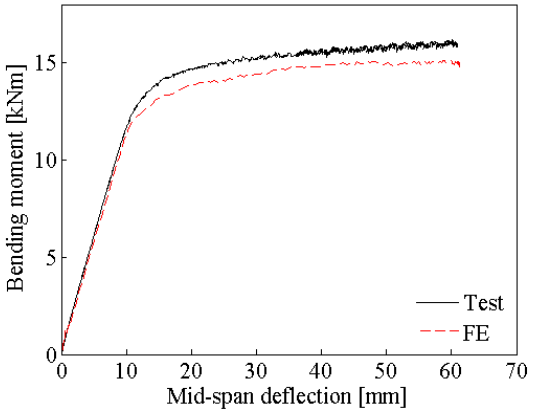

(c) 76.2×76.2×6.4-C

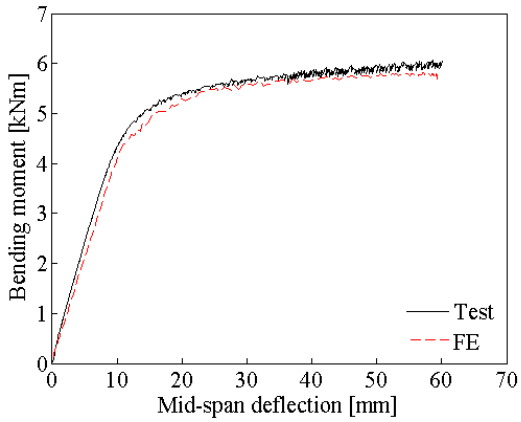

(d) 76.2×38.1×3.3-C

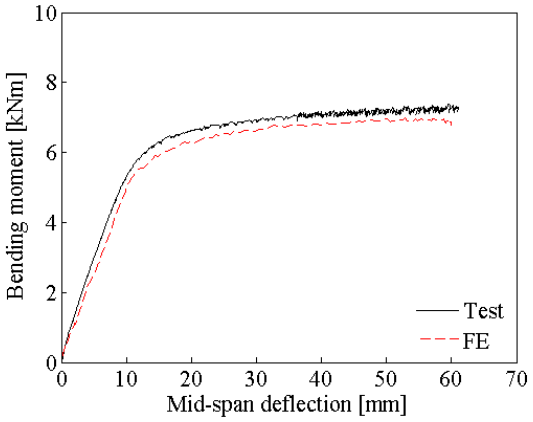

(e) 76.2×50.8×3.3-C

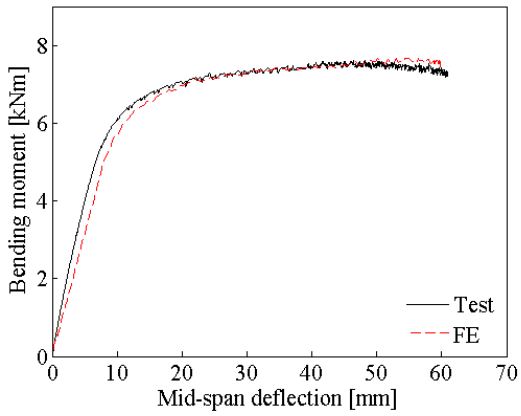

(f) 101.6×25.4×3.3-C

Figure B.4: Test and FE moment versus mid-span lateral deflection curves of CFAT beams.

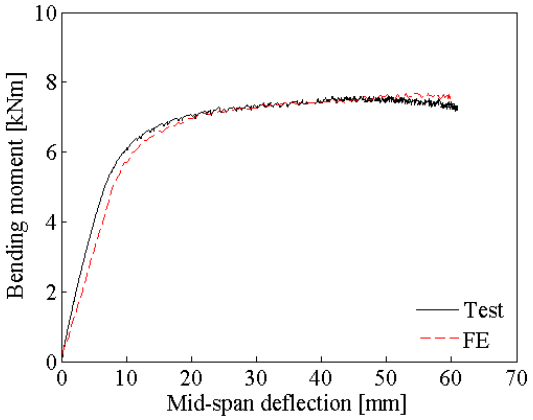

(g) 101.6×50.8×3.3-C

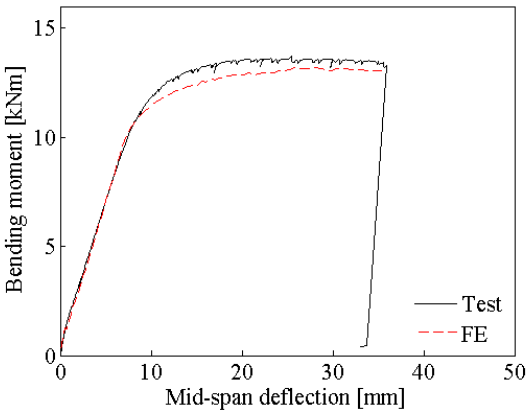

(h) 101.6×76.2×3.3-C

Figure B.4 (continued): Test and FE moment versus mid-span lateral deflection curves of CFAT beams.

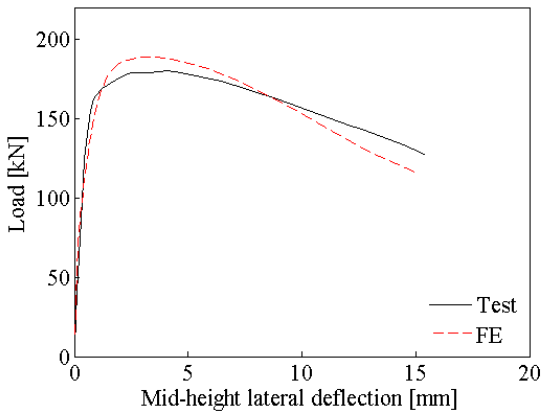

(a) S63.4×3.2-S19.2×1.6

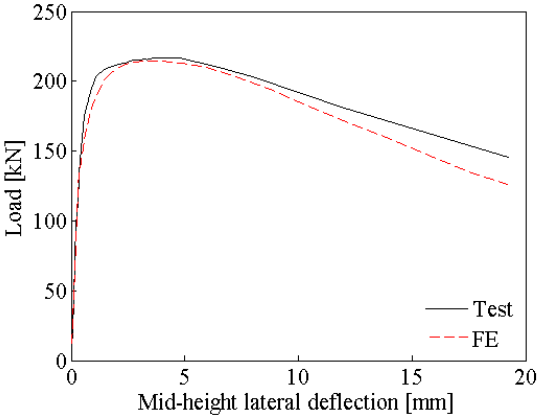

(b) S63.4×3.2-S25.4×3.2

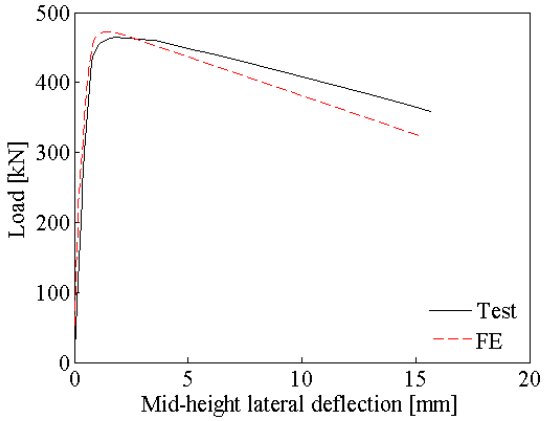

(c) S76.2×4.8-S19.2×1.6

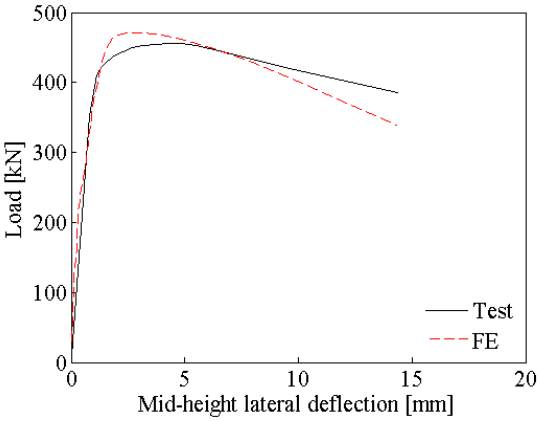

(d) S76.2×4.8-S25.4×1.6

Figure B.5: Test and FE load versus mid-height lateral deflection curves of CFDSAT columns.

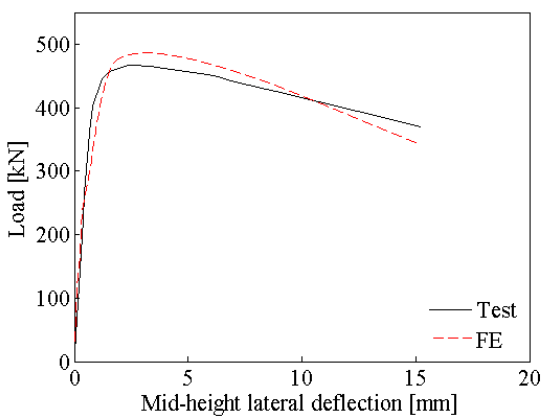

(e) S76.2×4.8-S25.4×3.2

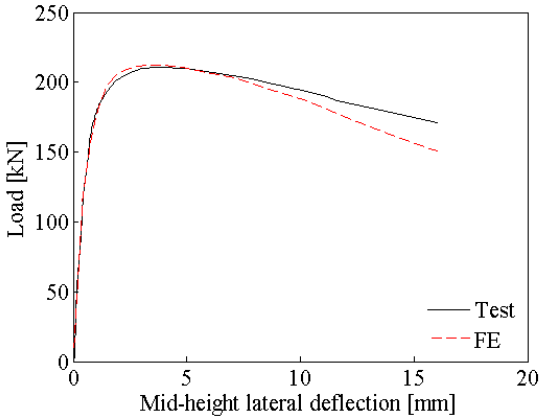

(f) S63.4×3.2-C19.2×3.2

Figure B.5 (continued): Test and FE load versus mid-height lateral deflection curves of CFDSAT columns.

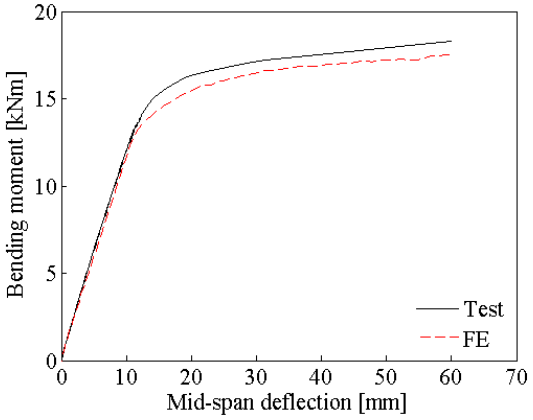

(a) S76.2×6.4-S25.4×3.2

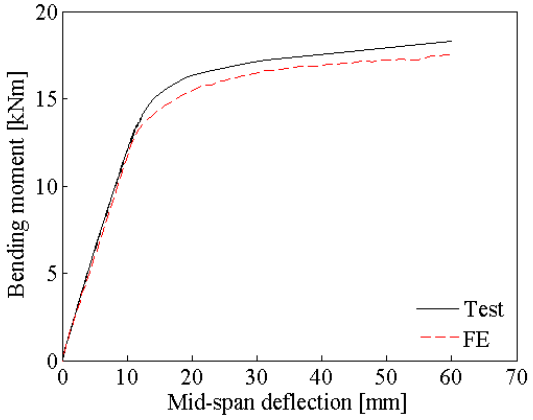

(b) S76.2×4.8-S25.4×3.2

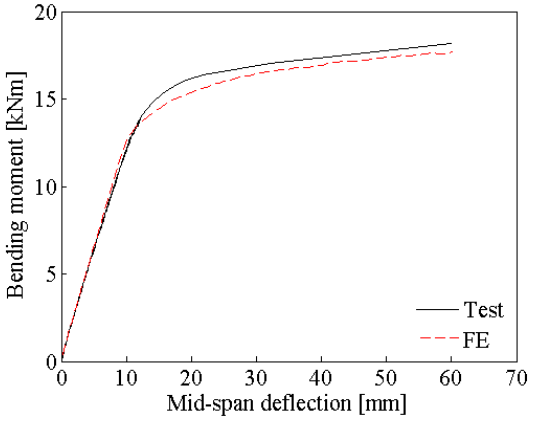

(c) S76.2×6.4-C25.4×3.2

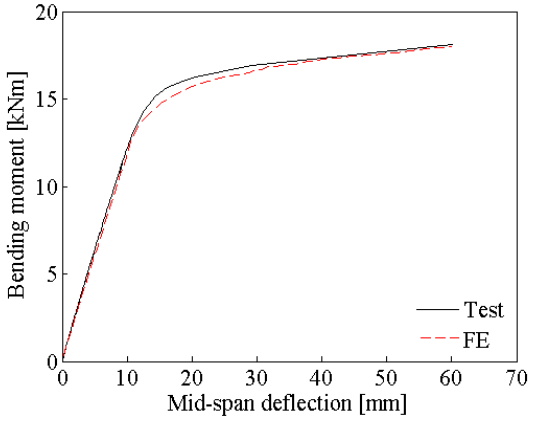

(d) S76.2×6.4-C38.2×1.6

Figure B.6: Test and FE moment versus mid-span lateral deflection curves of CFDSAT beams.

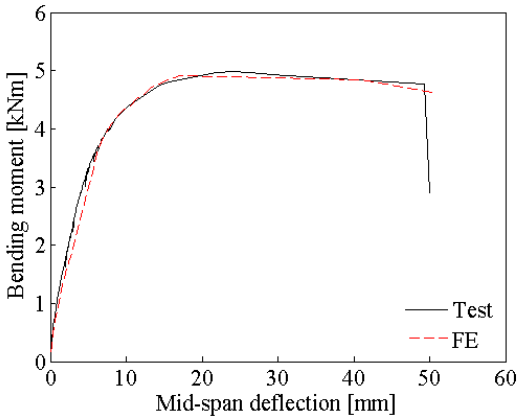

(e) C88.6×1.6-C25.4×3.2

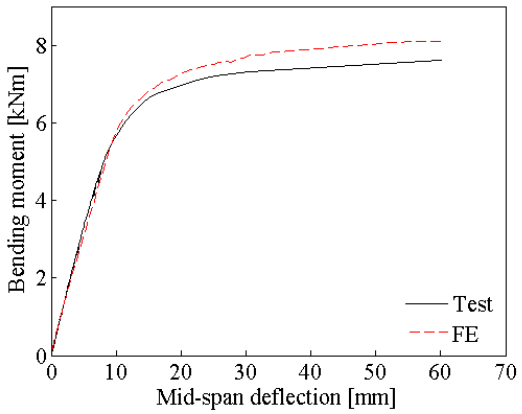

(f) C76.2×3.2-C38.2×1.6

Figure B.6 (continued): Test and FE moment versus mid-span lateral deflection curves of CFDSAT beams.

Appendix C : Parametric study data

Table C.1: Geometric dimensions, material properties and ultimate capacity of BAT and CFAT columns used in the parametric study.

Specimen	D (mm)	B (mm)	t (mm)		L (mm)		Class		f_c (MPa)	$N_{u,FE}$ (kN)	
			BAT	CFAT	BAT	CFAT	BAT	CFAT	CFAT	BAT	CFAT
50×50	50	50	1	1	150	500	4	4	30	30.9	106.4
	50	50	3	5	150	500	3	1	30	180.3	298.5
	50	50	5	1	150	500	1	4	50	322.0	148.8
	50	50	1	5	500	500	4	1	50	29.4	325.6
	50	50	3	1	500	500	3	4	70	171.1	189.0
	50	50	5	5	500	500	1	1	70	286.0	352.4
	50	50	1	1	800	1000	4	4	30	27.4	75.3
	50	50	3	5	800	1000	3	1	30	158.3	179.2
	50	50	5	1	800	1000	1	4	50	268.2	100.9
	50	50	1	5	1100	1000	4	1	50	23.2	185.2
	50	50	3	1	1100	1000	3	4	70	122.9	125.5
	50	50	5	5	1100	1000	1	1	70	213.1	192.7
	50	50	1	1	1400	1500	4	4	30	18.4	62.9
	50	50	3	5	1400	1500	3	1	30	82.7	92.5
	50	50	5	1	1400	1500	1	4	50	146.0	77.1
	50	50	1	5	1700	1500	4	1	50	14.6	104.0
	50	50	3	1	1700	1500	3	4	70	57.6	88.9
	50	50	5	5	1700	1500	1	1	70	102.4	111.4
100×50W	100	50	2	2	150	500	4	4	30	121.7	215.1
	100	50	6	10	150	500	3	1	30	550.6	745.1
	100	50	10	2	150	500	1	4	50	994.5	287.3
	100	50	2	10	500	500	4	1	50	114.7	788.7
	100	50	6	2	500	500	3	4	70	537.2	426.6
	100	50	10	10	500	500	1	1	70	904.9	829.2
	100	50	2	2	800	1000	4	4	30	102.6	173.3
	100	50	6	10	800	1000	3	1	30	494.6	438.6
	100	50	10	2	800	1000	1	4	50	828.6	227.9
	100	50	2	10	1100	1000	4	1	50	84.0	447.6
	100	50	6	2	1100	1000	3	4	70	423.6	275.8
	100	50	10	10	1100	1000	1	1	70	746.8	467.5
	100	50	2	2	1400	1500	4	4	30	65.9	135.7
	100	50	6	10	1400	1500	3	1	30	310.0	293.5
	100	50	10	2	1400	1500	1	4	50	572.2	170.8
	100	50	2	10	1700	1500	4	1	50	51.6	305.7
	100	50	6	2	1700	1500	3	4	70	219.7	197.4
	100	50	10	10	1700	1500	1	1	70	412.4	318.8

Table C.1 (continued): Geometric dimensions, material properties and ultimate capacity of BAT and CFAT columns used in the parametric study.

Specimen	D (mm)	B (mm)	t (mm)		L (mm)		Class		f_c (MPa)	$N_{u,FE}$ (kN)	
			BAT	CFAT	BAT	CFAT	BAT	CFAT	CFAT	BAT	CFAT
100×50S	100	50	2	2	500	1000	4	4	30	116.8	261.0
	100	50	6	10	500	1000	3	1	30	543.5	790.8
	100	50	10	2	500	1000	1	4	50	916.7	312.5
	100	50	2	10	1000	1000	4	1	50	114.3	833.5
	100	50	6	2	1000	1000	3	4	70	525.7	371.5
	100	50	10	10	1000	1000	1	1	70	856.1	876.1
	100	50	2	2	1300	1500	4	4	30	112.0	222.7
	100	50	6	10	1300	1500	3	1	30	492.4	656.7
	100	50	10	2	1300	1500	1	4	50	820.2	284.6
	100	50	2	10	1700	1500	4	1	50	106.3	668.7
	100	50	6	2	1700	1500	3	4	50	437.1	329.0
	100	50	10	10	1700	1500	1	1	70	741.7	689.4
	100	50	2	2	2300	2300	4	4	30	86.7	173.4
	100	50	6	10	2300	2300	3	1	30	296.9	333.2
	100	50	10	2	2300	2300	1	4	50	510.1	206.4
	100	50	2	10	3000	2300	4	1	50	57.7	346.1
	100	50	6	2	3000	2300	3	4	70	183.3	240.2
	100	50	10	10	3000	2300	1	1	70	316.5	356.5

Table C.2: Geometric dimensions, material properties and flexural strength of BAT and CFAT beams used in the parametric study.

Specimen	D (mm)	B (mm)	t (mm)		Class		f_c (MPa)	$M_{u,FE}$ (kN)	
			BAT	CFAT	BAT	CFAT	CFAT	BAT	CFAT
50×50	50	50	1.00	1	3	3	30	0.87	1.17
	50	50	2.00	1	1	3	40	2.05	1.20
	50	50	2.20	1	1	3	50	2.32	1.23
	50	50	2.30	2	1	1	30	2.41	2.47
	50	50	2.40	2	1	1	40	2.55	2.51
	50	50	2.50	2	1	1	50	2.70	2.54
	50	50	2.60	4	1	1	30	2.82	4.50
	50	50	2.80	4	1	1	40	3.03	4.53
	50	50	3.00	4	1	1	50	3.26	4.55
	50	50	4.00	6	1	1	30	4.22	6.03
	50	50	5.00	6	1	1	40	5.06	6.06
	50	50	6.00	6	1	1	50	5.81	6.09
75×75	75	50	1.00	1	4	4	30	1.39	2.07
	75	50	2.00	1	2	4	40	3.53	2.10
	75	50	2.15	1	2	4	50	3.96	2.13
	75	50	2.25	2	2	2	30	4.12	4.45
	75	50	2.35	2	2	2	40	4.37	4.52
	75	50	2.45	2	2	2	50	4.69	4.65
	75	50	2.65	4	2	1	30	4.98	8.41
	75	50	2.85	4	1	1	40	5.44	8.45
	75	50	3.00	4	1	1	50	5.73	8.55
	75	50	4.00	6	1	1	30	7.76	11.30
	75	50	5.00	6	1	1	40	9.41	11.34
	75	50	6.00	6	1	1	50	10.94	11.42
100×100	100	50	1.00	1	4	4	30	1.92	2.93
	100	50	1.20	1	4	4	40	2.68	3.13
	100	50	1.30	1	4	4	50	2.90	3.30
	100	50	1.40	2	4	3	30	3.20	6.70
	100	50	1.50	2	4	3	40	3.47	6.90
	100	50	1.60	2	4	3	50	3.81	7.24
	100	50	1.80	4	4	1	30	4.54	13.38
	100	50	2.00	4	3	1	40	5.27	13.41
	100	50	3.00	4	2	1	50	8.79	13.71
	100	50	4.00	6	1	1	30	11.96	18.11
	100	50	5.00	6	1	1	40	14.90	18.17
	100	50	6.00	6	1	1	50	17.46	18.29

Table C.3: Geometric dimensions, material properties and ultimate capacity of CFDSAT columns used in the parametric study.

Outer section	Inner section	D_o or B_o (mm)	t_o (mm)	Class	D_i or B_i (mm)	t_i (mm)	Class	L	$\bar{\lambda}$	f_c (MPa)	$N_{u,FE}$ (kN)
S45×45×1	S20×20×1	45	1.0	4	20	1	2	1000	1.08	30	63.87
	S20×20×1	45	1.0	4	20	1	2	1000	1.13	40	70.84
	S20×20×1	45	1.0	4	20	1	2	1000	1.19	50	78.51
S45×45×1.5	S20×20×1	45	1.5	4	20	1	2	500	0.59	30	106.22
	S20×20×1	45	1.5	4	20	1	2	1000	1.12	30	81.73
	S20×20×1	45	1.5	4	20	1	2	1500	1.65	30	56.87
S45×45×4	S20×20×1	45	4.0	1	20	1	2	1000	1.24	30	115.61
	S20×20×2	45	4.0	1	20	2	1	1000	1.26	30	118.62
	S20×20×5	45	4.0	1	20	5	1	1000	1.35	30	119.58
S45×45×8	S20×20×1	45	8.0	1	20	1	2	1000	1.36	30	159.74
	S25×25×1	45	8.0	1	25	1	3	1000	1.36	30	151.39
S60×60×1	S20×20×1	60	1.0	4	20	1	2	1000	0.79	30	102.07
	S20×20×1	60	1.0	4	20	1	2	1000	0.85	40	117.84
	S20×20×1	60	1.0	4	20	1	2	1000	0.90	50	134.73
S60×60×1.5	S20×20×1	60	1.5	4	20	1	2	500	0.43	30	158.63
	S20×20×1	60	1.5	4	20	1	2	1000	0.81	30	134.33
	S20×20×1	60	1.5	4	20	1	2	1500	1.19	30	113.75
S60×60×4	S20×20×1	60	4.0	2	20	1	2	1000	0.90	30	238.12
	S20×20×2	60	4.0	2	20	2	1	1000	0.91	30	240.80
	S20×20×5	60	4.0	2	20	5	1	1000	0.96	30	246.05
S60×60×8	S20×20×1	60	8.0	1	20	1	2	1000	0.98	30	350.17
	S25×25×1	60	8.0	1	25	1	3	1000	0.98	30	348.68
	S30×30×1	60	8.0	1	30	1	4	1000	0.97	30	346.75
	S35×35×1	60	8.0	1	35	1	4	1000	0.96	30	344.86
S75×75×1	S20×20×1	75	1.0	4	20	1	2	1000	0.62	30	161.92
	S20×20×1	75	1.0	4	20	1	2	1000	0.67	40	196.50
	S20×20×1	75	1.0	4	20	1	2	1000	0.72	50	228.95
S75×75×1.5	S20×20×1	75	1.5	4	20	1	2	500	0.34	30	214.33
	S20×20×1	75	1.5	4	20	1	2	1000	0.63	30	194.55
	S20×20×1	75	1.5	4	20	1	2	1500	0.93	30	177.05
S75×75×4	S20×20×1	75	4.0	3	20	1	2	1000	0.70	30	372.44
	S20×20×2	75	4.0	3	20	2	1	1000	0.71	30	377.16
	S20×20×5	75	4.0	3	20	5	1	1000	0.74	30	393.23
S75×75×8	S20×20×1	75	8.0	1	20	1	2	1000	0.76	30	565.32
	S25×25×1	75	8.0	1	25	1	3	1000	0.76	30	562.70
	S30×30×1	75	8.0	1	30	1	4	1000	0.75	30	558.15
	S35×35×1	75	8.0	1	35	1	4	1000	0.75	30	552.52
S100×100×1	S20×20×1	100	1.0	4	20	1	3	1000	0.46	30	278.27
	S20×20×1	100	1.0	4	20	1	3	1000	0.51	40	349.72
	S20×20×1	100	1.0	4	20	1	3	1000	0.55	50	417.63
S100×100×1.5	S20×20×1	100	1.5	4	20	1	3	500	0.25	30	340.66
	S20×20×1	100	1.5	4	20	1	3	1000	0.47	30	322.96
	S20×20×1	100	1.5	4	20	1	3	1500	0.69	30	288.62
S100×100×4	S20×20×1	100	4.0	4	20	1	3	1000	0.52	30	575.69

Table C.3 (continued): Geometric dimensions, material properties and ultimate capacity of CFDSAT columns used in the parametric study.

Outer section	Inner section	D_o or B_o (mm)	t_o (mm)	Class	D_i or B_i (mm)	t_i (mm)	Class	L	$\bar{\lambda}$	f_c (MPa)	$N_{u,FE}$ (kN)
	S20×20×2	100	4.0	4	20	2	1	1000	0.52	30	586.08
	S20×20×5	100	4.0	4	20	5	1	1000	0.54	30	609.91
S100×100×8	S20×20×1	100	8.0	1	20	1	3	1000	0.55	30	898.93
	S25×25×1	100	8.0	1	25	1	4	1000	0.55	30	895.97
	S30×30×1	100	8.0	1	30	1	4	1000	0.55	30	893.95
	S35×35×1	100	8.0	1	35	1	4	1000	0.55	30	892.90
S120×120×1	C20×1	120	1.0	4	20	1	3	1000	0.38	30	396.87
	C20×1	120	1.0	4	20	1	3	1000	0.42	40	504.40
	C20×1	120	1.0	4	20	1	3	1000	0.46	50	612.27
S120×120×1.5	C20×1	120	1.5	4	20	1	3	500	0.21	30	460.26
	C20×1	120	1.5	4	20	1	3	1000	0.39	30	448.41
	C20×1	120	1.5	4	20	1	3	1500	0.57	30	419.48
S120×120×4	C20×1	120	4.0	4	20	1	3	1000	0.42	30	751.21
	C20×2	120	4.0	4	20	2	1	1000	0.42	30	762.72
	C20×5	120	4.0	4	20	5	1	1000	0.43	30	787.24
S120×120×8	C20×1	120	8.0	2	20	1	3	1000	0.45	30	1160.76
	C25×1	120	8.0	2	25	1	4	1000	0.45	30	1158.33
	C30×1	120	8.0	2	30	1	4	1000	0.45	30	1154.85
	C35×1	120	8.0	2	35	1	4	1000	0.45	30	1152.24
S150×150×1	C20×1	150	1.0	4	20	1	3	1000	0.31	30	634.21
	C20×1	150	1.0	4	20	1	3	1000	0.34	40	814.66
	C20×1	150	1.0	4	20	1	3	1000	0.37	50	1004.72
S150×150×1.5	C20×1	150	1.5	4	20	1	3	500	0.16	30	688.63
	C20×1	150	1.5	4	20	1	3	1000	0.31	30	659.99
	C20×1	150	1.5	4	20	1	3	1500	0.45	30	626.00
S150×150×4	C20×1	150	4.0	4	20	1	3	1000	0.33	30	1040.46
	C20×2	150	4.0	4	20	2	1	1000	0.33	30	1051.51
	C20×5	150	4.0	4	20	5	1	1000	0.33	30	1078.04
S150×150×8	C20×1	150	8.0	3	20	1	3	1000	0.35	30	1584.07
	C25×1	150	8.0	3	25	1	4	1000	0.35	30	1583.52
	C30×1	150	8.0	3	30	1	4	1000	0.35	30	1581.23
	C35×1	150	8.0	3	35	1	4	1000	0.35	30	1578.02

Table C.4: Geometric dimensions, material properties and flexural strength of CFDSAT beams used in the parametric study.

Outer section	Inner section	D_o or B_o (mm)	t_o (mm)	Class	D_i or B_i (mm)	t_i (mm)	Class	f_c (MPa)	$M_{u,FE}$ (kN)
S60×60×1	S20×20×1	60	1	4	20	1	1	30	1.76
	S20×20×1	60	1	4	20	1	1	40	1.8
	S20×20×1	60	1	4	20	1	1	50	1.85
S60×60×1.5	S20×20×1	60	1.5	3	20	1	1	30	2.92
S60×60×4	S20×20×1	60	4	1	20	1	1	30	6.98
	S20×20×2	60	4	1	20	2	1	30	7.18
	S20×20×5	60	4	1	20	5	1	30	7.39
S60×60×8	S20×20×1	60	8	1	20	1	1	30	11.63
	S25×25×1	60	8	1	25	1	1	30	11.72
	S30×30×1	60	8	1	30	1	2	30	11.79
	S35×35×1	60	8	1	35	1	2	30	11.84
S75×75×1	S20×20×1	75	1	4	20	1	1	30	2.48
	S20×20×1	75	1	4	20	1	1	40	2.59
	S20×20×1	75	1	4	20	1	1	50	2.68
S75×75×1.5	S20×20×1	75	1.5	3	20	1	1	30	4.38
S75×75×4	S20×20×1	75	4	1	20	1	1	30	11.37
	S20×20×2	75	4	1	20	2	1	30	11.65
	S20×20×5	75	4	1	20	5	1	30	11.86
S75×75×8	S20×20×1	75	8	1	20	1	1	30	19.68
	S25×25×1	75	8	1	25	1	1	30	19.75
	S30×30×1	75	8	1	30	1	2	30	19.86
	S35×35×1	75	8	1	35	1	2	30	19.92
S100×100×1	S20×20×1	100	1	4	20	1	1	30	3.91
	S20×20×1	100	1	4	20	1	1	40	3.93
	S20×20×1	100	1	4	20	1	1	50	3.96
S100×100×1.5	S20×20×1	100	1.5	4	20	1	1	30	6.99
S100×100×4	S20×20×1	100	4	1	20	1	1	30	21.6
	S20×20×2	100	4	1	20	2	1	30	21.71
	S20×20×5	100	4	1	20	5	1	30	21.92
S100×100×8	S20×20×1	100	8	1	20	1	1	30	38.1
	S25×25×1	100	8	1	25	1	1	30	38.15
	S30×30×1	100	8	1	30	1	2	30	38.24
	S35×35×1	100	8	1	35	1	2	30	38.32
S120×120×1	C20×1	120	1	4	20	1	1	30	5.34
	C20×1	120	1	4	20	1	1	40	5.37
	C20×1	120	1	4	20	1	1	50	5.46
S120×120×1.5	C20×1	120	1.5	4	20	1	1	30	9.42
S120×120×4	C20×1	120	4	2	20	1	1	30	28.99
	C20×2	120	4	2	20	2	1	30	29.3
	C20×5	120	4	2	20	5	1	30	29.72
S120×120×8	C20×1	120	8	1	20	1	1	30	55.88
	C25×1	120	8	1	25	1	1	30	55.94
	C30×1	120	8	1	30	1	2	30	56.07
	C35×1	120	8	1	35	1	2	30	56.15

Table C.4 (continued): Geometric dimensions, material properties and flexural strength of CFDSAT beams used in the parametric study.

Outer section	Inner section	D_o or B_o (mm)	t_o (mm)	Class	D_i or B_i (mm)	t_i (mm)	Class	f_c (MPa)	$M_{u,FE}$ (kN)
C60×1	C20×1	60	1	4	20	1	1	30	1.5
	C20×1	60	1	4	20	1	1	40	1.55
	C20×1	60	1	4	20	1	1	50	1.6
C60×1.5	C20×1	60	1.5	3	20	1	1	30	2.08
C60×4	C20×1	60	4	1	20	1	1	30	4.35
	C20×2	60	4	1	20	2	1	30	4.5
	C20×5	60	4	1	20	5	1	30	4.64
C60×8	C20×1	60	8	1	20	1	1	30	7.5
	C25×1	60	8	1	25	1	1	30	7.59
	C30×1	60	8	1	30	1	2	30	7.68
	C35×1	60	8	1	35	1	2	30	7.79
C75×1	C20×1	75	1	4	20	1	1	30	2.29
	C20×1	75	1	4	20	1	1	40	2.37
	C20×1	75	1	4	20	1	1	50	2.45
C75×1.5	C20×1	75	1.5	3	20	1	1	30	3.27
C75×4	C20×1	75	4	1	20	1	1	30	7.54
	C20×2	75	4	1	20	2	1	30	7.65
	C20×5	75	4	1	20	5	1	30	7.72
C75×8	C20×1	75	8	1	20	1	1	30	11.9
	C25×1	75	8	1	25	1	1	30	12.01
	C30×1	75	8	1	30	1	2	30	12.12
	C35×1	75	8	1	35	1	2	30	12.22
C100×1	C20×1	100	1	4	20	1	1	30	3.75
	C20×1	100	1	4	20	1	1	40	3.82
	C20×1	100	1	4	20	1	1	50	3.9
C100×1.5	C20×1	100	1.5	4	20	1	1	30	5.75
C100×4	C20×1	100	4	1	20	1	1	30	14.28
	C20×2	100	4	1	20	2	1	30	14.4
	C20×5	100	4	1	20	5	1	30	14.5
C100×8	C20×1	100	8	1	20	1	1	30	24.53
	C25×1	100	8	1	25	1	1	30	24.61
	C30×1	100	8	1	30	1	2	30	24.84
	C35×1	100	8	1	35	1	2	30	25.28
C120×1	C20×1	120	1	4	20	1	1	30	5.32
	C20×1	120	1	4	20	1	1	40	5.49
	C20×1	120	1	4	20	1	1	50	5.58
C120×1.5	C20×1	120	1.5	4	20	1	1	30	8.26
C120×4	C20×1	120	4	2	20	1	1	30	20.27
	C20×2	120	4	2	20	2	1	30	20.55
	C20×5	120	4	2	20	5	1	30	20.65
C120×8	C20×1	120	8	1	20	1	1	30	35.01
	C25×1	120	8	1	25	1	1	30	35.42
	C30×1	120	8	1	30	1	2	30	35.6
	C35×1	120	8	1	35	1	2	30	35.93